DEVELOPMENT OF ADVANCED THERMODYNAMIC MODELS FOR CO_2 ABSORPTION

From numerical methods to process modelling

by

EDWARD JOHN GRAHAM

A thesis submitted for the Degree of
Doctor of Philosopy and the Diploma of
Imperial College London

Department of Chemical Engineering,
Imperial College London
London SW7 2AZ
United Kingdom

May 2020

Edward John Graham: *Development of advanced thermodynamic models for CO_2 absorption ,* From numerical methods to process modelling, © May 2020

SUPERVISORS:
Professor Claire S. Adjiman
Professor George Jackon
Professor Amparo Galindo

LOCATION:
London

DECLARATION OF ORIGINALITY

I herewith declare that all material presented in this thesis which is not my own work has been properly acknowledged.

London, May 2020

Edward John Graham

COPYRIGHT DECLARATION

Dedicated to my family.

ABSTRACT

This thesis considers the development of predictive thermodynamic models for amine-based carbon capture processes, motivated by the imminent requirement for the reduction in anthropogenically produced carbon dioxide emissions.

In the introduction, we show how the use of molecular-based equations of state, such as SAFT (Statistical Associating Fluid Theory), can be highly effective in this context. Due to the level of molecular detail captured in their theoretical development, one can reduce the reliance on experimental data by transferring their parameters based on sound physical arguments. In particular, the inherent chemical reactions in amine-based carbon dioxide absorption processes can be modelled by a physical association scheme, offering a vast simplification over the conventional treatments.

In the following chapter a rate-based absorber model is presented to investigate the reactive capture of carbon dioxide CO_2 using aqueous monoethanolamine (MEA) as a solvent. The SAFT-VR SW equation is used as the thermodynamic model. Due to the physical treatment of the reactions, the process model equations only needs to consider the apparent concentrations of the molecular species, while the reactions are implicit in the SAFT equation. With the assumption that the species diffuse as non-associated species, the rate of CO_2 absorption is over-predicted, providing an upper bound on the solvent performance. A single parameter is adjusted to the pilot plant data, reflecting the reduction in mass transfer rate in the apparent CO_2 in its aggregated form, which is found to be transferable over all of the pilot plant runs.

The development of new models for the SAFT-γ Mie equation is then considered for improvement of the thermodynamic model. This is because the thermodynamic models developed for the SAFT-VR SW (used in the absorber) provide an inaccurate description of the liquid heat capacity and the heat of absorption of CO_2. We consider a novel approach to the parameter estimation problem. It is shown that posing the parameter estimation as a multi-objective optimization problem offers numerous advantages over conventional (single-objective optimization) techniques. A robust and efficient algorithm that deals with multiple objective functions is tailored for this purpose. We consider objective functions that characterise the deviation between the SAFT model and experimental measurements for different thermodynamic property types. Using the multi-objective optimization technique we develop SAFT-γ Mie models for water where saturated liquid denisty, vapour pressure and isobaric heat capacity are treated as competing objectives. A single (non-spherical) model for water is chosen from the Pareto fronts obtained.

Next, we develop SAFT-γ Mie (or SAFT-VR Mie) models for the CO_2 + MEA + H_2O mixture, with focus on developing models that provide a simultaneous accurate description of the vapour-liquid equilibria and the caloric properties. In comparison with the previous models developed for the SAFT-VR SW equation of state, the new models provide a better description of key thermodynamic properties in the chemisorption process, in particular the vapour pressure of CO_2 above

the solvent mixture, the isobaric liquid heat capacity and the heat of absorption. We show that incorporating the new thermodynamic models in our process model for the absorber, we obtain a slightly better prediction of the column temperature profile.

In the last chapter we derive a classical density functional theory (DFT) that incorporates the SAFT-VR Mie equation of state (SAFT-VR Mie MF DFT). The proposed method is applicable for a wide variety of fluids, including fluids/ fluid mixtures that consist of associating molecules and molecules of varying chain length. We derive a theory that is numerically tractable and show a novel implementation of the DFT equations in gPROMS. We show that the theory can be used to accurately predict the experimental interfacial tension for the SAFT models developed in this thesis, and the predicted density profiles in the intefacial region compare favourably with molecular simulations. The SAFT-VR Mie MF DFT approach developed in this chapter is used throughout the thesis for validation of the thermodynamic models.

With thermodynamics, one can calculate almost everything crudely; with kinetic theory, one can calculate fewer things, but more accurately; and with statistical mechanics, one can calculate almost nothing exactly.— Eugene Wigner

ACKNOWLEDGEMENTS

First and foremost I would like to thank my three supervisors for their support during my PhD studies: Professor Amparo Galindo, Professor Claire Adjiman and Professor George Jackson. They have provided the right balance of allowing me to pursue my research ideas and putting me on track when needed. I am extremely grateful for their invaluable scientific guidance and their encouragement which has helped me greatly through these years.

This PhD would not have been possible without the continuous distractions and friendly atmosphere caused by my good friends in the MSE office, which it has been a privilege to be part of. To name just a few: Maz, Naveed, Tom, Harry, Isaac, Spiros, Dave, Stephanos, Karl, Felipe, Lauren, Sara, Hajar, Smitha, Eliana, Fabian, and also the endless list of friends I have made during the PhD.

I would like to also thank the thermodynamics group of Professor Hans Hasse in the University of Kaiserslautern, for accommodating me and making my time spent there a thoroughly enjoyable experience. In particular, I would like to thank Dr. Esther Forte and Prof. Jakob Burger. The multi-objective optimization work conducted in this thesis would not have been possible without them and their fruitful discussions. Furthermore, this work would not have been possible without the team at Process Systems Enterprise. In particular, I thank Vasileios Papaoioannou, Simon Dufal and Tom Lafitte for their correspondence and help with the gSAFT software and parameter estimation codes, and Costas Pantelides for his guidance in the solution to the density functional theory problem.

Of course, nothing would have been possible without the endless support from my friends and family, would always be there for me. Thanks to my parents, Dave and Corie, my brother Jamo, my American friend Liam, and my housemates who have put up with me for the past 4 years.

CONTENTS

LIST OF FIGURES

LIST OF TABLES

1 THESIS OVERVIEW

1.1 MOTIVATION AND OBJECTIVES

It is now generally accepted in the scientific community that anthropogenically emitted carbon dioxide (CO_2) is a major concern with regards to climate change and global warming. Recent studies show an almost linear relationship between the rate of global temperature change and the rate of increase in cumulative carbon emissions (Matthews et al., 2012; Friedlingstein et al., 2014; Raupach, 2013). The Cancun Agreements in 2010 set a limit for what could be considered a "dangerous" level of climate change: the global temperature should remain 2°C above pre-industrial levels, or approximately 1.4°C above current levels. However, two thirds of this corresponding CO_2 quota has already been used and the remaining will be exhausted in 30 years based on 2014 emission rates. Global emissions of CO_2 from combustion of fossil fuels and cement production have continued to grow over the past decade by 2.5% per year on average (2004-2013). There is an increasing incentive for companies to reduce their carbon emissions as the price of carbon increases and governments strive to meet their emission reduction targets. (Friedlingstein et al., 2014).

Fossil fuel power plants, in particular coal-fired plants, are the largest fixed point-source emitters, accounting for approximately one third of CO_2 emissions, and will remain so for the foreseeable future due to the high energy density, proven resource base and established infrastructure for fossil fuels (Mac Dowell et al., 2010; Choi et al., 2009a). Carbon Capture and Storage (CCS) technologies are seen to be the most promising short-term solution to the reduction of CO_2 emissions, and amine-based post-combustion capture processes are seen as the most promising near-term technology in terms of technological development and applicability (Sreenivasulu et al., 2015; Mac Dowell et al., 2010). The 'Capture' part of CCS in this instance involves the separation of CO_2 from the flue gas, consisting mainly of nitrogen (N_2) if the fossil fuel is combusted with air, and CO_2. Amine-based absorption processes exploit the reversible chemical reaction between CO_2 and the amine solvent, making the process suitable for capturing CO_2 from dilute and low pressure streams which can be fitted to existing fixed-point sources with relative ease. The main disadvantages of using this technology as it currently stands include the large energy penalty associated with solvent regeneration, and the environmental harm resulting from solvent losses and solvent degradation products (Jackson and Attalla, 2011).

Modelling studies can play an important role in addressing some of these issues. A key challenge for CO_2 capture is the design of solvents which constitute a process that is both economically and environmentally favourable, without the extensive reliance on experimental data. There is a lack of data to decide on an optimal solvent, particularly solvent mixtures (Kontogeorgis and Folas, 2010), and a lack of pilot plant data to decide on an optimal design of the absorber-desorber process.

The thermodynamic properties of CO_2-amine-H_2O mixtures give us vital information about their viability for use in a process and are required for the accurate modelling of a chemisorption plant. Some important thermodynamic properties in this context are those that determine the vapour-liquid equilibria such as the partial pressure of CO_2 above the loaded amine solution. This gives us information on the absorption capacity of the solvent and the selectivity towards CO_2. Caloric thermodynamic properties are important because they largely determine the energy requirement for regeneration in the desorber unit. The key thermodynamic quantities that contribute to this energy requirement are the liquid heat capacity, the heat of vapourization of water, and the heat of absorption (or desorption) of CO_2 in the solvent Gupta et al. (2013); Kim and Svendsen (2007); Arcis et al. (2011); Mathonat et al. (1998). Furthermore, surface tension can have a spectacular effect on the interfacial area and the rate of mass transfer within absorption/desorption columns (Zuiderweg and Harmens, 1958). In the context of designing better absorption-desorption processes, it is clear that accurate and predictive (i.e., applicable outside the domain of experimental data) thermodynamic models for CO_2-amine-H_2O systems, which correctly capture the phase equilibria, caloric properties, and surface tension, are required in order to model and optimize the chemisorption process. A key theme of this thesis is therefore developing thermodynamic models that suit this need.

In this thesis, we will work with a particular type of equation of state (EoS) known as SAFT (Statistical Associating Fluid Theory). SAFT models are EoSs with a firm theoretical grounding in statistical mechanics, a field which originates from the desire to describe thermodynamic systems in terms of mechanical principles, for which Clausius, Maxwell and Boltzmann were the founders. SAFT was first published in 1990 (Chapman et al., 1990), and a principle motivation for its development was the requirement for an equation of state for associating and non-spherical molecules which could not be described by traditional cubic EoSs. The most recent development of the SAFT-VR equation of state, SAFT-VR Mie Lafitte et al. (2013a), looks very promising as it provides excellent agreement with experimental data and can describe the phase equilibira and second-derivative (including C_P and the heat of absorption) thermodynamic properties simultaneously (Lafitte et al., 2007).

The association theory within SAFT is based on Wertheim's Thermodynamic Perturbation Theory (TPT) Wertheim (1984a,b, 1986a,b), which gives the change in free energy due to association for a fluid of monomers. Chemical association is mediated using "sticky spot" models, where molecules can interact via an attractive potential placed on the outside of a repulsive core. This directional interaction essentially captures quantum mechanical effects, corresponding to the change in internal electronic configurations, rotational degrees of freedom, etc. upon association. This free energy contribution represents types of intermolecular interactions that are highly-directional and short-ranged and is therefore typically used to represent a hydrogen-bond, of which there are numerous types of in the CO_2-amine-H_2O mixture. Furthermore, this technique (which we refer to as the 'physical approach') may be used to model the chemical reactions that occur in the mixture, with the ability to offer vastly simplified thermodynamic and process models compared to the more traditional chemical approaches. In this thesis we will demonstrate how one can implement this atypical physical approach for the

thermodynamic treatment of CO_2-amine-H_2O, and show how such a model can be incorporated into a rate-based absorber model.

The parameters within SAFT models define the intermolecular potential, and simulations of this potential have been shown to compare favourably Lafitte et al. (2013a). This validates the assumptions and approximations within the theoretical model. The situation becomes challenging when one wants to develop specific SAFT models for *real* fluids. In order to develop such models, one needs to estimate the parameters that define the intermolecular interactions using experimental data. Usually, there are many suitable parameters sets that successfully correlate the experimental data. Thus, the most suitable intermolecular potential is the one that best captures the physics of the system, like the structure of the fluid or it's dynamic properties.

Due to the simplifications made to describe the real intermolecular potential, it is difficult to simultaneously capture all of the desired thermodynamic properties in a simple model. One inevitably needs to choose a model that provides the best compromise between the predictions of various thermodynamic properties. This choice can change according to the specific scenario that the thermodynamic model is applied, and it is often unclear the trade-offs that are involved when choosing a particular model. With an increasing number of types of thermodynamic properties that we assess the model's performance with respect to, the choice of model becomes increasingly more difficult. We will address these issues in this thesis by developing a multi-objective optimization methodology, providing a novel approach to the estimation of SAFT parameters and general applicability to any parameter estimation problem.

We have discussed that surface tension is an important property for modelling the chemisorption process, as it can dramatically affect the interfacial area available for mass transfer. This pronounced effect can clearly be seen when soap accumulates at the air-water interface, leading to bubble formation. SAFT-VR Mie provides accurate predictions for the 'bulk' fluid phase properties, however it cannot be used directly to compute the surface tension. To evaluate the surface tension, one requires knowledge of small interfacial region that occurs between two phases: the density profile and the free energy as a functional of this density profile. In this thesis we develop a density functional theory (DFT) that can be used as a fully predictive method for evaluating the surface tension of SAFT-VR Mie models. This is useful from a process modelling aspect when one does not have this type of experimental data. Since this method introduces a new type of property to be compared to experiments, this is also useful for validating models during model development and reducing the degeneracy in the parameter space.

1.2 OVERVIEW OF CHAPTERS

In chapter 2 we provide a review of the molecular systems engineering (MSE) approach to carbon capture, with a brief mention of other work based on similar thermodynamic models. Here we discuss various approaches to modelling thermodynamic properties, with a special focus on the SAFT (Statistical Associating Fluid Theory) family of thermodynamic approaches. We pay special attention to show how one can take advantage of the physical association concept used with

the equation of state (EoS) to describe the reaction equilibria relevant to chemical absorption, and contrast this approach to the explicit approach that is more typically used in the modelling of such systems. Furthermore, we discuss approaches to the solution of the integrated solvent and process design problem that embed these thermodynamic models.

After presenting the SAFT approach used throughout this thesis, in chapter 3 we present a rate-based absorber model that incorporates a particular version of SAFT (SAFT-VR SW) to investigate the reactive capture of carbon dioxide CO_2 using aqueous monoethanolamine (MEA) as a solvent. We demonstrate how one can incorporate SAFT models that use a physical treatment of the reactions into a rate-based model, and demonstrate that the process model equations can be vastly simplified (compared to explicit approaches) using this technique. The process model equations only needed to consider the apparent concentrations of the molecular species, while the reactions are implicit in the SAFT equation. We show that by incorporating the SAFT-VR SW EoS and applying a physical association scheme to mediate reactions, one is able to make accurate predictions of the absorption process by comparing with pilot plant data and is therefore suitable for the rapid assessment of carbon capture solvents.

Following the work presented in chapter 3 we propose using a more recent equation of state (SAFT-γ Mie). This is to provide a better description of the thermodynamics, in particular the simultaneous description of the vapour-liquid equilibria and caloric properties of the mixtures discussed in chapter 3. These data types are vitally important for the accurate modelling of the CO_2 chemisorption process.

Due to the additional property types required to describe the caloric properties, in chapter 4 we propose a novel technique for regressing EoS parameters. Typically when regressing EoS parameters, deviations between the various property types are lumped together in a single weighted-sum objective function and a single set of parameters is obtained. By choosing weights arbitrarily (typically only a single weight vector is chosen) one has little control over the distribution of errors over the various property type, and this becomes an increasing issue the more property types are included. In this chapter we propose a multi-objective optimization (MOO) technique to deal with this problem, where the output is numerous different Pareto-optimal thermodynamic models. We demonstrate the effectiveness of this approach by applying the MOO technique to the development of SAFT-γ Mie for water, and identify a suitable water model from the Pareto front.

In chapter 5 we develop SAFT-γ Mie homonuclear models for the molecules and their mixtures present in the chemisorption process presented in chapter 3. Focus is made on developing models that provide a simultaneous accurate description of the vapour-liquid equilibria and caloric properties according to the findings in chapter 3. The MOO technique in chapter 4 is applied to develop the key thermodynamic parameters that mediate the chemical reactions. We show that using the proposed approaches, one is able to obtain an excellent description of the key thermodynamic properties that are required for modelling the CO_2 chemisorption process, in particular the the liquid heat capacity, the partial pressure of CO_2 and the heat of absorption of CO_2. Furthermore, we show that the physical approach to the reactions is able to predict the chemical speciation accurately. To conclude this chapter we assess the performance of the new models obtained against pi-

lot plant data for the absorption process discussed in chapter 3 and compare this performance with the previous result.

During the development of the thermodynamic models in chapters 4 and 5 we assess the robustness of the parameters obtained comparing the predicted values in the surface tension with experimental data. In order to calculate the interfacial tension for the homonuclear SAFT-γ Mie models, we develop a classical density functional theory (DFT) in chapter 6 that is suitable for this purpose. We validate the theory against molecular simulations, and show that one is able to use the proposed theory to accurately predict the interfacial tension and density profiles obtained in molecular simulations. This is shown for pure components and mixtures of up to three components. We then assess the performance of the model in predicting the vapour-liquid interfacial tension of the SAFT-γ Mie models for real molecules and mixtures relevant to this thesis. We identify an issue with using the DFT approach to predict the surface tension for SAFT-γ Mie models that contain association at low temperatures and propose some recommendations for future work.

We conclude the thesis in chapter 7 by summarising the key results and suggesting some avenues for future research.

2 BACKGROUND

2.1 INTRODUCTION

There is an increasing global concern about climate change, and an urgent need to mitigate anthropogenic CO_2 emissions. Carbon Capture, Utilisation and Storage (CCUS) comprises technologies to remove CO_2 from different sources (e.g., flue gases and from the atmosphere), followed by recycling this CO_2 for utilization or establishing permanent storage options. Carbon capture is a critical first step of CCUS. Although significant effort has been devoted towards the design and implementation of carbon capture technologies, current implementation remains costly, mainly due to the large energetic costs and the degradation of carbon capture materials associated with current processes. Among other options, CO_2 absorption using a liquid solvent is a competitive technology for CO_2 removal from gas streams (Olajire, 2010; Mac Dowell et al., 2010). A significant advantage of such processes are that they can be retro-fitted to existing processes that generate energy from fossil fuels. A solvent can absorb CO_2 through two main mechanisms: chemical absorption and physical absorption. In chemical absorption processes, reaction products are formed and CO_2 is chemically bound in the liquid phase, typically through the formation of ionic species. On the other hand, physical absorption processes are driven by weaker van der Waals forces between the solvent and CO_2.

The main advantages of chemical absorption over physical absorption are that chemical solvents have a higher capacity for CO_2 (Kenarsari et al., 2013), they can be applied to streams with relatively low CO_2 partial pressures, and the absorption rate is enhanced due to the depletion of CO_2 at the gas-liquid interface due to reactions. The regeneration of chemical solvents can be highly energy intensive however (Chakma, 1997), whereas carbon capture processes using physical solvents can be less energy intensive and the solvent can be regenerated with a less costly pressure-swing process.

Several carbon capture-solvents have been considered, and their potential viability for use in a CO_2 separation process have been assessed. The main classes of chemical solvents include alkanolamines, amino acids, ammonia, ionic liquids and aqueous piperazine (PZ). The reader is referred to Songolzadeh et al. (2014) for a summary of the advantages and disadvantages between these solvent types. Aqueous solutions of alkanolamines, particularly monoethanolamine (MEA), remain the most widely used class of chemisorption solvents. Common physical absorption process currently in use are Rectisol (methanol solvent), the Selexol process (using a blend of polyethylene glycol and a blend of dimethyl ethers), the Purisol process (N-methyl-2-pyrrolidone solvent), and the Fluor Solvent process (using a propylene carbonate solvent) Yu et al. (2012). Processes that use a mixture of physical and chemical solvents have also been investigated (Olajire, 2010), in addition to switchable solvents, for example reversible ionic liquids, where the

solvent species are non-ionic prior to reaction with CO_2 and an ionic liquid is formed upon reaction (Park et al., 2015).

The choice of solvent directly affects the performance of absorption technologies. Since there is a need to develop lower-cost and more sustainable CO_2 absorption processes, there have been numerous scientific investigations into new carbon capture solvents. In the search for new solvents and solvent blends, it is unlikely that a 'best' solvent or solvent mixture will be found. An optimal solvent will be a function of the thermodynamic conditions of the process (temperature, pressure and composition) and a function of the conditions of the gas feed (e.g., the pressure and chemical composition). Furthermore, there are process constraints that need to be considered (e.g., size constraints, restrictions on temperature and pressure, and restrictions on the available equipment). Traditionally, solvent selection and process design have been addressed as separate or consecutive problems, with little or no feedback between the two approaches (Eden et al., 2004). This makes solvent selection a laborious task. Laboratory scale experiments on candidate solvents are expensive and time consuming, and it is difficult to interpret experimental measurements (e.g., various physical properties of the solvent mixtures containing CO_2) within the highly dimensional solvent and process design space. It is therefore especially desirable to decouple process and molecular design problems, since large combinatorial spaces can theoretically be explored using computational methods. Such approaches can identify optimal solvents based on appropriate physical property models and only a small number of targeted experiments (Gani, 2004).

Computer-aided molecular design (CAMD) methods are useful for the solvent selection process. These are often focussed on providing a list of 'optimal' solvents based on a few important physicochemical properties (Gani, 2004; Duvedi and Achenie, 1996; Churi and Achenie, 1997; Apostolakou and Adjiman, 2002; Wang and Achenie, 2002; Samudra and Sahinidis, 2013). Several studies have been conducted in order to assess the impact of solvent properties on the overall performance of the process (Odele and Macchietto, 1993; Buxton et al., 1999; Bardow et al., 2009; Adjiman et al., 2014). Through such methods it is possible to determine the dependence of physicochemical properties on process variables (e.g., operating pressure and temperature), the values of which are often unknown at the time of solvent selection. It has become clear that choice of an optimal solvent is best considered as part of an integrated molecular and process design problem due to the strong interactions between optimal process variables and optimal molecular variables (Adjiman et al., 2014).

Several methodologies have therefore emerged for the simultaneous design of molecules (e.g., solvents) and processes, where process variables and molecular structure are optimized with respect to process objectives (e.g., cost). This is known as computer-aided molecular and process design (CAMPD). The CAMPD problem has been discussed by numerous authors (Hostrup et al., 1999; Buxton et al., 1999; Kim and Diwekar, 2002; Giovanoglou et al., 2003; Marcoulaki et al., 2000; Eden et al., 2004; Papadopoulos and Linke, 2006; Eljack et al., 2008; Bardow et al., 2009; Pereira et al., 2011a; Burger et al., 2015; Lampe et al., 2015; Ng et al., 2015; Papadokonstantakis et al., 2015; Zhou et al., 2015; Gopinath et al., 2016).

Since intermolecular interactions strongly affect the performance of absorption processes, CO_2 capture studies are well-suited for the application of a molecu-

lar systems engineering approach. Within an MSE approach, a detailed molecular model (e.g., a molecular-based thermodynamic model for fluids) is integrated with a process model (Adjiman et al., 2014; Adjiman and Galindo, 2011). Thus, predictive models are required that relate the physical properties of fluids (pure components and mixtures), in addition to predictive models of process units, in order to evaluate design objectives and constraints. Furthermore, optimization problems must be set up such that trade-offs between different design decisions cab be explored, and advanced algorithms are required in order to solve the challenging optimization problems that arise.

In the context of the integrated design of solvents and carbon-capture absorption processes, an MSE approach requires predictive models for a range physicochemical properties: bulk thermodynamic properties such as density and vapour-liquid equilibria, kinematic properties such as viscosity and interfacial properties such as surface tension. These properties should be readily calculated for a fluid as a function of the process operating conditions. Preferably, physical property models should provide a continuous and consistent description for the entire fluid region in order to avoid the use of different models (e.g., activity coefficient models and equations of state) for gas and liquid phases (Burger et al., 2015). This consistency is particularly important when modelling fluids close to vapour-liquid critical points, and when modelling unit operations that involve phase changes, in order to avoid having to identify phases before selection of an appropriate model. Furthermore, is desirable to use models that provide accurate predictions not only of vapour-liquid equilibrium properties but also second-derivative thermodynamic properties (e.g., heat capacity). Thus, it is important to use a consistent thermodynamic model for calculating different physical property types. It can be challenging to find models that are so widely applicable (Poling et al., 2001; Lafitte et al., 2013b; Papaioannou et al., 2014). Finally, in the context of modelling chemisorption processes it is challenging to predictively model chemical equilibrium and/or kinetics.

Several authors have developed CAMPD approaches to CO_2 capture in recent years. Bardow et al. (2009), Pereira et al. (2011a), Burger et al. (2015), and Lampe et al. (2015) have designed optimal solvents and process process conditions for CO_2 capture involving physical absorption of CO_2 into the solvent. Their work incorporated statistical associating fluid theory for describing physical properties. Chong et al. (2015) employed CAMD to determine suitable ionic liquids for carbon-capture. Salazar et al. (2013) and Zarogiannis et al. (2016) applied CAMD approaches for the design of alkanolamines and their blends. CAMPD has also been applied for determining novel chemisorption solvents (Bommareddy et al., 2010; Chemmangattuvalappil and Eden, 2013; Papadokonstantakis et al., 2015).

In this chapter we will review molecular systems engineering approaches to carbon capture. In Section 2.2, we will discuss thermodynamic models for CO_2 absorption processes, with a focus on SAFT-type equations of state. In Section 2.3 we will describe how one can model reactive systems using the physical association concept available to SAFT.

2.2 PREDICTIVE THERMODYNAMIC MODELS FOR CO_2 PHYSISORPTION PROCESSES

In order to accurately model physisorption processes, sophisticated thermodynamic models are required in order to capture the non-ideal behaviour of the mixtures involved. This non-ideal thermodynamic behaviour arises due to the presence of chemical functional groups that form hydrogen bonds (e.g, in water, methanol and ethers), the presence of non-spherical apolar compounds (hydrocarbons), and the presence of CO_2 which has a large quadrupole moment and a critical temperature (304 K) that is within the range of typical process operating conditions. Further complexity in the thermodynamic model arises when modelling solvent blends due to the larger number of model parameters required.

Thermodynamic models that are predictive outside of the domain of experimental data are required, and models derived from molecular theories and statistical mechanics, for example SAFT-based approaches are well-suited for this purpose. For an overview of such approaches, the reader is referred to (McCabe and Galindo, 2010), (Kontogeorgis and Folas, 2010) and references therein. These require fewer state-dependent parameters compared to more commonly used thermodynamic models. Within SAFT-based approaches, the impact of molecular shape and non-sphericity is accounted for by modelling molecules as chains of fused monomeric segments, and the strong directional interactions representative of a hydrogen bond or polar interactions can be mediated by the addition of association sites. Since SAFT-based models provide an equation of state (EoS), they are applicable over the entire fluid region and thus a consistent model may be used for gas and liquid phases. This is beneficial for modelling processes consisting of vapour-liquid and vapour-liquid-liquid equilibria. In this section, we will provide an overview of SAFT-based approaches and discuss the development of models (including group contribution models) that describe the thermodynamics of typical physical absorption processes.

2.2.1 *An Introduction to SAFT*

Given the extensive application of SAFT in this thesis for modelling the thermodynamics of CO_2 capture processes, it is imperative to provide a brief introduction to this statistical mechanical theory and highlight its applicability in process design. In the appendix to this chapter, section 2.5, we detail the full SAFT-VR Mie equation used throught this thesis.

Statistical associating fluid theory (SAFT) approaches are a family of state-of-the-art EoSs, predicting thermodynamic properties of a system based on molecular interactions of different moieties constituting the system. The first version of the SAFT EoS (Chapman et al., 1989, 1990) was proposed to accurately describe the thermodynamics of associating fluids, i.e., fluids that have directional, short-range interactions, thus improving upon previous modelling of said fluids using traditional cubic EoSs. In order to achieve this, a new association theory was developed to evaluate the contribution to the Helmholtz free energy due to association of a fluid composed of associating monomers, based on Wertheim's thermodynamic perturbation theory (TPT) Wertheim (1984a,b, 1986a,b). This association theory

models the contribution to the Helmholtz free energy due to association in a fluid of monomers. The directional forces due to association are accounted for by specifying off-center "association sites" on the monomers, which interact via a potential function that is typically of the square-well (SW) form. Accurate thermodynamic properties of associating fluids can thus be obtained with a SAFT equation with parameters that provide information on the intermolecular forces.

Within all SAFT models, molecules are represented as chains of spherical segments. These segments interact via intermolecular potentials that determine the forces between segments and between association sites. In homonuclear versions of SAFT, a molecule i is formed from m_i tangentially bonded spherical segments, i.e., the segment-segment separation is σ (see equations 1 and 2) defined later in this section. m_i should strictly take on integer values in the theory, but this constraint is generally relaxed so that m_i can take on non-integer values. In this case, segments may be referred to as 'fused'. To model real fluids and mixtures of real compounds, parameters are required that specify the number of segments and the intermolecular potential (i.e., the energy and range of interaction between segments and association sites). Homonuclear models may be used to represent whole molecules, where a single set of parameters is used to describe a specific compound. This contrasts with heteronuclear approaches where a set of parameters is prescribed to a particular chemical functional group.

Numerous homonuclear versions of SAFT exist to describe neutral molecules, where differences between approaches vary mainly in the form of the potential used to describe the repulsive and attractive interactions between monomer segments, the explicit inclusion of different interaction types (e.g., the inclusion or not of an explicit dipole contribution), and choices/ simplifications made in the statistical mechanical theory (e.g., the order of the perturbation expansion in the monomer free energy contribution and the choice of reference fluid). Some well known variants (Kontogeorgis and Folas, 2010) of SAFT are the original SAFT (Chapman et al., 1990, 1989), Chen and Kreglewski SAFT (CK-SAFT) (Huang and Radosz, 1991), simplified SAFT (Fu and Sandler, 1995), Lennard-Jones SAFT (LJ-SAFT) (Kraska and Gubbins, 1996b,a), variable-range SAFT, (SAFT-VR or SAFT-VR SW) (Gil-Villegas et al., 1997; Galindo et al., 1998), SAFT-VR Mie (Lafitte et al., 2013b; Dufal et al., 2015b), soft-SAFT (Blas and Vega, 1998), perturbed chain SAFT (PC-SAFT) (Gross et al., 2001), and simplified PC-SAFT (von Solms et al., 2003). Examples of SAFT that include an explicit polar/ dipolar contribution include a variant of SAFT-VR (Zhao and McCabe, 2006), a variant of CK-SAFT (Jog et al., 2001), variants of PC-SAFT (Tumakaka and Sadowski, 2004; Tumakaka et al., 2005; Sauer and Chapman, 2003; Karakatsani et al., 2005; Karakatsani and Economou, 2006; Karakatsani et al., 2006; Gross, 2005; Gross and Vrabec, 2006; Kleiner and Gross, 2006; Karakatsani and Economou, 2007; Kleiner and Sadowski, 2007), and a polar variant of SAFT-VR Mie (Cripwell et al., 2018). Extensions of the SAFT methodology that can be used to model electrolyte solutions have also been developed (Galindo et al., 1999; Liu et al., 1999; Gil-Villegas et al., 2001; Patel et al., 2003a; Behzadi et al., 2005; Cameretti et al., 2005; Held et al., 2008; Held and Sadowski, 2009; Schreckenberg et al., 2014; Eriksen et al., 2016). Furthermore, modifications to the SAFT methodology have been recently developed in order to describe quantum fluids (e.g., helium and hydrogen) (Aasen et al., 2019).

The SAFT-VR SW and SAFT-VR Mie equations of state are of most relevance to this thesis since they are used extensively. We will therefore briefly review the SW and Mie potentials, which describe the potential between monomeric segments. The SW potential used in SAFT-VR SW (Gil-Villegas et al., 1997; Galindo et al., 1998) is given by

$$\phi_{12}^{SW}(r_{12}) = \begin{cases} \infty & r_{12} < \sigma, \\ -\epsilon & \sigma \leqslant r_{12} < \lambda\sigma, \\ 0 & r_{12} \geqslant \lambda\sigma, \end{cases} \tag{1}$$

where ϕ_{12}^{SW} is the potential, r_{12} is the distance between the centres of two spherical monomeric segments 1 and 2, where σ is the diameter of the monomeric segments, ϵ is the depth of the potential well, and the range of attraction is characterised by λ. The SW potential is popular due to its simplicity, leading to exact statistical mechanical derivations, for example algebraic expressions of the second and third virial coefficients (Barker and Henderson, 1976).

In the more recently developed SAFT-VR Mie EoS (Lafitte et al., 2013b), the Mie (generalised Lennard-Jones) potential is used, which is given by

$$\phi_{12}^{Mie}(r_{12}) = C\epsilon \left[\left(\frac{\sigma}{r_{12}} \right)^{\lambda^r} - \left(\frac{\sigma}{r_{12}} \right)^{\lambda^a} \right], \tag{2}$$

where the coefficient C is defined such that the minimum of the potential corresponds to $-\epsilon$ and is given by

$$C(\lambda^r, \lambda^a) = \frac{\lambda^r}{\lambda^r - \lambda^a} \left(\frac{\lambda^r}{\lambda^a} \right)^{\frac{\lambda^r}{\lambda^r - \lambda^a}}. \tag{3}$$

where λ^r is the repulsive exponent and λ^a is the attractive exponent. λ^r is a key parameter which provides flexibility in characterising the softness or hardness of the repulsive interaction. The Mie potential consists of a relatively steep portion at short separations and a smooth shallow curve at greater separations which asymptotically approaches zero as r_{12} approaches infinity. A comparison with the SW potential is shown in Figure 1. The Mie potential is longer-ranged and smoother than the SW potential, allowing for a more realistic description of the true segment-segment interaction.

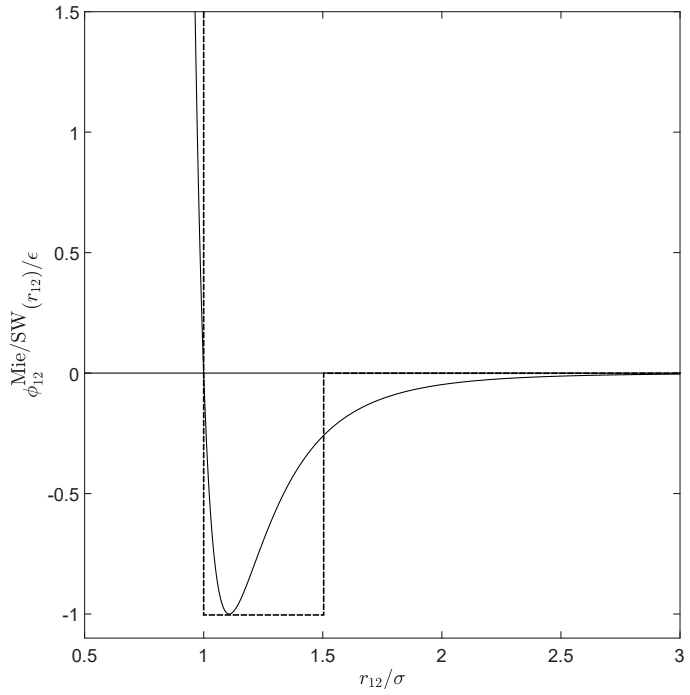

Figure 1: Examples of the Mie (continuous curve) and the SW (dotted line) potentials as a function of the monomer-monomer separation distance.

Within SAFT, association forces can be treated by adding off-centre, spherically symmetric bonding sites which interact via a potential that is typically of the SW form. This potential is used to characterise interactions that are highly directional and short-ranged, for example an interaction typical of a hydrogen bond (Dufal et al., 2015b). The interaction between two association sites 'a' and 'b' on two molecules of type i is characterized by an association energy ϵ^{HB}_{abii}, and a bonding volume K_{abii}.

Within SAFT, an equation for the total Helmholtz free energy developed by adding different perturbative contributions (representing different types of intermolecular force) to a reference free energy. In Figure 2 we demonstrate this concept. In this case, the reference fluid consists of monomeric spherical segments, as is the case in the SAFT-VR SW and SAFT-VR Mie EoSs. In dimensionless form the equation for the free energy is given by

$$\frac{A}{NkT} = \frac{A^{IDEAL}}{NkT} + \frac{A^{MONO.}}{NkT} + \frac{A^{CHAIN}}{NkT} + \frac{A^{ASSOC.}}{NkT}, \tag{4}$$

where N is the number of molecules, k the Boltzmann constant, and T the temperature. A^{IDEAL} is the free energy of an ideal gas (Figure 2a). For real molecules this contribution is typically determined from experimental information on the molecular ideal gas heat capacity. $A^{MONO.}$ is derived by perturbing from a reference hard-sphere fluid (here, a volume is perscribed to the segments), the perturbative contributions arise from the chosen inter-segment potential (Figure 2b). A^{CHAIN} represents the free energy due to spherical segments forming tangentially-bonded chains (Figure 2c). $A^{ASSOC.}$ is the free energy contribution due to interaction be-

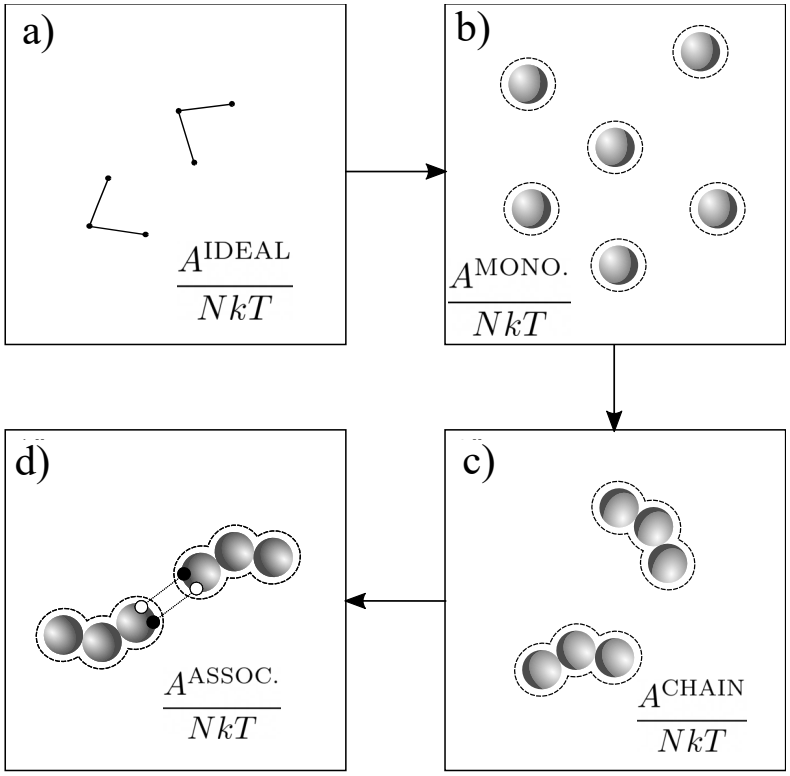

Figure 2: Schematic of a typical procedure for describing fluids within a SAFT EoS. a) The ideal gas contribution: this includes contributions to the free energy that are not due to intermolecular interactions (e.g., translational, rotational and vibrational contributions). b) The monomer contribution: interactions between spherical segments are considered, with the potential shown by the dotted circles. c) The chain contribution: the additive free energy due to molecules forming tangentially bonded segments. d)The association contribution: association sites are added which are able to bond to other sites. This figure is based on that of (Kontogeorgis and Folas, 2010).

tween association sites (Figure 2d). This term accounts for various types of complexation such as charge transfer and hydrogen bonding. Once the total Helmholtz free energy is known as a function of the thermodynamic variables (N, V, T), other thermodynamic properties can be obtained from known thermodynamic identities. For example, the pressure can be obtained from $P = -(\frac{\partial A}{\partial V})_{N,T}$, and the chemical potential μ can be obtained from $\mu = (\frac{\partial A}{\partial N})_{V,T}$.

The inclusion of the Mie potential in the more recent development in SAFT-VR (SAFT-VR Mie (Lafitte et al., 2013b; Dufal et al., 2015a,b)) is of particular relevance to this thesis. This potential has shown to be particularly advantageous for accurately describing properties that are second derivatives of the Helmholtz free energy. These properties include heat capacity, isothermal compressibility and the speed of sound, and SAFT-VR Mie is able to simultaneously provide a good description of both vapour-liquid equilibria (VLE) properties and second derivative properties (Lafitte et al., 2006b, 2013b; Dufal et al., 2015a,b). Second derivative properties are particularly sensitive to the nature of the repulsive interaction, and thus models may be finely tuned to such properties by varying λ^r. Furthermore,

SAFT-VR Mie includes a higher-order Barker-Henderson perturbation expansion of the monomer contribution (up to third order), compared to SAFT-VR SW (up to second order). This modification leads to an improved description of the critical point compared with SAFT-VR SW.

These improvements are vitally important when modelling solvent absorption processes for carbon capture, since the critical point of CO_2 is within the range of realistic process operating conditions. Additionally, the ability to accurately describe second-order derivative properties is important, in particular the heat capacity of liquid mixtures (the assumption of ideal mixing that is usually made to compute mixture heat capacities can be lifted), and heat of absorption of CO_2 in the solvent mixture as these properties are strongly correlated with the energetic cost of a carbon capture process. By using a consistent model to calculate key thermodynamic properties within a process model, less empirical correlations and experimental investigations are required. Although one more parameter is required to define the Mie potential compared to the SW potential, it has been shown that a conformal description of the thermodynamics can be obtained with an interrelationship between λ^r and λ^a under certain assumptions (Ramrattan et al., 2015). Thus, only λ^r or λ^a need to be determined during the model development, the other being fixed. Typically, λ^a is fixed to 6, corresponding to the attractive range of the London dispersion force, and λ^r is adjusted.

2.2.2 *Group contribution (GC) versions of SAFT*

Group contribution (GC) approaches (see e.g., (Papaioannou et al., 2011a)) make use of the concept that a set of relevant chemical compounds may be broken down into a significantly smaller number of chemical functional groups. For example, the thermodynamic properties for set of linear alkanolamines (MEA, (C_2H_7ON), MPA (C_3H_9ON), etc.) may be represented with a small number of chemical functional groups: CH_2 CH_2NH_2 and CH_2OH. This can greatly reduce the number of parameters required within the thermodynamic model, and once parameters have been obtained for functional groups, the thermodynamic properties of new molecules can be quickly assessed using the functional groups as building blocks. An assumption inherent in GC methods is that the free energy contribution due to the presence of each functional group is independent of its environment and connectivity (Fredenslund et al., 1975). This is a valid assumption assuming that there is no significant difference in the polarisation of the same functional group present in different compounds. Proximity effects may be accounted for in an effective manner by the inclusion of 'second-order' groups (Fredenslund et al., 1975; Constantinou and Gani, 1994; Abildskov et al., 1996; Kang et al., 2002).

There are numerous GC versions of SAFT, which differ mainly in the GC schemes (for example, mixing rules) used. The two GC methods can be classified into homonuclear and heteronuclear approaches.

In homonuclear approaches, molecules consist of identical monomeric segments. Examples of homonuclear GC SAFT approaches include that of Vijande et al. (2004), who proposed a GC version of PC-SAFT (Gross et al., 2001); Tobaly and co-workers (Tamouza et al., 2004; Thi et al., 2005) who proposed a GC extension to the original SAFT equation (Chapman et al., 1989, 1990), SAFT-VR (Gil-Villegas

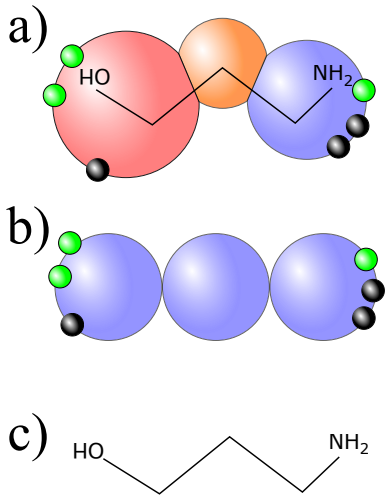

Figure 3: a) A heteronuclear model for MPA using the GC scheme of Chremos et al. (2016). The different segments represent the CH_2OH, CH_2 and CH_2NH_2 (from left to right). The association sites are represented by the small spheres: the lone pairs of electrons (green) and hydrogens (black) on the amino and hydroxyl functional groups. b) A homonuclear model for MPA with identical segments. c) The skeletal formula for MPA. This figure is based on that of Graham et al. (2017).

et al., 1997; Galindo et al., 1998) and PC-SAFT (Gross et al., 2001); and Tihic et al. (2007) who applied the GC scheme of Constantinou and Gani (1994) to a simplified version of PC-SAFT (von Solms et al., 2003). Within homonuclear GC approaches, the equation of state parameters are obtained by averaging parameters associated with chemical functional groups using group contribution rules (for example, Equations (11)-(14) in Tamouza et al. (2004) in Tamouza et al. (2004)). To ensure that the functional group parameters are applicable for a large number of different molecules, parameters are estimated from experimental data for a wide range of different molecules that contain the functional groups.

Within heteronuclear GC SAFT methods, the averaging step is not needed as the monomeric segments used to model compounds are not identical (Sauer et al., 2014). Heteronuclear GC SAFT methods include SAFT-γ SW (Lymperiadis et al., 2007, 2008a), GC-SAFT-VR (Peng et al., 2009), and SAFT-γ Mie (Papaioannou et al., 2014), which is a GC extension to SAFT-VR Mie (Lafitte et al., 2013b). More recently, a GC extension to perturbed-chain polar SAFT (GPC-SAFT) has also been proposed (Sauer et al., 2014).

In Figure 3 we demonstrate the difference between a homonuclear and heteronuclear SAFT model for 3-amino-1-propanol (MPA). In Figure 3a), a heteronuclear model is shown following the SAFT-γ SW model of Chremos et al. (2016). In Figure 3b) a homonuclear model of MPA is shown for comparison. In the molecular (homonuclear) version, each segment is identical, and it is not possible to assign a specific functional group to a monomeric segment. GC versions of SAFT extend the predictive capabilities of the SAFT approach and are highly suited for the formulation of CAMD and CAMPD problems.

2.2.3 *Model development in SAFT*

When developing a SAFT model for a molecule, typically a few parameters are assigned prior to the parameter estimation procedure. These define the basic structure of the molecular model: the number of segments and the association scheme (number and types of association sites). The remaining unknown parameters are then regressed by minimizing an objective function that characterises the deviations between the values of thermodynamic properties predicted by the model and the experimental measurements. In Table 1 we summarise the pure component parameters required for SAFT-VR SW and SAFT-VR Mie. The thermodynamic properties chosen are typically those that are easily measured experimentally (usually saturated liquid densities and vapour pressures). In Chapter 4 we will discuss in detail the inclusion of different types of thermodynamic property (in particular, second derivative properties such as heat capacity) in the parameter regression step, when formulating the parameter estimation as a multi-objective optimization problem.

The parameters required to model a functional group, k within a SAFT-γ SW and SAFT-γ Mie are listed in Table 2. Unlike group-group interactions may be obtained from pure component data alone within a GC approach, however, more robust parameter values can be obtained by including mixture data in the regression, e.g., enthalpies of mixing or binary phase equilibrium data. The main unlike interaction parameter to be estimated is the dispersive energy ϵ_{kl} between group k and group l. Unlike interaction parameters that are not regressed may be obtained using combining rules. These can be found in (Lymperiadis et al., 2007) for SAFT-γ SW, in (Dufal et al., 2015b) for SAFT-VR Mie, and in (Papaioannou et al., 2014) for SAFT-γ Mie.

In Chapter 4 we will discuss the issues regarding the formulation and solution of the parameter estimation problem, in particular the non-convexity of the optimization problem and issues regarding parameter degeneracy.

To develop mixture models based on homonuclear versions of SAFT, additional parameters often need to be estimated based on multicomponent (usually binary) phase-equilibrium data, such as vapour-liquid equilibrium or liquid-liquid equilibrium. It is usually sufficient to estimate unlike energy parameters for dispersive interactions (ϵ_{ij} between compounds i and j) and, if relevant, for association interactions (ϵ^{HB}_{abij} between sites of type a on compound i and sites of type b on compound j). Occasionally, the unlike range parameters also need to be estimated from the data to increase model accuracy (e.g., see (Papaioannou et al., 2016)). Once again, any unlike parameter not regressed to experimental data can be obtained from the like parameters using combining rules. For example, the unlike size parameter (σ_{ij}) required to describe the interactions between a compound i with diameter σ_i and a compound j with diameter σ_j can be obtained by taking the average of the like segment diameters:

$$\sigma_{ij} = \frac{\sigma_{ii} + \sigma_{jj}}{2}, \tag{5}$$

The combining rules for other unlike parameters can be found in (Galindo et al., 1998) for SAFT-VR SW, in (Dufal et al., 2015b) for SAFT-VR Mie, in (Lymperiadis et al., 2007) for SAFT-γ SW and in (Papaioannou et al., 2014) for SAFT-γ Mie.

Table 1: Parameters required to model pure components in SAFT-VR Mie and SAFT-VR SW homonuclear approaches.

Parameter	Definition	Potential
m_i	Number of segments in molecule i	Mie, SW
σ_i	Diameter of monomeric segments in molecule i	Mie, SW
ϵ_i	Depth of potential well between segments in molecule i	Mie, SW
λ_i	Width of potential well for segments in molecule i	SW
λ_i^a	Attractive exponent of the Mie potential for segments in molecule i (usually set to 6)	Mie
λ_i^r	Repulsive exponent of the Mie potential for segments in molecule i	Mie
NST_i	Number of site types on molecule i	Mie, SW
$n_{a,i}$	Number of sites of type a on molecule i, $a = 1, \ldots, NST_i$	Mie, SW
ϵ_{abii}^{HB}	Association energy between sites of types a and b on two molecules of type i, $a = 1, \ldots, NST_i$, $b = 1, \ldots, NST_i$	Mie, SW
r_{abii}^c or K_{abii}	Range of association or bonding volume between sites of types a and b on two molecules of type i, $a = 1, \ldots, NST_i$, $b = 1, \ldots, NST_i$	Mie, SW

Table 2: Parameters needed to model group self-interactions in SAFT-γ Mie and SAFT-γ SW heteronuclear group-contribution approaches.

Parameter	Definition	Potential
$\nu_{i,k}$	Number of groups of type k in molecule i	Mie, SW
ν_k^*	Number of identical segments in group k	Mie, SW
S_k	Shape factor of segments in group k (Proportional free energy contribution)	Mie, SW
σ_k	Diameter of segments in group k	Mie, SW
ϵ_k	Depth of potential well for segments in group k	Mie, SW
λ_k	Width of potential well for segments in group k	SW
λ_k^a	Attractive exponent of the Mie potential for segments in group k (usually set to 6)	Mie
λ_k^r	Repulsive exponent of the Mie potential for segments in group k	Mie
NST_k	Number of site types on group k	Mie, SW
$n_{a,k}$	Number of sites of type a on group k, $a = 1, \ldots, NST_k$	Mie, SW
ϵ_{abkk}^{HB}	Association energy between sites of types a and b on two groups of type k, $a = 1, \ldots, NST_k$, $b = 1, \ldots, NST_k$	Mie, SW
r_{abkk}^c or K_{abkk}	Range of association or bonding volume between sites of types a and b on two groups of type k, $a = 1, \ldots, NST_k$, $b = 1, \ldots, NST_k$	Mie, SW

2.2.4 *SAFT models for physical absorption systems*

In this section we present some examples of how CO_2 physical absorption mixtures have been treated using SAFT-VR and SAFT-γ equations of state. For an overview of the thermodynamic models discussed in this section and their incorporation into a process model for the formulation of a CAMPD problem, the reader is referred to Section 1.4.1 of Graham et al. (2017).

Pereira et al. (2011a) considered the series of n-alkanes as potential solvents for the separation of CO_2 from methane. The thermodynamics of these mixtures were modelled using SAFT-VR SW (Gil-Villegas et al., 1997; Galindo et al., 1998). Within this approach, the SAFT parameters were determined as a function of the average number of carbon atoms in the mixture, following McCabe and Jackson (1999) and Paricaud et al. (2004a). Pure component parameters for CO_2 and CH_4 were taken from a previous study (Galindo and Blas, 2002; Blas and Galindo, 2002), where the CO_2 parameters were scaled to match its critical point. Unlike interaction parameters between CH_4, CO_2 and the n-alkanes were determined from experimental data for CH_4, CO_2 and n-decane (C_{10}), and a single unlike interaction energy, ϵ_{ij}, was regressed for each pair of species. This lead to an accurate description of the phase behaviour for a wide range of CO_2+n-alkane mixtures (up to hexadecane). This is due to the transferability of SAFT-VR parameters within a homologous series (e.g., see (Galindo and Blas, 2002; Blas and Galindo, 2002)). The ternary phase behaviour of the CH_4+CO_2+C_{10} mixture was predicted accurately, and the cross-interaction parameters were found to be transferable to other mixtures of CH_4+CO_2+n-alkane. By formulating the SAFT parameters as a function of the number of carbon atoms, Pereira et al. (2011a) were able to formulate the full CAMPD problem using these models.

Burger et al. (2015) developed group parameters within the SAFT-γ Mie framework to describe linear alkanes and ethers, and oxygenated compounds sugh as diethers and glymes. Groups consisted of CH_3, CH_2, and two different oxygen functional groups, cO (an oxygen atom bonded to two CH_2 groups) and eO (an oxygen near the end of the molecule bonded to a CH_3 group). Two separate oxygen groups were considered in order to distinguish between structural isomers (e.g., methylpropylether and diethylether), and to account for the proximity effects of adjacent functional groups. Pure component vapour pressure and saturated liquid density, as well as binary phase equilibrium data was used to regress the group parameters. This lead to an accurate prediction of the vapour pressure for pure solvents not included in the parameter regression (e.g., a series of ethers).Then CO_2 and CH_4 parameters functional groups were taken from previous work Papaioannou (2013); Dufal et al. (2014). The unlike interactions between CO_2 and solvent functional groups were estimated from binary mixture data, and the models obtained were able to accurately predict the phase behaviour of binary mixtures of solvents and CO_2. This exemplifies that the SAFT-γ Mie EoS is able to accurately model a wide variety of solvents with only a small set of parameters. Through this group contribution approach, Burger et al. (2015) were able to formulate a CAMPD problem and identified penta(oxymethylene)dimethylether as an optimal solvent.

Another noteworthy example where SAFT has been applied to physisorption systems is the work of (Sauer et al., 2014), who developed models for the GPC-SAFT EoS. Sauer et al. (2014) developed GPC-SAFT parameters for non-polar and

polar functional groups, regressing parameters to pure component vapour pressure and saturated liquid density data. Polar groups required an additional term in order to describe interactions due to their dipole moment. Since CO_2 has a strong quadrupole moment, it can interact favourably with polar groups (Aschenbrenner and Styring, 2010), offering a different mode of absorption compared to non-polar solvents. Following this work Lampe et al. (2015) were able to formulate and solve the full CAMPD problem for the design of both polar and non-polar solvents for physisorption processes.

2.3 DESCRIBING CHEMICAL EQUILIBRIA WITH SAFT

In this section we will discuss thermodynamic approaches to modelling of fluids in which chemical reactions occur. Of particular interest in modelling CO_2 chemisorption processes are the reactions present in mixtures of CO_2 and aqueous alkanolamines. A number of theoretical and experimental investigations have been carried out in order to determine the reaction mechanisms and reaction kinetics of these systems (see e.g., (Caplow, 1968; Hikita et al., 1977; Danckwerts, 1979a; Astarita and Savage, 1980; Laddha and Danckwerts, 1981; Penny and Ritter, 1983; Blauwhoff et al., 1984; Arstad et al., 2007; McCann et al., 2009; Hwang et al., 2015)). Solvents composed of primary and seconday amines, e.g., monoethanolamine (MEA) and diethanolamine (DEA), react to form a carbamate. The true reaction mechanism is not fully understood (Hwang et al., 2015), but the key mechanisms proposed in the literature involve the formation of a zwitterionic form of the carbamate (McCann et al., 2009; Caplow, 1968; Arstad et al., 2007), followed by a proton exchange reaction with a base (either another amine molecule or water). The reaction can thus be represented as (Mac Dowell et al., 2010):

$$CO_2 + 2\,R_1R_2NH \quad \rightleftharpoons \quad [R_1R_2NCO_2^- + R_1R_2NH_2^+]. \quad \text{(r1)}$$

The other main reactions are carbamate hydrolysis:

$$R_1R_2NCO_2^- + H_2O \quad \rightleftharpoons \quad R_1R_2NH + HCO_3^-, \quad \text{(r2)}$$

and bicarbonate formation:

$$CO_2 + OH^- \quad \rightleftharpoons \quad HCO_3^-. \quad \text{(r3)}$$

The equilibrium governed by (r2) is only important at high CO_2 loadings for non-sterically hindered amines (e.g., MEA). For aqueous MEA, the CO_2 loading due to chemisorption is therefore limited to approximately 0.5 under practical process operating conditions, although further CO_2 can be absorbed by physisorption at high CO_2 partial pressures. For sterically hindered amines, e.g., MDEA (N-methyl diethanolamine) and AMP (2-amino-2-methyl-1-propanol), the carbamate hydrolysis reaction is important due to the presence of a bulky substituent adjacent to the amino group which leads to a reduced stability of the carbamate. Hence, for these amines carbamate reversion (r2) is favourable and loadings can approach approximately 1 under realistic operating pressures (Jou et al., 1982; Sartori and Savage, 1983; Mac Dowell et al., 2010).

2.3.1 *Chemical and physical approaches to modelling reactions*

In this section we will briefly compare two main types of thermodynamic approaches used to model chemical equilibrium: approaches based on chemical theory and approaches based on physical theory.

2.3.1.1 *The chemical approach*

Approaches based on chemical theory are most commonly used (see e.g., (Dolezalek, 1908; Fredenslund et al., 1975; Song and Chen, 2009; Zhang et al., 2011c; Fredenslund, 1977; Prausnitz et al., 1998)). In such methods, the reaction products are identified *a priori* and are treated explicitly within the thermodynamic model. To explain this point, we consider a simple mixture of 'A' and 'B' reactants and the reaction:

$$A + B \rightleftharpoons AB. \tag{6}$$

In chemical approaches, the fluid consists of three types of species: A, B and AB, which are in chemical equilibrium defined by the equation

$$K(T) = \frac{a_{AB}}{a_A a_B}, \tag{7}$$

where $K(T)$ is the equilibrium constant (a function of temperature) and a_i is the activity of species i. $K(T)$ is related to the standard change in Gibbs free energy (ΔG^0) of the forward reaction by $K(T) = \exp(-\Delta G^0/(RT))$, where R is the gas constant. (Gray et al., 2011). In Equation 7, activities can be replaced with concentrations when an ideal mixture is assumed, otherwise there are more sophisticated methods to relate the concentrations to activities (e.g. using an equation of state).

Electrolyte extensions to activity coefficient based models have been used to model CO_2+amine(aq) mixtures for a few well-known solvents (Austgen et al., 1989; Bollas et al., 2008; Faramarzi et al., 2009; Hessen et al., 2010; Zhang et al., 2011c; Al-Rashed and Ali, 2012; Sadegh et al., 2015). These approaches include eNRTL (Chen and Evans, 1986b; Bollas et al., 2008) and extended UNIQUAC (Thomsen and Rasmussen, 1999). Such methods are successful in correlating mixture properties where experimental data is available. The chemical or explicit approach can also be applied to SAFT-type equations for modelling the simultaneous chemical and phase equilibria of CO_2 capture mixtures, since extensions of SAFT EoSs have been developed to explicitly treat the ionic species formed from reactions (see e.g., (Galindo et al., 1999; Gil-Villegas et al., 2001; Patel et al., 2003a; Behzadi et al., 2005; Cameretti et al., 2005; Held et al., 2008; Held and Sadowski, 2009; Schreckenberg et al., 2014)). No complete SAFT-based model using the chemical approach for CO_2+amine+H_2O mixtures has yet been proposed, but Zhang et al. (2011c) proposed a chemical approach which utilises the eNRTL equation for the liquid phase and the PC-SAFT equation of state Gross et al. (2001) to obtain the fugacity coefficients of the vapour phase (assuming that no ionic species are present in the gas phase).

2.3.1.2 *The physical approach*

In contrast to chemical approaches, within physical approaches the reaction products are treated implicitly as aggregates of the reactants. Reaction products form due to intermolecular forces, similar to the association approach used to model hydrogen bonding. This does not require that the reaction products be defined explicitly, and any reaction product may form if this is permitted by the association scheme. Thus, aggregates such as dimers, trimers or higher *s*-mers (even chains of infinite length) may form if the association scheme permits this. Within SAFT reactions can be modelled by the addition of association sites that enable chemical binding. Referring back to Eq. (6), the thermodynamics of the mixture of 'A' and 'B' molecules can thus be defined as a function of the mixture temperature and pressure, and the apparent concentrations of the two species. The chemical equilibrium is defined implicitly by defining the association interactions, particularly the types, number, energy and bonding volumes of the association sites. The theory of chemical association within SAFT is due to a series of papers by Wertheim (Wertheim, 1984a,b, 1986a,b). Within this work, association is accounted for using "sticky spot" models, where molecules associate due to an attractive potential placed on the outside of a repulsive core. This interaction essentially captures a quantum mechanical effect, corresponding to the change in internal electronic configurations and rotational degrees of freedom upon association, which would otherwise appear in the enthalpy and entropy of formation in an explicit treatment of the reactions and thus present in A^{IDEAL}. With such an approach, it is possible to develop models for reactive mixtures (here, CO_2, water and solvent) without explicitly defining reaction products or specifying equilibrium constants (Gray et al., 2011). The species concentrations may be approximated via a statistical analysis on the fractions of association sites (computed implicitly within the SAFT equation) (Jackson et al., 1988; Rodríguez et al., 2012).

Various studies have been conducted in order to determine the equivalence between physical and chemical approaches. Economou and Donohue (1991) showed that results obtained by chemical and perturbation theory are essentially the same in terms of their functional form, given that the correct reaction stoichiometry is provided. This is shown for the association contribution to the compressibility factor, $Z^{\mathrm{ASSOC.}}$, and the mole fraction of monomers in the system predicted by both theories. The results were also shown to be numerically indistinguishable (Elliott Jr et al., 1990; Economou and Donohue, 1991). The equations which relate molecular to macroscopic properties in chemical theory contain parameters which are accessible experimentally, whereas the parameters within perturbation theories, although deterministic, cannot be readily accessed experimentally (although they can be fitted to experimental data) (Economou and Donohue, 1991). Bala and Lira (2016) showed that the association strength (Δ^{AB}) in Wertheim's theory is equivalent to the concentration-based equilibrium constant used in Flory's polymerization theory by considering chains with one acceptor and one donor site.

The parameters obtained within the physical theory to describe the association interactions (association strength and bonding volume) can thus be related to the equilibrium constant. An advantage of the physical approach over the chemical approach is that the parameters that define the association potential are not functions of the thermodynamic state. Since the equilibrium constant is a function of

temperature, large sets of experimental (speciation) data are required over various temperatures.

We will now illustrate how a physical association scheme can be used to model the reactions that occur when CO_2 absorbs into an aqueous MEA solution. This association scheme was proposed by Mac Dowell et al. (2011) and Rodríguez et al. (2012) for modelling the thermodynamics of this system using the SAFT-VR SW equation of state. The addition of two association sites, α_1 and α_2 on the CO_2 molecule which interact with the e^* site on the MEA molecule leads to the physical treatment of the following reactions (shown schematically in Figure 4):

$$\underset{}{CO_2} + \underset{\text{MEA}}{2\,HO(CH_2)_2NH_2} \rightleftharpoons \underset{\text{Carbamate pair}}{[HO(CH_2)_2NHCOO^- + HO(CH_2)_2NH_3^+]}, \quad \text{(r4)}$$

$$\underset{}{HO(CH_2)_2NHCOO^-} + \underset{}{H_3O^+} \rightleftharpoons \underset{\text{Bicarbonate pair}}{[HO(CH_2)_2NH_3^+ + HCO_3^-]}. \quad \text{(r5)}$$

The square brackets represent ion pairs and these are assumed to be tightly bound species. The carbamate pair consists of a CO_2 molecule that is associated with two MEA molecules, thus a CO_2 molecule for which both association sites are bonded is taken to exist in a carbamate structure. The bicarbonate pair consists of a CO_2 molecule that is bonded to one MEA molecule, thus a CO_2 molecule for which only one association site is bonded (α_1 or α_2), the CO_2 is taken to exist in the form of a bicarbonate ion pair (cf Figure 4). The inherent assumption made in this physical approach is that the ion pairs are aggregated species with no overall charge, which is somewhat justified by the low dielectric constant of aqueous alkanolamines relative to water, leading to stron ion pairing.

Although this treatment is simple compared to a with an explicit chemical approach, it can be used to predict the concentrations of carbamate and bicarbonate with remarkable accuracy over various CO_2 loadings and temperatures (Rodríguez et al., 2012; Chremos et al., 2016), given that no speciation data needs to be used in model development. One must be careful when using a physical approach if the reaction products are chemically very different from the reactants, since interactions between monomeric segments and the association sites in the reaction product may be different to that of the reactants.

For CO_2 reacting with aqueous amines, the physical description is a reasonable assumption since the ions are strongly paired and the reactions are reversible, indicating that the intermolecular potentials of species in their free or aggregated forms are similar.

2.3.1.3 *Comparison of chemical and physical approaches*

The majority of thermodynamic models used to describe CO_2 in aqueous amines follow a chemical approach to treat the reactions. Chemical approaches are usually more accurate than those based on physical theory. The current state-of-the-art model for CO_2 + aqeous MEA is that of Zhang et al. (2011c), who used the electrolyte NRTL model (Song and Chen, 2009) to model the relevant chemical equilibria. Within this model, the long-range ionic interactions and short range

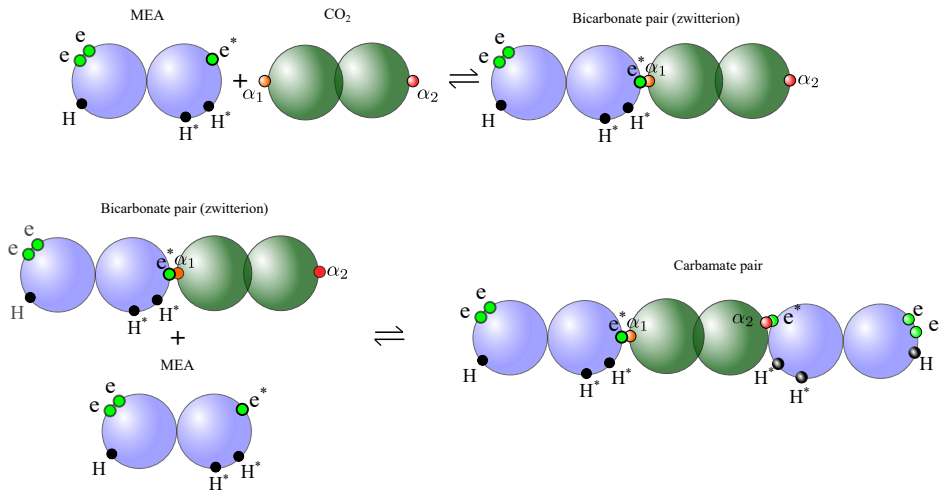

Figure 4: Schematic to show how the addition of association sites leads to the formation of the expected reaction products for CO_2 in an aqueous MEA solution: the bicarbonate pair (zwitterion) and carbamate pair. This association scheme was developed by Mac Dowell et al. (2011) and Rodríguez et al. (2012) .

interactions are treated explicitly for nine major ionic and neutral species in the solution. This model provides an accurate description of the vapour-liquid equilibria (VLE), heat capacity, and speciation. An accurate representation of the enthalpy of absorption is also achieved at low temperatures and for loadings of up to 0.5 mol CO_2 per mol of amine, with larger deviations observed at higher temperatures and/or higher loadings.

The high level of accuracy required a high experimental effort however, since different types of data were required over a wide range of thermodynamic conditions for the model parametrization. These properties included VLE, enthalpy of absorption, heat capacity and NMR spectroscopic data for the MEA–H2O–CO2 ternary system. Standard state properties of the amine ions, MEA protonate and carbamate were also required. Furthermore, when developing a chemical model, the reaction scheme must be postulated *a priori*. This becomes increasingly challenging as the number of reactions increases since temperature-dependent data is required to derive an expression for each equilibrium constant. As a result of this high reliance on experimental data, there is currently no chemical approach that enables the prediction of the thermodynamics of mixtures of CO_2 in solvents for which no data or very limited data are available.

Contrastingly, physical approaches (available to SAFT-type EoSs) can be developed with limited data (or even no data), offering a way to compare the likely performance of different solvents. To develop homonuclear models for a ternary mixture of CO_2 and aqueous amine, a relatively small amount of data is required (in terms of the number of data points and data types). Thus, it suffices to have vapour-liquid equilibrium data on the apparent mole fractions of CO_2, H_2O and amine at a few temperatures and pressures, and importantly no speciation data are required.

This is due to the temperature-independence of the SAFT parameters and the fact that only three components (CO_2, amine and H_2O) need to be modelled explicitly. Due to their strong theoretical basis, SAFT parameters can be highly transfer-

able between different compounds. For example, some of the association parameters in MEA can be obtained from models for alkanols and alkylamines (Mac Dowell et al., 2010, 2011), and parameters can be transferred from one alkanolamine to another Rodríguez et al. (2012). SAFT models for new solvents can therefore typically be derived using limited data sets. For heteronuclear models, Chremos et al. (2013, 2016) have shown that the SAFT-γ SW group contribution EoS can be successfully used to model these types of reactive systems. This gives a strong indication that different solvents and solvent blends can be modelled predictively without extensively relying on experimental data.

SAFT-based models combined with a physical approach to the reactions are clearly benificial for providing an initial assessment of the carbon capture potential of new solvents. Chemical models can then provide a more detailed representation of the thermodynamic behaviour once necessary experimental data are available for parameter regression. Physical models can thus help guide experimental effort towards promising candidate solvents, while chemical models can assist in the more detailed design of the CO_2 capture process. Due to the explicit treatment of all major species within a chemical model, reaction kinetics may be easily incorporated into a chemical model. Similarly, diffusion can be modelled rigorously, for example the effect of ionic strength on mass transfer can be explicitly accounted for. Chemical approaches are therefore vital for the accurate modelling of a carbon capture process, and are necessary in order to fully assess potential solvents.

The development of accurate chemical models is well-understood Zhang et al. (2011c), so we will focus the remainder of this section on the development of thermodynamic models for CO_2 chemisorption processes that follow a physical approach.

2.3.2 *Modelling aqueous mixtures of amine solvents and CO_2*

Button and Gubbins (1999) were the first authors to propose a SAFT model for CO_2 + aqueous amine mixtures. In their work, the original SAFT EoS (Chapman et al., 1989, 1990) was used to predict the VLE of mixtures consisting of CO_2, and MEA(aq) or DEA(aq). CO_2 was modelled using a four site association scheme to account for interactions occurring due to its strong quadrupole moment (including its ability to form complexes with amines). Water was modelled using a four-site (4C) association scheme. Five association sites were used to model MEA: two sites of type *e* (one representing the two lone pairs on the OH group and the other representing the lone pair on NH_2), and three identical sites of type H representing the hydrogen atoms. Since only two site types were used for MEA, this association scheme considers that the association parameters for hydrogen bonds formed by nitrogen atoms and oxygen atoms are the same (which is not in-keeping with the known differences in these bond strengths). This simplification leads to a reduction in the number of adjustable parameters. All pure component parameters were determined from pure component data (vapour pressure and saturated liquid density). For the binary mixtures (excluding CO_2 + amine), a single adjustable parameter (the dispersive energy) was adjusted to pressure - mole fraction data. All cross interaction parameters were determined using combining rules. Thus, thermodynamic calculations for the ternary mixture were fully predicted. Follow-

ing this method, predictions of reasonable accuracy were obtained for the liquid mole fractions in the ternary mixture, but small deviations in the liquid mole fractions lead to large deviations in the predicted CO_2 loading, leading to a relatively large average error (62%) in the pressure or composition for the MEA mixtures. Note that Button and Gubbins (1999) do not use experimental data for the reactive ternary mixture in the parameter regression.

Following the work of Button and Gubbins (1999), Mac Dowell et al. (2010) developed models for the SAFT-VR SW EoS to describe CO_2+MEA+H_2O. The authors considered a symmetric and asymmetric association scheme to model MEA. In the asymmetric scheme, the difference in association parameters between the amine and hydroxyl functional groups is considered explicitly, in contrast to the symmetric scheme as in the models proposed by Button and Gubbins (1999). The asymmetric model was found to offer a superior description of the MEA+H_2O phase behaviour and of the CO_2 partial pressure above the ternary mixture. This work exploited the transferability of the SAFT parameters by taking the hydrogen-bonding parameters for MEA from a separate study of ethanol and ethylamine and their aqueous solutions. The reactions were modelled using the physical association scheme outlined in Section 2.3. Ternary mixture data (CO_2 partial pressure) was required to regress the cross-association parameters for the α_1 and α_2 sites on CO_2.

In subsequent work, a similar treatment of the reactions was used to model CO_2 and aqueous alkylamines Mac Dowell et al. (2011) within the SAFT-VR SW framework, including n-alkylamines up to n-hexylamine. In this case, the reactions between CO_2 and the amines were modelled by including a single association site on CO_2 which interacts with the electron site on the n-alkylamine molecules. The parameters describing the interaction between CO_2 and NH_3 were obtained by comparison to experimental data for the NH_3+H_2O+CO_2 ternary mixture. These were found to be transferable to other n-alkylamines, providing accurate predictions of the phase behaviour for ternary mixtures of CO_2+n-propylamine+H_2O, CO_2+n-butylamine+H_2O and CO_2 + n-hexylamine + H_2O. The authors observed separate regions of vapour-liquid and liquid-liquid coexistence for the n-hexylamine + CO_2 + H_2O system. This de-mixing could be advantageous in a chemisorption process. If the loaded amine solution splits into two liquid phases after the absorber (e.g., upon heating), only the CO_2-rich phase needs to be input into the desorber (Svendsen et al., 2011), leading to a reduced energy requirement in the reboiler. Numerous experimental studies have been conducted to search for amine solvents that phase split (see e.g., (Zhang et al., 2011a,b, 2012a,b)). n-hexylamine has been identified as a promising thermomorphic biphasic solvent (Zhang et al., 2011b, 2012a,b) due to a liquid-liquid phase separation upon heating. The prediction of this phase split by Mac Dowell et al. (2011) demonstrates the advantage of using predictive thermodynamic models in the search for better CO_2 capture solvents.

Rodríguez et al. (2012) extended on the work of Mac Dowell et al. (2011) to include different multifunctional amines, including diethanolamine (DEA), methyldiethanolamine (MDEA), and 2-amino-2-methyl-1-propanol (AMP). Reliance on experimental VLE data was minimized by making use of the transferability of the SAFT parameters. Extensive use was made of parameter transferability in developing the models, with the aim to minimise reliance on VLE data. A good description of the vapour pressures and liquid densities of the binary and ternary

mixtures was obtained. The concentration of bicarbonate and carbamate for the MEA+CO_2+H_2O mixture was found to compare favourably with the NMR spectrocopic study of Böttinger et al. (2008).

Recently, Wang et al. (2018a) modelled MEA+CO_2+H_2O using the a physical approach using the PR-CPA equation of state. They used a similar approach to Mac Dowell et al. (2009), but also account for the solvation between CO_2 and H_2O via the addition of a single association site.

Given that the SAFT parameters were found to be highly transferable between different homonuclear models for describing CO_2 chemisorption solvents, Chremos et al. (2016) investigated the effectiveness of the group contribution equation of state, SAFT-γ SW for modelling various primary alkanolamines (for example, MEA and MPA). This is the first work where CO_2 chemisorption solvents have been considered within a group-contribution framework work. A small set of functional groups were developed (CO_2, H_2O, CH_2, CH_3, NH_2CH_2 and CH_2OH) in order to model a range of CO_2+H_2O+primary alkanolamine mixtures. Experimental data consisted of pure alkylamines and alkanolamines, and mixture data where available. Due to the transferability of the group parameters, a single set of parameters was sufficient to describe the phase behaviour of any primary alkanolamine with an alkyl chain length consisting of three or more carbons (monopropanolamine onwards). Accurate predictions were also obtained for molecules not included in the parameter estimation (5-amino-1-pentanol and 6-amino-1-hexanol), demonstrating the predictiveness of the approach. In order to treat MEA, Chremos et al. (2016) adopted the concept of second-order groups (see e.g., (Constantinou and Gani, 1994; Abildskov et al., 1996; Kang et al., 2002)). This was required due to the importance of proximity effects in this molecule, i.e., the CH_2 groups present in the molecule are polarised by nearby NH_2 and OH groups. An improved description of the MEA+H_2O system was then obtained, and the phase behaviour of the ternary CO_2+H_2O+MEA mixture was described with better accuracy. In addition, the concentrations of bicarbonate and carbamate were predicted accurately for this reactive mixture, as shown in Figure 5. The predictive capabilities of SAFT-γ were further demonstrated by predicting the solubility of CO_2 in a quaternary H_2O+CO_2+MEA+MPA mixture.

2.4 CONCLUSIONS

In this introductory chapter we have set the context of this thesis, i.e., the need to develop advanced thermodynamic models for CO_2 absorption processes. By combining predictive molecular-based thermodynamic models with computer-aided molecular and process design, one can provide design decisions on improved solvents in order to guide further experimental investigations. This helps reduce the time and investment required to design more optimal processes. The development of advanced thermodynamic models rooted in molecular theory, including techniques to describe reactions, is an important task in realizing this potential.

Due to the recent advancements in SAFT equations of state, in particular the development of a group contribution framework and the use of the Mie potential in the SAFT-γ Mie equation, one can reliably predict a range of thermodynamic properties over a wide range of process conditions for novel solvents and their

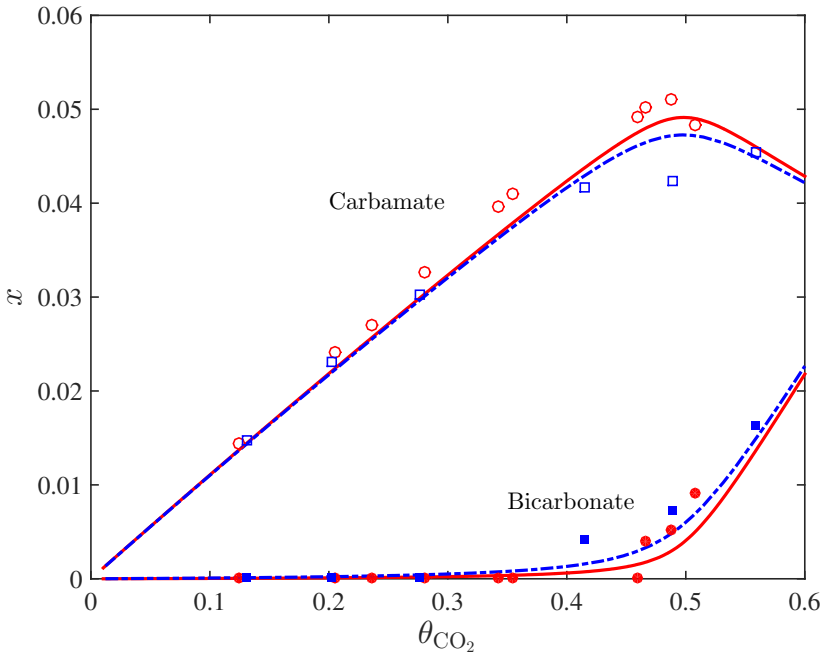

Figure 5: Predicted mole fraction, x, of carbamate and bicarbonate in the liquid phase of a 30 wt% MEA aqueous solution at T = 313.15 K (circles) and 333.15 K (squares) at vapour-liquid equilibrium for the ternary mixture of MEA + H_2O + CO_2 as a function of the CO_2 loading, θ_{CO_2}, defined as the number of moles of CO_2 absorbed in the liquid phase per mole of amine in the liquid. The symbols correspond to the experimental data (Jou et al., 1995; Böttinger et al., 2008) with open symbols corresponding to carbamate and filled symbols to bicarbonate. The curves correspond to the SAFT-γ SW predictions; continuous curves for 313.15 K and dot-dashed curves for 333.15 K. This figure is modified from reference (Graham et al., 2017).

mixtures. In the context of chemical absorption, the physical approach to association is particularly advantageous for the prediction of the phase and chemical equilibria of mixtures of CO_2, amines, and water. These models are thus particularly suited for molecular systems engineering approach, and thus new groups and their parameters are currently being developed (Papaioannou et al., 2016; Sadeqzadeh et al., 2016; Chremos et al., 2016; Dufal et al., 2014), so that an increasingly wide range of structures can be described within the SAFT framework.

Due to the advancements made in the thermodynamic model, several methodologies have been put forward to solve CAMPD problems that are able to span large search spaces. Although CAMD or CAMPD is not explored in this thesis, the use of SAFT-type models in such problems (see e.g., (Pereira et al., 2011a, 2008; Lampe et al., 2015; Papadokonstantakis et al., 2015; Burger et al., 2015)) is certainly advantageous for the design of suitable solvents/ solvent blends.

2.5 APPENDIX: THE SAFT-VR MIE EQUATIONS

In this appendix we will summarize the main equations used in the SAFT-VR Mie equation of state. For a more detailed description of the equation and its derivation, the reader is referred to Lafitte et al. (2013a). The equtaions presented here have the same notation as Dufal et al. (2015a) and Dufal et al. (2015b).

The general SAFT EoS for a nonassociating system can be expressed as:

$$A = A^{\text{ideal}} + A^{\text{monomer}} + A^{\text{chain}} + A^{\text{assoc}} \tag{8}$$

where A is the Helmholtz free energy. The right hand side represents the additive contributions corresponding to a different type of molecular interaction. Conceptually, one can imagine first an ideal gas of particles. The monomer term on the right hand side of Equation 8 represents the change in free energy when adding an interaction between monomeric segments. The chain term represents the change in free energy due to grouping molecular segments as chains (each comprising of m monomeric segments), thus inferring a shape to the molecule. The association term accounts for non-spherical interactions such as hydrogen bonding interactions or other types of association.

2.5.1 *Ideal term*

The ideal term is given by:

$$A^{\text{ideal}} = N k_B T(\ln(\rho\Lambda^3) - 1) \tag{9}$$

where N is the number of molecules, k_B is the Boltzmann constant, T the absolute temperature, $\rho = N/V$ the volume and Λ^3 is the de Broigle volume which incorporates all of the kinetic (rotational, translational and vibrational) contributions to the partition function.

2.5.2 *Monomer term*

Within SAFT-VR Mie, the Helmholtz free energy of a monomer fluid is expressed as a high-temperature (Barker Henderson) perturbation expansion up to third order in inverse temperature:

$$\frac{A^{\text{monomer}}}{NK_BT} = m\left(a^{HS} + \frac{a_1}{k_BT} + \frac{a_2}{(k_BT)^2} + \frac{a_3}{(k_BT)^3}\right). \tag{10}$$

For pure components the free energy of the reference hard sphere (HS) sstem is obtained from the Carnahan and Starling EoS:

$$a^{HS} = \frac{4\eta - 3\eta^2}{(1-\eta^2)} \tag{11}$$

where $\eta = \rho_s \pi d^3/6$ is the packing fraction of the reference HS system and $\rho_s = N_s/V$ is the segment density of the Mie fluid with $N_s = Nm$, i.e., the total number density of segments. The Barker and Henderson effective HS diameter $d(T)$ is given by:

$$d(T) = \int_0^\infty 1 - \exp(\frac{u^{\text{Mie}(r)}}{k_BT})dr. \tag{12}$$

The first-order perturbation contribution of the SAFT-VR Mie EoS is given by

$$a_1 = C(\lambda_r, \lambda_a)\left[x_0^{\lambda_a}(a_1^S(\eta;\lambda_a) + B(\eta;\lambda_a)) - x_0^{\lambda_r}(a_1^S(\eta;\lambda_r) + B(\eta;\lambda_r))\right], \tag{13}$$

where $x_0 = \sigma/d$ and

$$B(\eta,\lambda) = 12\eta\varepsilon\left(\frac{1-\eta/2}{(1-\eta)^3}\left(\frac{1-x_0^{3-\lambda}}{\lambda-3}\right) - \frac{9\eta(1+\eta)}{2(1-\eta)^3}J_\lambda(\lambda)\right), \tag{14}$$

where

$$J_\lambda(\lambda) = -\frac{x_0^{4-\lambda}(\lambda-3) - x_0^{3-\lambda}(\lambda-4) - 1}{(\lambda-3)(\lambda-4)} \tag{15}$$

for $\lambda = \lambda_a$ or $\lambda = \lambda_r$. a_1^S is given by:

$$a_1^S(\eta,\lambda) = -12\varepsilon\eta\left(\frac{1}{\lambda-3}\right)\frac{(1-\eta^{eff}(\eta;\lambda)/2)}{(1-\eta^{eff}(\eta;\lambda))^3}, \tag{16}$$

where

$$\eta_{eff}(\eta,\lambda) = c_1(\lambda)\eta + c_2(\lambda)\eta^2 + c_3(\lambda)\eta^3 + c_4(\lambda)\eta^4. \tag{17}$$

For the coefficients c_1, c_2, c_3 and c_4 the reader is referred to Lafitte et al. (2013a) (Equation 41). The second order perturbation term is given by

$$\begin{aligned} a_2 = &\frac{K^{HS}}{2}(1+\chi)\varepsilon C^2(\lambda_r,\lambda_a)[x_0^{2\lambda_a}(a_1^S(\eta;2\lambda_a) + B(\eta;2\lambda_a)) \\ &- 2x_0^{\lambda_a+\lambda_r}(a_1^S(\eta;\lambda_a+\lambda_r) + B(\eta;\lambda_a+\lambda_r)) \\ &+ x_0^{2\lambda_r}(a_1^S(\eta;2\lambda_r) + B(\eta;2\lambda_r))], \end{aligned} \tag{18}$$

where K^{HS} is the isothermal compressibility of the hard-spere reference fluid, obtained from the Carnahan and Starling expression for the compressiblity factor as

$$K^{HS} = \frac{(1-\eta)^4}{1+4\eta+4\eta^2-4\eta^3+\eta^4} \tag{19}$$

and

$$\chi = f_1(\alpha)\eta x_0^3 + f_2(\alpha)(\eta x_0^3)^5 + f_3(\alpha)(\eta x_0^3)^8. \tag{20}$$

$f_i(\alpha)$ are given by

$$f_i(\alpha) = \frac{\sum_{n=0}^{3} \phi_{i,n}\alpha^n}{1+\sum_{n=4}^{6} \phi_{i,n}\alpha^{n-3}} \tag{21}$$

where the integrated attractive energy α is given by

$$\alpha = C(\lambda_a,\lambda_r)\left(\frac{1}{\lambda_a-3}\frac{1}{\lambda_r-3}\right). \tag{22}$$

For the coefficients $\phi_{i,n}$ the reader is referred to Table 2 of Lafitte et al. (2013b).

The third perturbation term is given by

$$a_3 = -\varepsilon^3 f_4(\alpha)\eta x_0^3 \exp(f_5(\alpha)\eta x_0^3 + f_6(\alpha)\eta^2 x_0^6) \tag{23}$$

2.5.3 *Chain term*

The chain term is given by

$$\frac{A^{chain}}{NkT} = -(m-1)\ln g^{Mie}(\sigma). \tag{24}$$

The radial distribution function of the Mie fluid is evaluated at monomer separations σ and is given by

$$g^{Mie}(\sigma) = g_d^{HS}(\sigma)\exp\left[\frac{g_1(\sigma)}{g_d^{HS}(\sigma)}\frac{\varepsilon}{k_BT} + \frac{g_2(\sigma)}{g_d^{HS}(\sigma)}\frac{\varepsilon^2}{(k_BT)^2}\right]. \tag{25}$$

The radial distribution function of the HS fluid with spheres of diameter d evaluated at σ is given by

$$g_d^{HS}(\sigma) = \exp[k_0 + k_1 x_0 + k_2 x_0^2 + k_3 x_0^3], \tag{26}$$

where the k_i are given by

$$k_0 = -\ln(1-\eta) + \frac{42\eta - 39\eta^2 + 9\eta^3 - 2\eta^4}{6(1-\eta)^3} \tag{27}$$

$$k_1 = \frac{-12\eta + 6\eta^2 + \eta^4}{2(1-\eta)^3} \tag{28}$$

$$k_2 = \frac{-3\eta^2}{8(1-\eta)^2} \tag{29}$$

and

$$k_3 = \frac{3\eta + 3\eta^2 - \eta^4}{6(1-\eta^3)}. \tag{30}$$

The first order perturbation term in Equation 25 is given by

$$g_1(\sigma) = \frac{1}{2\pi\varepsilon d^3}\left[3\frac{\partial a_1}{\partial \rho_s} - C(\lambda_r,\lambda_a)\lambda_a x_0^{\lambda_a}\frac{a_1^S(\eta;\lambda_a)+B(\eta;\lambda_a)}{\rho_s} + C(\lambda_r;\lambda_a)\lambda_r x_0^{\lambda_r}\frac{a_1^S(\eta;\lambda_r)+B(\eta;\lambda_r)}{\rho_s}\right]. \tag{31}$$

The second order perturbation term is given by

$$g_2(\sigma) = \frac{1+\gamma_c}{2\pi\varepsilon^2 d^3}\left\{3\frac{\partial a_2/(1+\chi)}{\partial \rho_s} - \varepsilon K_{HS} C^2(\lambda_r,\lambda_a) \times\left(\lambda_r x_0^{2\lambda_r}\frac{a_1^S(\eta;2\lambda_r)+B(\eta;2\lambda_r)}{\rho_s} - (\lambda_r+\lambda_a)x_0^{\lambda_r+\lambda_a}\frac{a_1^S(\eta;\lambda_r+\lambda_a)+B(\eta;\lambda_r+\lambda_a)}{\rho_s} + \lambda_a x_0^{2\lambda_a}\frac{a_1^S(\eta;2\lambda_a)+B(\eta;2\lambda_a)}{\rho_s}\right)\right\} \tag{32}$$

where

$$\gamma_c = \phi_{7,0}(-\tanh(\phi_{7,1}(\phi_{7,2}-\alpha)+1))\eta x_0^3 \times\left(\exp\left(\frac{\varepsilon}{k_B T}-1\right)\exp(\phi_{7,3}\eta x_0^3+\phi_{7,4}\eta^2 x_0^6)\right). \tag{33}$$

The coefficients for $\phi_{7,i}$, $i=\{0,3,4\}$ can be found in Lafitte et al. (2013b).

2.5.4 *The association term*

The association contribution to the free energy is given as (Jackson et al., 1988)

$$\frac{A^{assoc}}{N k_B T} = \sum_{a=1}^{s}\left(\ln X_a - \frac{X_a}{2}\right)+\frac{s}{2}, \tag{34}$$

where s represents the number of association types per molecule. The fraction of molecules X_a with given sites a not bonded is obtained from

$$X_a = \frac{1}{1+\rho\sum_{b=1}^{s} X_b \Delta_{ab}}. \tag{35}$$

The integrated association strength in the case that the reference fluid is a Lennard Jones fluid is given by (Dufal et al., 2015b)

$$\Delta_{ab} = 4\pi F_{ab} K_{ab}^{HB} I \tag{36}$$

where

$$F_{ab} = \exp[\varepsilon_{ab}^{HB}/(k_B T)]-1 \tag{37}$$

and

$$I = \sum_{i=0}^{4}\sum_{j=0}^{4} a_{ij}[\rho^*]^i[T^*]^j, \tag{38}$$

where the coefficients a_{ij} can be found in Dufal et al. (2015a). K_{ab}^{HB} and ε_{ab}^{HB} are the bonding volume and association energy as used throughout the thesis.

3 MODELLING AN ABSORPTION COLUMN WITH SAFT-VR SW

The introductory chapter has set the context for this research, a key theme being that molecular-based equations of state can be highly predictive due to the transferable nature of their parameters. Our focus from this point on will be on the chemisorption of carbon dioxide in an aqueous MEA solvent. Although group contribution methods have been shown to be highly predictive for alkanolamines, the modelling of MEA requires second-order groups due to the proximity effect of alkanol and amino functional groups (Chremos et al., 2016). Homonuclear methods are preferred in this study, as it will provide a fair comparison between the SAFT-VR SW and SAFT-VR Mie equations of state, which we will show in future chapters. Additionally, homonuclear approaches tend to be more accurate as the parameters are particular to the compound in question. A thorough understanding is required as to how to model processes when a physical approach to the reactions is used as the technique is relatively novel, and therefore we want to mitigate any uncertainty in the thermodynamic model as much as possible.

In this chapter, we expose a published paper on the modelling of an absorption column using the SAFT-VR SW models of Rodríguez et al. (2012). The paper can be found in reference (Brand et al., 2016). The majority of this work is based on the thesis of Brand (2013); however some improvements were made to this work for the published paper (for which I am second author). The key contributions from myself are outlined as follows:

- SAFT-VR SW code previously being used had an inconsistency in the specification of the Boltzmann constant, k_B, which lead to an error in the energy balance. The corrected code was implemented in this work.
- In the work of Brand (2013), a correction to the energy balance was made due to a large discrepancy between the calculated heat of absorption and experiments (see Figure of Brand (2013)). It was found that the heat of absorption was previously calculated incorrectly and the correction to the energy balance was removed for the paper.
- All process modelling results were reproduced with the corrected thermodynamic model and process model, and diffusivity scaling parameter, τ, was re-estimated.
- A large part of the discussion was re-written, to focus more on the physical vs chemical approach to reactions and the usefulness of the general approach in the context of solvent design.

3.1 INTRODUCTION

Carbon dioxide (CO_2) emissions are generally considered to play a major role in climate change and particularly in global warming. Fossil fuel power plants are

the major fixed point-source emitters of CO_2. In response to the threat posed by global warming, the Roadmap for 2050 set by the European Commission in 2011 suggested a reduction of greenhouse gas emissions in Europe to 25% of the 2011 value by 2020 and to 80% of the 2011 value by 2050 (The European Commission, 2011). In the recent Paris climate conference (COP21), an agreement was made between participating parties to cut greenhouse gas emissions to a level that limits the global average temperature to "well below" 2 °C above pre-industrial levels and to "pursue efforts to limit the temperature increase to 1.5 °C" (UNFCCC, 2015). In this context, the development of carbon capture systems must be addressed in the short term, and amine-based post-combustion capture processes are seen as the most promising near-term technology in terms of development and applicability, e.g., see Mac Dowell et al. (2010). In this technique, absorption is achieved both physically and chemically, so that significant CO_2 removal can take place even at the challenging low partial pressures of the greenhouse gas. The major advantage of this technology is that it can be retrofitted to existing power plants.

There are however several concerns with this technology, in particular the large energy requirements associated with solvent regeneration, the degradation of the solvent, which is exacerbated by the presence of oxygen in the flue gas, and the environmental and health impact that may result from solvent losses and solvent degradation products. These issues are particularly important because of the scale of deployment required to have a meaningful impact on CO_2 emissions. There are significant experimental programmes to identify new solvents (Paul et al., 2008; Mangalapally et al., 2009; Bardow et al., 2010; Barzagli et al., 2012; Mangalapally et al., 2012; Li et al., 2012; Salkuyeh and Mofarahi, 2012; Chen et al., 2015; Kortunov et al., 2015) and several pilot-plant studies are under way (Tontiwachwuthikul et al., 1992; Dugas, 2006; Tobiesen and Svendsen, 2006; Gabrielsen et al., 2007; Habaki et al., 2007; Godini and Mowla, 2008; Cottrell et al., 2009; Notz et al., 2012; Akram et al., 2016). Modelling studies can play an invaluable and complementary role in addressing some of these issues, including the choice of solvent and operating conditions that yield optimal performance.

A key challenge in realising the benefits of a model-based approach to design is the development of models that can accurately predict the behaviour of the CO_2 capture process under different conditions and for a range of solvents. This is particularly difficult in the case of CO_2 absorption due to the complex reaction chemistry that occurs and the large number of ionic species present in the process. For example, in the case of absorption of CO_2 using the most common solvent, an aqueous solution of MEA (MEA, $HOC_2H_4NH_2$), the key reactions, excluding the speciation of water, are (Astarita, 1967; Hikita et al., 1977; Danckwerts, 1979b; Laddha and Danckwerts, 1981; Astarita et al., 1983; Penny and Ritter, 1983; Blauwhoff et al., 1984):

$$
\begin{aligned}
CO_2 + HOC_2H_4NH_2 &\rightleftharpoons HOC_2H_4NH_2^+CO_2^- \\
HOC_2H_4NH_2^+CO_2^- + HOC_2H_4NH_2 &\rightleftharpoons HOC_2H_4NHCO_2^- + HOC_2H_4NH_3^+ \\
HOC_2H_4NH_2^+CO_2^- + H_2O &\rightleftharpoons HOC_2H_4NHCO_2^- + H_3O^+ \\
HOC_2H_4NHCO_2^- + H_2O &\rightleftharpoons HOC_2H_4NH_2 + HCO_3^- \\
HOC_2H_4NH_2^+CO_2^- + H_2O &\rightleftharpoons HOC_2H_4NH_3^+ + HCO_3^- \\
CO_2 + OH^- &\rightleftharpoons HCO_3^- \\
HOC_2H_4NH_3^+ + H_2O &\rightleftharpoons HOC_2H_4NH_2 + H_3O^+ \\
CO_2 + H_2O &\rightleftharpoons HCO_3^- + H^+
\end{aligned}
$$

The main reaction products are therefore the zwitterion ($HOC_2H_4NH_2^+CO_2^-$), the carbamate ($HOC_2H_4NHCO_2^- + HOC_2H_4NH_3^+$), and bicarbonate ($HCO_3^-$).

Given the complexity of the underlying chemical and physical phenomena, detailed models of the thermodynamics, kinetics, and process units relevant to the absorption systems have been developed for the simulation, optimisation, and design of CO_2 capture processes for a given solvent, as for example in the work of Kucka et al. (2003a), Zhang et al. (2011c), and Kale et al. (2013). The elucidation and characterization of the speciation, reaction mechanism, equilibria and kinetics for mixtures relevant to CO_2 chemisorption are, however, required before detailed models can be developed, and this necessitates extensive experimental investigation. The types of data that are required include data specific to the solvent involved, such as reliable physicochemical (e.g., vapour-liquid equilibrium (VLE) and liquid phase speciation) and kinetic (including reaction rate constants and diffusion coefficients) data, and information regarding the effect of the column specifications, for instance the type of packing material employed. This presents a significant barrier to the rapid development of improved processes for carbon capture.

To overcome this difficulty, the task of identifying solvents that lead to improved CO_2 absorption processes can be subdivided into two main steps. The first is the rapid identification of a list of promising solvents by assessing a wide solvent search space as fully as possible and analysing key performance indicators that relate closely to process performance, energetics, environmental impact, and solvent degradation. To minimize the reliance on experimental data and accelerate the search for new solvents, models that make it possible to predict physical and chemical properties from molecular structure are highly desirable. The motivation for this first step is to reduce the number of solvents to be considered in more detail, and the models used should therefore offer broad predictive capabilities, which may require making simplifying assumptions in model development. In the second step, promising solvents can be further analysed and some of the assumptions made in the first step can be re-assessed. Once a list of candidate solvents is obtained, experiments can be conducted on a subset of these solvents, with the aim of obtaining the information required for a more detailed evaluation of each solvent and the corresponding carbon dioxide process.

To explore the space of possible solvents, there is a need to develop models that offer adequate predictive capabilities without exhaustive reliance on experimental data, and that can provide a quantitative insight into the behaviour of the process; the use of a thermodynamic model to capture the phase and chemical equilibria of mixtures of carbon dioxide, water, and alkanolamine within a process model

is investigated in this chapter, as a means of obtaining an estimate of the performance of the absorption. As an initial assessment of the method, we focus on MEA because as a ubiquitous solvent for CO_2 capture there is extensive experimental data available to test the validity of the predictions. Before presenting the model, we first place the proposed approach in the context of other modelling work in the area.

There is an extensive body of literature concerning the process modelling and simulation of CO_2 absorption in packed columns. The modelling approaches that have been proposed to date differ in the choice of thermodynamic and kinetic models, and, where appropriate, heat- and mass-transfer models. Most of the effort has focused on the performance of aqueous MEA solutions, due to their widespread industrial use and the availability of pilot-plant data, although there have been some models developed for other solvents, notably aminomethylpropanol (AMP) (Aboudheir et al., 2006; Gabrielsen et al., 2006, 2007; Choi et al., 2009b; Afkhamipour and Mofarahi, 2013). In modelling an absorber, the column is usually divided into hypothetical stages, each representing a (sometimes infinitesimal) section of packing in the column (Taylor and Krishna, 1993; Khoury, 2005). Each stage can be modelled using either an equilibrium or a rate-based model. In an equilibrium model, vapour-liquid equilibrium is assumed at each stage, everywhere on the stage. A rate-based model accounts for heat- and mass-transfer limitations. For chemisorption processes with fast reaction kinetics, as is the case for the process of interest (Blauwhoff et al., 1984; Ying and Eimer, 2013), a rate-based process is more reliable. Indeed, Lawal et al. (2009) have compared the two approaches using the same physical property model and concluded that the rate-based model provided a better description of the pilot-plant (Dugas, 2006) temperature profiles where MEA was used as a solvent. A similar comparison was made by Afkhamipour and Mofarahi (2013) for CO_2 absorption in AMP solution, and a rate-based model was found to give a better prediction of the temperature and composition profiles of the pilot-plant runs (Tontiwachwuthikul et al., 1992).

When using a rate-based approach, an important aspect in model development is the choice of approach to treat heat- and mass-transfer phenomena. The concentration and temperature profiles across hypothetical films in a two-film model can be imposed, taking into account the effect of chemical reactions on mass transfer with an enhancement factor, defined as the ratio of the amount of gas absorbed in a reacting liquid to the amount which would be absorbed if there were no reaction (Danckwerts, 1970; DeCoursey, 1982; van Swaaij and Versteeg, 1992). The enhancement factor varies along the length of the column and can often be adjusted to pilot-plant data. This is the route followed in most models of CO_2 absorption (e.g., Sivasubramanian et al. (1985); Tontiwachwuthikul et al. (1992); Pintola et al. (1993); Pacheco and Rochelle (1998); Al-Baghli et al. (2001); Tobiesen et al. (2007); Faramarzi et al. (2010); Khan et al. (2011); Neveux et al. (2013); Saimpert et al. (2013); Jayarathna et al. (2013b); Afkhamipour and Mofarahi (2014)). A comparative review of the rate-based models that have been used to specifically treat CO_2 absorption in aqueous MEA solutions can be found in reference (Llano-Restrepo and Araujo-Lopez, 2015).

As an improvement on film theory, Tobiesen et al. (2007) developed a penetration model, where the two films at the interface are described continuously, which was found to describe their own pilot-plant data well. A more rigorous approach

is that followed by Kucka et al. (2003a), in which the Maxwell-Stefan formalism is used together with film discretization. This more detailed model leads to better predictions of concentration and temperature profiles at the pilot-plant scale (Tontiwachwuthikul et al., 1992) than other models, without the need to adjust any parameters to pilot-plant data (Kucka et al., 2003a). The Maxwell-Stefan formalism has also been applied by Lawal et al. (2010) and Biliyok et al. (2012). Kale et al. (2013) have recently investigated a rate-based model with film discretization, and studied the sensitivity of the calculations to several key parameters. They found that good predictions of column profiles can be obtained with a sufficiently fine discretization.

In all rate-based models, empirical mass-transfer correlations are required to take into account the type of packing used and the operating conditions. The correlations of Onda et al. (1968a),(Onda et al., 1968b) and Bravo and Fair (1982) were developed specifically for random packing, whereas the correlations of Rocha et al. (1996) were developed for structured packing, but can be applied to random packing by using an equivalence relation linking the random packing characteristics to the structured packing. Correlations developed by Billet and Schultes (1999) are also available as they apply to both structured and random packing. In a detailed comparison applied to a model of a CO_2 capture pilot plant presented by Faramarzi et al. (2010), it appears that the main operating conditions to consider when choosing a mass-transfer correlation are the flowrates of the flue gas and the lean solvent.

Another important consideration in modelling CO_2 absorption is the representation of the chemical reactions and fluid phase equilibria of the mixture of MEA, CO_2 and H_2O. In the earliest absorber models, the thermodynamics of the gas and liquid phases were described with the assumption of ideal gas and ideal solution behaviour. This is the case for example of the model developed by Pandya (1983) and later used by Tontiwachwuthikul et al. (1992). However, this model was too simplified to describe the complex interactions between the CO_2 and the solvent, and may not be suitable when transferred to other solvents. Two different approaches are typically followed when developing more accurate models of mixtures exhibiting reaction equilibria: those based on physical theories and those based on chemical theories. Most commonly, a chemical approach (e.g., see references (Dolezalek, 1908; Fredenslund et al., 1975; Prausnitz et al., 1998; Song and Chen, 2009; Zhang et al., 2011c; Fredenslund, 1977)) is adopted. In such approaches, all of the reaction species in solution are modelled explicitly, requiring the *a priori* specification of the relevant reaction schemes and their corresponding temperature-dependent equilibrium constants. Hence, the use of a chemical approach requires experimental data on the concentration of species in solution at various temperatures.

Most models proposed to date that specifically treat CO_2-amine-H_2O systems are based on this class of chemical approach; an explicit treatment of the major ionic and non-ionic species formed due to reaction is adopted. Such methods rely on the use of reaction kinetics and equilibrium constants derived from experimental data specific to each reaction (Austgen et al., 1989, 1991; Kucka et al., 2002; Noeres et al., 2003; Kenig et al., 2003; Kucka et al., 2003a,b; Zhang et al., 2011c). The methodology of combining the electrolyte-NRTL approach (Chen and Evans,

1986a; Austgen et al., 1989) with a Henry's constant to describe CO_2 solubility has attracted much interest and has been used in recent studies (Lawal et al., 2010). The eNRTL approach has also been corrected for inconsistencies by Bollas et al. (2008). More recently, Zhang et al. (2011c) developed a detailed model of the CO_2-MEA-H_2O amine system using a chemical approach, for which an eNRTL (Song and Chen, 2009) model was developed for the treatment of the liquid phase, the perturbed chain statistical associating fluid theory (PC-SAFT) (Gross et al., 2001) was used to obtain the vapour phase fugacity coefficients, and Henry's law constants were obtained to provide a full description of the phase equilibria. While this approach arguably provides the most accurate representation of the behaviour of these mixtures to date, a major drawback of these models is that they contain a large number of parameters, requiring ample experimental data for vapour-liquid equilibrium (VLE) and reaction kinetics, thus making it difficult to use for different conditions and solvents. A similar approach (Kucka et al., 2003a) is to combine the Soave-Rechlich-Kwong (SRK) equation of state (EoS) (Poling et al., 2001) with the eNRTL model. Tobiesen et al. (2007) have adapted an activity coefficient model from Hoff (2003) to correlate VLE experimental data, using an experimentally-derived equilibrium constant (Weiland et al., 2004). As an alternative to reduce the number of parameters to be determined and the computational effort needed to solve the vapour-liquid equilibrium, Gabrielsen et al. (2005) developed their own thermodynamic model to determine the VLE of MEA, CO_2 and H_2O. They proposed a simple correlation derived from experimental data of CO_2 solubility in aqueous MEA, which is valid for MEA over the conditions considered: in this case CO_2 loading (defined as the number of moles of CO_2 per mole of MEA in the liquid phase) varied from 0 to 0.5 at 313 K and 393 K. As a simplification, a single chemical equilibrium reaction (carbamate formation) was considered, reducing the number of adjustable parameters required.

The combined reaction and activity coefficient models developed to date provide an accurate representation of CO_2-MEA-H_2O systems over a range of conditions. However, they require extensive parametrization and the model parameters obtained are not transferable to other solvents. These models are therefore more suited for their application in step two of the solvent selection process, the detailed quantitative analysis of the performance of the most promising solvents.

An alternative treatment of reactions follows a physical approach. Such approaches have previously been proposed to model the phase and chemical equilibria of mixtures of alkanolamines, CO_2, and H_2O (Button and Gubbins, 1999; Mac Dowell et al., 2010, 2011; Rodríguez et al., 2012). SAFT approaches to modelling such systems has been discussed in some detail in chapter 2.

The use of the SAFT-VR thermodynamic approach within process models of CO_2 absorption has previously been explored for high-pressure physical absorption in alkanes (Pereira et al., 2011b), ethers and ether derivatives (Burger et al., 2015), and also for chemisorption. In an early study the modelling of the absorption process was also considered and explored in the context of solvent blend design (Mac Dowell et al., 2010). The absorber model was further developed (Brand et al., 2012) showing reliable results for a set of pilot-plant data. Mac Dowell et al. (2013) have proposed a dynamic model of a CO_2 absorber, based on the SAFT-VR thermodynamic treatment, which has been used in investigations of the control (Arce et al., 2012) and economics (Mac Dowell and Shah, 2013; Alhajaj et al., 2016)

of post-combustion CO_2 capture processes. Qualitative agreement with data from two pilot-plant runs from (Tontiwachwuthikul et al., 1992) was found in these studies (Mac Dowell et al., 2013; Arce et al., 2012; Mac Dowell and Shah, 2013). The column profiles obtained by Mac Dowell et al. (2013) are somewhat difficult to interpret as the location of the plant data points reported in the paper does not match the location of the sensors reported in the physical pilot plant. Nevertheless, the findings of this body of work indicate that a physical approach to the modelling the chemical and physical equilibria allows one to capture the process behaviour accurately with a limited set of parameters.

Overall, the models developed to date can be used to adequately represent the general behaviour of the absorber column. However, only the model of Tontiwachwuthikul et al. (1992) provides an accurate description of the temperature of the rich solvent at the outlet, and in all published models, the bulge in the temperature profile, which is a well-known characteristic of this absorption process (Kvamsdal and Rochelle, 2008), is reproduced qualitatively but not quantitatively. Existing models reproduce either its magnitude or its location along the column, but not both.

In view of foregoing discussion, the potential benefits of a novel absorption model in which a SAFT-VR thermodynamic treatment and a rate-based column model are integrated are explored based on CO_2 absorption in aqueous MEA. The proposed approach is based on a two-film model. Because the reactions are treated implicitly with the SAFT-VR EoS, only the key molecular species (i.e., MEA, CO_2, H_2O and N_2) need to be taken into account explicitly at the level of mass and energy balances. The detailed model presented in this chapter includes several modifications over previous work (Mac Dowell, 2010; Mac Dowell et al., 2010), leading to enhanced model reliability. In section 3.2, we describe the SAFT-VR EoS and the heat- and mass-transfer relations used in the rate-based absorber model. The validation of the model, its predictive capabilities, and a sensitivity analysis are presented in section 3.3. Two scenarios are investigated, corresponding to different levels of data availability: in the first scenario, it is assumed that no pilot-plant data are available, and the suitability of the model to provide a best-case analysis of process performance is studied; in the second scenario, one pilot-plant run is considered and employed to obtain a more realistic quantification of mass-transfer limitations. The transferability of this analysis is then tested against data at other conditions.

3.2 MODELLING METHODOLOGY

The development of a rate-based model of a CO_2 absorber is described in this section. In subsection 3.2.1, the thermodynamic model used for the vapour liquid equilibrium (VLE) and the chemical equilibrium is presented. The non-equilibrium stage approach is introduced in subsection 3.2.2.

3.2.1 *Thermodynamic Model*

The treatment of the chemical-reaction equilibria relevant to the absorption process is a key aspect of the modelling strategy adopted in this work. In the physical

approach followed here, the chemical and physical interactions are treated on an equal footing, within the SAFT-VR SW EoS. Background information is provided in this section to help the reader understand the models used and the underlying assumptions.

The SAFT family of equations stems from the first-order thermodynamic perturbation theory (TPT1) of Wertheim (Wertheim, 1984a,b, 1986a,b; Jackson et al., 1988; Chapman et al., 1988). In SAFT approaches molecules are modelled as chain of fused spherical segments with embedded short-range association sites incorporated to mediate hydrogen bonding which lead to aggregate formation (speciation). The EoS is developed in terms of the Helmholtz free energy using a perturbation approach, such that the free energy of a chain molecule is obtained with respect to the properties (free energy and radial distribution function) of a reference monomeric (non-bonded) system. The original version of SAFT (Chapman et al., 1989, 1990) has been revisited and modified by a number of researchers so that several versions are now available (Huang and Radosz, 1990, 1991; Blas and Vega, 1997; Gil-Villegas et al., 1997; Galindo et al., 1998; Gross et al., 2001; Gross and Sadowski, 2002a; Lafitte et al., 2006a, 2007, 2013b). A historical account of perturbation theories for polar and associating liquids has recently been presented by Gubbins (2016).

In the SAFT-VR formulation (Gil-Villegas et al., 1997; Galindo et al., 1998) used here, a square-well (SW) potential is used to describe the interaction between spherical molecular segments of the reference fluid. The more recent versions of the SAFT-VR EoS incorporate the Mie (generalized Lennard-Jones) potential (SAFT-VR Mie (Lafitte et al., 2013b)), and allows for more reliable representation of the near-critical region and second derivative properties (e.g., heat capacities) which depend mainly on the specific form of the repulsive part of the potential (Lafitte et al., 2006a, 2013b; Dufal et al., 2015a,b). Additionally, group contribution (GC) (Papaioannou et al., 2011b) versions of the SAFT-VR equations of state, namely SAFT-γ SW (Lymperiadis et al., 2007, 2008b) and SAFT-γ Mie (Papaioannou et al., 2014), have also been proposed. These offer additional predictive capabilities in that the properties of a new solvent that has never been synthesized can be predicted (without data specific to that solvent) provided that parameters for the functional groups appearing in that molecule are available. The assessment of the integration of the molecular-based SAFT-VR SW EoS within an absorption model presented in this chapter can readily be extended to a group contribution formulation.

In the SAFT-VR SW approach, a molecule i is modelled as a chain of m_i fused homonuclear spherical segments of diameter σ_{ii}. The interactions between two identical segments are described by a square-well potential of range λ_{ii} and depth ε_{ii} (cf. figure 6). For each molecule i, the number of site types $N_{s,i}$ must be defined, as well as the number of sites of each type a, $N_{s,ia}$. The sites are characterized by SW site-site energetic $\varepsilon^{HB}_{ab,ii}$ and range $r_{c;ab,ii}$ parameters (cf. figure 6).

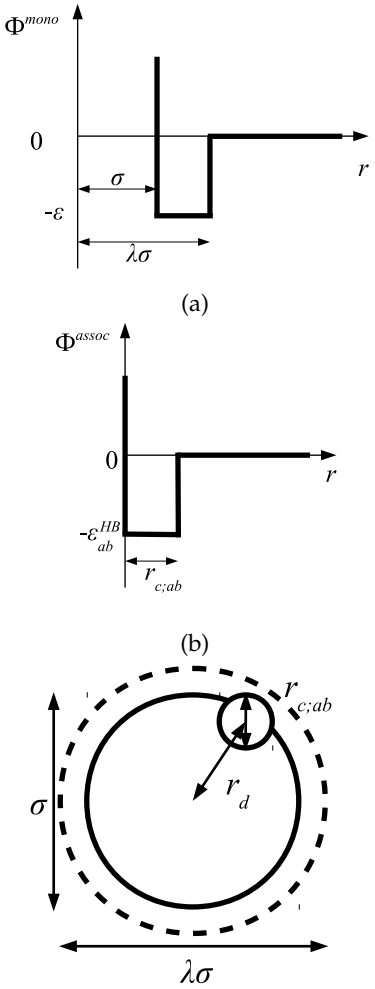

Figure 6: The square-well potentials for a monomer, Φ^{mono}, and association between the sites, Φ^{assoc}, employed in the SAFT-VR approach. (a) Φ^{mono} is characterized by a hard-core with a diameter σ, range of attraction $\lambda\sigma$ and depth ε. (b) Φ^{assoc} is defined by an off-centre potential of depth ε^{HB}_{ab} and of range $r_{c;ab}$. (c) The centre of the site is at a distance r_d from the centre of the segment. This figure is reproduced from (Brand et al., 2016).

In order to model mixtures, combining rules based on the Lorentz-Berthelot approach (cf. Haslam et al. (2008)) are used to describe the unlike interaction between segments on two different molecules i and j:

$$\sigma_{ij} = \frac{\sigma_{ii} + \sigma_{jj}}{2} \tag{39}$$

$$\varepsilon_{ij} = (1 - k_{ij})\sqrt{\varepsilon_{ii}\varepsilon_{jj}} \tag{40}$$

$$\lambda_{ij} = \frac{\sigma_{ii}\lambda_{ii} + \sigma_{jj}\lambda_{jj}}{\sigma_{ij}} \tag{41}$$

where k_{ij} is an adjustable parameter that characterizes the unlike dispersion attractive interaction. Parameters to describe association between different molecules are estimated using experimental data for the specific mixtures of interest, or for chemically similar mixtures (Mac Dowell et al., 2010; Rodríguez et al., 2012).

In recent work (Mac Dowell et al., 2010; Rodríguez et al., 2012; Chremos et al., 2013, 2016) the reactions involved in aqueous amine solutions of CO_2 have been treated implicitly within the SAFT-VR and SAFT-γ frameworks, with the products of the chemical reaction represented as aggregates of the reactant molecules. In the case of MEA the overall set of reactions can be reduced to (Blauwhoff et al., 1984)

$$\begin{aligned} CO_2 + HOC_2H_4NH_2 &\rightleftharpoons [HOC_2H_4NH_2^+ + CO_2^-], \\ [HOC_2H_4NH_2^+ + CO_2^-] + HOC_2H_4NH_2 &\rightleftharpoons HOC_2H_4NH_3^+ + HOC_2H_4NHCO_2^-, \end{aligned}$$

and association sites that allow the complexation of CO_2 and amine are introduced in the SAFT-VR molecular models. The reaction products can thus be modelled as neutral aggregates of CO_2 and MEA, bonded at association sites as shown in figure 7.

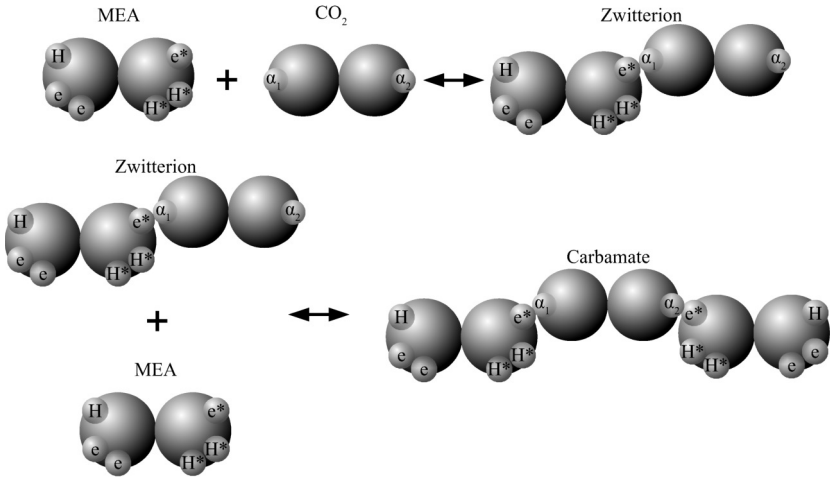

Figure 7: Schematic representation of the association scheme between MEA and CO_2 (in aqueous media) showing two reaction products.

An accurate overall representation of the vapour-liquid phase equilibria of MEA + CO_2 + H_2O can be obtained in this manner by estimating the molecular parameters from experimental fluid-phase equilibria data, for both the pure components and mixtures. One important implication of the physical treatment of chemical equilibrium is that there is no need to explicitly specify a reaction scheme or reaction products. The types of products formed (e.g., carbamates or bicarbonates) are dictated by the association scheme chosen (number of sites and strength of their interactions), and the relative extent of formation of the different products depends on the temperature-independent intermolecular parameters that describe the association energies. The fraction of molecules bonded at a given site is an output of the SAFT-VR model and the distribution of reaction products can be determined from a statistical analysis of the values of these fractions at the thermodynamic state of interest (Economou and Donohue, 1991). Thus, although no speciation data are used in deriving the SAFT-VR parameters, the speciation equilibria can nonetheless be predicted successfully (Rodríguez et al., 2012; Chremos et al., 2016).

This type of physical approach greatly reduces the number of parameters needed to describe the mixture compared to explicit approaches such as eNRTL, in which every species must be described as a separate entity and temperature-dependent equilibrium constants must be derived for all the relevant reactions. The SAFT-VR approach has been shown to be applicable to the absorption of CO_2 in a wide range of aqueous alkanolamines solution (Rodríguez et al., 2012). In many cases, it is possible to transfer parameters from one alkanolamine to another based on molecular similarity, further reducing the need for experimental data.

One key assumption in adopting this type of physical approach is that all reactions are assumed to be at equilibrium, which is only applicable to processes in the physical regime, i.e., where mass transfer is the rate limiting process. In the case where a specific treatment of the charged electrolytic species is required, the SAFT-VRE approach (Galindo et al., 1999; Gil-Villegas et al., 2001; Patel et al., 2003a; Behzadi et al., 2005; Paricaud et al., 2010; Schreckenberg et al., 2014) can be adopted coupled to a chemical approach as appropriate. It is also possible to represent some or all species explicitly where any chemical reactions that are not at equilibrium can then be modelled via a separate kinetic model. We do not follow this route here, which would fall within the class of chemical approaches, but instead assess the adequacy of the physical approach.

The molecules considered in our study are MEA, H_2O, CO_2, and N_2. A schematic of the molecular models used in the SAFT-VR SW EoS is presented in figure 8. The values of all parameters are listed tables 4-7. Note that some of the k_{ij} values for the binary mixtures shown in Table 5 show large deviations from 1. $k_{ij} = 0.48$ for MEA + CO_2 is large since this parameter was regressed to the ternary reactive mixture (MEA + CO_2 + H_2O), representing a highly non-ideal interaction. The large negative $k_{ij} = -0.3635$ between H_2O and N_2 may indicate an associative force which isnt explicitly accounted for in the model. The MEA molecule is represented as 2 tangent spherical segments with 2 association sites of type e (electron lone pairs on the oxygen atom), 1 site of type e^* (corresponding to the lone pair on the nitrogen atom), 1 site of type H (the hydrogen atom on the hydroxyl group), and two sites of type H* (hydrogen atoms on the amine group) (Mac Dowell et al., 2010). The H_2O is represented as 1 spherical segment with 2 e sites and 2 H sites (Clark et al., 2006). The CO_2 model comprises 2 segments and has 1 α_1 site and 1 α_2 site (acceptor sites) that interact only with the e^* sites of MEA (Rodríguez et al., 2012). The N_2 model is modelled as a fused non-spherical diatomic, with an aspect ratio of $m = 1.4$, and does not have association sites as it is chemically inert and apolar (Paricaud et al., 2004b; Mac Dowell, 2010). A site of type e/e^* can bond with a site H/H* and vice versa. For example, when an e site from MEA and an H site from water come within the cut-off range $r^{HB}_{c,eH,MEA-H_2O}$ of each other, there is a site-site hydrogen-bonding associative interaction of energy $-\varepsilon^{HB}_{c,eH,MEA-H_2O}$. A representative example of the good overall description of the temperature and pressure dependence of the absorption VLE behaviour of CO_2 in aqueous MEA obtained with the SAFT-VR SW models can be seen in figure 9 over several orders of magnitude for the partial pressure of CO_2. In the standard Wertheim TPT1 treatment at the heart of the SAFT EoS, association into linear-chain, branched-chain, and network aggregates are considered. Association into ring-like structures (Sear and Jackson, 1994a; Ghonasgi et al., 1994; Sear and Jackson, 1996a; Galindo et al., 2002) (and even double bonding (Sear and

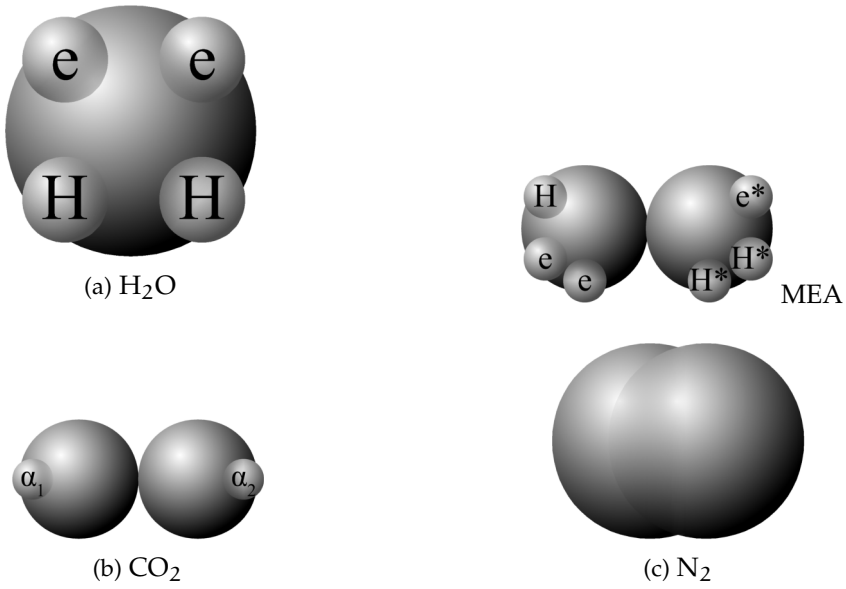

(a) H_2O (b) CO_2 (c) N_2

Figure 8: A schematic of the molecular models used in the SAFT-VR SW approach: (a) H_2O, (b) MEA, (c) CO_2 and (d) N_2.

Jackson, 1994b) and bond cooperativity (Sear and Jackson, 1996b)) can be taken into account but this is not considered for the systems described in our current work.

3.2.2 *Non-equilibrium stage model for the absorption column*

The absorber is a counter-current vapour-liquid multistage separation column, with a liquid feed at the top stage and a vapour feed at the bottom stage. The vapour product comes off the top stage and the liquid product off the bottom stage. The inside of the column is filled with an inert packing material designed for a maximum mass transfer between the vapour and the liquid and for a low pressure drop. The vapour and liquid compositions vary continuously with packing height.

The modelling of such a column can be either discrete or continuous in the vertical direction. In a discrete model, the column is divided in hypothetical stages, each of which represents a section of packing in the packed column. For rate-based models, a greater number of stages provides a better description (Taylor and Krishna, 1993). Taken to the limit, using an infinite number of stages is equivalent to modelling the column continuously. Although both models could be used, we choose the discrete approach for our study.

The modelling of the stages can be equilibrium or rate-based. In an equilibrium model, it is assumed that vapour-liquid equilibrium is achieved at each stage, everywhere on the stage. A rate-based model accounts for limitations due to transport phenomena. Due to the complexity of the process modelled in this case, a rate-based approach is chosen over an equilibrium one in order to capture some of the key physical phenomena (Krishnamurthy and Taylor, 1985a,b).

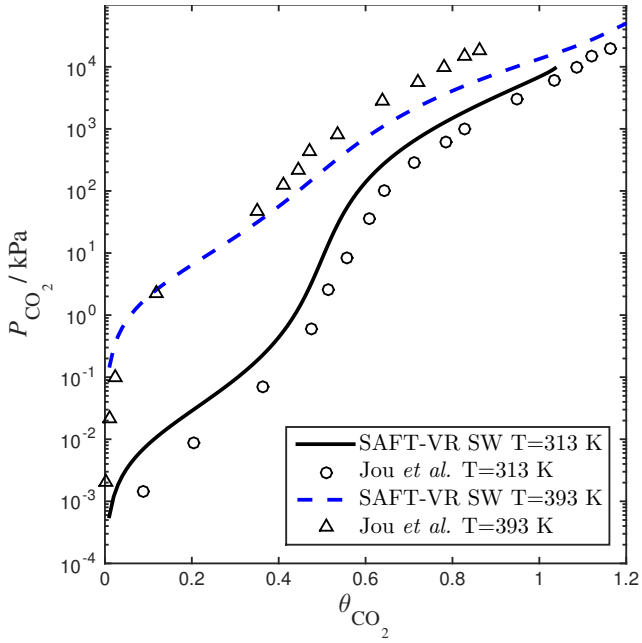

Figure 9: Solubility of CO_2 in a 30 wt% aqueous solution of MEA expressed as the CO_2 loading in the liquid solvent (defined as the number of moles of CO_2 per mole of MEA in the liquid phase) as a function of the partial pressure. SAFT-VR model predictions (dashed and continuous curves) using parameters from Rodríguez et al. (2012) and experimental data (triangles and circles) from Jou et al. (1995).

For absorber model, the assumption is made that the two phases are distinct, and each phase is perfectly mixed at each stage. A diagram of a non-equilibrium stage is presented in figure 10. Vapour from the stage below is brought into contact with liquid from the stage above and the two phases exchange mass and energy through their common interface represented in the diagram by the wavy line. In a rate-based model, separate mass balances are written for each phase. The two phases are in contact through their interface where material lost by the vapour phase is gained by the liquid phase. The heat transfer is treated in a similar way. There is one energy balance in each phase, and the phases are linked via the rate of energy transferred across the phase interface. The compositions of the two phases at the interface are determined assuming equilibrium conditions at the interface.

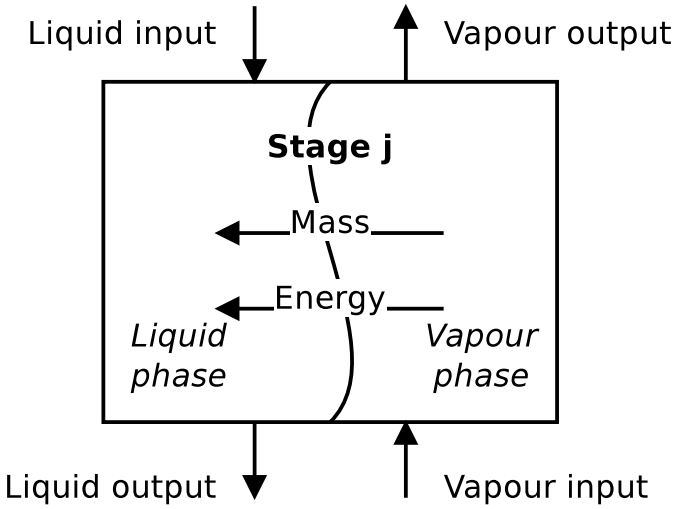

Figure 10: A schematic of a non-equilibrium stage. This stage represents a section of packing in a packed column.

The behaviour at the phase interface in the rate-based stages is described with a two-film theory (Krishnamurthy and Taylor, 1985a). Each phase is split into two parts: the bulk phase; and the film in which the heat and mass transfer occur. In the bulk phase, the concentration, pressure, and temperature are assumed to be uniform, whereas there could be a gradient in composition and temperature in the film. A liquid–gas interface between the two films is sketched in figure 11, where the profiles for composition of component i, temperature and pressure are represented.

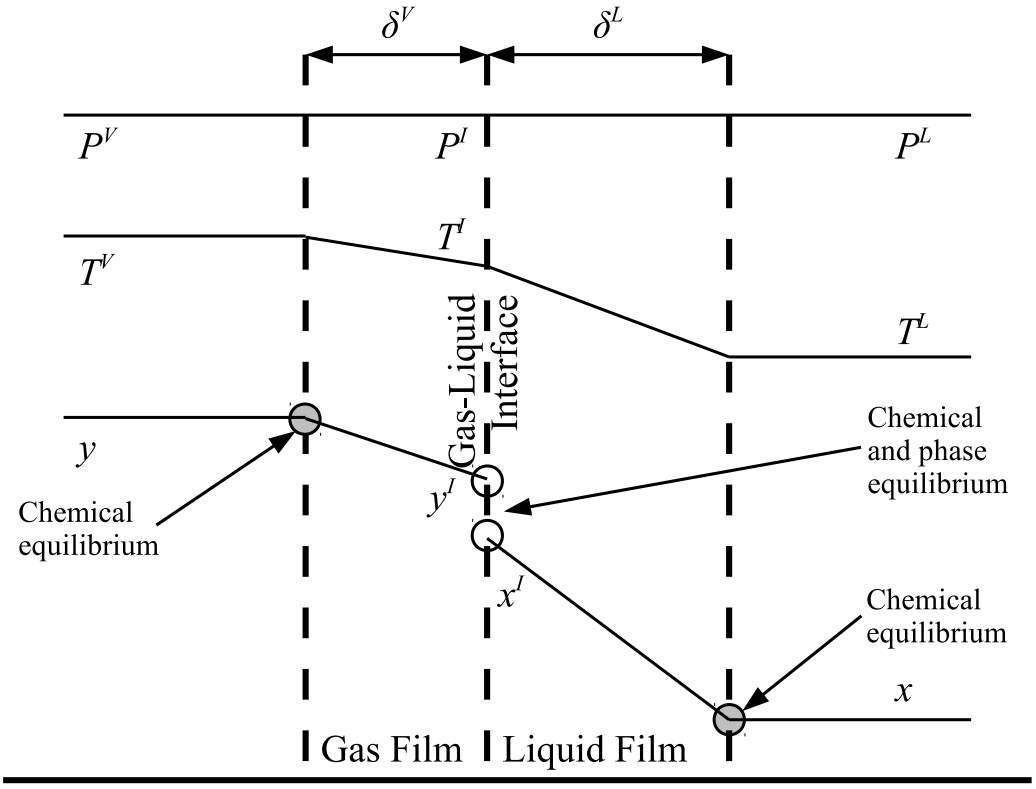

Figure 11: A schematic of the two-film model of a column stage. δ^V and δ^L represent the thickness of the gas and liquid films, respectively. P^V, P^I, and P^L are the pressure in the bulk vapour phase, at the gas-liquid interface and in the bulk liquid, respectively. As can be seen an isobaric profile is assumed. The temperatures of the bulk vapour phase, at the gas-liquid interface, and of the bulk liquid are denoted by T^V, T^I, and T^L, respectively. Finally, y_i and x_i are the mole fractions of component i in the bulk vapour and liquid phases, respectively, and y_i^I and x_i^I are the mole fractions of component i at the vapour-liquid interface in the vapour and the liquid phases, respectively.

The following assumptions are made:

- The model is steady state.
- The bulk phases and films are at chemical equilibrium everywhere (i.e., the reaction rates are faster than the mass transfer rates) (Laddha and Danckwerts, 1981; Blauwhoff et al., 1984).
- The interface is at phase and chemical equilibrium - this is a reasonable assumption for MEA due to the high rate of reactions.
- The interfacial surface area is the same for both heat and mass transfer following (Laddha and Danckwerts, 1981).
- The effective area is equal to the wetted area (Laddha and Danckwerts, 1981).
- The absorption column is considered to be adiabatic since it is insulated (Tontiwachwuthikul et al., 1989).
- There is no pressure drop along the column.

3.2.3 *Model equations*

In this subsection, we present the equations used to model a packed column subsection (stage). The equations are grouped into different categories: energy and mass balances, rate equations, equilibrium equations, mass-transfer correlations, heat-transfer correlations, and diffusion correlations. We list explicitly all of the model equations to clarify the radically different approach followed here. One important model parameter τ is introduced in this section to account for a scaling of the CO_2 diffusivity. This parameter will be estimated from experimental data. In the following equations, the subscript i refers to the i^{th} component, j to the j^{th} stage, c is the total number of components, and N_s is the number of stages in the column. The number of stages is fixed to 50 which is amply sufficient to assure numerical convergence without significantly impacting the computational time.

3.2.3.1 *Heat and mass balances*

The liquid and vapour phase mole balances for component i on stage j are given by

$$L_{j-1}x_{i,j-1} + N^L_{i,j} = L_j x_{i,j} \qquad i = 1, 2..., c;\ j = 1, 2..., N_s \tag{42}$$

$$V_{j+1}y_{i,j+1} - N^V_{i,j} = V_j y_{i,j} \qquad i = 1, 2..., c;\ j = 1, 2..., N_s \tag{43}$$

where L_j and V_j (mol s^{-1}) are the total liquid and vapour molar flowrate leaving stage j respectively, $x_{i,j}$ and $y_{i,j}$ are the bulk liquid and vapour mole fractions of component i on stage j, $N^L_{i,j}$ (mol s^{-1}) is the net gain of species i in the liquid phase due to interphase transport for stage j, and $N^V_{i,j}$ (mol s^{-1}) is the net loss of species i in the vapour phase due to interphase transport for stage j.

The mole fractions in the streams leaving each stage must sum to unity:

$$\sum_{i=1}^{c} x_{i,j} = 1 \quad \text{and} \qquad \sum_{i=1}^{c} y_{i,j} = 1; \qquad j = 1, 2..., N_s \tag{44}$$

The energy balances for the liquid and vapour phases respectively are

$$L_{j-1}H^L_{j-1}(T^L_{j-1}, P, \underline{x}_{j-1}) + E^L_j = L_j H^L_j(T^L_j, P, \underline{x}_j) \qquad j = 1, 2..., N_s, \tag{45}$$

$$V_{j+1}H^V_{j+1}(T^V_{j+1}, P, \underline{y}_{j+1}) - E^V_j = V_j H^V_j(T^V_j, P, \underline{y}_j) \qquad j = 1, 2..., N_s, \tag{46}$$

where H^L_j and H^V_j (J mol^{-1}) are the molar enthalpies of the liquid and gas phases respectively of stage j. E^L_j (W) is the net gain of energy of the liquid phase through the interface at stage j, and E^V_j (W) is the net loss of energy from the vapour phase through the interface at stage j. The molar enthalpies H^L_j and H^V_j are determined from SAFT-VR as functions of the temperature of the bulk phases, T^L_j and T^V_j (K), the molar volumes of the phases, V^L_j and V^V_j (m^3 mol^{-1}), and the composition (vectors) of the phases, $\underline{x}_j$ and $\underline{y}_j$.

There is no accumulation of mass or energy at the vapour–liquid interface:

$$N^L_{i,j} = N^V_{i,j} \qquad i = 1, 2..., c; \qquad j = 1, 2..., N_s, \tag{47}$$

$$E^L_j = E^V_j \qquad i = 1, 2..., c; \qquad j = 1, 2..., N_s. \tag{48}$$

3.2.3.2 *Rate equations: mass transfer*

According to the film model for mass transfer, we define the mass-transfer rates as follows:

$$N^L_{i,j} = k^L_{i,j} a_{T,j} (C^{I,L}_{i,j} - C^L_{i,j}) \qquad i = 1, 2..., c;\ j = 1, 2..., N_s, \tag{49}$$

$$N^V_{i,j} = k^V_{i,j} a_{T,j} (C^V_{i,j} - C^{I,V}_{i,j}) \qquad i = 1, 2..., c;\ j = 1, 2..., N_s, \tag{50}$$

where $a_{T,j}$ (m^2) is the total interfacial area on stage j available for heat or mass transfer, $k^L_{i,j}$ ($m\ s^{-1}$) is the liquid-phase mass-transfer coefficient for component i of stage j, $k^V_{i,j}$ ($m\ s^{-1}$) is the vapour-phase mass-transfer coefficient for component i of stage j, $C^L_{i,j}$ and $C^V_{i,j}$ ($mol\ m^{-3}$) are the concentrations of component i in the bulk liquid and vapour phases of stage j, and $C^{I,L}_{i,j}$ and $C^{I,V}_{i,j}$ ($mol\ m^{-3}$) are the concentrations of component i at the vapour-liquid interface in the liquid and vapour phases of stage j.

The total area for heat and mass transfer is given by the product of the effective specific area and the stage volume:

$$a_{T,j} = a'_j A_{section} D_z \qquad j = 1, 2..., N_s, \tag{51}$$

where a'_j ($m^2\ m^{-3}$) is the interfacial area density on stage j, $A_{section}$ (m^2) is the cross sectional area of the column, and D_z (m) is the stage height given by $h_{packing}/N_s$, with $h_{packing}$ (m) as the total packing height.

3.2.3.3 *Rate equations: heat transfer*

The energy fluxes in the liquid and gas phases at stage j are given by the sum of the conductive and diffusive heat fluxes:

$$E^L_j = Q^L_{cond,j} + Q^L_{diff,j} \qquad j = 1, 2..., N_s, \tag{52}$$

$$E^V_j = Q^V_{cond,j} + Q^V_{diff,j} \qquad j = 1, 2..., N_s, \tag{53}$$

where $Q^L_{cond,j}$ and $Q^L_{diff,j}$ (W) are the conductive and diffusive heat fluxes at the interface into the liquid phase on stage j, and $Q^V_{cond,j}$ and $Q^V_{diff,j}$ (W) are the conductive and diffusive heat fluxes at the interface out of the vapour phase on stage j.

The conductive heat-transfer rate into the liquid phase and out of the vapour phase on stage j are driven by temperature gradients between the bulk phases and the interface, and are given by

$$Q^L_{cond,j} = h^L_{T,j} a_{T,j} (T^I_j - T^L_j) \qquad j = 1, 2..., N_s, \tag{54}$$

$$Q^V_{cond,j} = h^V_{T,j} a_{T,j} (T^V_j - T^I_j) \qquad j = 1, 2..., N_s, \tag{55}$$

where $h^L_{T,j}$ and $h^V_{T,j}$ ($W\ m^{-2}\ K^{-1}$) are the heat-transfer coefficients in the liquid and gas phases on stage j, respectively , and T^I_j (K) is the temperature at the vapour-liquid interface on stage j.

The diffusive heat fluxes account for the variation in enthalpy in the liquid and vapour streams associated with the transfer of mass from one phase to another. This is obtained based on the individual component fluxes and the corresponding enthalpies of the pure components:

$$Q^{L}_{diff,j} = \sum_{i=1}^{c} N^{L}_{i,j} H^{L}(T^{L}_{j}, P, \underline{z}_i) \qquad j = 1, 2..., N_s, \tag{56}$$

$$Q^{V}_{diff,j} = \sum_{i=1}^{c} N^{V}_{i,j} H^{V}(T^{V}_{j}, P, \underline{z}_i) \qquad j = 1, 2..., N_s, \tag{57}$$

where $H(T^{L}_{j}, V^{*L}_{i,j}, \underline{z}_i)$ and $H(T^{V}_{j}, V^{*V}_{i,j}, \underline{z}_i)$ (J mol^{-1}) are the molar enthalpies of pure component i in the bulk liquid and vapour phase respectively, as calculated with SAFT-VR SW. The variable $\underline{z}_i$ denotes the molar composition vector of a stream consisting of pure component i defined by $z_{k,i} = 1$ if $i = k$ and $z_{k,i} = 0$ otherwise. $V^{*L}_{i,j}$ and $V^{*V}_{i,j}$ (m^3 mol^{-1}) are the molar volumes of pure component i at stage j in the bulk liquid and vapour phases respectively, given by

$$P^{L}_{j} = P(T^{L}_{j}, V^{*L}_{i,j}, \underline{z}_i) \qquad i = 1, 2..., c;\ j = 1, 2..., N_s, \tag{58}$$

$$P^{V}_{j} = P(T^{V}_{j}, V^{*V}_{i,j}, \underline{z}_i) \qquad i = 1, 2..., c;\ j = 1, 2..., N_s, \tag{59}$$

where P^{L}_{j} and P^{V}_{j} (MPa) are the pressure of the bulk liquid and vapour phases at stage j respectively and $P(T^{L}_{j}, V^{*L}_{i,j}, \underline{z}_i)$ and $P(T^{L}_{j}, V^{*L}_{i,j}, \underline{z}_i)$ represent evaluations of the pressure using the SAFT-VR SW EoS.

When equating the vapour and liquid fluxes, one obtains an expression which includes the difference between the enthalpies in the vapour phase and in the liquid phase for a pure component i; this is the enthalpy of vaporisation of this component. As we will see, the enthalpy of vaporisation of water plays a significant role in the process. We assume that the contribution of N_2 due to its change of enthalpy between the two phases is negligible as its mass transfer is very small, and that the enthalpy of vaporisation of CO_2 is negligible as the operating conditions are close to or above its critical point. In the case where only one phase is stable for a pure component at the conditions of interest, as is typically the case for CO_2, one can access the hypothetical phase information by providing an adequate initial guess for the molar volume to the SAFT-VR SW EoS.

3.2.3.4 *Equilibrium relations*

Both chemical and phase equilibrium are assumed to prevail at the interface so that the conditions of equality of pressure, temperature, and chemical potential must be satisfied:

$$\mu^{L}(T^{I}_{j}, P, \underline{y}^{I}_{j}) = \mu^{V}(T^{I}_{j}, P, \underline{x}^{I}_{j}) = \mu^{I,L}_{i,j} = \mu^{I,V}_{i,j} \qquad i = 1, 2..., c;\ j = 1, 2..., N_s \tag{60}$$

where $\mu^{I,L}_{i,j}$ and $\mu^{I,V}_{i,j}$ (J mol^{-1}) are the chemical potentials of component i on stage j in the liquid and vapour phases respectively, $V^{I,L}_{j}$ and $V^{I,V}_{j}$ (m^3 mol^{-1}) are the molar volumes of the liquid phase and the vapour phases at the vapour-liquid interface on stage j, and P^{I}_{j} (MPa) is the pressure at the liquid-vapour interface on

stage j. The chemical potentials and the molar volume are determined using the SAFT-VR SW EoS.

The mole fractions at the interface must sum to unity:

$$\sum_{i=1}^{c} x_{i,j}^{I} = 1 \quad \text{and} \qquad \sum_{i=1}^{c} y_{i,j}^{I} = 1 \qquad j = 1, 2..., N_s. \tag{61}$$

Each stage is assumed to be at mechanical equilibrium, so that

$$P_j^V = P_j^L = P_j^I \quad j = 2..., N_s, \tag{62}$$

where

$$P_j^V = P(T_j^V, V_j^V, \underline{y}_j) \qquad j = 1, 2..., N_s, \tag{63}$$

$$P_j^L = P(T_j^L, V_j^L, \underline{x}_j) \qquad j = 1, 2..., N_s. \tag{64}$$

Finally, the column pressure drop is assumed to be negligible.

$$P_j^V = P_{j+1}^V; \qquad j = 1, 2..., N_s. \tag{65}$$

All pressure terms present in the model are thus equated to the pressure of the gas inlet stream, $P_{N_s+1}^V$. This assumption can easily be removed at a later stage of the model development. Preliminary results have indicated that the pressure drop has a negligible effect on the process used for the validation of our model.

The equations presented in the remainder of this section apply to each stage. The subscript j has been omitted for the purpose of clarity.

3.2.3.5 *Mass-transfer correlations*

The interfacial area, the liquid-phase mass-transfer coefficient, and the gas-phase mass-transfer coefficient are obtained using the correlations from Onda et al. (1968a)/(Onda et al., 1968b). Other correlations are available, the most commonly used being the ones developed by Rocha et al. (1996) and Billet and Schultes (1999). Faramarzi et al. (2010) compared the performance of the correlations and found that all three correlations provide a good description; they expressed a slight preference for the correlations of Rocha et al. (1996) but could not draw a general conclusion which is applicable to all operating conditions. The correlations of Rocha et al. (1996) apply to structured packing and have to be adapted for use in random packing, whereas those developed by Onda et al. (1968a)/(Onda et al., 1968b) have been developed specifically using random Berl saddle packing, the same as the one employed in the pilot plant by Tontiwachwuthikul et al. (1992). This last set of correlations is sometimes re-parametrized when used in commercial software such as Aspen or ProTreat. The correlations developed by Onda et al. (1968a)/(Onda et al., 1968b), as reported by Treybal (1981), are implemented in our model of the absorber column. The liquid-phase mass-transfer coefficient for component i is given by (Treybal, 1981)

$$k_i^L = 0.0051 \left(\frac{\eta^L g}{\rho^L}\right)^{1/3} (Re^{L\prime})^{2/3} (Sc_i^L)^{-1/2} (a_p L_p)^{0.4} \qquad i = 1, 2..., c, \tag{66}$$

where ρ^L (kg m^{-3}) is the density of the liquid phase, η^L (kg m^{-1} s^{-1}) is the dynamic viscosity of the liquid phase, g (m s^{-2}) is the gravitational acceleration, $Re^{L\prime}$ is the liquid-phase Reynolds number based on the interfacial area, Sc_i^L is the Schmidt number of component i in the liquid phase, a_p (m^2 m^{-3}) is the specific surface area of the packing, and L_p (m) is the nominal packing size.

The Reynolds number and the Schmidt number for component i in the liquid phase are

$$Re^{L\prime} = \frac{\rho^L u^L}{a' \eta^L}, \tag{67}$$

$$Sc_i^L = \left(\frac{\eta^L}{\rho^L D_i^L}\right); \qquad i = 1, 2..., c, \tag{68}$$

where D_i^L (m^2 s^{-1}) is the diffusion coefficient of component i in the liquid phase, u^L (m s^{-1}) is the liquid velocity, and a' is the interfacial area density defined in equation (72).

The vapour-phase mass-transfer coefficient is obtained from

$$k_i^V = 2 a_p D_i^V Re^{V\,0.7} Sc_i^{V\,1/3} (a_p L_p)^{-2}; \qquad i = 1, 2..., c, \tag{69}$$

where D_i^V (m^2 s^{-1}) is the diffusivity of component i in the vapour-phase, Re^V is the vapour-phase Reynolds number, and Sc_i^V is the Schmidt number of component i in the vapour phase.

The Reynolds number and the Schmidt number for the vapour phase are

$$Re^V = \frac{\rho^V u^V}{a_p \eta^V}, \tag{70}$$

$$Sc_i^V = \left(\frac{\eta^V}{\rho^V D_i^V}\right); \qquad i = 1, 2..., c, \tag{71}$$

where ρ^V (kg m^{-3}) is the density of the vapour phase, η^V (kg m^{-1} s^{-1}) is the dynamic viscosity of the vapour phase, and u^V (m s^{-1}) is the vapour velocity.

The interfacial area density a' is obtained from (Onda et al., 1968a,b)

$$\frac{a'}{a_p} = 1 - \exp[-1.45(\frac{\sigma_c}{\sigma})^{0.75} (Re^L)^{0.1} (Fr^L)^{-0.05} (We^L)^{0.2}], \tag{72}$$

where σ_c (N m^{-1}) is the critical surface tension of the packing material, σ (N m^{-1}) is the vapour-liquid surface tension, Re^L is the liquid-phase Reynolds number based on the specific surface area, Fr^L is the liquid-phase Froude number, and We^L is the liquid-phase Weber number. The interfacial area density, together with the three dimensionless numbers used in equation (72), are properties of the mixture, not properties of individual components.

The expressions for the dimensionless numbers are

$$Re^L = \frac{\rho^L u^L}{\eta^L a_p}, \tag{73}$$

$$Fr^L = \frac{a_p u^{L\,2}}{g}, \tag{74}$$

$$We^L = \frac{\rho^L u^{L\,2}}{a_p \sigma}. \tag{75}$$

The velocities of each phase are

$$u^L = \frac{\dot{v}^L}{A_{section}}, \tag{76}$$

$$u^V = \frac{\dot{v}^V}{A_{section}}, \tag{77}$$

where $\dot{v}^L$ and $\dot{v}^V$ ($m^3\ s^{-1}$) are the volumetric flowrate of the liquid and gas phase respectively.

3.2.3.6 *Heat-transfer correlations*

For the gas and liquid heat-transfer coefficients we use the correlations presented in Treybal's *Mass Transfer Operations* (Treybal, 1981). Once again these expressions apply to each stage. The expression for the liquid-phase heat-transfer coefficient is

$$\frac{h_T^L d_s}{\lambda_T^L} = 25.1 \left(\frac{d_s L_{spec}}{\eta^L} \right)^{0.45} (Pr^L)^{0.45}, \tag{78}$$

where h_t^L ($W\ m^{-2}\ K^{-1}$) is the liquid-phase heat-transfer coefficient , d_s (m) is the diameter of a sphere of the same surface area as a single packing particle (not the same as a_p), λ_T^L ($W\ m^{-1}\ K^{-1}$) is the liquid thermal conductivity, L_{spec} ($kg\ s^{-1}$) is the specific liquid flowrate, and Pr^L is the liquid phase Prandtl number. The latter is obtained from the following expression:

$$Pr^L = \frac{C_p^L \eta^L}{\lambda_T^L}, \tag{79}$$

where C_p^L ($J\ kg^{-1}\ K^{-1}$) is the specific isobaric heat capacity of the liquid phase. The vapour-phase heat-transfer coefficient is given by

$$\frac{h_T^V}{C_p^V V_{spec}} Pr^{V\,2/3} = 1.195 \left(\frac{d_s V_{spec}}{\eta^V (1 - \epsilon_{L_0})} \right)^{-0.36}, \tag{80}$$

where h_T^V ($W\ m^{-2}\ K^{-1}$) is the vapour-phase heat-transfer coefficient , C_p^V ($J\ kg^{-1}\ K^{-1}$) is the specific isobaric heat capacity of the vapour phase, Pr^V is the Prandtl number for the gas phase, V_{spec} ($kg\ s^{-1}$) is the specific vapour flowrate, and ϵ_{L_0} is the operating void space in the packing. It is assumed to be equal to the void fraction ϵ. The Prandtl number for the gas phase is obtained from

$$Pr^V = \frac{C_p^V \eta^V}{\lambda_T^V}, \tag{81}$$

where λ_T^V ($W\ m^{-1}\ K^{-1}$) is the vapour thermal conductivity.

3.2.3.7 *Vapour-phase diffusion coefficient*

The vapour-phase diffusion coefficient used in equation (71) is obtained from the expression of Fuller and co-workers (Fuller and Giddings, 1965; Fuller et al., 1966,

1969) as reported by Poling et al. (2001). It is assumed that the components are diffusing through air:

$$D_i^V = 10^{-4} \frac{0.00143 T^{V\,1.75}}{10 P^V M_{i-air}^{1/2} [\Sigma_{v_i}{}^{1/3} + \Sigma_{v_{air}}{}^{1/3}]} \quad i = 1, 2..., c, \tag{82}$$

where Σ_v (Å) is the atomic diffusion volume, and M_{i-air} is given by

$$M_{i-air} = 2[(1/M_{air}) + (1/M_i)]^{-1} \quad i = 1, 2..., c, \tag{83}$$

where M_i (g mol^{-1}) is the molar mass of component i.

3.2.3.8 *Liquid-phase diffusion coefficient*

The liquid-phase binary diffusion coefficients are described with different correlations. The mutual diffusion coefficients of CO_2 at very low concentration in pure MEA and pure H_2O are derived from the Wilke-Chang correlation (Wilke and Chang, 1955; Poling et al., 2001):

$$D^{\circ}_{CO_2,k} = \frac{7.4 \times 10^{-8} (\phi_k M_k)^{1/2} T^L}{\eta_k^L (V^m_{CO_2})^{0.6}} \quad k = H_2O, MEA, \tag{84}$$

where ϕ_k is the "association factor" of solvent k, and $V^m_{CO_2}$ (cm^3 mol^{-1}) is the molar volume of CO_2 at its normal boiling temperature.

These mutual diffusion coefficients are used in the correlation of Takahashi (Takahashi et al., 1982) to determine the diffusivity of CO_2 in a liquid mixture of H_2O and MEA:

$$D^L_{CO_2} = \tau 10^{-4} \left(\frac{V^L}{\eta^L}\right)^{1/3} \sum_{k=H_2O,MEA} x_k D^{\circ}_{CO_2,k} \left(\frac{\eta^L_k}{V^{*L}_k}\right)^{1/3}, \tag{85}$$

where we have introduced the scaling prefactor τ to the correlation. The presence of this scaling factor provides an effective approach to modelling several effects that are not accounted for due to the use of a physical approach and the consequent implicit treatment of the reaction products: the acceleration of mass-transfer due to the depletion of CO_2 via chemical reactions (Danckwerts, 1970); the reduction in mass transfer due to the ion pairs formed and their electrostatic interaction with other species (Danckwerts, 1970); and the reduction in the mass transfer due to CO_2 being present in larger aggregated product species (bicarbonate and carbonate species). The latter effect was observed by Han et al. (2013) in a molecular dynamics study of the diffusion coefficient of CO_2 in MEA, indicating a significant decrease in the diffusion coefficient with increasing CO_2 loading. The value of the parameter τ and its impact on model predictions are discussed in section 3.3. Finally, the Perkins and Geankoplis (Perkins and Geankoplis, 1969) method is used to calculate the diffusivity of H_2O, MEA, and N_2 in the liquid phase:

$$D^L_i = 10^{-4} \frac{7.4 \times 10^{-8} (\phi M)_i^{1/2} T}{1000 \eta^L (V^m_i)^{0.6}} \quad i = H_2O, MEA, N_2, \tag{86}$$

where V_i^m ($cm^3\ mol^{-1}$) is the molar volume of component i at its normal boiling temperature, and the term $(\phi M)_i$ ($g\ mol^{-1}$) represents the "association factor" of component i in the liquid mixture which is derived from

$$(\phi M)_i = \sum_{\substack{j=1 \\ j \neq i}}^{n} x_j \phi_j M_j \quad i = H_2O, MEA, N_2 \tag{87}$$

The other correlations of experimental data used in our model are listed in table 8.

3.2.3.9 *Properties computed with SAFT*

In Table 3 we make it explicit which variables in the process model are computed using the SAFT EoS.

Table 3: Table to show which variables in the process are calculated with the SAFT-VR SW equation.

Variable	Definition
H^i	Enthalpy of phase i
P^i	Pressure of phase i
μ^i	Chemical potential of phase i
C_P^i	Isobaric heat capacity of phase i
ρ^i	Density of phase i

3.3 RESULTS

The model described in section 3.2.2 is implemented in gPROMS (Process Systems Enterprise, 2016) and an in-house implementation of the SAFT-VR SW EoS (Kakalis et al., 2004) is accessed via a Foreign Object Interface.

In this section, we investigate the predictive capabilities of the proposed model by thorough comparisons with the the pilot-plant data obtained by Tontiwachwuthikul et al. (1992). The inputs required to model these data and relevant assumptions are discussed in section 3.3.1. As discussed in section 3.3.2, we first assume that there are no pilot-plant data available for the solvent in question and analyse the performance of the model when using the available mass transfer correlations in the literature by fixing $\tau = 1$. It is then assumed that only one pilot-plant run is available and the corresponding concentration profiles are used to estimate the single parameter τ, related to mass transfer limitations, as summarized in section 3.3.3. The transferability of this parameter is assessed by comparing model predictions against data for other pilot-plant runs. Finally, in section 3.3.4, the sensitivity of the model to several parameters is explored, providing insights into the behaviour of CO_2 absorption columns.

3.3.1 *Model inputs*

The absorption column studied by Tontiwachwuthikul et al. (1992) has an internal diameter of 0.1 m and a total packed height of 6.6 m; care has to be taken not to mistake the total column height of 7.2 m with the packed height, which is the relevant dimension in modelling the absorber. The absorption column internals are randomly packed 12.7 mm ceramic Berl saddles. The gas inlet stream is assumed to be free of MEA and the liquid solvent inlet stream free of N_2. The input values used are listed in Table 9 and the characteristics of the column and the packing are listed in Table 10. Some of the data needed for the simulation of the process were not explicitly reported by Tontiwachwuthikul et al. (1992): in particular, the temperature of the flue gas, and the concentration of water in the flue gas. Close inspection of an earlier paper detailing the experimental apparatus (Tontiwachwuthikul et al., 1989) reveals that the temperature of the flue gas is controlled to be that of the lean solvent with a thermostatic bath. The inlet vapour stream is composed of ambient air and bottled CO_2. Typical values of relative humidity of air (defined as the mole fraction of water vapour divided by the mole fraction of air saturated with water at the same temperature and pressure) lie between 20% to 70%, which, at 20°C and 1 bar, corresponds to a mass fraction of H_2O in the flue gas of between $\omega^V_{H_2O}$ 0.003 and 0.01 (ASHRAE, 2011). A sensitivity analysis of the extent of humidity indicates that the variation of $\omega^V_{H_2O}$ between 0 and 0.072 (corresponding to a mole fraction 0.12) has a negligible impact on the temperature and composition profiles. The effect of the amount of water in the flue gas is discussed in more detail in section 3.3.3.2. For our working model, the nominal amount of water in the inlet flue gas is fixed to $\omega^V_{H_2O} = 0.0058$, corresponding to 50% humidity at 20°C and 1 bar.

3.3.2 *Scenario 1*

In the absence of pilot-plant data, the scaling factor τ for the diffusion coefficient of CO_2, cf. equation (85), is set to 1. The predictions with τ=1 are presented in figures 12 and 14-22 as dashed curves. In all but one case (Run T18, figure 19), the rate of absorption of CO_2 throughout the column is found to be over-predicted as the predicted value of the gas-phase CO_2 concentration profiles y_{CO_2} all fall under the measured values. With the exception of Run T18, the temperature profiles T_L and the liquid-phase CO_2 loading profiles θ_{CO_2} (defined as the number of moles of CO_2 per mole of MEA in the liquid phase) are similarly under-predicted. Complete absorption occurs at approximately stage 30, whilst an analysis of the pilot-plant data suggests that this occurs between stages 10 to 20. The size of the column required to achieve maximum absorption is therefore underestimated based on these predictions alone.

In Run T18 (figure 19), there are two competing effects: the overestimation of the absorption of CO_2 tends to increase the temperature of the liquid phase, which in turn tends to decrease the extent of absorption of CO_2 in the liquid. Since this is the only run in which the CO_2 in the inlet gas is not completely absorbed within the column, the cooling effect of the liquid feed is not as apparent as in other runs. Given the relatively low recovery of CO_2 and the fact that equilibrium is

not reached at the bottom of the column, our findings indicate that the model is best used as an indicator of process performance by modelling a sufficiently large absorber to achieve equilibrium.

In most cases (apart from run T18), an optimistic prediction of process performance is thus obtained with the model when no pilot-plant data are used (τ=1). Indeed, although the depletion of CO_2 through chemical reactions has an accelerating effect on mass transfer, the reduced diffusivities of the product species lead to an overall reduction in mass transfer rates. This suggests that the proposed predictive model could be used to obtain a preliminary assessment of novel solvents in the absence of pilot-plant data: if their best-case ($\tau = 1$) performance is found to be significantly less than that of MEA or another suitable benchmark, these solvents would be eliminated from further consideration without undertaking an experimental programme.

3.3.3 *Scenario 2*

3.3.3.1 *Estimation of the scaling factor*

In order to investigate whether the proposed model can be used to provide a quantitative agreement with the pilot-plant runs, the value of τ is then estimated by fitting to selected pilot-plant data. In keeping with our requirement to rely on only a limited amount of experimental data in the first step of the solvent selection process (and the exploration of a large space of solvents), the value τ is estimated from only one pilot-plant run (Run T22 of Tontiwachwuthikul et al. (1992)) in our current work. Additionally, this value is determined by minimizing the absolute deviation between the model predictions and the gas and liquid composition profiles, y_{CO_2} and θ_{CO_2}. The resulting temperature profile for Run T22 is hence predicted since this data was not used in estimating τ. The value of τ that results in the minimum deviation from the compositional pilot-plant data corresponds to a scaling of the liquid-phase diffusivity to 4.1% of its original value (i.e., τ = 0.041). The liquid-phase temperature, gas-phase CO_2 concentration, and liquid-phase CO_2 concentration profiles for Run T22, determined with and without the scaling factor for the diffusivity of CO_2, are represented in figure 12 as continuous and dashed curves, respectively.

As the parameter τ is estimated from pilot-plant data, the value found for τ may be correcting any potential errors in the chosen mass-transfer correlation rather than the diffusivity alone. To the best of our knowledge, there is no published experimental data for the diffusion of the carbamate product in aqueous MEA. In order to assess the impact of the choice of mass-transfer correlation on the value of τ, we implement the mass-transfer correlations of Rocha et al. (1993)/(Rocha et al., 1996) in our current model of the absorber with the same scaling factor of τ = 0.041. The liquid-phase temperature, gas-phase CO_2 concentration, and liquid-phase CO_2 concentration profiles for Run T22 obtained with the two different mass transfer correlations are compared in figure 13. With the correlation of Rocha et al. (1993)/(Rocha et al., 1996) there is a slight underestimation of the composition of CO_2 in the liquid and gas phases; the temperature profile obtained with the correlation of Rocha et al. (1993)/(Rocha et al., 1996) is more faithful to the pilot-plant data than that of Onda et al. (1968a)/(Onda et al., 1968b),

though one should bear in mind that the diffusivity parameter is estimated from the data using the former correlation. In conclusion, the value of τ is found to be essentially independent of the choice of the mass-transfer correlation (at least for this set of process conditions), confirming our hypothesis that a scaling of the diffusivity is required.

3.3.3.2 *Model predictions*

All the runs with the pilot-plant MEA absorber process can now be simulated in a predictive manner using the value of the diffusivity parameter (τ=0.041) obtained based on Run T22. The predictions for the temperature profiles in the liquid phase, and for the gas-phase CO_2 concentration and liquid-phase CO_2 loading profiles for the different Runs T13 to T21 are represented in figures 14 to 22 with continuous curves. These runs represent a variety of operating conditions in terms of amine concentration, inlet liquid-phase CO_2 loading, inlet gas-phase CO_2 concentration, and gas-to-liquid flowrate ratio (see Table 9).

Good agreement is found between the model predictions and the pilot-plant data for Runs T13, T14, T16, T17, T19, and T20 in relation to the liquid-phase temperature and the liquid- and gas-phase composition profiles along the entire length of the column. There is an over-prediction of approximately 5 K in the temperature profile for Runs T15 and T21, and an over-prediction of the composition profiles, although the compositions at the top and at the bottom of the column are accurately described. The outlet liquid temperature in Run T18 is overestimated by about 12 K; there is a good match between the model predictions and the experimental values for the composition profiles. A good representation of the temperature bulges in Runs T16 and T20 can be seen in terms of its location along the column, and the amplitude is predicted accurately for both of these runs. To the best of our knowledge, no other published models provide a description of the temperature bulge to this level of fidelity (Kucka et al., 2003a; Gabrielsen et al., 2006; Faramarzi et al., 2010; Mac Dowell et al., 2013).

In all runs except Run T18, flat profiles are observed toward the top of the column. This plateau means that a maximum in the absorption is reached, indicating that equilibrium is achieved not only at the vapour-liquid interface but also between the bulk liquid and the bulk vapour phases. As a result the profiles would not be affected by making the column any higher. This plateau is depicted in figure 23 for Run T22. It can be seen that the temperatures of the liquid phase, the vapour phase, and the vapour-liquid interface are all equal between stages 1 and 15 (i.e., at the top of the column). Similarly, the CO_2 gas-phase composition in the bulk vapour phase and at the vapour interface are equal between stages 1 and 15, as are the CO_2 loadings in the liquid phase and at the interface. Additionally, the profiles for the temperature of the liquid phase and the temperature at the interface are almost identical, suggesting that all the heat-transfer resistance is in the vapour film.

Run T18 stands out from this set of runs as it does not exhibit a plateau in the profiles as found for the other operating conditions, meaning that the whole length of the column is used for absorption. The lack of a plateau region is clearly apparent from figure 24. From Table 9, one can see that Run T18 has the lowest

amount of MEA in the lean solvent and the highest amount of CO_2 in the flue gas compared to the other runs. This explains why the whole column is required for absorption. In other runs, the totality of CO_2 is absorbed as the gas travels up the column between stages 50 and 15, so that lean solvent flowing at the top of the absorber (stages 1 to 15) has no CO_2 left to absorb. Run T18 is the only run where there is still CO_2 in the gas stream leaving the absorber, so the lean solvent starts absorbing CO_2 as soon as it enters the column at the top. These differences explain why a larger discrepancy is observed between the predicted and measured profiles for Run T18.

The behaviour of Runs T15, T18 and T21 could be represented more accurately by estimating specific values τ for these runs. However, this would not be in keeping with our objective to develop a predictive modelling platform to support solvent design activities. The good overall quantitative agreement achieved with a unique value of τ indicates that the scaling factor can be applied in a transferable manner at different operating conditions (at least for similar types of column packing).

An analysis of the deviation between the column profiles presented here and those obtained when a different run is chosen to estimate τ is also undertaken. The same method is applied to estimate τ based on pilot plant runs T13 – T21. The values of τ range between 0.027 (for Run T19) and 0.076 (for Run T21). These extreme values are then used to predict the column profiles (T_L, y_{CO_2} and θ_{CO_2}). The absolute errors between the values for each variable obtained with $\tau = 0.041$ (for Run T22) and the values obtained from the extreme values of τ is calculated, and averaged over all stages and all column profiles. The calculated mean errors are 4.35 K for T_L, 0.080 for θ_{CO_2} and 0.023 for y_{CO_2}. These values provide an indication of the error bounds for the profiles presented in our current work, based on choosing any single pilot plant run arbitrarily to estimate the value of τ.

3.3.4 *Sensitivity analysis*

A sensitivity analysis is now employed to assess the relative importance of selected mass- and heat-transfer parameters. Different key parameters in the model are altered to observe their impact on the predicted profiles. The values tested are listed in Table 11.

3.3.4.1 *Mass transfer*

The mass transfer in the model is mediated via mass-transfer coefficients (Onda et al., 1968a,b). These coefficients are highly dependent on the viscosity, the diffusivity, and to a certain degree the surface tension of the fluid considered; these properties are thus considered as key parameters in the model and their influence on the temperature and composition profiles are assessed. The values of the parameters used in the sensitivity analysis are varied within physically realistic ranges. We should note that though marked variations are expected for the diffusivity and viscosity for the reacting system of this type, the change in the vapour-liquid surface tension is expected to be somewhat less dramatic. The values of the vapour and liquid diffusivities are doubled and halved, and the vapour-liquid surface tension is varied within $\pm$ 10 mN/m from the nominal value. Varying the diffusivity

or viscosity in the gas phase has no visible effect on the liquid temperature profile or the composition profiles. However, varying these parameters in the liquid phase results in a significant variation in the profiles. The effect on the profiles due to the variation of the liquid viscosity and the diffusivity in the liquid phase is represented in figures 25 and 26. It is clear from figure 25 that the column temperature and composition profiles are highly sensitive to the value of τ. Varying the vapour-liquid interfacial tension produces a less significant variation in the profiles as can be seen in figure 27. The data that are originally considered for the surface tension correlation in our model is for a mixture of only H_2O and MEA (Vazquez et al., 1997). Jayarathna et al. (2013c) recently published experimental data of the surface tension of liquid mixtures of H_2O, MEA and CO_2, finding an increase in the vapour-liquid interfacial tension on absorption of CO_2. A new correlation from these data is also implemented in our process model. A comparison of the temperature and composition profiles obtained with the two different correlations is shown in figure 27. The difference in the profiles is negligible so changing the surface tension correlation is not considered necessary. This also suggests that the process model is less sensitive to realistic changes in the interfacial tension than the corresponding changes in the the diffusivity and viscosity. We should note that the vapour-liquid surface tension can also be determined from the SAFT-VR EoS within a density functional treatment Gloor et al. (2004a, 2007b); Llovell et al. (2010); Rodríguez et al. (2012). We do not however pursue this approach here since accurate experimental data for the surface tension of the H_2O-MEA-CO_2 mixture is available. We will derive a classical density functional theory for the SAFT-VR Mie EoS in chapter 6 for the purpose of obtaining surface tension values predictively.

It should be noted that the values of the mole fractions and temperatures at the outlets are not affected by the variations of the surface tension or the viscosity and diffusivity in the liquid phase. It would be safe to assume that under these operating conditions, where the residence time is large enough for the system to reach equilibrium, the outlet values are determined solely by thermodynamic quantities while the composition profiles are mostly dependent on mass transfer.

3.3.4.2 *Heat transfer*

The major source of heat in the absorption process is a consequence of the exothermic reaction between MEA and CO_2, which occurs in the liquid phase. This heat can then be transferred to the vapour phase. Another major element in the energy balance is the heat associated with the transfer of water from one phase to the other. In the model, the heat transfer is mediated via the heat-transfer coefficients (Treybal, 1981). Two notable thermal parameters can be identified in the model: the heat-transfer coefficient for the liquid phase, and the heat-transfer coefficient for the gas phase. In addition, the magnitude of the enthalpy changes as the components are transferred from one phase to another or as the temperature changes in the gas and liquid streams affect the overall temperature profile. For instance, Kvamsdal and Rochelle (2008) and Faramarzi et al. (2010) have identified the heat capacities as sensitive parameters for the temperature profiles. Here, we consider the impact of the heat of vaporisation of water on model predictions. Although

it is a well characterized thermodynamic quantity, its variation provides insights into the behaviour of the column.

The value of the heat of vaporisation of water is doubled and halved relative to the value predicted by the SAFT-VR EoS, and the values of the heat transfer coefficients are multiplied by 10 and divided by 10 (Table 11). The variation of the liquid heat-transfer coefficient has no visible effect on the liquid-phase temperature and composition profile. The effects on the profiles resulting from varying the heat-transfer coefficients and the heat of vaporisation of water are presented in figures 28 and 29, respectively.

As can be seen from figure 28, despite a variation of one order of magnitude in the vapour heat-transfer coefficient, the effect on the temperature profile is very limited. It can be concluded that for the operating conditions under consideration, the model is insensitive to the heat-transfer coefficients and there is no need to investigate heat-transfer correlations further.

The variation of the heat of vaporisation of water is found to have a significant impact on the liquid phase temperature profile when its value is doubled, and a lesser impact on the composition profiles; it has a limited effect on the end-point values. An increase in the heat of vaporisation magnifies the amplitude of the temperature bulge, whereas a reduction eliminates the bulge. This suggests that the heat of vaporisation of H_2O is responsible for the rate at which the liquid heats up and cools down. A similar effect is observed when a sensitivity analysis is carried out on the heat of absorption of CO_2, however the analysis is not presented here because the adjustment of both properties leads to similar (but opposite) corrections to the energy balance. The key elements to predict the temperature bulge accurately are therefore the enthalpy of absorption of CO_2 and the enthalpy of vaporisation of water. The absorption of CO_2 releases energy that heats both phases. As the gas temperature increases upon entering the column, water is transferred from the liquid phase to the gas phase through evaporation to maintain saturation; this results in an absorption of energy, and a consequent decrease in temperature.

In conclusion, the competition between these two thermal effects (the absorption of CO_2 increases the temperature and the vaporisation of water decreases the temperature) is responsible for the observed and predicted temperature bulge. This interpretation is consistent with that reported in Mac Dowell et al. (2013).

3.3.4.3 *Effect of humidity in the flue gas*

The amount of water in the flue gas is considered to be important in determining the position of the temperature bulge in the absorber (Kvamsdal and Rochelle, 2008; Kvamsdal et al., 2010). In the case of the pilot plants studied by Tontiwachwuthikul et al. (1992) and Dugas (2006), the inlet flue gas is not saturated in water, while the flue gas is saturated in the pilot-plant studies of Tobiesen et al. (2007) and Gabrielsen et al. (2007). In order to assess the impact of humidity in our model of the absorber, we vary the amount of water in the inlet flue gas from $\omega^{V}_{H_2O} = 0$ to 0.072 (corresponding to a mole fraction of 0.12) (water-rich). The effect on the profiles is represented in figure 30. It is apparent that varying the amount of water in the flue gas does not have a significant impact on the composition profiles. The effect is visible only for the liquid-phase temperature profile, where the outlet tem-

perature value is higher by approximately 5 K for the saturated gas $\omega^{V}_{H_2O} = 0.072$ (corresponding to a mole fraction of 0.12) than for the dry gas $\omega^{V}_{H_2O} = 0$. Biliyok et al. (2012) also find that increasing the moisture content of the flue gas affects the absorber temperature profile, however the increase in temperature is more significant in their study because a larger change in moisture content is considered ($\omega^{V}_{H_2O}$ varies between 0.015 and 0.15, where the latter value represents a two-phase aqueous system). The negligible effect on the composition profiles is in contrast to the work of Mac Dowell et al. (2013) who found a large effect of the humidity of the inlet gas on the flux profiles in the mass transfer zone.

3.4 CONCLUSIONS

An absorber model for CO_2 capture is developed with the aim of being as predictive as possible, in order to support solvent design activities prior to extensive experimental investigations. The heat- and mass-transfer are described with rate-based equations, in common with many other process models. Unusually, however, a physical approach is taken to model the chemical reactions taking place in the absorber. Both vapour-liquid equilibrium and the chemical equilibrium are treated within the SAFT-VR thermodynamic framework, ensuring a consistent and accurate representation of the physical interactions in the system under the assumption that reaction kinetics are not rate-determining. This approach lends itself to extension to other solvents, as a consequence of the transferable nature of the SAFT molecular models and the relatively small number of parameters and data required to develop them.

Without making use of pilot-plant data in model development, we find that the proposed model can generally be used to obtain a best-case performance of the solvent in question. This modelling approach is valuable for narrowing the solvent search space as solvents may be quickly rejected by comparing their performance in such a test. With very limited pilot-plant data we find that by adjusting a single parameter that corrects for the diffusivity of CO_2 in the liquid phase, the model can be used to predict with quantitative accuracy a variety of different operating conditions. Excellent predictions are obtained for the liquid-phase temperature profiles and the liquid- and gas-phase compositions along the column in most cases, with moderate deviations in a few cases. The comparison of the absorption performance of different solvents via this method may further aid in the narrowing of the solvent search space, and then a more quantitative comparison could be carried out.

Following accurate predictions of the column profiles, a careful sensitivity analysis is conducted. We find that the liquid viscosity and diffusivity, and to a lesser extent the vapour-liquid surface tension, are key properties for the prediction of the composition profiles. The column profiles are also shown to be sensitive to the thermodynamic properties that are major sources of heat generation or dissipation.

The main benefit of the proposed modelling framework, which is based on the physical modelling of the underlying chemical reactions, is the ability to assess new solvents for which there may be limited data available. This can be further enhanced through the adoption of a group-contribution EoS, which makes use of

the same physical concepts, such as the SAFT-γ Mie EoS (Papaioannou et al., 2014). The modification of the proposed model to use this group-contribution approach is straightforward and offers an additional predictive capability as new solvents may be analysed for which no experimental data are available. Additionally, it is clear that an extension of the work presented here to the desorption process and the coupling of the absorber and desorber is required (Brand et al., 2013). This would allow a much more comprehensive predictive assessment of new solvents and allow the rapid evaluation of many alternative multifunctional amines for the optimal capture of CO_2 from flue gas.

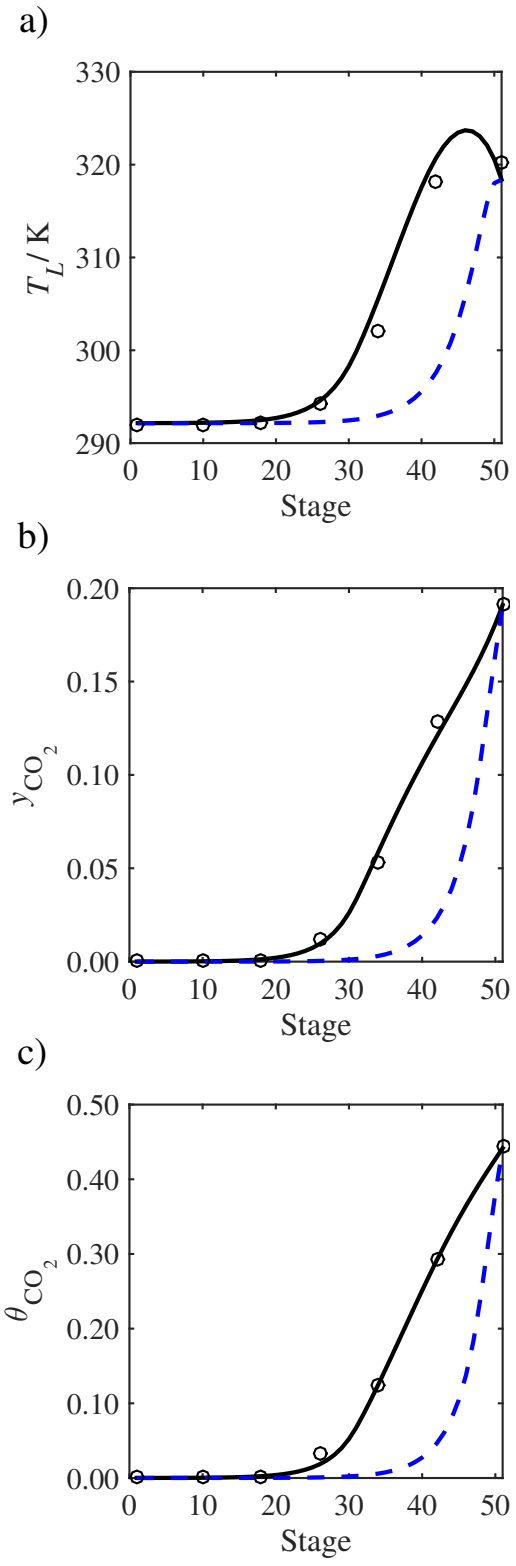

Figure 12: Comparison of the pilot-plant data (circles) (Tontiwachwuthikul et al., 1992) and the result of our model (curves) for Run T22 for the absorption of CO_2 in an 18wt% solution of MEA. The dashed curves represent the results obtained without scaling the CO_2 diffusivity ($\tau = 1$) and the continuous curves the results obtained by scaling the CO_2 diffusivity in the liquid phase to 4.1% of its original value ($\tau = 0.041$). a) Temperature profile for the liquid phase, b) gas-phase CO_2 concentration profile, and c) liquid-phase CO_2 loading (defined as the number of moles of CO_2 per mole of MEA in the liquid phase). Stage 50 corresponds to the bottom of the column.

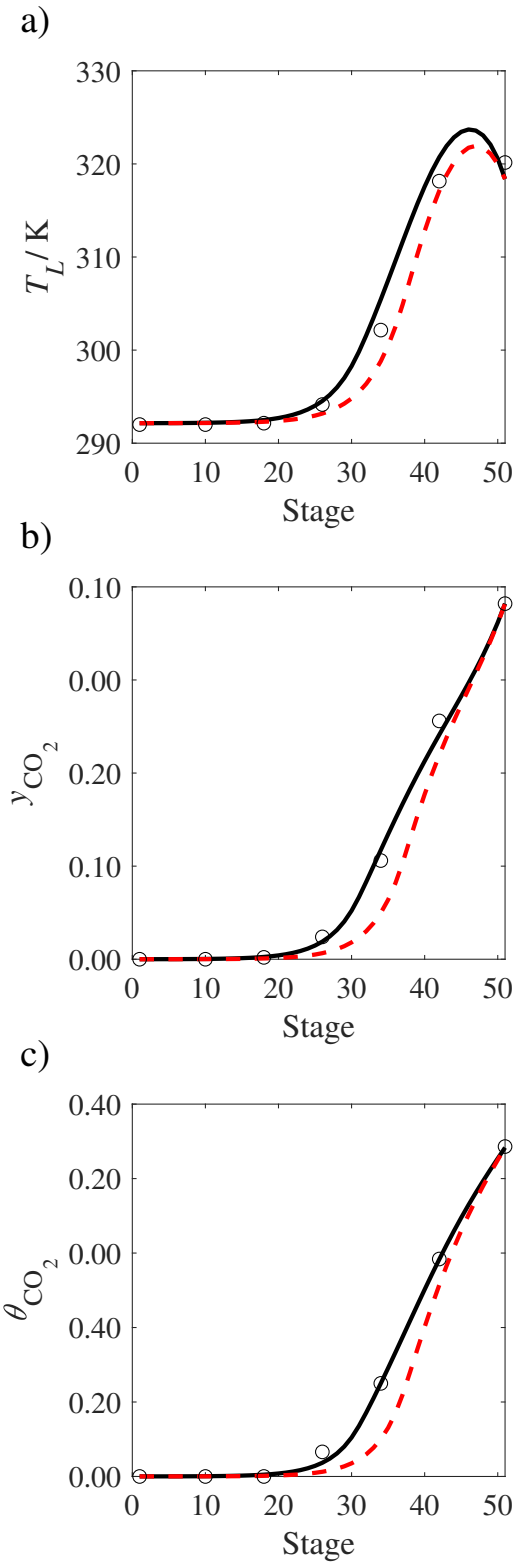

Figure 13: Sensitivity analysis of the mass transfer correlation on the profiles predicted with our model compared with the experimental pilot-plant data of Run T22 (Tontiwachwuthikul et al., 1992): Mass-transfer correlations from Onda et al. (1968a),(Onda et al., 1968b) (continuous black curve); mass-transfer correlations from Rocha et al. (1993),(Rocha et al., 1996) (dashed red curve). (a) Temperature profile for the liquid phase, (b) gas phase CO_2 concentration profile, and (c) liquid phase CO_2 loading. Stage 50 corresponds to the bottom of the column.

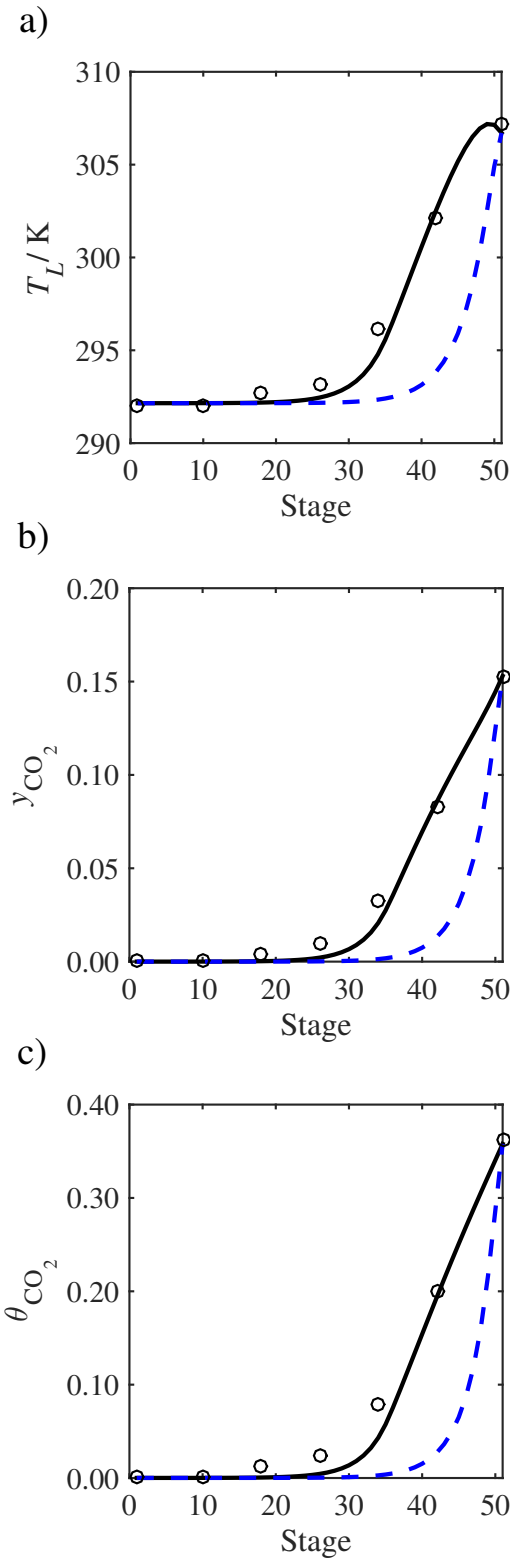

Figure 14: Comparison of the pilot-plant data (circles) (Tontiwachwuthikul et al., 1992) and the result of our model (curves) for Run T13. The dashed curves represent the results obtained without scaling the CO_2 diffusivity ($\tau = 1$) and the continuous curves the results obtained by scaling the CO_2 diffusivity in the liquid phase to 4.1% of its original value ($\tau = 0.041$). a) Temperature profile for the liquid phase, b) gas-phase CO_2 concentration profile, and c) liquid-phase CO_2 loading. Stage 50 corresponds to the bottom of the column.

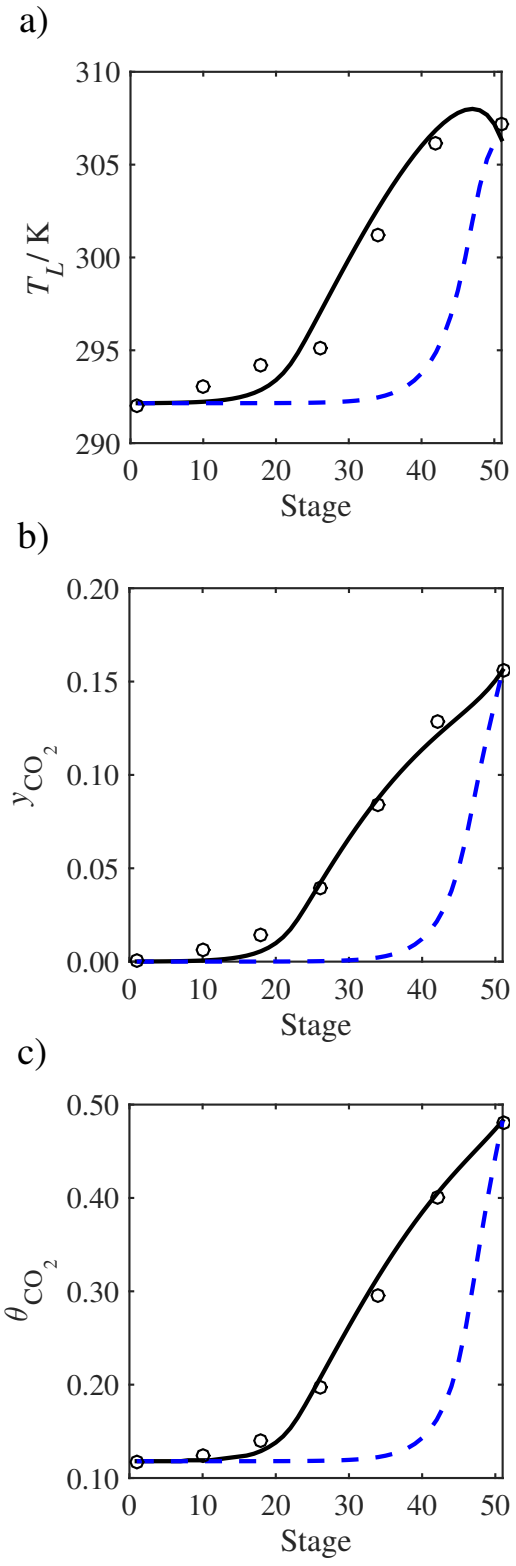

Figure 15: Comparison of the pilot-plant data (circles) (Tontiwachwuthikul et al., 1992) and the result of our model (curves) for Run T14. The dashed curves represent the results obtained without scaling the CO_2 diffusivity ($\tau = 1$) and the continuous curves the results obtained by scaling the CO_2 diffusivity in the liquid phase to 4.1% of its original value ($\tau = 0.041$). a) Temperature profile for the liquid phase, b) gas-phase CO_2 concentration profile, and c) liquid-phase CO_2 loading. Stage 50 corresponds to the bottom of the column.

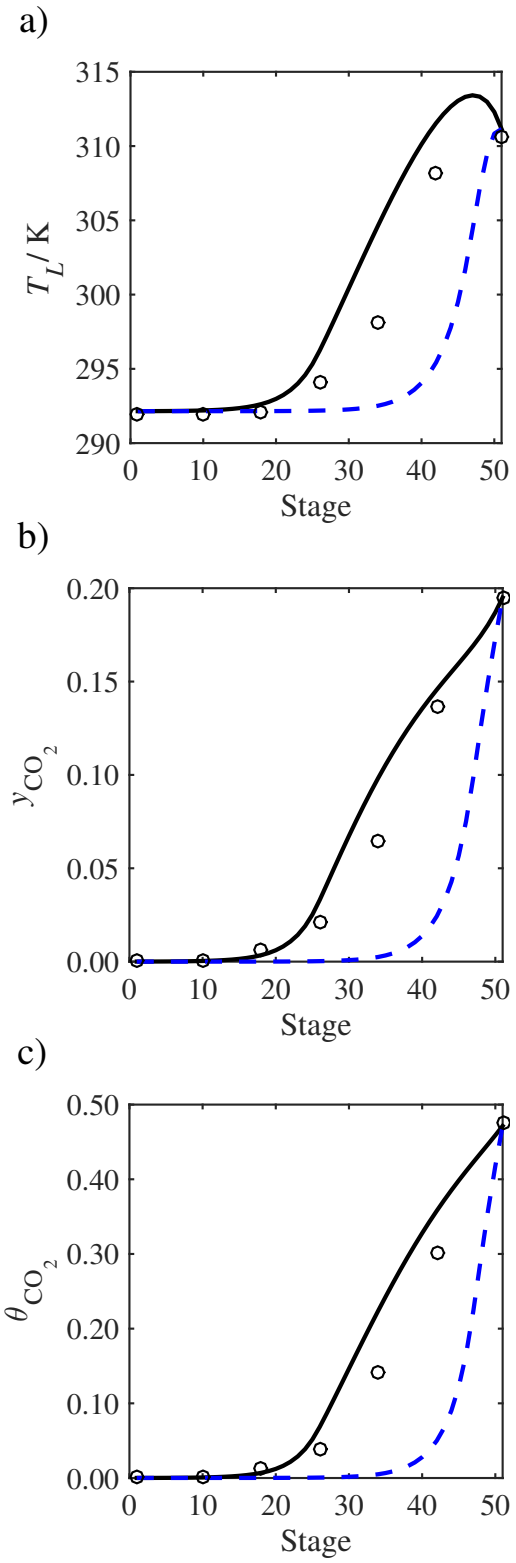

Figure 16: Comparison of the pilot-plant data (circles) (Tontiwachwuthikul et al., 1992) and the result of our model (curves) for Run T15. The dashed curves represent the results obtained without scaling the CO_2 diffusivity ($\tau = 1$) and the continuous curves the results obtained by scaling the CO_2 diffusivity in the liquid phase to 4.1% of its original value ($\tau = 0.041$). a) Temperature profile for the liquid phase, b) gas-phase CO_2 concentration profile, and c) liquid-phase CO_2 loading. Stage 50 corresponds to the bottom of the column.

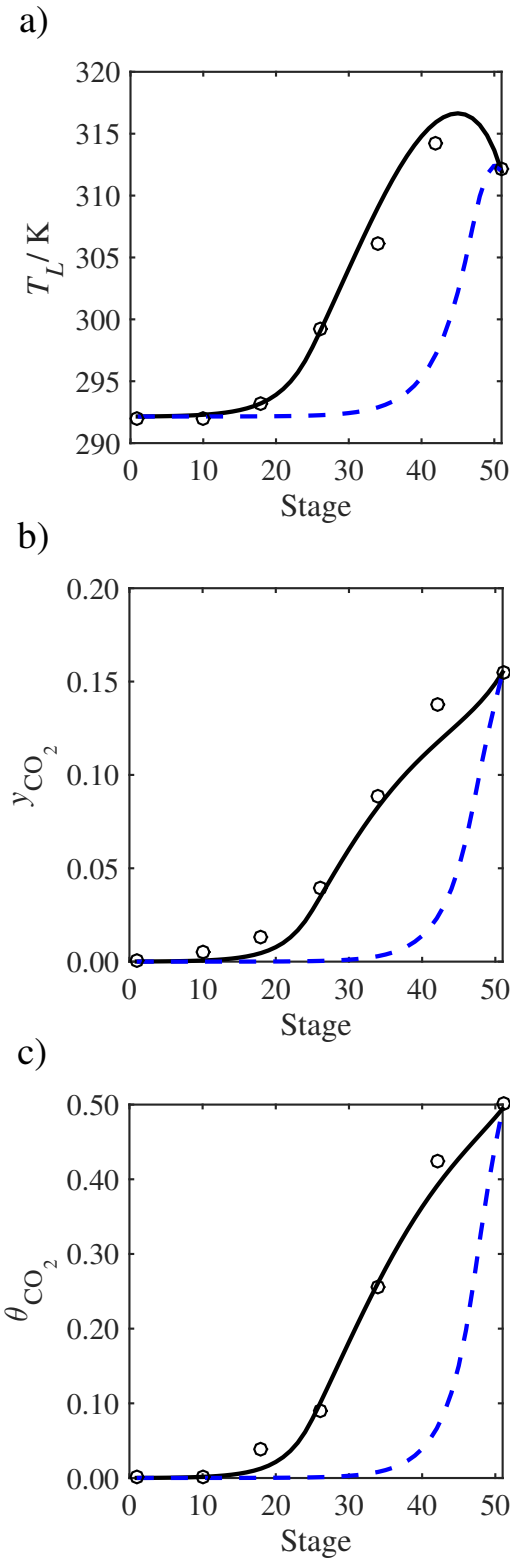

Figure 17: Comparison of the pilot-plant data (circles) (Tontiwachwuthikul et al., 1992) and the result of our model (curves) for Run T16. The dashed curves represent the results obtained without scaling the CO_2 diffusivity ($\tau = 1$) and the continuous curves the results obtained by scaling the CO_2 diffusivity in the liquid phase to 4.1% of its original value ($\tau = 0.041$). a) Temperature profile for the liquid phase, b) gas-phase CO_2 concentration profile, and c) liquid-phase CO_2 loading. Stage 50 corresponds to the bottom of the column.

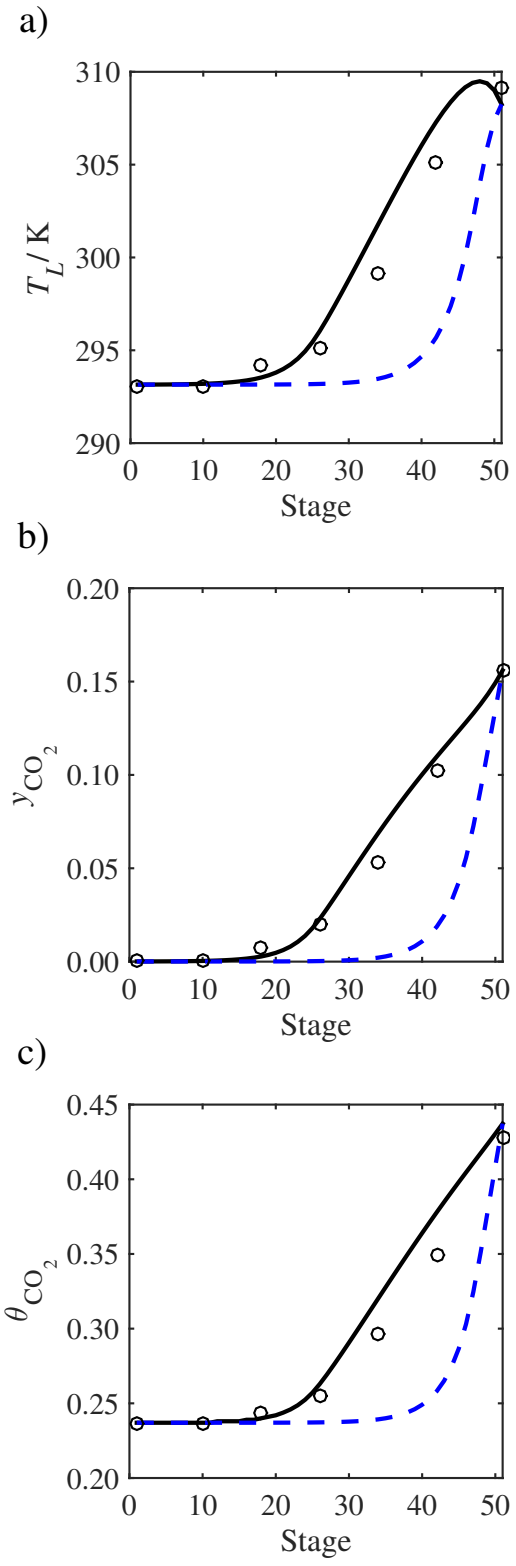

Figure 18: Comparison of the pilot-plant data (circles) (Tontiwachwuthikul et al., 1992) and the result of our model (curves) for Run T17. The dashed curves represent the results obtained without scaling the CO_2 diffusivity ($\tau = 1$) and the continuous curves the results obtained by scaling the CO_2 diffusivity in the liquid phase to 4.1% of its original value ($\tau = 0.041$). a) Temperature profile for the liquid phase, b) gas-phase CO_2 concentration profile, and c) liquid-phase CO_2 loading. Stage 50 corresponds to the bottom of the column.

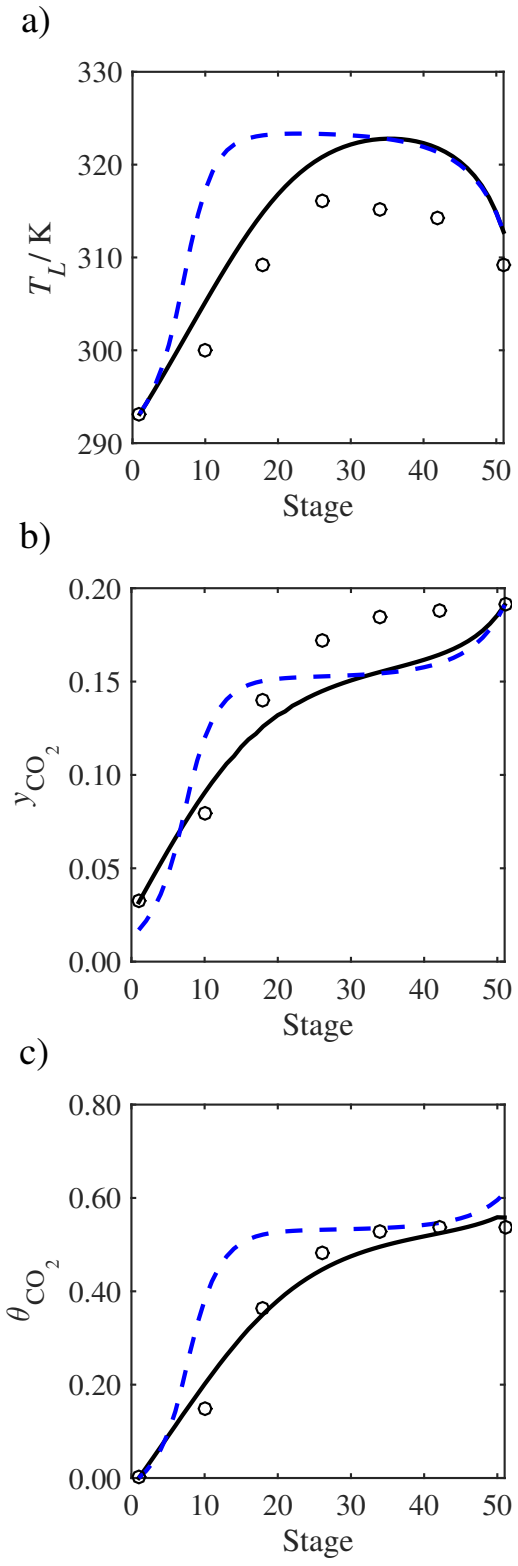

Figure 19: Comparison of the pilot-plant data (circles) (Tontiwachwuthikul et al., 1992) and the result of our model (curves) for Run T18. The dashed curves represent the results obtained without scaling the CO_2 diffusivity ($\tau = 1$) and the continuous curves the results obtained by scaling the CO_2 diffusivity in the liquid phase to 4.1% of its original value ($\tau = 0.041$). a) Temperature profile for the liquid phase, b) gas-phase CO_2 concentration profile, and c) liquid-phase CO_2 loading. Stage 50 corresponds to the bottom of the column.

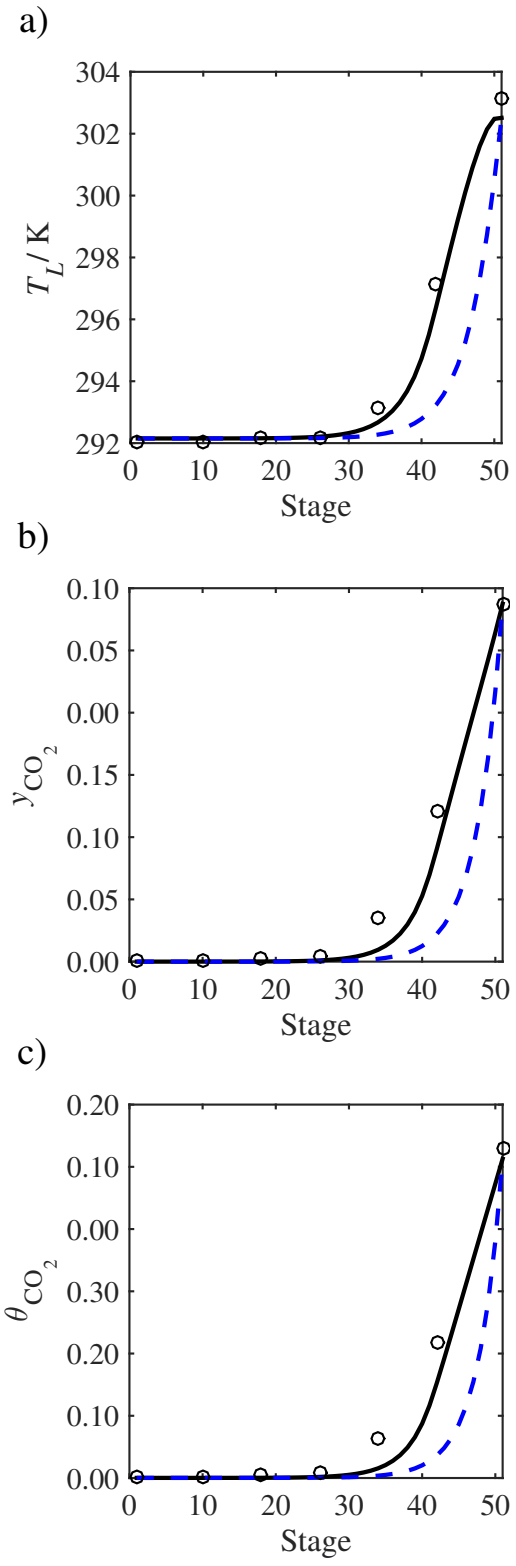

Figure 20: Comparison of the pilot-plant data (circles) (Tontiwachwuthikul et al., 1992) and the result of our model (curves) for Run T19. The dashed curves represent the results obtained without scaling the CO_2 diffusivity ($\tau = 1$) and the continuous curves the results obtained by scaling the CO_2 diffusivity in the liquid phase to 4.1% of its original value ($\tau = 0.041$). a) Temperature profile for the liquid phase, b) gas-phase CO_2 concentration profile, and c) liquid-phase CO_2 loading. Stage 50 corresponds to the bottom of the column.

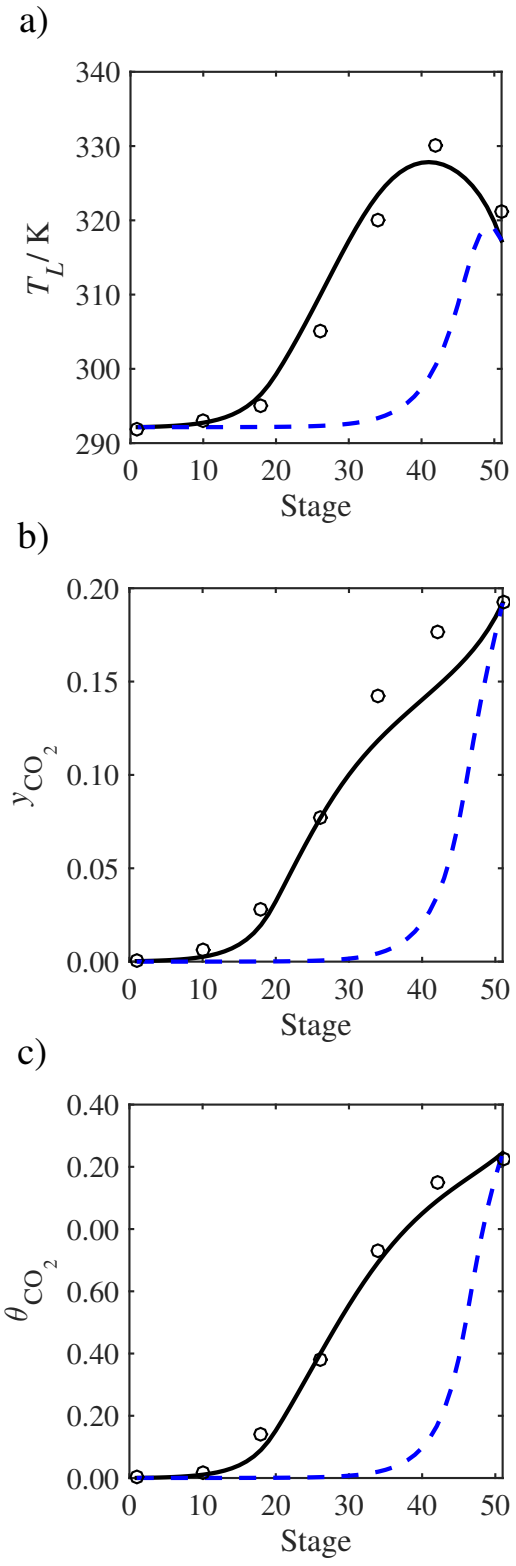

Figure 21: Comparison of the pilot-plant data (circles) (Tontiwachwuthikul et al., 1992) and the result of our model (curves) for Run T20. The dashed curves represent the results obtained without scaling the CO_2 diffusivity ($\tau = 1$) and the continuous curves the results obtained by scaling the CO_2 diffusivity in the liquid phase to 4.1% of its original value ($\tau = 0.041$). a) Temperature profile for the liquid phase, b) gas-phase CO_2 concentration profile, and c) liquid-phase CO_2 loading. Stage 50 corresponds to the bottom of the column .

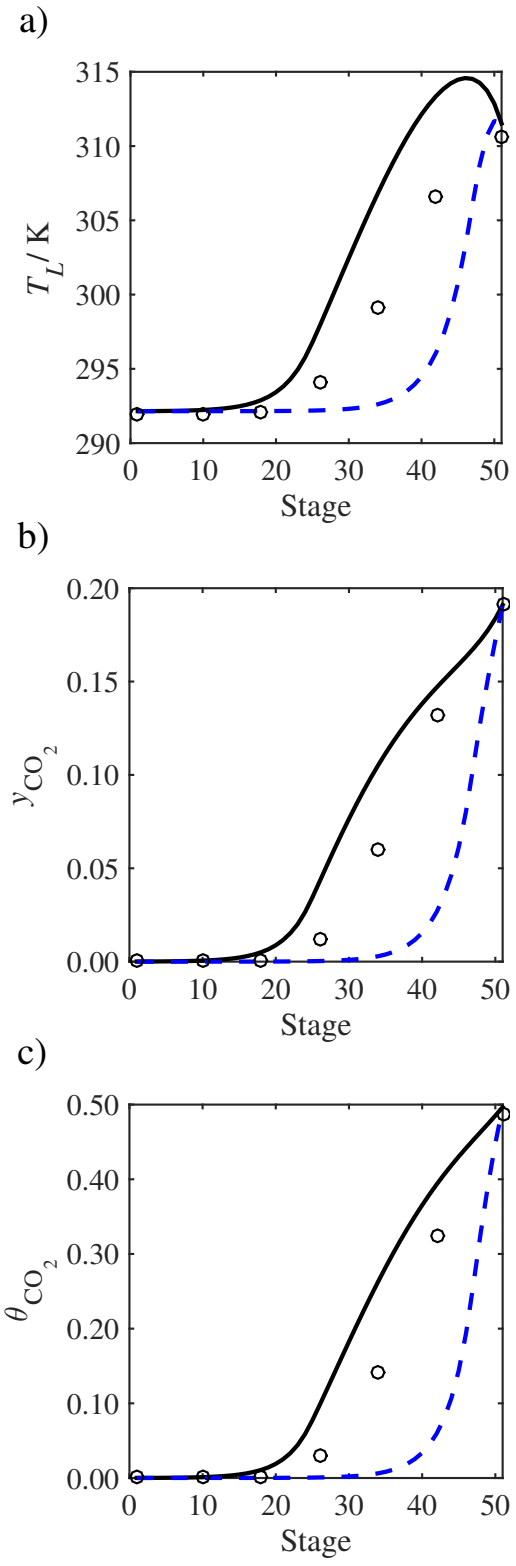

Figure 22: Comparison of the pilot-plant data (circles) (Tontiwachwuthikul et al., 1992) and the result of our model (curves) for Run T21. The dashed curves represent the results obtained without scaling the CO_2 diffusivity ($\tau = 1$) and the continuous curves the results obtained by scaling the CO_2 diffusivity in the liquid phase to 4.1% of its original value ($\tau = 0.041$). a) Temperature profile for the liquid phase, b) gas-phase CO_2 concentration profile, and c) liquid-phase CO_2 loading. Stage 50 corresponds to the bottom of the column.

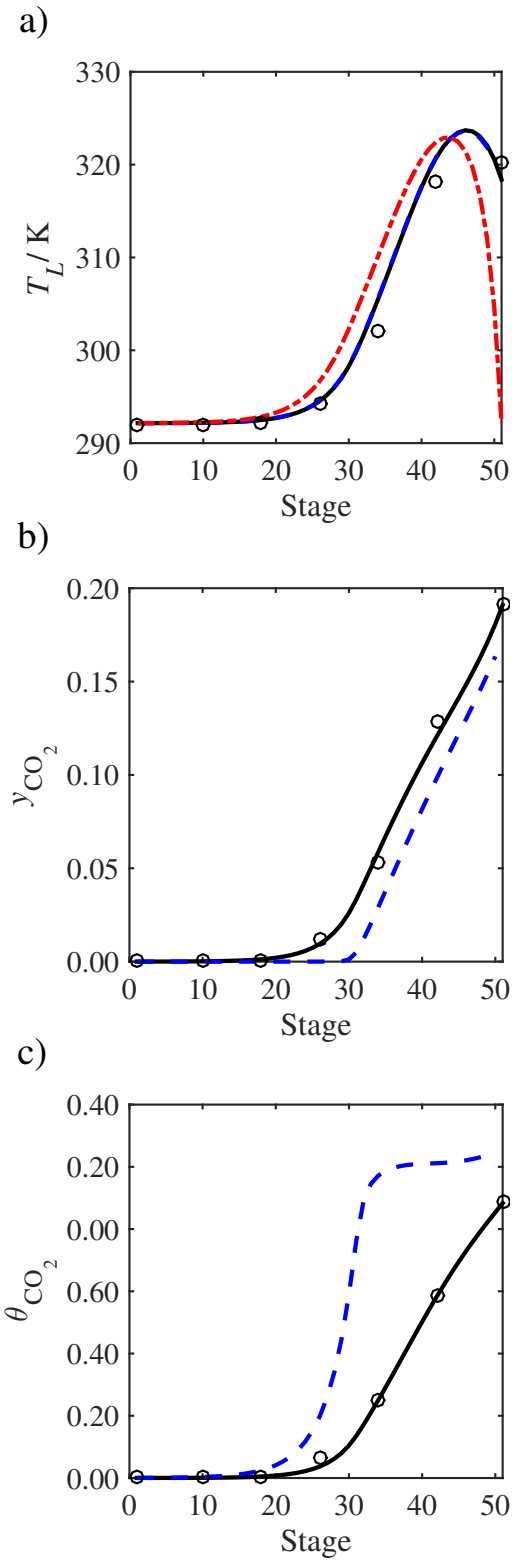

Figure 23: Run T22 of the pilot-plant data from Tontiwachwuthikul et al. (1992). Comparison of the predictions of our model for: (a) temperature of the bulk liquid phase (continuous curve), the temperature at the vapour-liquid interface (dashed curve), and the temperature for the bulk vapour phase (dot-dashed curve); (b) the gas phase CO_2 concentration in the bulk vapour phase (continuous curve) and at the interface (dashed curve); (c) the liquid phase CO_2 loading in the bulk liquid phase (continuous curve) and at the interface (dashed curve).

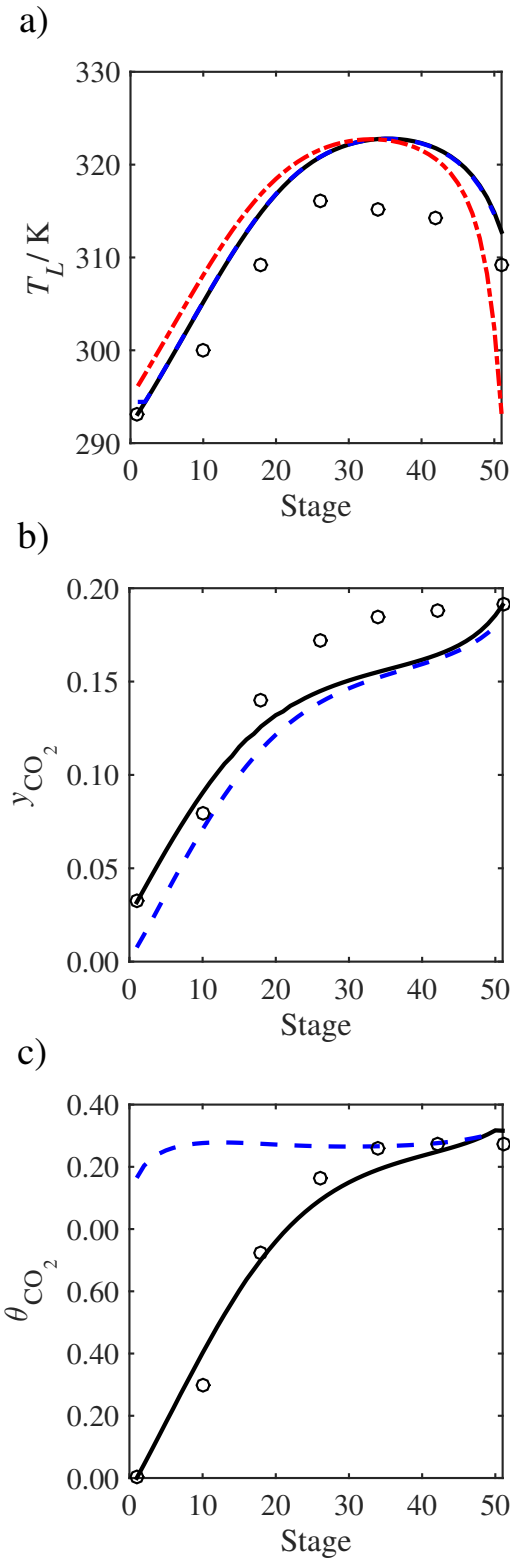

Figure 24: Run T18 of the pilot-plant data from Tontiwachwuthikul et al. (1992). Comparison of the predictions of our model for: (a) temperature of the bulk liquid phase (continuous curve), the temperature at the vapour-liquid interface (dashed curve), and the temperature for the bulk vapour phase (dot-dashed curve); (b) the gas phase CO_2 concentration in the bulk vapour phase (continuous curve) and at the interface (dashed curve); (c) the liquid phase CO_2 loading in the bulk liquid phase (continuous curve) and at the interface (dashed curve).

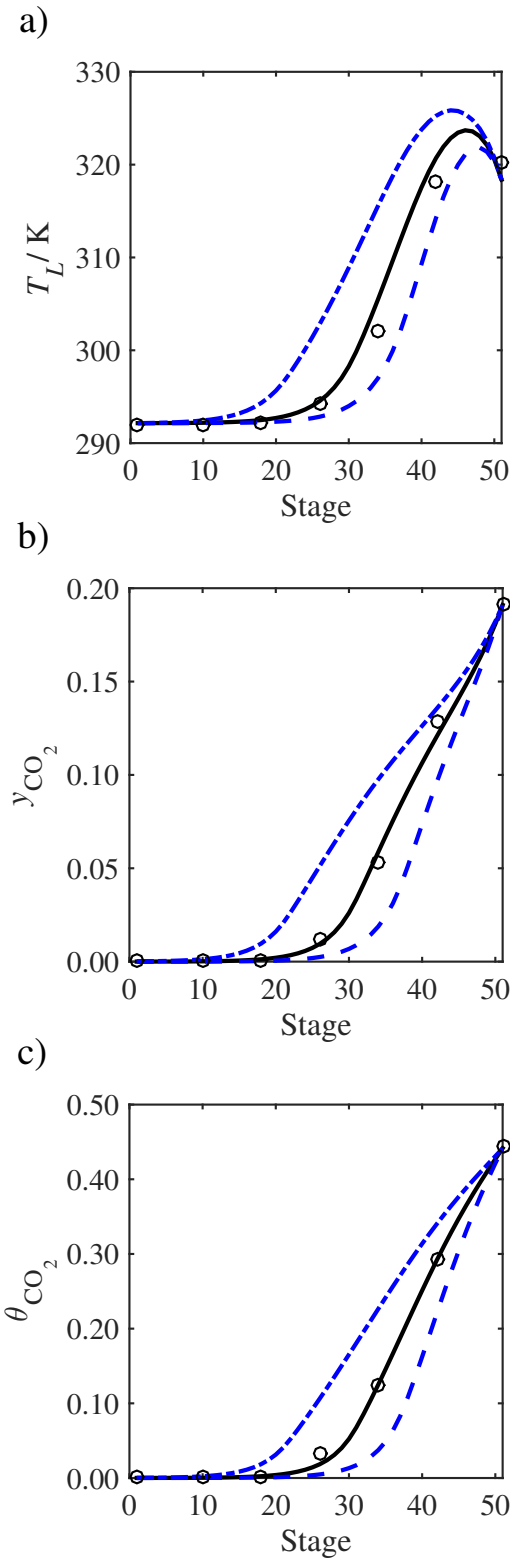

Figure 25: Sensitivity analysis of the CO_2 diffusivity in the liquid phase on the profiles predicted with our model in terms of the scaling parameter τ compared with the experimental pilot-plant data of Run T22 from Tontiwachwuthikul et al. (1992). $\tau = 0.041$ (continuous curve), $\tau = 0.082$ (dashed curve), and $\tau = 0.021$ (dot-dashed curve). (a) Temperature profile for the liquid phase, (b) gas phase CO_2 concentration profile, and (c) liquid phase CO_2 loading.

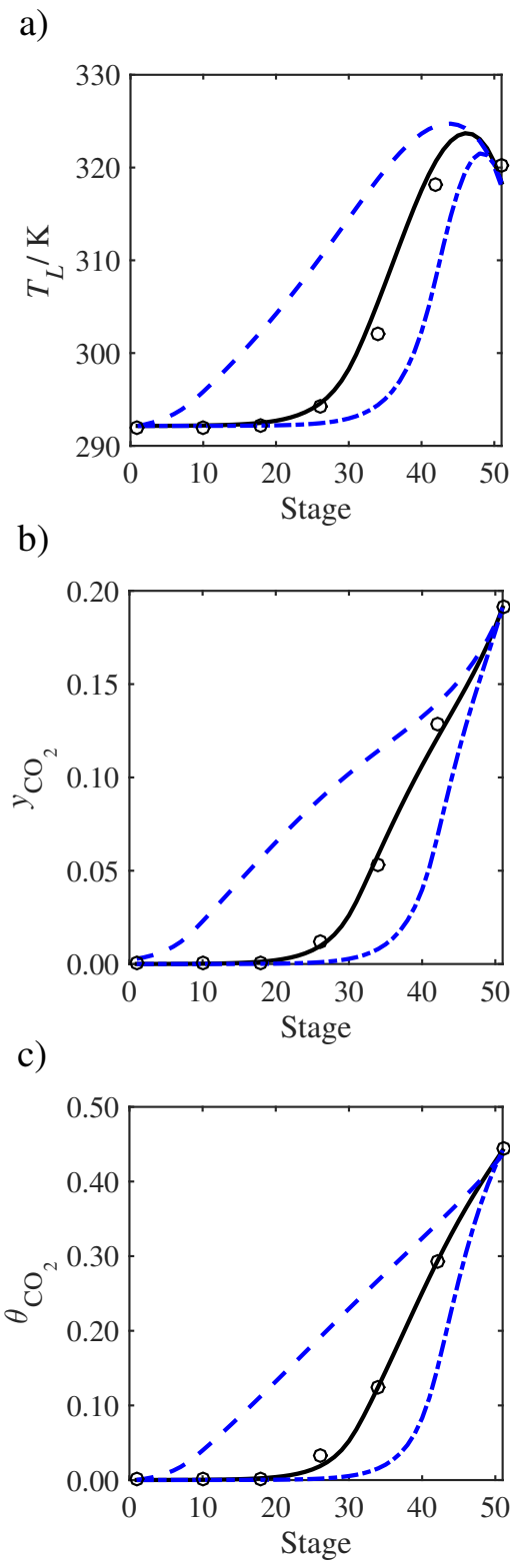

Figure 26: Sensitivity analysis of the liquid viscosity on the profiles predicted with our model compared with the experimental pilot-plant data of Run T22 from Tontiwachwuthikul et al. (1992): Nominal value (continuous curve), viscosity doubled (dashed curve), and viscosity halved (dot-dashed curve). (a) Temperature profile for the liquid phase, (b) gas phase CO_2 concentration profile, and (c) liquid phase CO_2 loading.

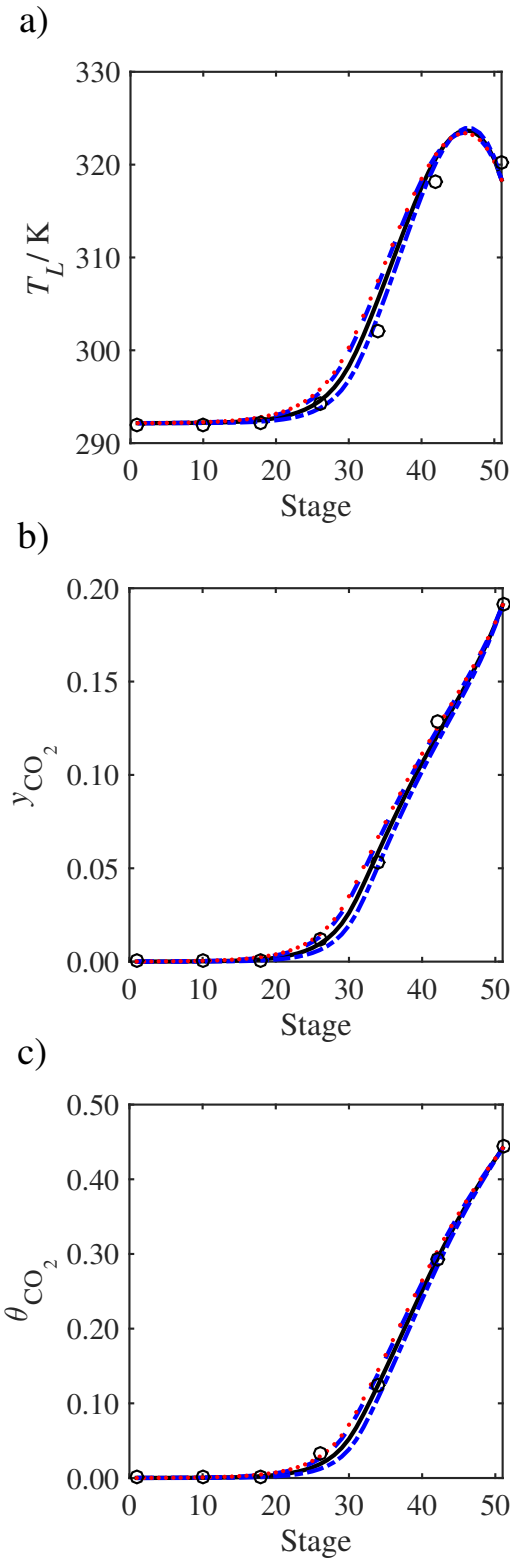

Figure 27: Sensitivity analysis of the vapour-liquid surface tension on the profiles predicted with our model compared with the experimental pilot-plant data of Run T22 from Tontiwachwuthikul et al. (1992): Nominal value (continuous curve) (Vazquez et al., 1997), +10 mN/m (dashed curve), -10 mN/m (dot-dashed curve), and the surface tension correlation for the loaded MEA solution obtained from Jayarathna et al. (2013c) (dotted curve). (a) Temperature profile for the liquid phase, (b) gas phase CO_2 concentration profile, and (c) liquid phase CO_2 loading.

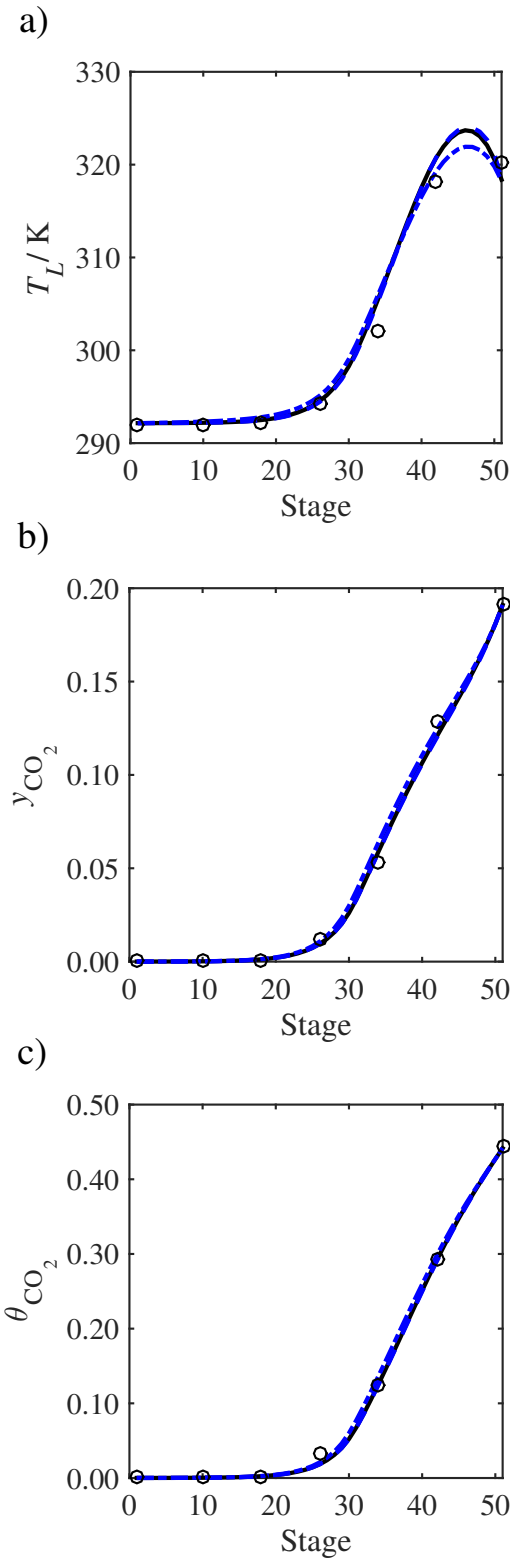

Figure 28: Sensitivity analysis of the vapour-phase heat-transfer coefficient on the profiles predicted with our model compared with the experimental pilot-plant data of Run T22 from Tontiwachwuthikul et al. (1992). Nominal value (continuous curve), coefficient value increased ten times (dashed curve), and coefficient value reduced ten times (dot-dashed curve). (a) Temperature profile for the liquid phase, (b) gas phase CO_2 concentration profile, and (c) liquid phase CO_2 loading.

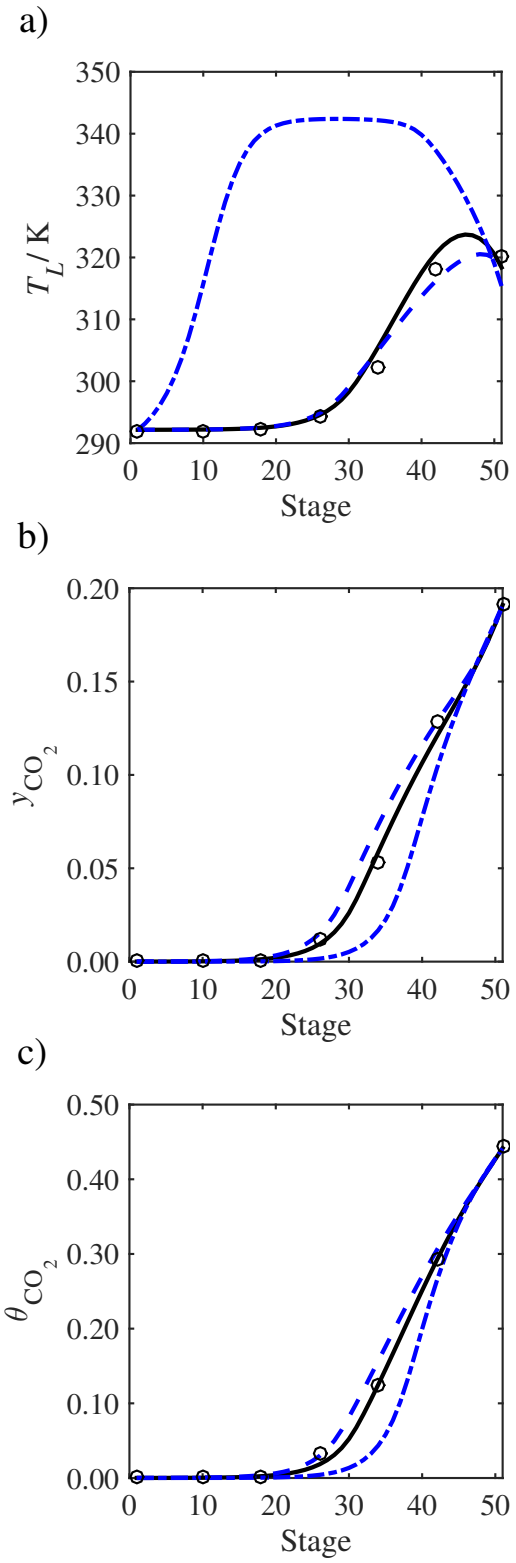

Figure 29: Sensitivity analysis of the enthalpy of vaporisation of water on the profiles predicted with our model compared with the experimental pilot-plant data of Run T22 from Tontiwachwuthikul et al. (1992). Nominal value (continuous curve), enthalpy doubled (dashed curve), and enthalpy halved (dot-dashed curve). (a) Temperature profile for the liquid phase, (b) gas phase CO_2 concentration profile, and (c) liquid phase CO_2 loading.

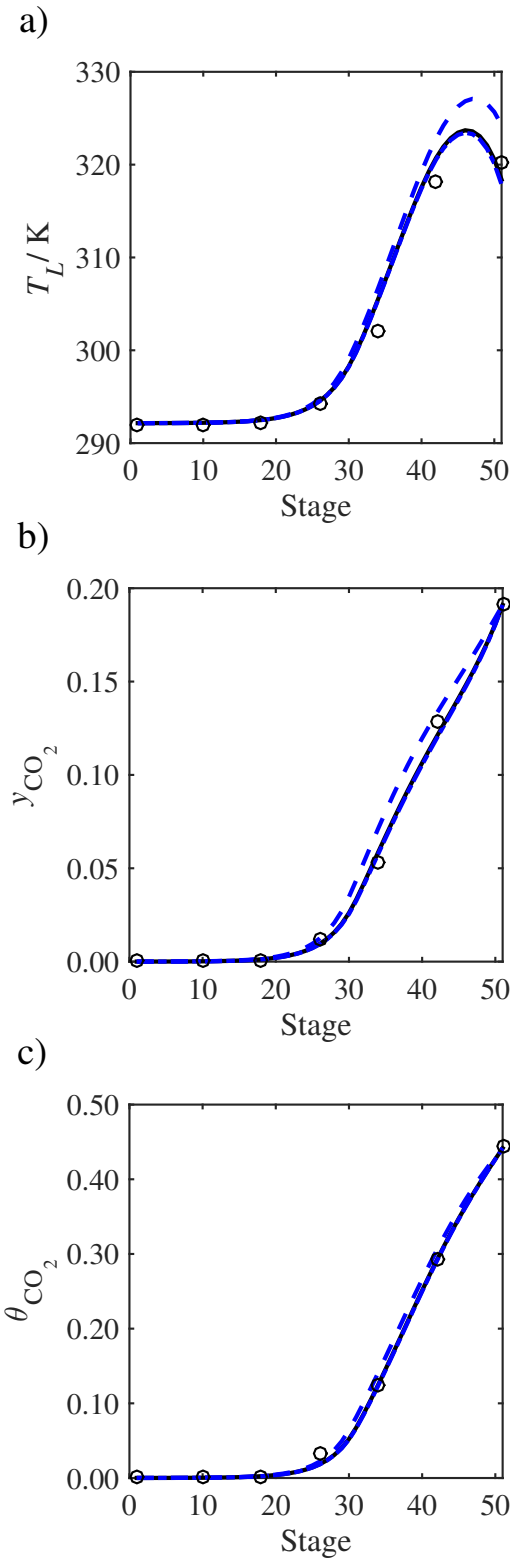

Figure 30: Sensitivity analysis of the amount of water in the inlet flue gas on the profiles predicted with our model compared with the experimental pilot-plant data of Run T22 from Tontiwachwuthikul et al. (1992). Nominal value (continuous curve), $y_{H_2O} = 0.072$ (dashed curve), and $y_{H_2O} = 0$ (dot-dashed curve). (a) Temperature profile for the liquid phase, (b) gas phase CO_2 concentration profile, and (c) liquid phase CO_2 loading.

Table 4: The SAFT-VR parameters characterising the pure component models used in this work: the number of segments m_i, the diameter of the spherical core σ_{ii}, the depth ε_{ii} and range λ_{ii} of the dispersive square well potential, the type and the number of hydrogen–bonding sites.

i	m_i	σ_{ii}(Å)	ε_{ii}/k (K)	λ_{ii}	e-sites	H-sites	e*-sites	H*-sites	α_1-sites	α_2-sites	source
H_2O	1.0	3.03420	250.00	1.78890	2	2	0	0	0	0	Clark et al. (2006)
MEA	2.0	3.57229	305.00	1.58280	2	1	1	2	0	0	Mac Dowell et al. (2010)
CO_2	2.0	2.78640	179.27	1.51573	0	0	0	0	1	1	Rodríguez et al. (2012)
N_2	1.4	3.07357	74.587	1.58795	0	0	0	0	0	0	Mac Dowell (2010)

Table 5: Binary interaction parameters for the mixtures relevant to this work. k_{ij} characterizes the strength of the dispersion interaction between molecules of types i and j, cf. equation (40).

i	+	j	k_{ij}	Source
MEA	+	CO_2	0.47878	Rodríguez et al. (2012)
MEA	+	H_2O	0.01	Mac Dowell et al. (2010)
MEA	+	N_2	0.03	Mac Dowell (2010)
CO_2	+	H_2O	-0.06	Mac Dowell et al. (2010)
CO_2	+	N_2	-0.0599	Mac Dowell (2010)
H_2O	+	N_2	-0.3635	Mac Dowell (2010)

Table 6: The site-site association energies $\varepsilon^{HB}_{ab,ij}$ for MEA, H_2O, and CO_2 (cf. figure 8). The interaction matrix is symmetrical, i.e., $\varepsilon^{HB}_{eH,ii} = \varepsilon^{HB}_{He,ii}$; the lower diagonal part has been left blank and is implied. The unlike association between sites of the same type is assumed to be symmetric, i.e., $\varepsilon^{HB}_{eH,ij} = \varepsilon^{HB}_{He,ij} = \varepsilon^{HB}_{eH,ji} = \varepsilon^{HB}_{He,ji}$ (Mac Dowell et al., 2010; Rodríguez et al., 2012).

		$\varepsilon^{HB}_{ab,ij}/k_B$ (K)							
		MEA				H_2O		CO_2	
	b\a	e	H	e*	H*	e	H	α_1	α_2
MEA	e	0	2357.79	0	900	0	1780.7121	0	0
	H	-	0	550	0	1780.7121	0	0	0
	e*	-	-	0	960	0	1517.1049	5200	3982.66
	H*	-	-	-	0	1517.1049	0	0	0
H_2O	e	-	-	-	-	0	1400.00	0	0
	H	-	-	-	-	-	0	0	0
CO_2	α_1	-	-	-	-	-	-	0	0
	α_2	-	-	-	-	-	-	0	0

Table 7: The site-site range parameters $r_{c;ab,ij}$ for mixtures containing MEA, H_2O, and CO_2 (cf. figure 8). The interaction matrix is symmetrical, i.e., $r_{c;eH,ii} = r_{c;He,ii}$ and so the lower diagonal part has been left blank. The unlike association between sites of the same type is assumed to be symmetric, i.e., $r_{c;eH,ij} = r_{c;He,ij} = r_{c;eH,ji} = r_{c;He,ji}$ (Mac Dowell et al., 2010; Rodríguez et al., 2012).

		$r_{c;ab,ij}$(Å)							
		MEA				H_2O		CO_2	
	b\a	e	H	e*	H*	e	H	α_1	α_2
MEA	e	0	2.08979	0	2.65064	0	2.10763	0	0
	H	-	0	2.65064	0	2.10763	0	0	0
	e*	-	-	0	2.32894	0	2.22626	1.97978	1.96999
	H*	-	-	-	0	2.22626	0	0	0
H_2O	e	-	-	-	-	0	2.10822	0	0
	H	-	-	-	-	-	0	0	0
CO_2	α_1	-	-	-	-	-	-	0	0
	α_2	-	-	-	-	-	-	0	0

Table 8: Correlations used in the process model of the absorber.

Physical property	Component	Source
Liquid phase viscosity	H_2O	Westmeier (1977)
	MEA	Leibush and Shorina (1947)
	Mixture	Maham et al. (2002)
Vapour phase viscosity		Kestin et al. (1966)
Vapour-liquid surface tension		Vazquez et al. (1997)
Heat conductivity		Haynes (2011)
Liquid phase diffusion coefficient	CO_2	Takahashi et al. (1982)
	H_2O, MEA, N_2	Perkins and Geankoplis (1969)
Vapour phase diffusion coefficient	CO_2, H_2O, MEA, N_2	Poling et al. (2001)

Table 9: Inputs to absorber column model for Runs T13 to T22 (Tontiwachwuthikul et al., 1992).

Input variable	T13	T14	T15	T16	T17	T18	T19	T20	T21	T22
Inlet gas flow (mol m^{-2} s^{-1})	17.54	17.54	18.4	17.51	17.54	18.29	16.72	18.32	13.72	18.3
Inlet gas pressure (MPa)	0.1	0.1	0.1	0.1	0.1	0.1	0.1	0.1	0.1	0.1
Inlet gas temperature (K)	292.15	292.15	292.15	292.15	293.15	293.15	292.15	292.15	292.15	292.15
Inlet gas CO_2 mole fraction	0.153	0.156	0.195	0.155	0.156	0.191	0.115	0.192	0.191	0.191
Inlet gas H_2O mass fraction	0.0058	0.0058	0.0058	0.0058	0.0058	0.0058	0.0058	0.0058	0.0058	0.0058
Inlet liquid flow (m^3 m^{-2} h^{-1})	13.5	13.5	13.5	9.5	13.5	9.5	13.5	9.5	9.5	9.5
Inlet liquid temperature (K)	292.15	292.15	292.15	292.15	293.15	293.15	292.15	292.15	292.15	292.15
Inlet MEA concentration (kmol m^{-3})	2.00	2.00	2.03	2.08	3.08	2.00	2.00	2.55	2.00	3.00
Lean loading, θ_{CO_2}	10^{-4}	0.118	10^{-4}	10^{-4}	0.237	10^{-4}	10^{-4}	10^{-4}	10^{-4}	10^{-4}

Table 10: Characteristics of the column and the packing

Name	Value	Source
$A_{section}$ (m^2)	0.00785	Tontiwachwuthikul et al. (1992)
a_p ($m^2.m^{-3}$)	466	Treybal (1981)
σ_c (N m−1)	61	Perry and Green, 2008, pg. 18-34, table 18-11
L_p (m)	0.0127	Tontiwachwuthikul et al. (1992)
ϵ	0.63	Treybal, 1981, pg. 198, table 6.3
D_z (m)	0.132	Tontiwachwuthikul et al. (1992)
d_s (m)	0.31622	Treybal, 1981, pg. 206, table 6.5

Table 11: Sensitivity analysis of key parameters in the model

Parameter description	Variation	Effect
Vapour diffusivity	doubled halved	negligible effect
Liquid diffusivity	doubled halved	significant effect see figure 25
Vapour viscosity	doubled halved	negligible effect
Liquid viscosity	doubled halved	significant effect see figure 26
Surface tension	+10 mN/m -10 mN/m	negligible effect see figure 27
Heat transfer liquid	$\times$ 10 $\div$10	negligible effect
Heat transfer vapour	$\times$ 10 $\div$10	limited effect see figure 28
Heat of vaporisation of water	doubled halved	significant effect see figure 29
Mass fraction of water in inlet flue gas	varied between 0 and 0.072	negligible effect see figure 30

4

MULTI-OBJECTIVE OPTIMIZATION OF EQUATION OF STATE PARAMETERS WITH APPLICATION TO WATER

Following the modelling of the absorption column in the previous chapter, it was found that the thermodynamic model of Rodríguez et al. (2012) under-predicted the liquid heat capacity at 1 bar by approximately 15% and heat of absorption by approximately 20% at the absorber conditions and 30 wt % MEA. This potentially led to a cancellation of errors, meaning that the temperature profile was predicted well but without the thermodynamic model correctly capturing the true physics of the situation. The heat capacity of pure water for the SAFT-VR SW model of Clark et al. (2006) under-predicts the experimental value by approximately 15% in the liquid phase at 300K, which is a likely cause for the under-estimation of the mixture heat capacity of the solvent. To continue, we aim to develop SAFT-VR Mie models for the CO_2-MEA-H_2O system, noticing that the more recent equation can provide a good simultaneous description of the vapour-liquid equilibria and second derivative properties (Lafitte et al., 2006b, 2007, 2013b; Dufal et al., 2015b) (which include heat capacity and the heat of absorption). In this chapter, we show a novel technique to parameter estimation, where we treat the procedure as a multi-objective optimization, and develop a new SAFT-VR Mie model for water using this technique.

4.1 INTRODUCTION

The typical approach to determining equation of state (EoS) parameters is to solve a single objective optimization, where the objective function is constructed using a weighted-sum of various error functions, each representing the deviation between the prediction of a certain thermodynamic property and the experimental measurement. The weighted-sum optimization, WSP($\boldsymbol{w}$), is defined by:

$$\begin{aligned} \underset{\boldsymbol{x}}{\text{minimize}} \quad & \boldsymbol{w}^T \boldsymbol{f}(\boldsymbol{x}) = \sum_{i=1}^{N_{dim}} w_i f_i(\boldsymbol{x}) \\ \text{subject to} \quad & \boldsymbol{x} \in X, \end{aligned} \tag{WSP($\boldsymbol{w}$))}$$

where f_i is the error function for property type i, N_{dim} is the number of property types, w_i is the weighting given to property type i, and $\boldsymbol{x}$ is a vector of model parameters to be estimated. X refers to the feasible set of parameters, which implicitly includes any inequality constraints, such as lower and upper bounds on the EoS variables, or equality constraints, for example the use of combining rules. There are various factors to consider in constructing WSP($\boldsymbol{w}$), and the final EoS model (to be used in e.g., a process simulation) will depend on the choice of the specific form of WSP($\boldsymbol{w}$). In particular, the definition of f_i, the choice of which property types to use, and the choice of $\boldsymbol{w}$.

The precise definition of f_i is important as it not only affects the values of the parameters but also their statistical properties (Englezos and Kalogerakis, 2000). An example of f_i is a relative least-squares objective function:

$$f_i(\boldsymbol{x}) = \sum_{j=1}^{N_i} \left[\frac{Y_{i,j}^{\text{exp.}}(\boldsymbol{k}) - Y_{i,j}^{\text{model.}}(\boldsymbol{k}, \boldsymbol{x})}{Y_{i,j}^{\text{exp.}}(\boldsymbol{k})} \right]^2, \tag{88}$$

where N_i is the number of data points for each property type i, $\boldsymbol{k}$ is a vector of independent variables that are fixed in the model and the experiment (e.g., thermodynamic variables such as temperature and pressure), $Y_{i,j}^{\text{exp.}}$ is the experimental result for property type i and data point j, and $Y_{i,j}^{\text{model.}}$ is the calculated result given by the EoS for property type i and data point j. Typically, f_i is averaged over N_i such that f_i represents the average deviation for each property type:

$$f_i(\boldsymbol{x}) = \frac{1}{N_i} \sum_{j=1}^{N_i} \left[\frac{Y_{i,j}^{\text{exp.}}(\boldsymbol{k}) - Y_{i,j}^{\text{model.}}(\boldsymbol{k}, \boldsymbol{x})}{Y_{i,j}^{\text{exp.}}(\boldsymbol{k})} \right]^2. \tag{89}$$

Note that the objective functions defined in Equations 88 and 89 lead to the same functional form of WSP($\boldsymbol{w}$), so the constant prefactors present in Equation 89 may either be used in the definition of f_i or subsumed into the weighting w_i.

Due to the highly nonlinear behaviour of the more sophisticated thermodynamic models, finding the solution to WSP($\boldsymbol{w}$) can be challenging because the objective function may have a non-convex behaviour and exhibit many local optima. Therefore, utilizing global optimization routines in the model development can achieve better results than local optimization methods (Costa et al., 2000). Furthermore, the calculation of phase equilibrium properties can be difficult since when regressing parameters one needs to ensure that the results correspond to stable equilibria. This becomes particularly difficult to achieve in the case of modelling multi-component mixtures. Sophisticated methods have been developed to deal with this problem during parameter estimation (see for example Glass et al. (2018)) .

The values of the parameters and the individual f_i at the optimal solution to WSP($\boldsymbol{w}$) are determined by the choice of weightings, but it is generally difficult to decide upon the precise weighting given to each property *a priori*. One class of methods suited for determining a suitable weight vector are Bayesian-type approaches. Common methods include the error-in-variables-measured (EVM), the weighted least squares (WLS) approach, and the maximum-likelihood estimator (Bard, 1974; Wang et al., 2018b), which seek to find the set of parameters that are most statistically significant with respect to the experimental data. These methods require prior knowledge of the experimental uncertainty, such as the variance and distribution of measurement errors, which are sometimes not known or reported. Furthermore, if the equation of state is not able to predict the experimental data to within the range of experimental uncertainty, then weighting properties according to the inverse of their variance can lead to an unfair weighting towards certain thermodynamic properties.

For these reasons, the weight vector is typically chosen arbitrarily in the development of EoS parameters. In the majority of cases, an equal weighting is given to each property type. In other cases, a small number of weight vectors are cho-

sen and the thermodynamic model is picked by looking at the f_i obtained from the different models and judging which one gives the best balance between the different properties (see for example Lafitte et al. (2007)). However, it is difficult to decide systematically upon the weight vectors. It is often not clear how changes in the weight vector will affect the individual f_i, particularly as the number of dimensions increases, as the dependence of f_i on the weights can be highly non-linear (Marler and Arora, 2010). Furthermore, there may not be a 'best' set of parameters for a particular compound or mixture. This will depend upon the intended use of the model, and a single set of parameters may not suffice.

An alternative approach, recently outlined by Forte et al. (2018), is to formulate the parameter estimation as a multi-criteria (or multi-objective) optimization problem. Within this approach, the different thermodynamic properties are treated as competing objectives, and the output is a set of non-dominated (or Pareto-optimal) models, from which a model may be chosen after the parameter estimation procedure. Importantly, the multi-objective optimization approach removes any arbitrariness in selection of the weight vector. The authors demonstrate this novel method of parameter estimation by developing Pareto-optimal models for water using the PC-SAFT EoS (Gross and Sadowski, 2000; Gross et al., 2001), using saturated liquid density and vapour pressure as two competing objectives. They considered models for water which differ in their association scheme (2-site, 3-site and 4-site models), and the inclusion or not of a dipolar term (Gross and Vrabec, 2006). It was shown that knowledge of the Pareto front provides a useful means of comparison between different model types, as one is able to simultaneously compare the full set of Pareto-optimal solutions. They concluded that the 2- and 4-site association schemes provide very similar predictions, and that the addition of a dipolar term only offers a small improvement in the Pareto front if the literature value of the dipole moment is used, while a vast improvement in the Pareto front is seen if one treats the dipole moment of water as an adjustable parameter.

In addition to the determination a suitable set of weightings as an input to WSP($\boldsymbol{w}$), the choice of the particular data types used is of crucial importance. In the context of modelling of industrial processes, it is preferable that the equation of state can accurately predict both phase equilibira and second derivative properties, in particular, the caloric properties such as the heats of vaporization and isobaric heat capacities (Hendriks et al., 2010). The more recent versions of molecular-based SAFT EoSs that incorporate a soft repulsive core have been shown to provide an excellent simultaneous description of the phase equilibria and second derivative properties, allowing for the possibility of including more data types in the model parametrisation (Lafitte et al., 2013b; Llovell and Vega, 2006; Lafitte et al., 2007). The agreement with the experimental properties included in the objective function is not the only concern however. In molecular-based EoSs, where the parameters characterise the intermolecular potential, one needs to make sure that the model correctly captures the physics in order for the equation to have any predictive capacity. For example, the ability to predict properties at other thermodynamic conditions, the ability to transfer some potential parameters to predict properties for chemically similar compounds, or the ability to predict mixture properties. When estimating the SAFT parameters for real molecules, the ability to generate parameters that provide a good approximation of the true intermolecular potential becomes difficult if there is a large amount of parameter degeneracy, where the

experiments do not provide enough information to distinguish between different models. Typically this degeneracy increases with the number of parameters.

When chemical association is present and is explicitly accounted for in the thermodynamic model, for example in the SAFT family of equations of state, it is clear from the literature that data types beyond vapour pressure and saturated liquid density alone are required in order to decouple the energy of interaction due to dispersive and hydrogen bonding interactions. This is evidenced by the work of Clark et al. (2006) for the SAFT-VR SW equation of state, and Dufal et al. (2015b) for the SAFT-VR Mie equation of state, when developing SAFT models for water. The authors observed large shallow regions in the objective function space when plotted against discretised pairs of parameters, particularly the energy of dispersive interactions and the energy of hydrogen bonding interactions. This indicates a high degree of degeneracy between these two parameters. Their discretisation method allows for a visualisation of the parameter space and allows one to generate a variety of models that do not necessarily minimize the objective function but are within a certain acceptable error. Through analysing these water models, Clark et al. (2006) found the heat of vaporisation was not a suitable data type for discriminating between the different models due to the similar prediction of this property for models along the "optimal" valley. The authors found that vapour-liquid surface tension calculated using the SAFT-VR DFT of Gloor et al. (2004b) provided some capacity to discriminate between the different models, but the predicted values overestimate the experimental surface tension in all cases due to the models overestimating the critical temperature. The predictions of the fraction of association sites not bonded between the different models were much more varied, and hence the authors were able to discriminate between models by comparison with the spectroscopic data by Luck (1980). Similarly, Dufal et al. (2015b) were able to validate their water models (regressed to only VLE data) to the degree of association. However, in this case the authors used the degree of association predicted by Monte Carlo simulations of the SPC/E and TIP4P/2005 force fields as pseudo-experimental data, and the authors discussed the questionable accuracy of the spectroscopic data by Luck (1980). Cripwell et al. (2018) used a similar approach to discretisation to determine models for the SAFT-VR Mie-GV (polar variant of SAFT-VR) equation of state, whereby near-optimal solutions were discriminated with respect to their ability to predict vapour-liquid equilibria. Another pure-component property suitable for reducing the parameter degeneracy and obtaining a reliable set of parameters is the vapour-liquid surface tension (Gloor et al., 2002; Gloor, 2003; Gloor et al., 2007a), where the authors showed that via a suitable density functional theory (SAFT-VR DFT), the surface tension may be used to determine the balance between the dispersive and associative forces. Oliveira et al. (2016) demonstrated that for highly associating molecules, if only saturated liquid density and vapour pressure is used to fit the parameters (using the soft-SAFT equation of state), one is unable to obtain a good prediction of various derivative properties (the speed of sound, isochoric heat capacity, thermal expansion coefficient, isothermal compressibility, and isobaric heat capacity). Such data types are useful as these properties are readily computed from an EoS, and are relatively easy to obtain from experimental measurements. In this work they showed that C_P is much better described by a water model that accounts for non-sphericity.

The isobaric heat capacity, C_P, is a promising data type to use in the objective function as it can be measured accurately and its accurate prediction is vitally important for the modelling of chemical processes. It also provides specific information on the structure of the liquid due to its relationship with entropy ($C_P = T(dS/dT)_P$). Cerdeirina et al. (2007) showed that a simple two state association model, TSAM (Cerdeiriña et al., 2004) is able to capture the various trends of the temperature dependence of $C_P(T)$, at specific isobars, and observed that this dependence for associating molecules is only sensitive to the ideal and association contributions to the isobaric heat capacity. This provides a good indication that one may be able to use this property to decouple the dispersive and association forces. Note that in using C_P to regress EoS models one also requires experimental information (or some means to accurately estimate) the ideal gas heat capacity.

In conclusion, we have identified that multiple different property types (beyond saturated liquid density and vapour pressure alone) may be required for the regression of equation of state parameters to experimental measurements. By constructing an optimization problem of the form described in WSP($\boldsymbol{w}$) for the regression, it is clear that increasing the number of different property types makes it even more difficult for the user to define which weights should be specified in the optimization problem. In the present work, we extend the application of the novel multi-objective approach to EoS parameter estimation of Forte et al. (2018) to include more that two data types (or two objectives, f_i). We first discuss in detail the theory behind multi-objective optimization and methodologies for providing an efficient approximation of the Pareto front. We expose an algorithm that is ideally suited for the parametrisation of EoS models, and that can be retrofitted with existing methods and code bases, provided that the objective function is of the form described in WSP($\boldsymbol{w}$). The sandwich algorithm we implement for determining an efficient sequence of weight vectors used in WSP($\boldsymbol{w}$) is closely related to that of Bokrantz and Forsgren (2011), and is applicable to any number of dimensions (N_{dim}). The method is applied to the generation of a number of Pareto-optimal models for water using the SAFT-VR Mie equation of state (Lafitte et al., 2013a; Dufal et al., 2015b). We include three data types in the parameter regression: saturated liquid density, vapour pressure, and isobaric heat capacity. The thermodynamic properties of water are notoriously difficult to predict with any EoS due to the complex interplay between association, dispersive and polar forces. Hence, the objectives are indeed conflicting and we are able to generate Pareto fronts from which a choice of model must be made. Finally, we choose a particular model for water that shows a good compromise between the objectives, and assess the ability for the model to predict other properties that are not included in the objective function.

4.2 METHODOLOGY

4.2.1 *Definition of the multi-objective optimization problem and non-dominance*

The following multi-objective optimization problem is considered:

$$\begin{aligned} &\underset{\boldsymbol{x}}{\text{minimize}} && \boldsymbol{f}(\boldsymbol{x}) = [f_1(\boldsymbol{x}), f_2(\boldsymbol{x}), ..., f_{N_{\text{dim}}}(\boldsymbol{x})] \\ &\text{subject to} && \boldsymbol{x}^{\text{LB}} \leqslant \boldsymbol{x} \leqslant \boldsymbol{x}^{\text{UB}}, \end{aligned} \tag{MOP}$$

where $\boldsymbol{f}$ is a vector of individual objective functions, in our case, some scalar functions $f_i, i = 1, ..., N_{\text{dim}}$, that characterise the deviations between model and experiment for property type i; $\boldsymbol{x}$ is a vector of equation of state parameters, which we refer to as a "model" throughout; $N_{\text{dim}} \geqslant 2$ is the number of objectives; and superscripts LB and UB represent the lower and upper bound constraints on the model parameters respectively. Throughout this chapter, vector inequalities imply that the inequalities hold for all components of the vector with the same index. If it is possible to minimise all f_i simultaneously, i.e., the objective functions are not conflicting, then the solution is a single optimal model. Otherwise, the solution is a (potentially infinite) set of models that are non-dominated. A model with parameters $\tilde{\boldsymbol{x}}$ is non-dominated if there exists no other feasible set of parameters $\boldsymbol{x}$ such that:

$$\boldsymbol{f}(\tilde{\boldsymbol{x}}) \in \boldsymbol{f}(\boldsymbol{x}) + C \setminus \{0\}, \tag{90}$$

where C is an ordering cone that is closed and pointed.

We follow the approach of Bokrantz and Forsgren (2011) by considering polyhedral ordering cones of the form $C = \{Q\boldsymbol{\mu} : \boldsymbol{\mu} \geqslant 0\}$, whereby we specify the maximum admissible trade-offs between pairs of objectives to obtain Q. Let t_{ij} ($t_{ij} \geqslant 0$) be the reciprocal of the maximum admissible increase in f_i per unit decrease in f_j. Then C can be represented by a set of inequality constraints: $C = \{\boldsymbol{z} : T\boldsymbol{z} \geqslant 0\}$, where T is a matrix with dimensions N_{dim}, with ones on the diagonal and off-diagonal elements t_{ij}. The dual cone to C, C^*, is the cone generated by T: $C^* = \{T\boldsymbol{\mu} : \boldsymbol{\mu} \geqslant 0\}$.

To find the generating matrix, Q, we use Minkowski's theorem for closed convex pointed cones (Blekherman et al., 2012; Fawzi, 2017), which says that any point in C can be described by the conical hull of its extreme rays. The extreme rays of C can be found by setting $(N_{\text{dim}} - 1)$ inequality constraints that define C to be active. In this work, we set all maximal admissible trade-offs between objective pairs to be equal and remove the subscripts: $t_{ij} = t$. This allows us to simplify the extreme ray representation of C. In three dimensions:

$$C = \left\{ \boldsymbol{z} : \begin{bmatrix} 1 & t & t \\ t & 1 & t \\ t & t & 1 \end{bmatrix} \begin{bmatrix} z_1 \\ z_2 \\ z_3 \end{bmatrix} \geqslant \begin{bmatrix} 0 \\ 0 \\ 0 \end{bmatrix} \right\}. \tag{91}$$

Taking the first two inequality constraints to be active, we obtain $z_1 = z_2 = \frac{-t}{1+t} z_3$. Setting $z_3 = 1$ (the length of the extreme ray is arbitrary), we obtain an extreme ray and row of Q: $[\frac{-t}{1+t}, \frac{-t}{1+t}, 1]$. The other extreme rays can be found similarly by appealing to symmetry, giving:

$$Q = \begin{bmatrix} 1 & \frac{-t}{1+t} & \frac{-t}{1+t} \\ \frac{-t}{1+t} & 1 & \frac{-t}{1+t} \\ \frac{-t}{1+t} & \frac{-t}{1+t} & 1 \end{bmatrix}. \tag{92}$$

Using similar arguments for N_{dim} dimensions, Q is given by a matrix with ones along the diagonal and off-diagonal elements $\frac{-t}{1+(N_{dim}-2)t}$. If $t = 0$ then Q and T equal the identity matrix, which leads to the conventional Pareto ordering, i.e., a model $\boldsymbol{x}$ is Pareto-optimal if there is no other feasible model $\tilde{\boldsymbol{x}}$ such that $\boldsymbol{f}(\tilde{\boldsymbol{x}}) \leqslant \boldsymbol{f}(\boldsymbol{x})$ with at least one strict inequality. In Figure 31a we demonstrate this concept: a model is dominated if it lies anywhere above and to the right of another model.

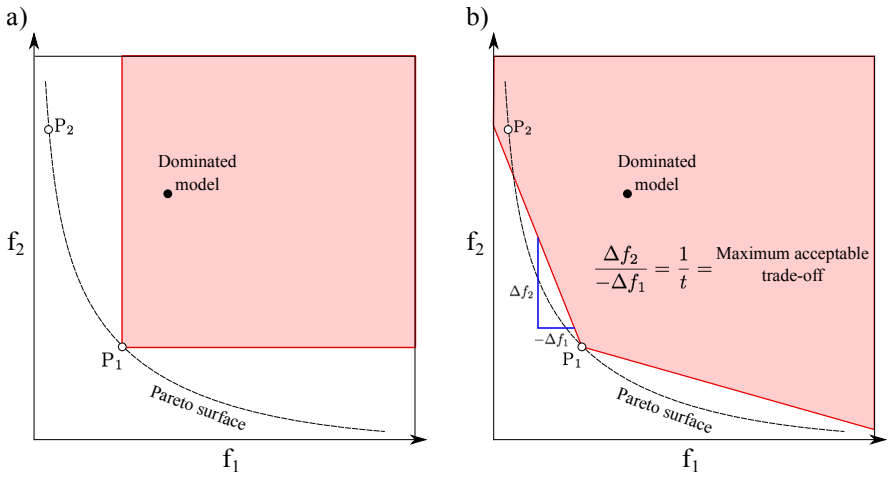

Figure 31: Schematic illustrating Pareto-optimality and dominance in two dimensions. We show two Pareto points, P_1 and P_2 (open circles), that lie on the Pareto front (dotted line). The region shaded in red is P_1 + C; any model that lies in this region is dominated by P_1. In a), the ordering cone C ($t = 0$) implies the conventional Pareto ordering between objectives f_1 and f_2, where models are dominated if they are above and to the right of a Pareto-optimal model. In b) we illustrate the dominance criterion for a broader ordering cone, C, when $t > 0$. We specify $1/t$, the maximum acceptable increase in f_2 (Δf_2) for a unit decrease in f_1 ($-\Delta f_1$), which corresponds to the gradient of the left-most extreme ray of C. This broader ordering cone leads to P_2 becoming dominated.

Throughout, we refer to the complete set of Pareto-optimal models as the Pareto front, and refer to the discrete set of non-dominated models by a matrix P, where the k-th row ($k = 1, ..., N_P$) corresponds to a non-dominated point which we refer to as P_k. N_P is the number of Pareto points. The algorithm proposed in this chapter will always produce points that are Pareto-optimal in the conventional sense, but some Pareto-optimal points may be discarded when $t > 0$ due to the dominance criterion, which removes parts of the Pareto front where trade-offs are unfavourable. In Figure 31, we provide a visual interpretation of non-dominance and Pareto dominance in two dimensions for an ordering cone C generated by $t = 0$ (Figure 31a), and $t > 0$ (Figure 31b). In Figure 31b, we illustrate how Pareto-optimal models are dominated when a broader ordering cone is chosen.

4.2.2 *Approximating the non-dominated set*

The goal of multi-objective optimization is to find the non-dominated set, i.e., solutions to problem MOP, where non-dominance is defined in Equation 90 with a user-defined ordering cone, C.

Typically, it is difficult to find the complete set of non-dominated points since a closed-form solution to MOP is not always available. The single objective optimization (SOO) problem (WSP($\boldsymbol{w}$)) is nonlinear and NP-hard, i.e., it cannot be solved in polynomial time with respect to the number of parameters. For approaches that incorporate a scalarization method, the MOO is at best an infinite set of SOO problems and is therefore even more NP-hard. Thus, various methods have been developed for approximating the non-dominated set, the outputs of which are a finite number of non-dominated points. The two main classes of approaches are stochastic and deterministic.

Stochastic methods such as evolutionary algorithms work by sampling a large area of the parameter space and are not typically gradient-based (Rangaiah, 2009). They can therefore be effective regardless of the nature of the objective functions and constraints (Marler and Arora, 2004).

Most deterministic methods make use of a particular type of scalarization, whereby the MOP is converted into an SOO, allowing for gradient-based techniques as solution methods. Common examples of scalarization techniques include the ε-constraint method (YV et al., 1971), whereby inequality constraints are added to the individual objective functions; the Pascoletti-Serafini scalarization (Pascoletti and Serafini, 1984) which relates the objectives via an equality constraint; and the weighted-sum method (WSP($\boldsymbol{w}$)) (Zadeh, 1963). For a more detailed review of the different scalarization methods used in MOO problems, the reader is referred to Eichfelder (2008).

Some scalarization approaches such as the Pascoletti-Serafini and ε-constraint method are able to generate Pareto-optimal points on the non-convex regions of the Pareto front. These approaches are able to explore non-convex regions by adding hard constraints on the objective functions. Here we refer to 'hard' constraints as constraints that must be satisfied, in contrast to 'soft' constraints which may be incorporated into the objective function via penalty functions (Boyd and Vandenberghe, 2004). In non-convex scalarization techniques, the algorithms that determine the scalarization variables do not scale favourably with problem dimensionality. For example, in the hyper-boxing algorithm proposed by Serna (2009), the number of Pascoletti-Serafini scalarizations required to provide a desired optimization quality increases exponentially with the number of dimensions, making the method numerically challenging above a certain number of dimensions (e.g., $N_{dim} > 12$ (Serna, 2009)).

Although the weighted-sum method is only able to capture the convex regions of the Pareto front, it is computationally easier than the other scalarization methods, and has some unique properties that are useful in determining bounds on the Pareto front, as detailed in the next section. From our practical experience with two and three dimensional problems and when the individual objectives f_i represent the sum of squared relative errors between the model and experiment, the majority of the Pareto front is convex. We thus focus on the weighted-sum scalarization, which allows the proposed algorithm to make use of existing methods and code bases for weighted-sum single-objective model parametrisation, without having to change the particular form of the objective function and constraints.

4.2.3 *The weighted-sum scalarization and sandwich algorithms*

In this section we first show how weighted-sum scalarizations of the MOP can be used to generate Pareto-optimal solutions and provide outer approximations to the Pareto front. We then show how inner approximations to the Pareto front can be constructed based on a discrete set of Pareto points, P, and the ordering cone, C, in the case that the MOP is a convex problem. Finally, we describe sandwich algorithms and how they can be used to efficiently generate Pareto points and inner (in the case of convex Pareto fronts) and outer approximations to the Pareto front.

4.2.3.1 *The weighted-sum scalarization*

For convenience, we repeat the definition of WSP($\boldsymbol{w}$) in order to describe the properties of the weighted-sum scalarization in more detail:

$$\underset{\boldsymbol{x}}{\text{minimize}} \qquad \boldsymbol{w}^T \boldsymbol{f}(\boldsymbol{x}) = \sum_{i=1}^{N_{dim}} w_i f_i(\boldsymbol{x}) \tag{93a}$$

$$\text{subject to} \qquad \boldsymbol{x} \in X. \tag{93b}$$

We define the region Z as the set of all feasible vectors in objective space: $Z = \{\boldsymbol{f}(\boldsymbol{x}) \mid \boldsymbol{x} \in X\}$, and refer to vectors in objective space by $\boldsymbol{z}$. The minimization of a weighted-sum scalarization of the MOO can be interpreted geometrically as shifting a hyperplane (a line in 2 dimensions, a plane in 3 dimensions, etc.), with a normal vector equal to the weight vector, as close as possible to the origin in the feasible objective space. A geometric illustration of the optimization is shown in Figure 32, in two dimensions, and where some regions of the Pareto front are non-convex. Solving the weighted-sum scalarized problem with the k-th weight vector $\boldsymbol{w_k}$ that lies in C^* will give an optimal solution $\boldsymbol{x^*}$, corresponding to the k-th non-dominated Pareto point, $P_k = \boldsymbol{f}(\boldsymbol{x^*})$. We can then define a hyperplane that has normal vector $\boldsymbol{w_k}$, and passes through P_k, by $\boldsymbol{w_k}^T \boldsymbol{f} = \boldsymbol{w_k}^T P_k = b_k$, and its associated positive half space, $\{\boldsymbol{z} \mid \boldsymbol{w_k}^T \boldsymbol{z} \geqslant b_k, \boldsymbol{z} \in Z\}$.

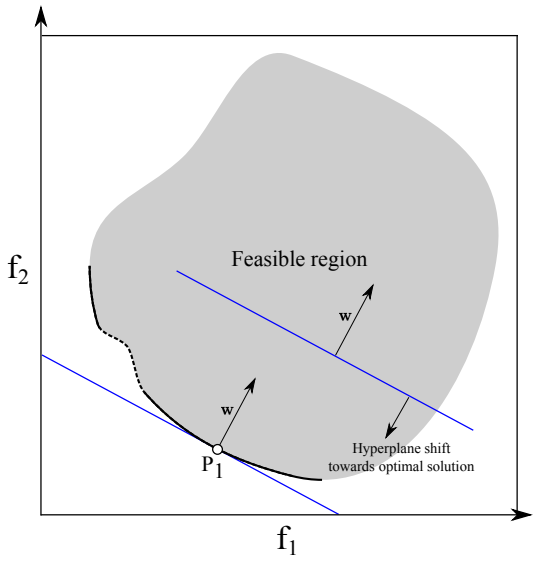

Figure 32: Schematic illustrating the weighted-sum scalarization in objective space for the two objectives f_1 and f_2. The grey area represents the feasible region; the solid black curve represents all of the Pareto-optimal solutions that are accessible by weighted-sum scalarization, whilst the dotted section of this curve represents Pareto-optimal solutions that are inaccessible by weighted-sum scalarization. The weight vector, $\boldsymbol{w}$, used for the scalarization is normal to the blue hyperplanes. At the Pareto point, P_1 (open circle), the hyperplane is tangential to the Pareto front and provides an outer approximation; any feasible point in objective space must lie above (or equal to) this hyperplane.

4.2.3.2 *Definition of the outer approximation, Z^{out}*

By solving the weighted-sum scalarization with a single weight vector to global optimality, not only do we always obtain a Pareto-optimal solution, but we also obtain a positive half-space that provides a lower bound on the feasible region, and thus a lower bound on the Pareto front. Equivalently, there is no feasible solution that lies in the associated negative half-space. With multiple Pareto points and their associated weight vectors, we define an outer approximation to the feasible objective space, $Z^{\text{out}} \subseteq Z$, by the set of positive half-spaces:

$$Z^{\text{out}} = \{\boldsymbol{z} \mid W^{\mathsf{T}}\boldsymbol{z} \geqslant \boldsymbol{b}\}, \tag{94}$$

where W is a matrix with each row corresponding to a particular weight vector, and $\boldsymbol{b}$ is a column vector where the k-th element is obtained by the scalar product between the k-th row of W and the k-th row of P. Note that Z^{out} is an outer approximation even if the Pareto front is non-convex.

4.2.3.3 *Definition of the inner approximation, Z^{in}*

An inner approximation to the Pareto front can be found via polyhedral approximations if the Pareto front is convex. Sufficient conditions for the convexity of MOP are that all $f_i, i = 1, \ldots, N_{\text{dim}}$ are convex, the inequality constraint functions are convex, and the equality constraints are affine (Boyd and Vandenberghe, 2004). However, the convexity of the Pareto front only requires that the feasible region,

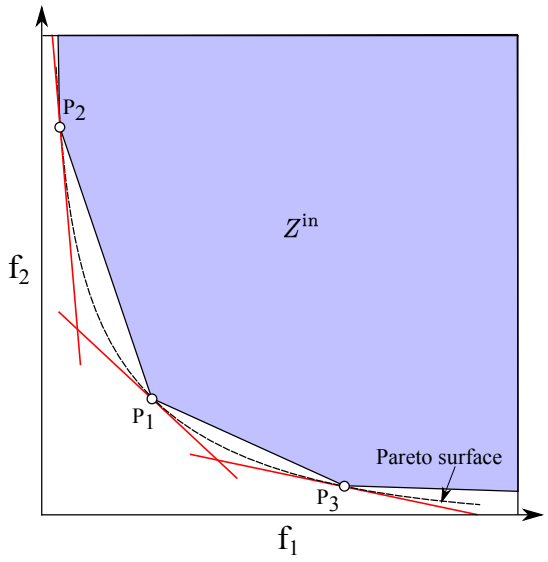

Figure 33: Schematic illustrating the region described by the inner and outer approximations, Z^{in} and Z^{out} respectively, for three Pareto points (open circles). The dashed curve is the Pareto front which is convex. Z^{in} is defined in Equation 95 . The lower edge of Z^{in} is shown by the straight black lines, some of which connect the Pareto points, the others lie on the extreme ray of C that originates from the two extreme Pareto points P_2 and P_3. The blue shaded region is the convex hull of Z^{in}. The red lines represent the lower region of Z^{out}, defined in Equation 94. The whole region defined by Z^{out} lies above or on the red lines. The Pareto front is 'sandwiched' in the region $Z^{out} \setminus Z^{in}$.

Z, is *p-directionally convex* (Holtzman and Halkin, 1966), as demonstrated by Lin (1976). This is because the Pareto front is always on the boundary of Z (Marler and Arora, 2010). The definition of p−directionally convex is as follows (Marler and Arora, 2010):

p-Directionally Convex: Given a nonzero vector $\boldsymbol{p}$, Z is said to be p-directionally convex if given any two different points in Z, $\boldsymbol{f_1}$ and $\boldsymbol{f_2}$, and any two positive scalars, w_1 and w_2, with $w_1 + w_2 = 1$, there is a positive number β such that $w_1 \boldsymbol{f}_1 + w_2 \boldsymbol{f_2} + \beta \boldsymbol{p} \in Z$.

The Pareto front may be convex even if $f_i, i = 1, ..., N_{dim}$, are non-convex functions. Assuming convexity of the Pareto front, an inner approximation can be defined by convex combinations of the Pareto points *plus* the ordering cone, $C = \{Q\boldsymbol{\mu} : \boldsymbol{\mu} \geqslant 0\}$. The inner approximation is given by the set Z^{in} (Bokrantz and Forsgren, 2011):

$$Z^{in} = \{\boldsymbol{z} \mid P^T \boldsymbol{\lambda} + Q^T \boldsymbol{\mu} : \boldsymbol{\lambda}, \boldsymbol{\mu} \geqslant 0 \quad \text{and} \quad \boldsymbol{e}^T \boldsymbol{\lambda} = 1\}, \tag{95}$$

where $\boldsymbol{e}$ is a vector of ones with the same dimensions as $\boldsymbol{\lambda}$. Any feasible choice of parameters $(\boldsymbol{\lambda}, \boldsymbol{\mu})$, defines a point in objective space that must lie either above or on the Pareto front. In Figure 33, we provide a geometric interpretation of Z^{in} and Z^{out}. For non-convex surfaces, the inner approximation described here will provide an upper bound to points that lie in the convex hull of the feasible region.

As every weight vector will provide a Pareto-optimal solution to WSP($\boldsymbol{w}$), one may naively choose to run several optimizations with many weight vectors to produce the Pareto front. For example, by using a grid of equally distributed weights.

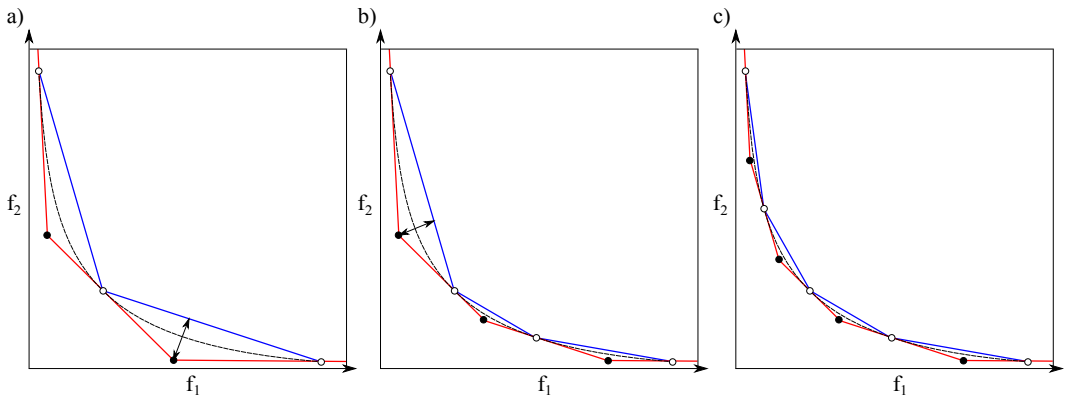

Figure 34: Geometric interpretation of the sandwich algorithm for objectives f_1 and f_2. The dotted line represents the true Pareto front, discrete Pareto points are shown as open circles, the red lines represent the outer approximation, the blue lines represent the inner approximation, the filled black circles are the extreme vertices of the outer approximation. In a), we start with an initial selection of Pareto points by solving the weighted-sum problem with three weight vectors and construct the inner and outer approximation. The area with the largest error between the inner and outer approximation (represented by the line with arrows) is chosen and the normal vector to the facet of the inner approximation in this area is chosen as the scalarization vector for the next weighted-sum optimization. The error measure is some scalar quantity that characterises the distance between the inner and outer approximations, and the specific error measure (the Hausdorff distance) used in this work is defined in step 2 of the sandwiching algorithm described in section 4.2.5. This creates a new Pareto point in b), and the algorithm repeats until the error measure is below a certain tolerance in c). The Pareto front is sandwiched between the inner and outer approximations.

However, it is well known that an even distribution of weights does not typically produce an evenly distributed set of points on the Pareto front (Das and Dennis, 1997), i.e., points become clustered towards certain regions. A grid search may become numerically intractable, particularly as the number of dimensions increases.

Sandwich algorithms provide an efficient way to approximate the Pareto front. The output is a finite number of non-dominated points, and a polytope (or collection of facets) that approximates the true Pareto front to within a known degree of accuracy. In essence, sandwich algorithms iteratively produce increasingly tighter inner and outer approximations to the Pareto front by solving a sequence of weighted-sum scalarizations of the MOO, and they terminate once a user-defined convergence criterion is met. Assuming convexity of the MOO problem, the true Pareto front is 'sandwiched' between the inner and outer approximations. At each iteration of the algorithm, a new weight vector is selected to solve the weighted-sum problem that leads to the largest improvement in the approximation quality. In this way, the algorithm seeks to obtain the desired approximation quality in as few weighted-sum optimizations as possible. The general idea behind the sandwich algorithm is shown in Figure 34 for two objectives. Note that this geometrical interpretation is only applicable in two dimensions. Furthermore, we show in Figure 35 that although the Pareto front is non-convex, the sandwich algorithm still converges.

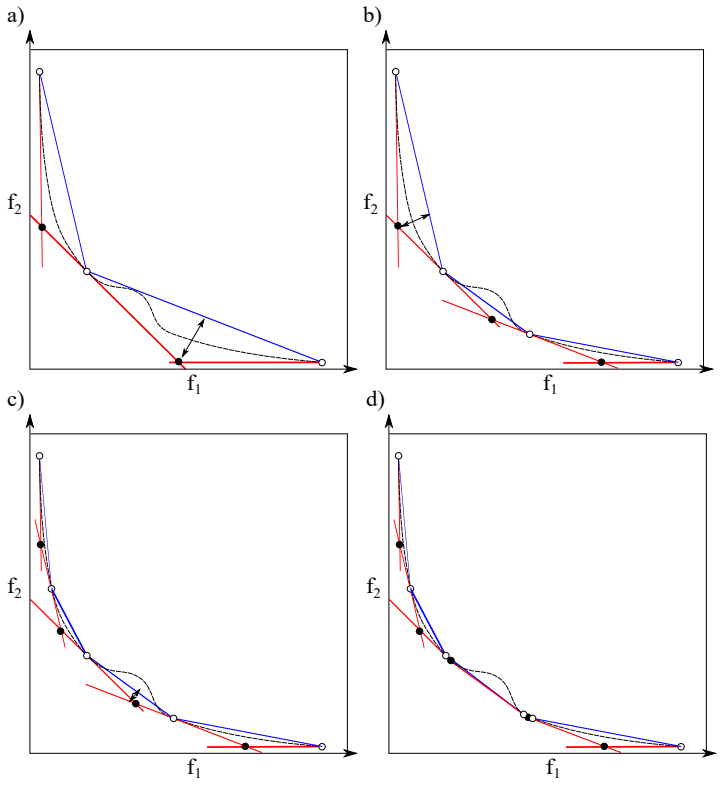

Figure 35: Geometric interpretation of the sandwich algorithm for objectives f_1 and f_2 when there are nonconvex regions within the Pareto front. The dotted line represents the true Pareto front, discrete Pareto points are shown as open circles, the red lines represent the outer approximation, the blue lines represent the inner approximation, the filled black circles are the extreme vertices of the outer approximation. In a), we start with an initial selection of Pareto points by solving the weighted-sum problem with three weight vectors and construct the inner and outer approximation. The area with the largest error between the inner and outer approximation (represented by the line with arrows) is chosen and the normal vector to the facet of the inner approximation in this area is chosen as the scalarization vector for the next weighted-sum optimization. The error measure is some scalar quantity that characterises the distance between the inner and outer approximations, and the specific error measure (the Hausdorff distance) used in this work is defined in step 2 of the sandwiching algorithm described in section 4.2.5. This creates a new Pareto point in b). Note that in b) there are parts of the Pareto front that lie outside of the the 'inner' approximation. In c) a new Pareto point is created in the convex region of the Pareto front. The next largest error measure is then associated with the inner and outer approximations close to the non-convex region. In d) we show that the inner and outer approximations essentially converge to eachother in the non-convex region and thus the algorithm will terminate even if there are non-convex regions in the Pareto front.

4.2.4 *Literature review of existing sandwich algorithms*

The various sandwich algorithms in the literature differ mainly in the way in which the inner approximation is formulated and the choice of the error measure used to quantify the deviation between the inner and outer approximations to the Pareto front. All methods use a similar formulation of the outer approximation (Equation 94). Here we give a brief overview of the various sandwich algorithms in the literature and note some of their drawbacks and advantages.

In the seminal work of Solanki et al. (1993), the authors propose an algorithm, XNISE1, where the inner approximation is represented by the convex hull of the Pareto points. This convex hull is represented by a collection of facets, F_s (e.g., line segments in two dimensions, planes in three dimensions, and hyperplanes in n-dimensions) where s represents the s-th face of the convex hull. Each facet of this inner approximation is given an error, δ_s, which is defined by the minimum Euclidean distance between the facet and a point $\boldsymbol{z}^*$ in the outer approximation that satisfies $\boldsymbol{z}^* = \min(\boldsymbol{w}^{*\mathsf{T}}\boldsymbol{z})$ subject to $\boldsymbol{z} \in Z^{\text{out}}$, where $\boldsymbol{w}^*$ is the inner-facing normal vector of the facet. Inner-facing means that it points towards the inside of the convex hull of the set of Pareto points. The weight vector normal to the facet F_t with maximum error δ_t is then used to solve the weighted-sum optimization, producing a new Pareto point and additional half-space to be added to the outer approximation. The new inner approximation is then the convex hull of the new Pareto point and the previous set of Pareto points. The algorithm repeats by calculating a new error measure δ_t, and iterates until this error reaches a certain maximum tolerance. Such an algorithm may be termed "facet enumerative", because the error δ_s is associated with the s-th facet. This contrasts to 'vertex enumerative' sandwich algorithms where an error is assigned to the extreme vertices of Z^{out}, which we will discuss in more detail later in this section. A particular issue with this approach lies in the definition of the inner approximation: in dimensions higher than two, some facets F_s of the inner approximation (particularly facets close to the boundaries of the Pareto front) can have mixed normals, i.e., some components of the normal vector are positive and some negative. A simple example of a case where mixed normals arise is shown in Figure 36. Solving a weighted-sum optimization with negative weightings given to some objectives produces solutions that are non-dominated. The authors mediate this issue by limiting f_i such that the new solutions do not lie too far from the Pareto front, but optimizations using negative weights is not a desirable property as carrying out each weighted-sum optimization is time consuming. However, Rennen et al. (2009) showed that the error measure associated with mixed-normal facets is overly pessimistic.

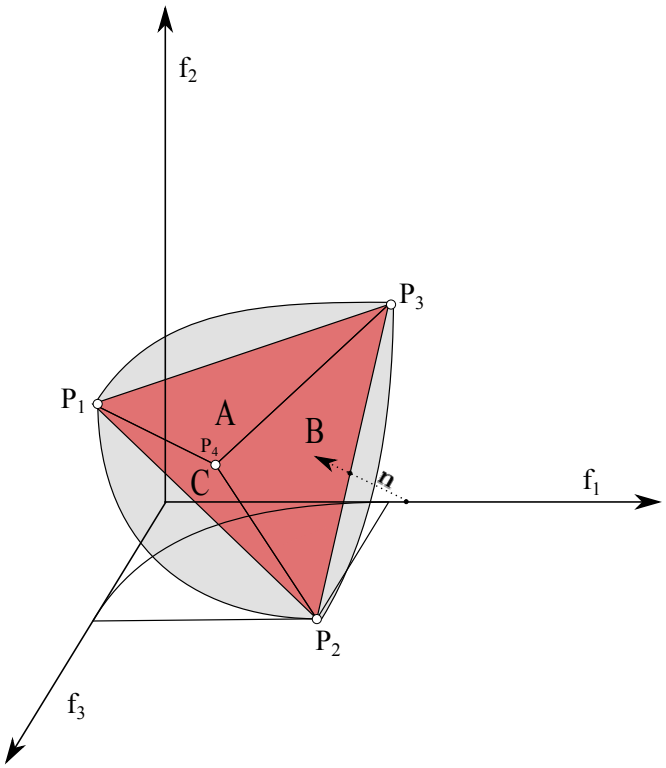

Figure 36: Illustration of the facet representation of the inner approximation when only the Pareto points are considered in the convex hull. The Pareto front, indicated in grey, is the lower eighth of a sphere. The Pareto points are open circles. Points P_1, P_2 and P_3 represent the minimum values of f_1, f_2 and f_3 respectively. Point P_4 represents the point on the Pareto front where all $f_i, i = 1, 2, 3$ are equal. The facets A, B and C are generated from the convex hull of the P_i and have normal vectors with both positive and negative elements. Note that the fourth facet in the convex hull that connects points P_1, P_2 and P_3 is omitted from the diagram. For facet B, we show its normal vector, $\boldsymbol{n}$, that points towards the inside of the convex hull of the Pareto points and passes through the midpoint of P_2 and P_3. Vector $\boldsymbol{n}$ points in the direction of increasing f_2 and f_3, but decreasing in f_1.

A similar approach was proposed by Craft et al. (2006), but rather than performing weighted-sum optimizations scalarized with weight vectors that include negative components for facets with mixed normals, a convex combination of the weight vectors at the facet vertices is chosen. In this way, only positive weights are used in the optimization. However, this method may lead to Pareto-optimal solutions that do not reduce the error measure in subsequent iterations, i.e., the same facet may exist in the convex hull of the previous Pareto points and the new point (Rennen et al., 2009). This leads to issues in convergence of the algorithm since in each iteration one is not guaranteed to reduce the error measure and thus heuristic methods must be used, e.g., flagging facets for which the normal vector has already been used in the weighted-sum optimization. Our tests with this algorithm show that the convergence is relatively poor, and the Pareto points become clustered towards the edges of the Pareto front.

Rennen et al. (2009) proposed a modification of the algorithm of Solanki et al. (1993), where rather than generating facets by computing the convex hull of the Pareto points only, additional 'dummy' points are added to expand the convex

hull (and inner approximation), such that the resulting facets of the inner approximation do not have any mixed normals. This method for defining the inner approximation is akin to finding the convex hull of the set-wise summation of the Pareto points and the positive orthant, and is therefore similar to Z^{in} as defined in Equation 95, with the ordering cone C defined with Q and T equal to the identity matrix. By defining dummy points according to Definition 10 in Rennen et al. (2009), the relevant facets that include the dummy points have a zero normal vector in at least one dimension. Using weight vectors with zero elements in the weighted-sum optimization is not particularly desirable as it can produce weakly dominated Pareto points. At the weakly Pareto optimal points, it is possible to improve some objective functions without penalizing others. Additionally, if a thermodynamic property i has zero weighting, the value of f_i at the solution is large, which leads to large values in the distance metric even in regions of the Pareto front where the curvature is steep. In our tests with the algorithm of Rennen et al. (2009), many of the weight vectors used in the optimization have zero elements, particularly at the start of the algorithm.

As we are mainly interested in regions of the Pareto front where the trade-offs between objective pairs are desirable, it is preferable to use an algorithm that incorporates a generalised ordering cone, such that elements of the weight vectors are greater than zero. This provides additional flexibility in specifying maximum admissible trade-offs prior to generating points on the Pareto front. In any case, the use of ordering cones, even the conventional Pareto ordering cone, eliminates artefacts that typically occur close to the boundary of the Pareto front (Hernández, 2011; Bokrantz and Forsgren, 2011).

Two sandwich algorithms that explicitly include ordering cones are those of Hernández (2011) and Bokrantz and Forsgren (2011). The sandwich algorithm described by Hernández (2011) is a modification of the inner-outer approximation described by Klamroth et al. (2003). An error measure is reduced iteratively by maximizing block norms centred on a point $z \in Z + C$. A block norm is a polyhedral gauge that is symmetric with respect to the origin (see Hernández (2011) and references the formal definition). The block norm is constructed in a particular way such that its facets in the positive orthant have normals that are guaranteed to lie within the dual cone of C. This algorithm has been used in several chemical engineering applications that involve multi-objective optimization (Bortz et al., 2014; Burger et al., 2015; Forte et al., 2018). In these works, no more than two objective functions are considered.

In Bokrantz and Forsgren (2011), the authors proposed a 'vertex enumerative' algorithm, whereby the error measure is calculated for each extreme vertex of the outer approximation. This method avoids the explicit construction of the structurally complex polyhedra that form the inner and outer approximations by treating the facet normals as free variables in a linear programming problem. The authors showed that their algorithm scales better with the number of objectives compared to the facet-enumerative approach of Rennen et al. (2009), and were able to solve problems with up to 12 objectives within a practical computational time.

4.2.5 *Description of the Sandwich algorithm used in this work*

Due to the advantages discussed in the previous section, we use an algorithm that closely follows that of Bokrantz and Forsgren (2011). In Algorithm 1 we summarise the essential steps of the sandwich algorithm. Each step of the algorithm is explained in detail in the following text.

1. *Determining initial Pareto points*
   The first step is to compute an initial set of Pareto points, P, from which we can then construct Z^{in} and Z^{out}. The first N_{dim} Pareto points are found by solving a weighted-sum optimization with weight vectors equal to the extreme rays of C^* (the rows of T), with $\sum_{i=1}^{N_{dim}} w_i = 1$. If needed the objectives f_i are normalised between 0 and 1. We next compute a single Pareto point with equal weightings and $\sum_{i=1}^{N_{dim}} w_i = 1$. The Pareto points and their corresponding weights are appended to matrices P and W respectively, and $\boldsymbol{b}$ is initialised for the outer approximation.

2. *Determining the error measure between Z^{out} and Z^{in}*

   The error criterion, η, that defines the deviation between Z^{in} and Z^{out} is the smallest value of ϵ such that $Z^{out} \subseteq (Z^{in} - \epsilon)$. This error measure is equivalent to the Hausdorff distance. Since $Z^{out} \supset Z^{in}$, the Hausdorff distance is given by (Bokrantz and Forsgren, 2011)

   $$d_{\text{Hausdorff}} = \max_{z \in Z^{out}} \min_{z' \in Z^{in}} d(z, z'), \tag{96}$$

   where d is the distance function representing the maximum positive distance between two points in any dimension of the objective space:

   $$d(z, z') = \max_{i=1,\dots,N_{dim}} (0, z'_i - z_i). \tag{97}$$

   Note that the infinity-norm used in Equation 97 is a design choice and may be replaced with a different norm (for example, the Euclidean norm). η can then be determined by solving the bi-level optimization problem (Bokrantz and Forsgren, 2011):

   $$\underset{z \in Z^{out}}{\text{maximize}} \left\{ \begin{array}{ll} \underset{\eta, \boldsymbol{\lambda}, \boldsymbol{\mu}}{\text{minimize}} & \eta \\ \text{subject to} & \eta \boldsymbol{e} \geqslant P^T \boldsymbol{\lambda} + Q^T \boldsymbol{\mu} - \boldsymbol{z} \\ & \boldsymbol{e}^T \boldsymbol{\lambda} = 1 \\ & \eta, \boldsymbol{\lambda}, \boldsymbol{\mu} \geqslant 0 \end{array} \right\}, \tag{BLP}$$

   where $\boldsymbol{e}$ is a row vector of ones with length defined its context, $\boldsymbol{\lambda}$ is a column vector corresponding to the weights used in a convex combination of the Pareto points, $\boldsymbol{\mu}$ is a column vector corresponding to the weights used in a conic combination of the extreme rays of the ordering cone Q. Here, we solve BLP by enumerating candidate values for $\boldsymbol{z}$ in the outer problem.

As Z^{out} consists of linear constraints, it can be shown (Bokrantz and Forsgren, 2011) that the values of z that are optimal to BLP lie on the extreme vertices of the outer approximation, i.e., points where the hyperplanes that define the outer approximation intersect. Denoting an extreme vertex by v, the following linear programming problem is solved for each v:

$$\begin{aligned} \underset{\eta,\lambda,\mu}{\text{minimize}} \quad & \eta \\ \text{subject to} \quad & \eta e \geqslant P^T\lambda + Q^T\mu - v \\ & e^T\lambda = 1 \\ & \eta, \lambda, \mu \geqslant 0. \end{aligned} \tag{PLP(v)}$$

The extreme vertices are calculated using the "CON2VERT" function available on MATLAB file exchange, which returns a set of vertices given a system of inequalities (in our case, $W^T z \geqslant b$). The function employs a primal-dual polytope method, which requires that the constraints are bounded. To ensure boundedness, we provide a lower bound $z \geqslant 0$, and a large upper bound, $z \leqslant 1E10$. The extreme vertices that lie at the upper bound are removed from the function output.

A geometric interpretation of PLP(v) for a particular v is shown in Figure 37. In Figure 37a), we show the region (in blue) defined by a convex combination of the Pareto points ($P^T\lambda, \lambda \geqslant 0$, $e^T\lambda = 1$), and the same region plus the ordering cone defined by $Q^T\mu$ and $\mu \geqslant 0$. In Figure 37b), we show a geometric interpretation of the right hand side of the first set of inequality constraints in PLP(v), where d_1 and d_2 are the z_1 and z_2 components of the vector $P^T\lambda + Q^T\mu - v$. It is clear that because η is minimized, the optimal solution will lie on an inner edge of $P^T\lambda + Q^T\mu$, and either $\eta = d_1 (d_1 \geqslant d_2)$, or $\eta = d_2 (d_2 \geqslant d_1)$, or $\eta = \max(d_1, d_2)$. Additionally, $\eta \geqslant 0$, so both d_1 and d_2 vary between 0 and some positive value, so there is a solution where $d_1 = d_2$. At this point of equality of the two distance metrics, any reduction in either d_1 or d_2 leads to an increase in the other distance, hence, the solution is when the first set of inequality constraints are active and where $\eta = d_1 = d_2$. In general, the first set of equality constraints will always be active, as the supporting hyperplane to Z^{in} at the optimal solution will have a normal vector with all of the elements being positive by construction. Hence, at a point on a hyperplane where are all d_i are equal, it is not possible to choose another point in the hyperplane without increasing at least one of the other d_i.

Let v^* be the extreme vertex that gives the largest value of η in PLP(v). If this value is below a user-defined tolerance η^{max}, then the algorithm terminates here, as the inner and outer approximations are suitably close. Otherwise we continue to step 3.

3. *Choosing the next weight vector to run*
After finding v^*, the next step is to find the weight vector that is normal to Z^{in} at $P^T\lambda^* + Q^T\mu^*$, where λ^* and μ^* are the optimal solutions to PLP(v^*), to use in the next weighted-sum problem. In Bokrantz and Forsgren (2011),

the dual problem to PLP($\boldsymbol{v}$) is solved in order to find the next weight vector. Instead, we use the property that the first set of inequality constraints in PLP($\boldsymbol{v}$) are active, and therefore the Lagrange multipliers (or dual variables) for these constraints, provided by the linear optimization program, is precisely the normal vector needed. This avoids having to solve a separate linear programming problem. We denote these Lagrange multipliers and the next weight vector to be run by $\boldsymbol{w}^*$.

4. *Solving WSP($\boldsymbol{w}$)*
   If WSP($\boldsymbol{w}$) is a non-convex problem the output of the chosen optimization routine can be highly dependent on the initial parameter guess as one may get trapped in minima that are locally but not globally optimal. To mediate this issue, we use a multi-start approach whereby initial guesses for $\boldsymbol{x}$ are chosen, which lie within the parameter bounds $\boldsymbol{x}^{\mathbf{LB}}$ and $\boldsymbol{x}^{\mathbf{UB}}$, based on a Sobol' sequence (Sobol', 1967). We choose to use powers of 2 for the number of Sobol' points due to local minima observed in the "discrepancy", a measure of how uniformly the parameter space is sampled (Morokoff and Caflisch, 1994).

   Once an initial number, N_s, of Pareto points and their corresponding parameters are determined with a large number of Sobol' points, subsequent optimizations are run by using parameters already obtained from previous Pareto points (nearby solutions in objective space) and their convex combinations. This implicitly assumes that nearby points on the Pareto front will have similar parameters. The point $P^T\boldsymbol{\lambda}^* + Q^T\boldsymbol{\mu}^*$ lies on a hyperplane that connects the points P_k, where k corresponds to the indices of the non-zero elements of $\boldsymbol{\lambda}^*$. We expect that this point will lie close to the true Pareto point obtained in the next weighted-sum optimization. Hence, sensible initial guesses to solve WSP($\boldsymbol{w}$) are $\boldsymbol{x}_k$ and the convex combination: $\boldsymbol{\lambda}_{\boldsymbol{k}}^{*T}\boldsymbol{x}_k$. Note that this technique may lead to suboptimal points being identified if there are discontinuities in the optimal set of Pareto-optimal parameters. The likelihood of this issue arising can be mitigated by increasing N_s.

   After solving WSP($\boldsymbol{w}$), the new Pareto point is appended to P and $\boldsymbol{w}^*$ is appended to W.

5. *Removing Pareto points*
   At each addition of the new Pareto point, we perform checks to ensure that all of the Pareto points in P lie within Z^{out}. If this is not the case, then some of solutions to WSP($\boldsymbol{w}$) in previous iterations were not globally optimal, or at least optimal with respect to the other Pareto points. For each weight vector $\boldsymbol{w}_k$ in W we compute the scalar product of this weight vector and all of the Pareto points. If the minimum scalar product does not correspond to $\boldsymbol{w}_k^T P_k$, i.e., another Pareto point lies below the hyperplane associated with $\boldsymbol{w}_k$ in the outer approximation, then we remove the kth row from P and W. Note that this check will also remove any dominated points from P, and will help with the convergence of the sandwich algorithm. At this point we return to step 2 of the algorithm.

The following bullet points summarize how the algorithm differs from that of Bokrantz and Forsgren (2011):

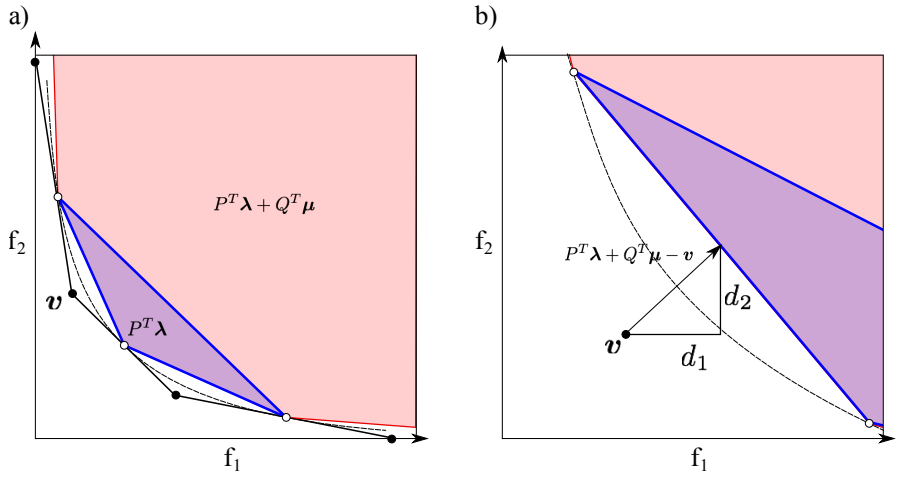

Figure 37: Geometric interpretation of the minimization of the error measure in two dimensions. The open circles are the computed Pareto points; the blue region is the convex hull of the Pareto points ($P^T\lambda$, $\lambda \geqslant 0, e^T\lambda = 1$); the region shaded red is the obtainable region when adding the ordering cone to each point in the convex hull. In b) we zoom in on an extreme vertex of the outer approximation, v, to show the geometric interpretation of the error measure, η, where $\eta \geqslant d_1$ and $\eta \geqslant d_2$.

Algorithm 1 Sandwich algorithm, based on that of Bokrantz and Forsgren (2011)

input:

- A multi-objective optimization problem.
- A quality threshold, η^{max} (default 0.01).
- Reciprocal of the maximum admissible trade-offs between objective pairs, t (default 0.01).

output:

- A set of non-dominated points, P.
- A polyhedron that approximates the Pareto front.

begin

1: Solve WSP(w) with w equal to the extreme rays of C^*.
Solve WSP(w) with an equal weight vector.
Construct Z^{in} and Z^{out}.
Set $\eta = \infty$.

while $\eta > \eta^{max}$ **do** ▷ Terminate if quality criteria is met

2. Compute the extreme vertices, V, of the outer approximation.
For each v in V, compute η' by solving PLP(v) and set $\eta = \max(\eta, \eta')$.
3. For the solution of PLP(v) corresponding to η, set the next weight vector, w^*, normal to Z^{in} at the optimal solution.
4. Solve WSP(w) with w^* and update P and Z^{out}.
5. Remove Pareto points from P and inequality constraints from Z^{out} that correspond to suboptimal solutions to WSP(w).

- In step 3., a different method is used in order to determine the weight vector to be used in WSP($\boldsymbol{w}$), making use of the result of the solutions to PLP($\boldsymbol{v}$).
- A global optimization routine is used to solve WSP($\boldsymbol{w}$) since the objective function may be highly non-convex, and an additional method is developed in order to provide good initial guesses to the optimization and reduce the computational effort in finding the optimal solution to WSP($\boldsymbol{w}$). These points are addressed in step 4. of the algorithm.
- After solving WSP($\boldsymbol{w}$) and appending the new point to P, we check if all Pareto points lie within Z^{out}. If this is not the case, we remove Pareto points P_k for which their lower-bounding half-space $\{\boldsymbol{z}|\boldsymbol{w}_k^T\boldsymbol{z} \geqslant b_k\}$ lies above any of the other Pareto points. This is to ensure that solutions to WSP($\boldsymbol{w}$) are globally optimal, or at least optimal with respect to the other Pareto points generated. This is detailed in step 5. of the algorithm.

4.3 APPLICATION

In the previous section (section 4.2) we have discussed the general methodologies for solving the multi-objective optimization problem (MOP), and have detailed a specific algorithm that is suitable for the estimation of equation of state (EoS) parameters. In this section we will first detail the appropriate form of the objective functions f_i, and then apply the sandwich algorithm to develop accurate SAFT-γ Mie models for water in order to illustrate the benefits of the MOO approach.

4.3.1 *Definition of* f_i

The individual objective functions are defined as follows:

$$f_i(\boldsymbol{x}) = \frac{10^4}{N_i}\sum_{j=1}^{N_i}\left[\frac{Y_{i,j}^{exp.}(\boldsymbol{k}) - Y_{i,j}^{model.}(\boldsymbol{k},\boldsymbol{x})}{Y_{i,j}^{exp.}(\boldsymbol{k})}\right]^2, \tag{98}$$

where $\boldsymbol{k}$ is a vector of independent variables that are fixed in the model and the experiment (e.g., thermodynamic variables such as temperature and pressure), $\boldsymbol{x}$ is the parameter vector, $Y_{i,j}^{exp.}$ is the experimental data point for property type i and measurement j, $Y_{i,j}^{model.}$ is the calculated result given by the EoS for property type i and data point j and N_i is the number of data points for property type i. This objective function assumes that for each experiment, an equal weight is given to each data point. In our work this is a valid assumption since a constant relative error is quoted for the data considered. The prefactor of 10^4 is used in this instance so that the values of f_i on the Pareto surface are a suitable order of magnitude. We avoid normalisation in step 1. of the sandwich algorithm because the f_i, described in Equation 98, are non-dimensional and we want to avoid any bias towards particular objectives. This least-squares type of objective function is chosen as it is mathematically well-behaved and it is typically used in the estimation of EoS parameters. We also report the absolute average deviation ($AAD_i\%$) for property type i to describe the accuracy of the fit to experimental data since it

provides a more intuitive indication of the deviation, although we stress that this is not used within the objective function:

$$AAD_i\%(\boldsymbol{x}) = \frac{100}{N_i}\sum_{j=1}^{N_i}\left|\frac{Y_{i,j}^{exp.} - Y_{i,j}^{model.}(\boldsymbol{x})}{Y_{i,j}^{exp.}}\right|. \tag{99}$$

4.3.2 *Application of the MOO approach to SAFT-VR Mie models for water*

We will now apply the proposed algorithm to develop a water model for SAFT-VR Mie (or SAFT-γ Mie) using up to *three* properties. In the introductory section (4.1) we outlined the benefits of adding additional property types in the parameter estimation, and explained why C_P is a suitable property to add above the standard properties ρ_L^{sat} and P^{vap}. We will therefore develop models using these three property types within the MOP.

4.3.2.1 *Literature review of SAFT models for water*

In this section we provide a brief overview of how SAFT-type equations of state can be used to model water. We will review some of the literature models and their development. This will help us decide upon the particular set of SAFT-VR Mie parameters that are defined before the parameter estimation, in particular the parameters that define the association scheme and the sphericity of the model. The literature review will also give us an idea as to which values the parameters will take, and will help us specify suitable parameter bounds $\boldsymbol{x}^{\mathbf{LB}}$ and $\boldsymbol{x}^{\mathbf{UB}}$.

Within SAFT approaches, molecules are modelled as chains of spherical segments with repulsive cores, which may be either hard (e.g., the square-well potential), or soft (e.g., the Mie potential). Association is mediated by adding off-centre, spherically symmetrical square-well bonding sites with attractive short-range interactions.

In the case of water, these association sites are chosen to represent the directional, short range interactions representative of a hydrogen-bond. It is widely known that water can form up to four hydrogen bonds, as seen in hexagonal ice, and water is therefore typically modelled using a four 4 site association scheme (4C in the notation of Huang and Radosz (1990)). In this model, two association sites of type e and two association sites of type H are used, which correspond to the two lone pairs of electrons on the oxygen atom and the two hydrogen atoms respectively and their ability to form hydrogen-bonds. In this model, only e-H bonding is allowed. Due to the symmetry of the association scheme, all sites have the same nonbonded fraction ($X_e = X_H$). This represents the statistical consideration that all of the sites are equally likely to participate in hydrogen bonding, and thus effects such as bond coorperativity (Sear and Jackson, 1996c) are typically neglected in SAFT models for water. Other association schemes have been used to model water with SAFT using the 2B (one e and one H) and 3B (one e and two H) association schemes. The 4C scheme is generally chosen however, since it is verified by molecular orbital calculations (Wolbach and Sandler, 1997), it is successful in representing pure component VLE properties (see e.g., (Clark et al., 2006)), and transferring the parameters for this model to aqueous mixtures gener-

ally provides better predictions than the other association schemes (Kontogeorgis and Folas, 2010). Furthermore, it is apparent from the work of Forte et al. (2018) that the non-polar 4C association scheme outperforms the 2B and 3B association schemes for the majority of the Pareto front, with objective functions defined by $AAD_{\rho_L^{sat}}(\%)$ and $AAD_{Pvap}(\%)$.

Another important parameter to consider when defining a water model is m, the number of tangential spherical segments used to represent the molecule. In Figure 38 we show a spherical and non-spherical SAFT model for water using a 4C association scheme.

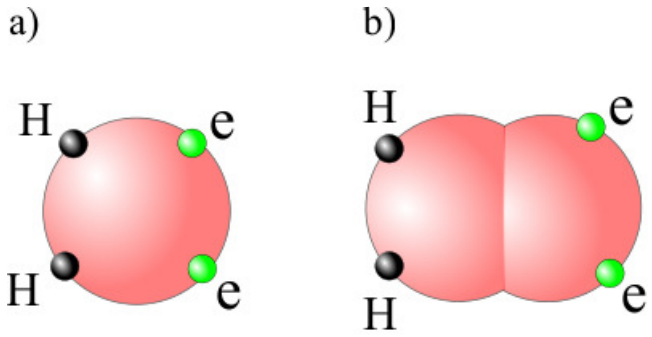

Figure 38: Schematic for two typical SAFT model for water. The molecule is represented by a number of spherical segments (m), which interact via a potential (in SAFT-VR Mie this is the Mie potential) with repulsive core diameter σ. The Mie potential is characterised by a repulsive exponent (λ^r), an attractive exponent (λ^a), and a well depth ϵ. These segments are indicated by the spheres shaded red. In a) the molecule is spherical ($m = 1$). In b) the molecule is non-spherical and $1 < m < 2$. The latter molecule is represented by two fused spheres. In a) and b) the the model is represented by a 4-site association scheme (2 e sites and 2 H sites). These correspond to the two lone pairs of electrons on the oxygen atom and the two hydrogen atoms respectively. These association sites interact via a square-well potential with a hydrogen-bonding association interaction $-\epsilon^{HB}_{e,H}$ and bonding volume $K^{HB}_{e,H}$. Only e-H bonding is allowed.

In Table 12 we summarise some of the parameters for SAFT water models in the literature, extending on the review by Kontogeorgis and Folas (2010) by including some of the more recently developed models of relevance to this work. When the value of m is fixed, it is typically set to $m = 1$, representing a spherical model. In such cases, the chain contribution to the SAFT free energy (used to describe non-spherical molecules) is omitted. This model type is generally chosen due to its simplicity and due to its rigorously defined geometry. The other models are non-spherical and have values of m that vary within $0.98 \leqslant m \leqslant 3.792$. There is evidence from quantum mechanical calculations as to the approximate value m should take. Sheldon et al. (2006) derived values for m by mapping the shapes of the electron orbitals obtained from Hartree-Fock calculations onto a spherocylinder, and estimated the value of $m = 1.0968$ for the SAFT-VR EoS.

In Table 12 we show the values of the dispersion energy and association energy for the various water models. There is a large variation in the values of the dispersion energy (between 42.8 K and 740.5 K), and a large variation in association energy parameters (between 825 K and 2507 K). Although one cannot directly

compare the parameter values between the different SAFT theories, these ranges give an idea as to the order of magnitude the parameters should take.

An additional choice when defining a SAFT model for water is whether or not to explicitly include the long-range dipolar interactions present in water. Extensions to the theory to include this type of interaction are available (see e.g., (Gross and Vrabec, 2006)). In the recent work of Forte et al. (2018), a variety of water models were obtained for PC-SAFT (Gross and Sadowski, 2000; Gross et al., 2001) and the polar version of PC-SAFT (Gross and Vrabec, 2006) to account for the dipolar interaction. They developed non-polar water models which varied in their association scheme (2-site (2B), 3-site (3B) and 4-site (4C)) and developed polar water models which included 2B and 4C schemes. The authors showed that using the experimental value of the dipole moment of water in the gas phase ($\mu = 1.86$ D), the polar 2B model outperforms the non-polar 2B model Pareto surface with objective functions $AAD_{\rho_L^{sat}}(\%)$ and $AAD_{P^{vap}}(\%)$ at all points. However, they found that there is a region of the Pareto front (close to the Pareto-knee where there is a large curvature in the Pareto front), where the two Pareto fronts essentially coincide, with $AAD_{\rho_L^{sat}}(\%)$ and $AAD_{P^{vap}}(\%) \approx 0.5$. The authors found that by adjusting μ to ρ_L^{sat} and P^{vap} for the polar 2B and 4C models they were able to capture a good agreement with respect to both properties ($AAD_{\rho_L^{sat}}(\%)$ and $AAD_{P^{vap}}(\%) < 0.1$). In this work we will not consider the explicit treatment of the diplolar interaction; the orientational and average energetic features of a dipolar fluid will be accounted for through the regression of the typical SAFT parameters to the experimental data.

Following the arguments made in this literature review and in section 4.1, we will consider the development of water models for the SAFT-VR Mie EoS that use the 4C association scheme. For the specific version of the SAFT-VR Mie EoS that we will use, there is only one existing model in the literature, where water is treated as a spherical molecule ($m = 1$) (Dufal et al., 2015b). In this work, we will also consider models where $m \geqslant 1$ by treating m as an adjustable parameter due to evidence from quantum mechanics Sheldon et al. (2006) and due to the majority of literature models having a value of m different to 1. Through application of the proposed MOO approach and analysis of the Pareto fronts this will provide a rigorous comparison between the two model types and will make clear if it is beneficial to choose a non-spherical model over a (simpler) spherical model.

4.3.3 *The SAFT-VR Mie EoS*

For a comprehensive description of the SAFT-VR Mie EoS we will use, the reader is referred to Lafitte et al. (2013b), and the modifications to the association term described in Dufal et al. (2015b). Specifically, the equations used to model the association contribution are those which use the Lennard-Jones reference fluid as the basis for the free energy perturbation, as opposed to the using the generalised Mie fluid as a reference (Dufal et al., 2015b). This Equation is identical to the group contribution counterpart, SAFT-γ Mie (Papaioannou et al., 2014), in the case where molecules consist of identical functional groups. The ideal gas contribution to the heat capacity is calculated using the third order polynomial coefficients in Reid et al. (1977).

Table 12: Parameters for various different SAFT models for water in the literature. Table adapted from Kontogeorgis and Folas (2010).

SAFT Variant	Reference	m	Dispersion energy/ K	Association energy/ K
SRK-CPA	(Kontogeorgis et al., 1999)	-	-	2003
CK-SAFT	(Huang and Radosz, 1990)	1.179	528.2	1809
SAFT 3 site	(Economou and Tsonopoulos, 1997)	1.179	528.2	1809
SAFT 4 site	(Economou and Tsonopoulos, 1997)	1.236	431.7	1368
Simplified SAFT	(Fu and Sandler, 1995)	2	188.2	826
CK-SAFT	(Button and Gubbins, 1999)	1.047	504.4	1365
Original SAFT, 4 site	(Li and Englezos, 2004)	0.980	433.9	1195
PSAFT	(Karakatsani et al., 2005)	1	52.1	1982
PC-PSAFT	(Karakatsani et al., 2005)	1	42.8	1973
CK-SAFT	(Boulougouris et al., 2001)	2.850	167.0	1634
PR-CPA	(Wu and Prausnitz, 1998)	-	-	1477
SAFT-VR	(Patel et al., 2003b)	1	253.0	1366
CK-SAFT 3 site HF	(Wolbach and Sandler, 1997)	1.278	385.1	2286
CK-SAFT 4 site HF	(Wolbach and Sandler, 1997)	1.406	212.9	1809
CK-SAFT 3 site DFT	(Wolbach and Sandler, 1997)	1	615.9	1627
CK-SAFT 4 site DFT	(Wolbach and Sandler, 1997)	1	546.6	1237
APACT 2 site	(Economou and Donohue, 1992)			2418
APACT 3 site	(Economou and Donohue, 1992)			2618
Original SAFT 4C	(Li and Englezos, 2003)	0.982	433.9	1195
SRK-CPA	(Voutsas et al., 2000)	-		1794
CK-SAFT	(Voutsas et al., 2000)	2.853	167.1	1635
PC-PSAFT	(Karakatsani and Economou, 2006)	1.750	169.5	1131
tPC-PCAFT	(Karakatsani and Economou, 2006)	1.600	58.1	1640
tPC-PSAFFT 4C	(Karakatsani et al., 2006)	2.815	150.7	1575
PC-SAFT 2B	(Gross and Sadowski, 2002b)	1.066	366.5	2501
sPC-SAFT 4C	(Grenner et al., 2006)	1.500	180.3	1804
sPC-SAFT 4C	(Grenner et al., 2007)	2.610	140.4	1695
PC-SAFT 3B	(Kleiner and Sadowski, 2007)	3.254	196.2	1801
PC-SAFT 4C	(Kleiner and Sadowski, 2007)	3.792	138.6	1718
PC-SAFT 4C	(Forte et al., 2018)	2.500	147.9	1582
PC-SAFT 2B	(Forte et al., 2018)	1.785	233.8	2507
PCP-SAFT 2B	(Forte et al., 2018)	2.216	214.5	1544
SAFT-VR Mie (LJ Kernel)	(Dufal et al., 2015b)	1	266.7	1985
SAFT-VR Mie (Mie Kernel)	(Dufal et al., 2015b)	1	418.0	1600
SAFT-VR	(Clark et al., 2006)	1	250.0	1400
SAFT-VR	(Sheldon et al., 2006)	1.0968	740.5	367

4.3.4 *The choice of water model*

The SAFT parameters that characterise the water model, along with their physical descriptions, are summarised in Table 13.

Table 13: Description of the parameters used to characterise water.

	Units A	Description
m	-	Number of spherical segments
σ	Å	Size of each spherical segment
λ^r	-	Repulsive exponent of the Mie potential
λ^a	-	Attractive exponent of the Mie potential
ϵ/k_B	K	Depth of the Mie potential
$\epsilon^{HB}_{e,H}/k_B$	K	Depth of association potential between sites e and H
$K^{HB}_{e,H}$	Å^3	Bonding volume between sites e and H
NST_e	-	Number of site types of type e
NST_H	-	Number of site types of type H

The attractive exponent of the Mie potential, λ^a is fixed to 6, corresponding to the attractive range of the London dispersion force, as it has been shown that a conformal description of the thermodynamics can be achieved with an interrelationship between λ^r and λ^a (Ramrattan et al., 2015). Following the arguments made in section 4.3.2.1, we choose to use a four-site association scheme to model water, where $NST_e = 2$ and $NST_H = 2$. A schematic for this model type is shown in Figure 38. For spherical models of water, the value of m is fixed to 1. In Table 14 we define the lower and upper bounds to each parameter.

Table 14: Upper and lower bounds on parameters

	m	σ / Å	λ^r	λ^a	(ϵ/k_B) / K	$(\epsilon^{HB}_{e,H}/k_B)$ / K	$K^{HB}_{e,H}$ / Å^3
Lower Bound	1	2.5	8	6	100	1000	0.1
Upper Bound	2	3.5	40	6	500	2500	500

4.4 RESULTS

The multi-objective optimization technique is applied to two types of water model: "spherical" models, where $m = 1$, and "non-spherical" models where $m \geqslant 1$ following the arguments made in section 4.3.2.1. These two model types are chosen for the analysis as one may prefer to choose a spherical model over a non-spherical one due to it being a simpler model, and we show in detail the level of improvement that one may obtain by treating m as adjustable.

Following the arguments made in the introductory section (section 4.1) we will apply the MOO technique to the development of water models where three different experimental property types are considered as competing objectives: saturated

liquid density (ρ_L^{sat}), saturated vapour pressure (P^{vap}), and isobaric heat capacity data (C_P).

In the first scenario, we will analyse the two-dimensional Pareto fronts for spherical and non-spherical models of water when two experimental properties, saturated liquid density (ρ_L^{sat}) and vapour pressure (P^{vap}), are used as objective functions. These are the most common data types used to regress pure component EoS parameters (Kontogeorgis and Folas, 2010), and will therefore provide some insight into the objective space and the models typically obtained when solving WSP($\boldsymbol{w}$).

In the second scenario, we will analyse the three-dimensional Pareto fronts where C_P is included in the the MOP. This will show how the addition of a second-derivative property affects the objective functions and the water models obtained.

Finally, we will pick some preferable Pareto-optimal water models from the Pareto front and analyse their level of agreement with respect to the experimental data, including the prediction of thermodynamic properties not included in the objective function.

4.4.1 *Calculation details*

The experimental data for water is taken from the National Institute of Standards and Technology (NIST) (E.W. Lemmon and Friend, 2018). Saturation property data are taken at temperatures between the triple point of water, 273.16 K, to 613.16 K, to ensure that temperatures do not exceed 95% of the critical point. This is the same range of temperatures considered by Dufal et al. (2015b) and therefore the models obtained in this work provide a useful comparison with the existing SAFT-VR Mie literature model. We choose data points with temperature intervals of 10 K following Forte et al. (2018). The experimental values for the isobaric liquid heat capacity are taken at 1 atm, and between the triple point and 10 K below the saturation temperature, i.e., 273.16 K - 363.16 K. As the heat capacity function in gSAFT requires temperature and pressure as inputs, temperatures close to the saturation temperature are not included in the estimation to limit the risk of evaluating a gas phase heat capacity. This prevents having large discontinuities in the objective function. The uncertainties in all thermodynamic properties are expected to be below 0.1 % within the temperature and pressure ranges considered (E.W. Lemmon and Friend, 2018).

The sandwich algorithm is implemented in MATLAB R2018a, whilst the optimization problems are solved externally using the 'lmfit' module in Python (Newville et al., 2016) with the default options, which follows a Levenberg-Marquardt algorithm. The thermodynamic properties within the optimization routine are evaluated with gSAFT (Lafitte et al., 2017), which has an in-built flash algorithm to solve for phase equilibira. To determine the convex hull of the set of Pareto points and the normal vectors to the facets, the C++ implementation of Qhull (Barber et al., 1996) is used.

In all cases, we set the reciprocal of the maximum admissible trade-off between objective pairs to be $t = 0.01$. This represents a relatively narrow ordering cone, but limits the non-dominated solutions to have reasonable trade-offs and limits the f_i such that they do not take on extremely large values. Furthermore, fixing

$t > 0$ as opposed to $t = 0$ avoids generating weight vectors with zero elements which can lead to weakly dominated solutions, as discussed in Section 4.2.4.

The maximum admissible error, η^{max}, is set to 0.1 in all cases, meaning that any point on the inner edge of Z^{in} will not be further than 0.1 away from the true Pareto front in any dimension in objective space, assuming that the Pareto front is convex. To solve WSP($\boldsymbol{w}$), a total of 2048 Sobol' points are used for the first 40 Pareto points calculated ($N_s = 40$ in step 4. of the algorithm). This is to provide us with some confidence that the first 40 Pareto points are globally optimal. Further optimizations are run using the initial guesses for the parameters of the previous Pareto points and their convex combinations as described in step 4.

4.4.2 *Scenario 1: Two-dimensional MOO with data types ρ_L^{sat} and P^{vap}*

In Figure 39a, we display the inner edge of Z^{in} for the two Pareto fronts and in Figure 39b we display the corresponding AAD% for each objective. In the appendix to this chapter, we provide information attributed to each Pareto point in Table 16 (spherical) and Table 17 (non-spherical). It is clear from Figure 39 that the proposed sandwich algorithm works effectively as the Pareto points are equally distributed along the Pareto front. This equal distribution is achieved with a sequence of weight vectors generated by the sandwich algorithm, and these weight vectors are not evenly distributed (this is particularly the case for the non-spherical models, c.f. Table 17). This suggests that the sandwich algorithm is more efficient than a brute-force approach (e.g., solving WSP($\boldsymbol{w}$) with uniformly distributed weight vectors). The true Pareto front appears to be convex in both cases as there are no obvious areas with large gaps in the Pareto front. Therefore it appears we have efficiently captured a good approximation of the full set of non-dominated solutions to both model types for the two dimensional MOP, and any model that lies on the Pareto front may be acceptable. By visual inspection of the Pareto fronts, it is possible to make rigorous comparisons between the two model types. It is clear that by relaxing the constraint on m, we are able to obtain significantly lower values of $f_{\rho_L^{sat}}$ whilst keeping the deviation in vapour pressure to reasonably small values. For example, if we desire a water model with AAD (P^{vap}) $< 0.5\%$ then the non-spherical model is able to capture the liquid density with AAD (ρ_L^{sat}) $< 1\%$, whereas for the spherical model AAD (ρ_L^{sat}) $> 3\%$. The Pareto fronts coincide at the lowest values of $f_{\rho_L^{sat}}$ because m hits the lower bound of 1 where the two model types are identical.

In Figures 40 and 41, we show the prediction of ρ_L^{sat} and P^{vap} in addition to the second derivative property, C_P, for the non-dominated models that only consider ρ_L^{sat} and P^{vap} in the objective function. These figures correspond to the Pareto points as labelled in Figure 39b.

For spherical models (Figure 40), the prediction of the isobaric heat capacity is relatively poor, with f_{C_P} and AAD% (C_P) exceeding 110 and 10% respectively at points towards the centre of the Pareto front. If we consider the 'standard' model that is obtained by weighting the two objectives equally (point 8), we obtain a model with AAD vector [AAD% (ρ_L^{sat}), AAD% (P^{vap}), AAD% (C_P)] = [0.88,1.50,10.45]. This is a fairly significant deviation of C_P. At point 24, corresponding to a weight vector of $[w_{\rho_L^{sat}}, w_{P^{vap}}]$ = [0.0335,0.9665], where most

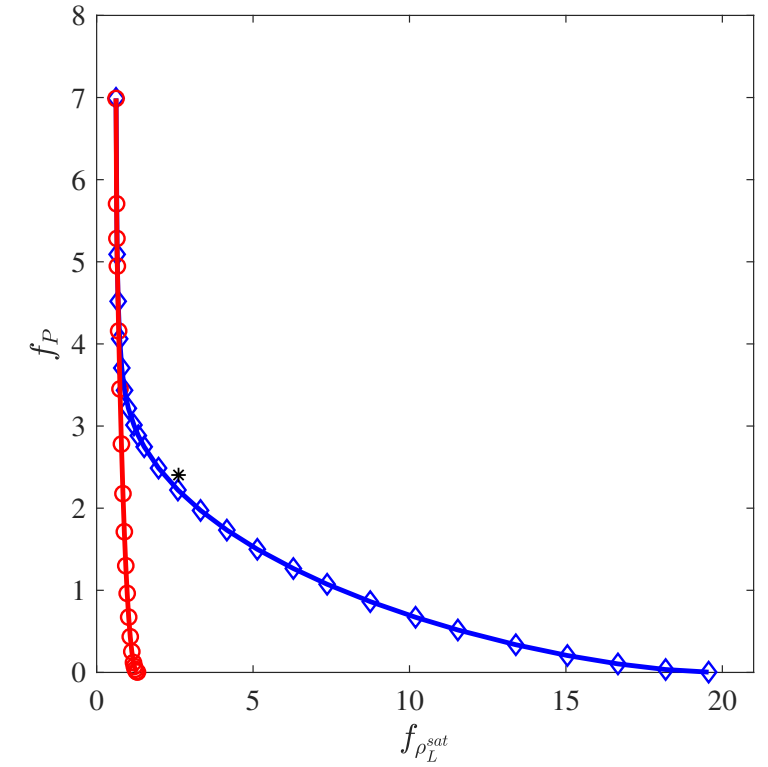

(a)

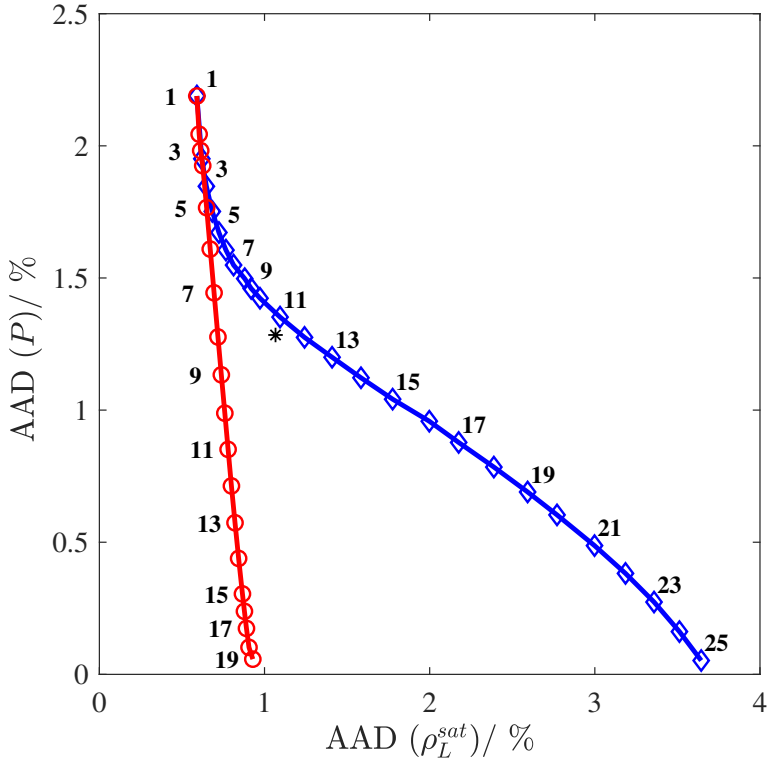

(b)

Figure 39: (a) Pareto frontiers for the two objectives f_P and $f_{\rho_L^{sat}}$. The blue diamonds are the calculated Pareto points for spherical models of water where $m = 1$, the blue line is the inner approximation of the Pareto front. The red circles are the calculated Pareto points for models for water where $m \geqslant 1$ and the red line is the inner approximation of the Pareto front. (b) As for (a), but the AAD for each point is shown, and the lines are a guide to the eye joining the Pareto points. The black star is the result obtained when using the parameters in (Dufal et al., 2015b).

of the weighting is given to the vapour pressure, we obtain an AAD% vector [3.51,0.16,0.45]. By comparing point 24 with point 8, point 24 sacrifices a small difference in AAD% (ρ_L^{sat}) (2.63%) for an improvement in AAD% (P^{vap}) of 1.34% and a vast improvement in AAD% (C_P) of 10%. This illustrates that a model that is potentially more preferable may be obtained by assigning a relatively extreme weight vector in WSP($\boldsymbol{w}$) (i.e., it would generally not be chosen *a priori*). Numerous Pareto points obtained using the proposed technique may be evaluated against other properties not included in the regression (for example, property types that are practically difficult to include within the objective function).

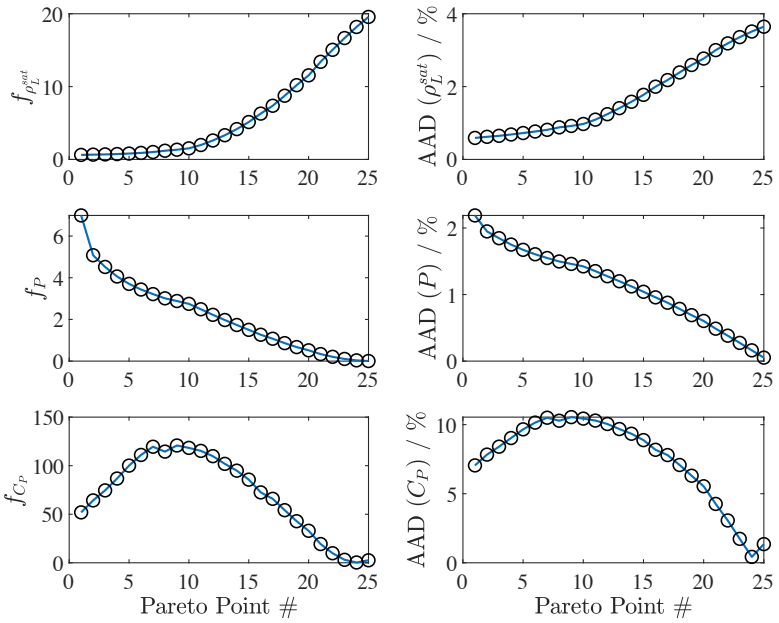

Figure 40: The individual objectives, f_i and the AAD (i) for non-dominated spherical models of water where only $f_{\rho_L^{sat}}$ and f_P are considered in the MOO. The deviation of the C_P predictions are also shown.

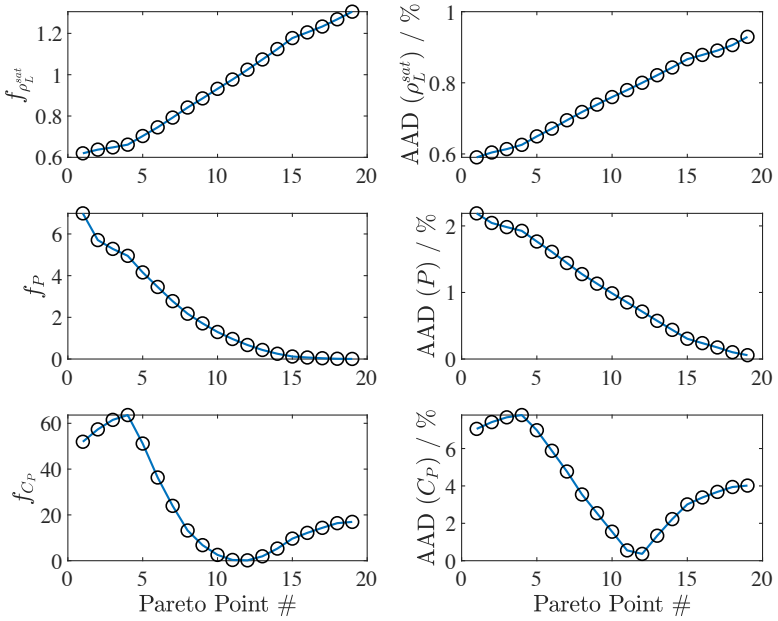

Figure 41: The individual objectives, f_i and the AAD (i) for non-dominated models of non-spherical water ($m \geqslant 1$), where only $f_{\rho_L^{sat}}$ and f_P are considered in the MOO. The deviation of the C_P predictions are also shown.

For the Pareto-optimal non-spherical models (Figure 41) we show that the prediction in C_P (AAD% (C_P)) is between 0.4 % and 7.8 %. The point obtained with equal weighting is point 17 with [AAD% (ρ_L^{sat}), AAD% (P^{vap}), AAD% (C_P)] = [0.89,0.17,3.68]. Note that AAD% (P^{vap}) is fairly close to the expected experimental uncertainty (relative error 0.1%) reported on NIST (E.W. Lemmon and Friend, 2018). Model 12 is potentially more preferable with an AAD vector [0.80,0.71,0.41], and is obtained with $[w_{\rho_L^{sat}}, w_{P^{vap}}]$ = [0.85,0.16].

From the analysis of the Pareto fronts obtained when ρ_L^{sat} and P^{vap} are used in WSP($\boldsymbol{w}$), C_P is predicted accurately for some Pareto points but other points present significant deviations. This may provide an indication that VLE data alone does not provide sufficient information in predicting the second derivative property, and that there is some degeneracy in the parameter space.

In Figure 42 we show the trends in parameters versus the Pareto point number, with indices indicated in Figure 39b. Along the Pareto front for spherical models, the values of ϵ/k_B vary between 270 K and 440 K and $\epsilon_{e,H}^{HB}/k_B$ vary between 1550 K and 1980 K. These represent relatively large ranges for the two energetic parameters, and there is a clear inverse relationship between the two parameters along the Pareto front, which could indicate degeneracy. The value of σ remains fairly constant at just over 3Å. σ and ϵ show almost identical curvature, and similarly with λ^r and $K_{e,H}^{HB}$, indicating a close relationship between these two pairs of parameters and how they affect the individual objectives.

The model of Dufal et al. (2015b) lies close to the calculated Pareto curve for spherical models of water that we find, and these models are close to the Pareto knee. We obtain very similar parameters to the literature model in this region. The parameters for models of water where $m \geqslant 1$ are shown in Figure 39b. There is a

clear relationship between m and σ. The value of λ^r remains fairly constant and shows both a minima and a maxima along the Pareto front.

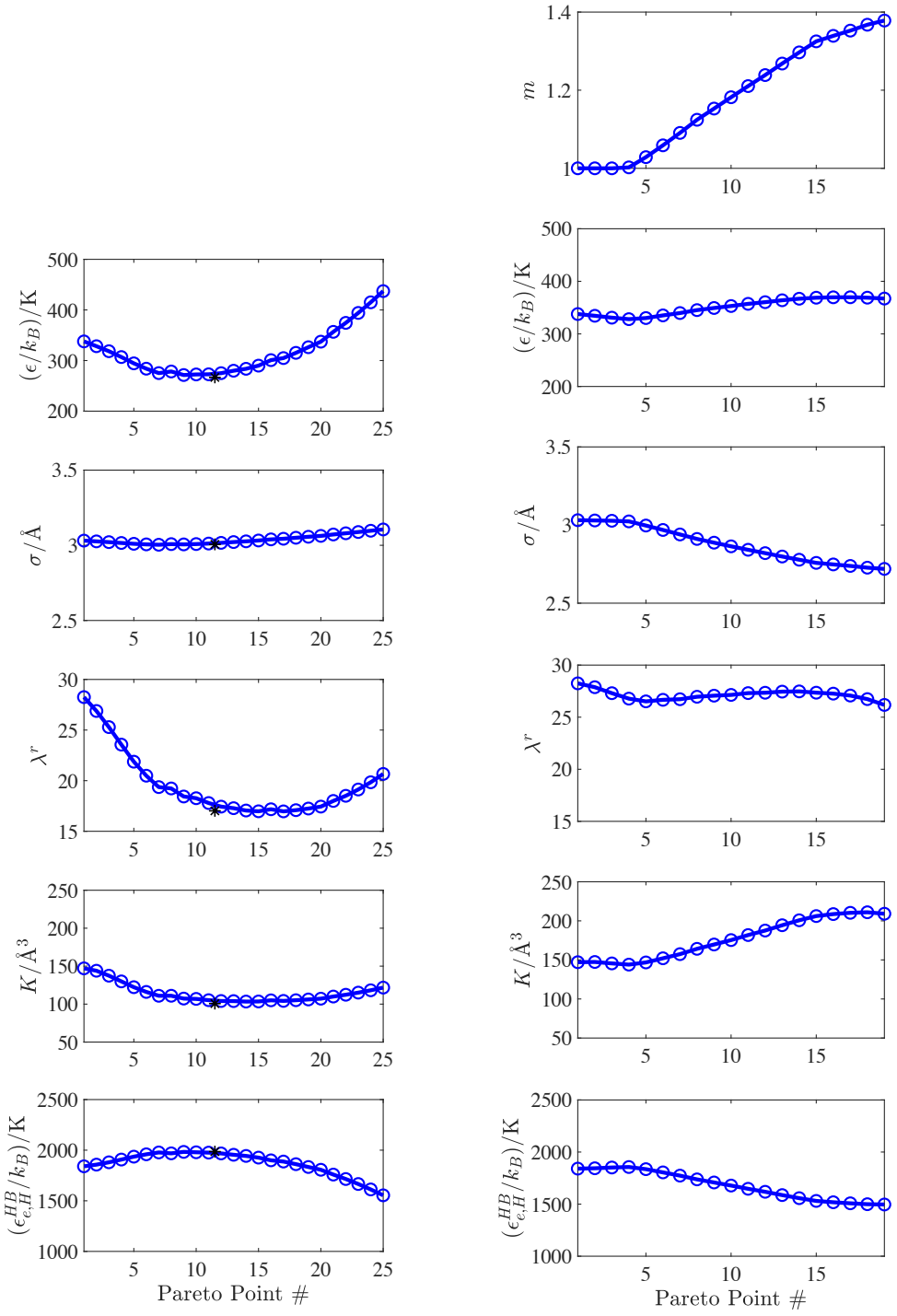

Figure 42: Pareto fronts in parameter space, where the numbers on the x axis correspond to the Pareto points labelled in Figure 39b. (a) Parameters for Pareto-optimal water models where $m = 1$. The black stars correspond to the set of parameters in (Dufal et al., 2015b). (b) Parameters for Pareto-optimal water models where $m \geqslant 1$.

4.4.3 *Scenario 2: Three-dimensional MOO with data types* ρ_L^{sat}, P^{vap} *and* C_P

In the second scenario, we analyse the Pareto fronts when we include C_P as an additional property in the MOP.

Before proceeding with the MOP we will first look at the affect adding C_P has on a single weighted-sum objective function compared to the two-dimensional case. In Figure 43 we show a contour plot of the weighted-sum objective function (with equal weighting given to ρ_L^{sat} and P^{vap}) versus discretized pairs of ϵ and $\epsilon_{e,H}^{HB}$. A similar analysis was conducted by Clark et al. (2006) and Dufal et al. (2015b). We see that the objective function surface consisting of only saturated liquid density and vapour pressure has a large shallow region of relatively similar values. The addition of C_P data reduces the size of the region with similar values, and reduces the degeneracy between ϵ and $\epsilon_{e,H}^{HB}$. We also show that treating m as an adjustable parameter reduces the parameter degeneracy, while the addition of C_P and treating m adjustable has the most dramatic effect on reducing the size of the region with close local minima.

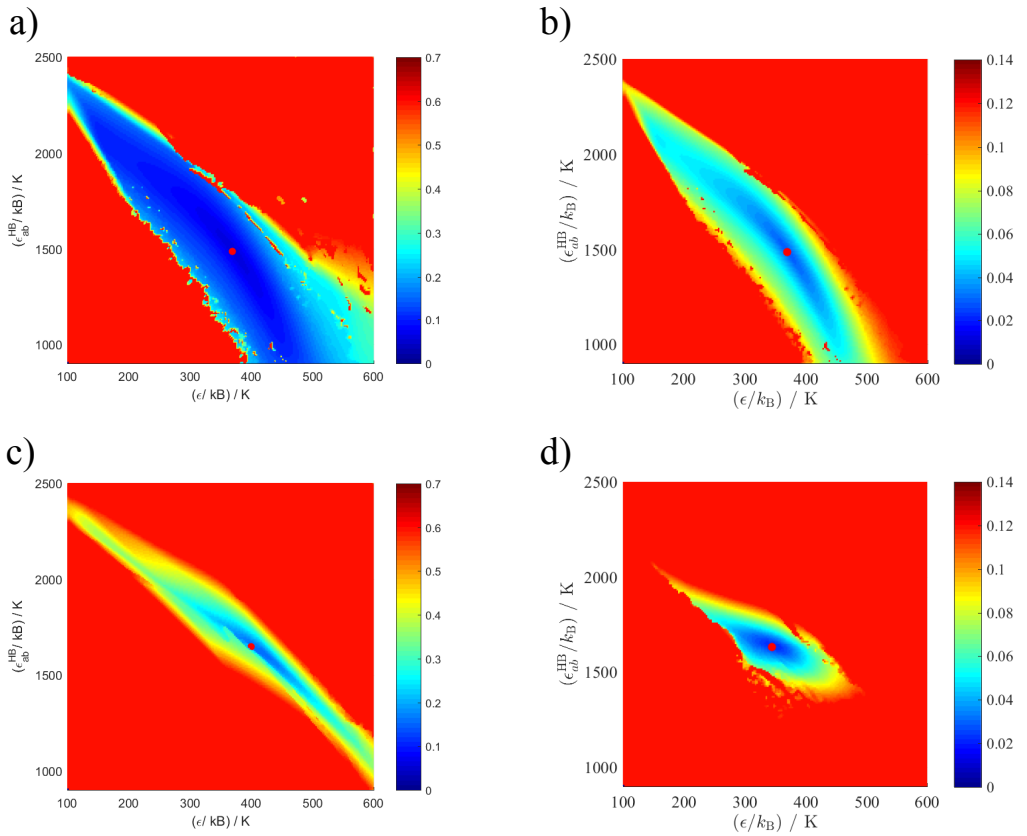

Figure 43: The weighted-sum objective function for water models where we have discretized the energetic parameters ϵ and $\epsilon^{HB}_{e,H}$ in a 1000 x 1000 grid with each parameter varying between the upper and lower bounds defined in Table 14. Each point represents an individual optimization where ϵ and $\epsilon^{HB}_{e,H}$, are fixed and the other parameters are optimized. The weight vectors are normalised to sum to 1 and an equal weighting is given to each property type. The four sub-figures are different in the type of water model and the types of experimental data used in the optimization: a) Spherical water with ρ_L^{sat} and P^{vap} used as experimental data types. b) Non-spherical water with ρ_L^{sat} and P^{vap} used as experimental data types. c) Spherical water with ρ_L^{sat}, P^{vap}, C_P used as experimental data types. d) Non-spherical water with ρ_L^{sat} and C_P used as experimental data types.

In Figure 44, we provide a similar analysis of the objective function as described in the previous paragraph, but rather than discretizing ϵ and $\epsilon^{HB}_{e,H}$ in a uniform grid, we plot the objective function obtained when using a Sobol' sequence to obtain the initial parameter guesses. Note that this result may either be local optima or simply the output of the optimization routine after numerical failure. For non-spherical water models the figure demonstrates that by adding C_P data (in addition to ρ_L^{sat} and P^{vap} data) we greatly reduce the number of locally optimal solutions, with almost all of the initial guesses converging close to the global optimum. Hence, another advantage of adding C_P is that it reduces the computational effort in finding the global optimum.

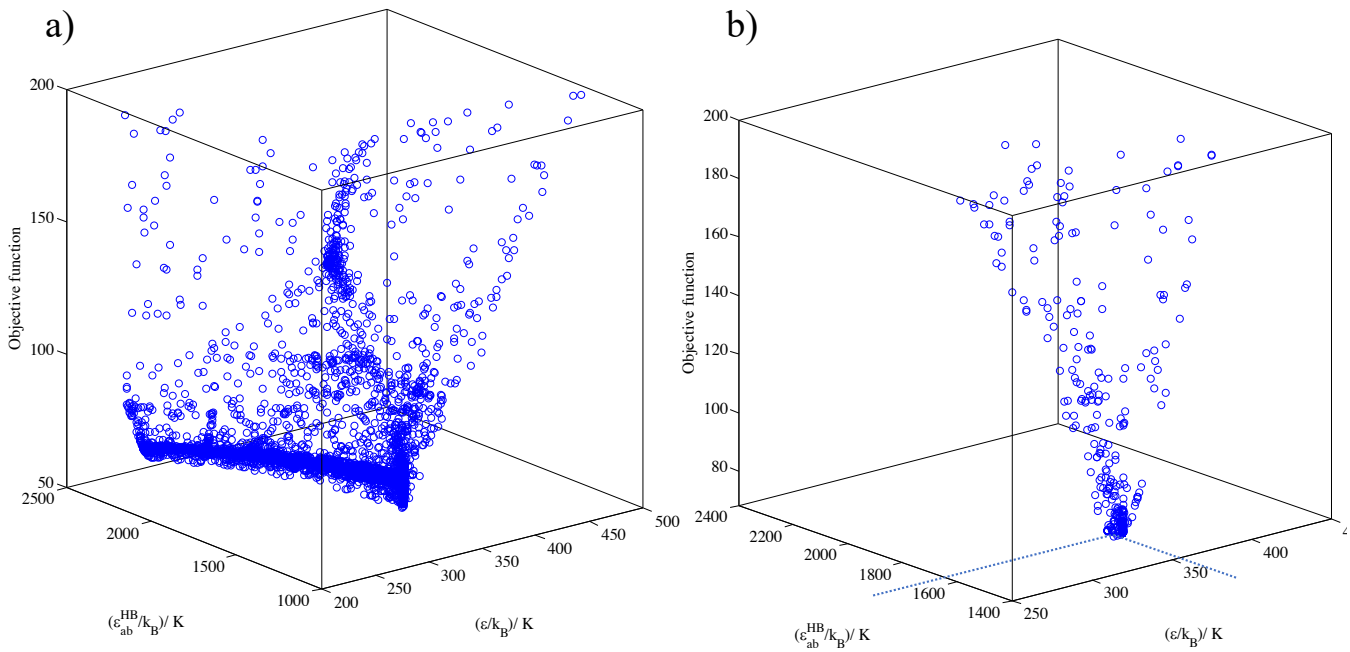

Figure 44: The weighted-sum objective function for non-spherical water models where we use 10^4 initial guesses (Sobol' points) for the optimization. Each blue open circle represents a local optimum that is obtained as a result of solving WSP($\boldsymbol{w}$) with a different initial guess, and we plot the objective function against two parameters, ϵ and $\epsilon_{e,H}^{HB}$. The objective function corresponds to an equal weighting for each property. In a), we include ρ_L^{sat} and P^{vap} only as experimental data types. In b), we also include C_P.

In Figure 45, we show the Pareto front in a contour plot, along with the corresponding AADs for each parameter. Note that when we plot the Pareto front in 3 dimensions, we show the inner edge of Z^{in} without addition of the ordering cone, which is equivalent to plotting the facets of the convex hull of P^{vap} which consist of only positive inward-facing normals. This is to ensure that models in-between the Pareto points may be determined from the convex combinations of the parameters at the facet vertices. The information on each Pareto point is tabulated in Table 18. We first note that the Pareto points are evenly distributed throughout the Pareto front and the Pareto front appears to be convex since there are no obvious regions with large gaps. Thus, the sandwich algorithm has worked efficiently in choosing a series of weight vectors in WSP($\boldsymbol{w}$). The Pareto front shows the trade-offs that are involved in choosing a particular model, and it is clear that the three objectives are indeed conflicting. We also show the Pareto-optimal solutions of the two dimensional MOP when heat capacity is not considered in the objective function. These models do not show on the 3D front because the gradients between objective functions are extremely steep within this area, and hence the models become non-dominated with respect to the specified ordering cone. There are clearly compromises that need to be made upon choosing a model from this Pareto front, as the regions with low to moderate curvature cover a fairly large region in objective space (e.g., 2-3% in AAD).

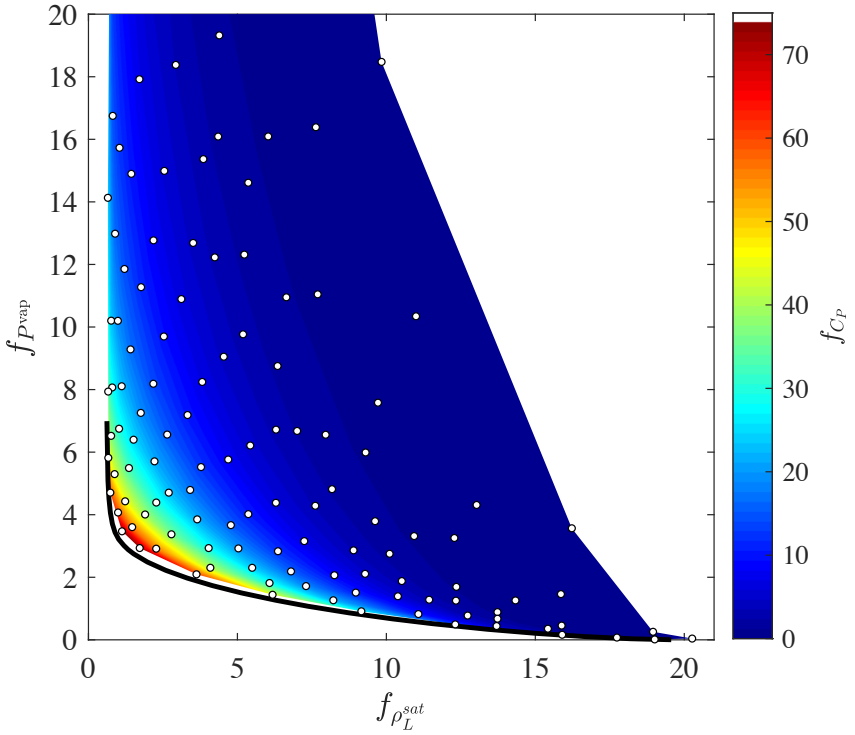

(a)

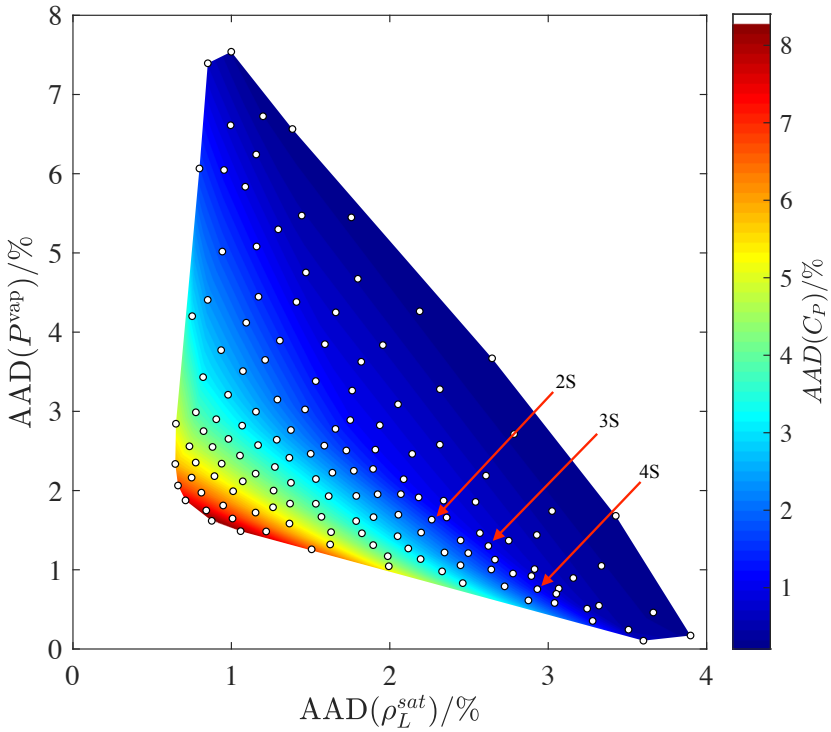

(b)

Figure 45: Pareto front for three objectives $f_{P^{vap}}$, $f_{\rho_L^{sat}}$ and f_{C_P} for spherical models of water. The open circles are the individual Pareto points calculated by the sandwich algorithm. The black line corresponds to the Pareto curve when only $f_{P^{vap}}$ and $f_{\rho_L^{sat}}$ are considered, i.e., the blue curve in Figure 39a. The Pareto front is indicated by the coloured region. The white areas indicate either that there are no models with such combinations of objective function values or that such models are dominated. The red arrows and their labels refer to the models that we will analyse further as described in section 4.4.3.1.

In Figure 46 we show the Pareto front for the non-spherical water models for the three objective scenario, and we display information for each Pareto point in Table 19. The surface is extremely steep at the inner edge, so we also show the same Pareto front by swapping the f_{C_P} and f_P coordinate axes in Figure 47. This steepness provides a good indication that C_P as a data type is highly suited for reducing the parameter degeneracy, since providing very small weighting to heat capacity leads to a highly accurate prediction of this property with a negligible decrease in the quality of the vapour pressure and saturated liquid density prediction. We also note that all of the parameters are within a relatively small range. The non-spherical models can be used to predict all three properties extremely well (all properties to within 0.8 % AAD), and the deviations are well below those attainable with the spherical water models. We also notice that in some regions of the Pareto front, heat capacity is not conflicting with the other two objectives. For example, in the region where $f_{\rho_L^{sat}}$ is close to 1, the 3D Pareto front essentially coincides with the 2D Pareto front where C_P is not considered in the objective function. If we consider the 2D Pareto point number 7 in Table 17 with an AAD(P^{vap}) of 0.7 % in vapour pressure, the corresponding AAD(C_P) is approximately 5%. We can choose a model that does equally well in terms of vapour pressure and saturated liquid density but with an AAD in C_P of 0.2% with a small weighting given to C_P of 0.07 (Pareto point 9 in Table 19). In Figure 47, this region where C_P does not conflict with the other two objectives is visible where $f_{\rho_L^{sat}}$ is approximately 1 due to the white area above this value. Points in this region of the Pareto front are dominated due to the limit of steepness defined in the ordering cone C, rather than the surface being non-convex in this area. Although not shown here, we were able to obtain Pareto-optimal points within this region by specifying a very small value for w_{C_P}.

In Table 19 it can be seen that the values of m vary only slightly above unity (between 1.12 and 1.33), and the parameter converges to a value only slightly above unity and close to what we would expect from the quantum mechanical predictions ($m = 1.1$) of Sheldon et al. (2006).

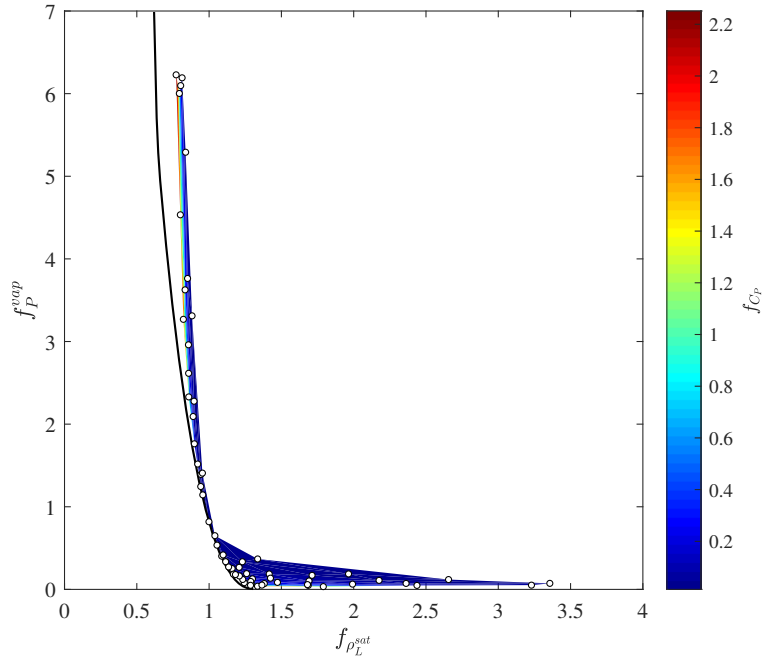

(a)

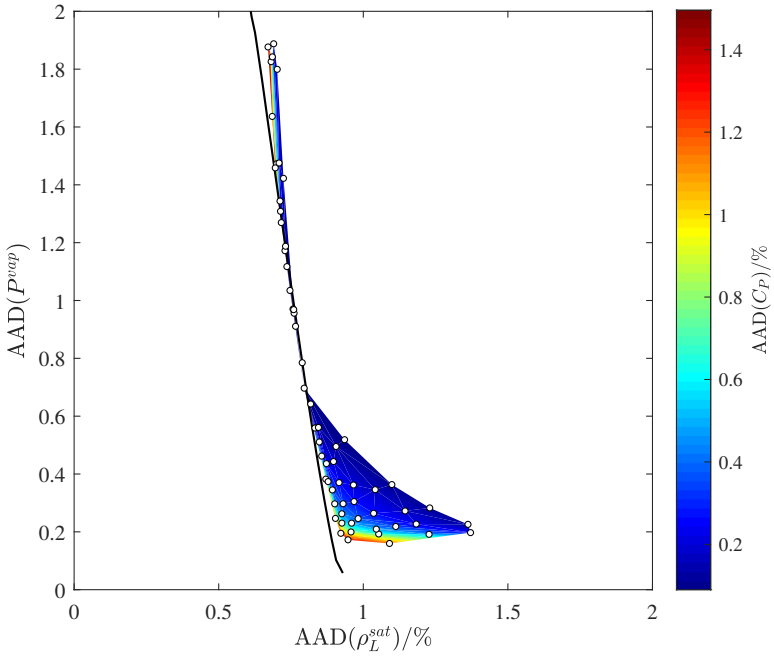

(b)

Figure 46: Pareto front for three objectives $f_{P^{vap}}$, $f_{\rho_L^{sat}}$ and f_{C_P} for spherical models of water. The open circles are the individual Pareto points calculated by the sandwich algorithm. The black line corresponds to the Pareto curve when only f_P and $f_{\rho_L^{sat}}$ are considered, i.e., the blue curve in Figure 39a. The Pareto front is indicated by the coloured region. The white areas indicate either that there are no models with such combinations of objective function values or that such models are dominated.

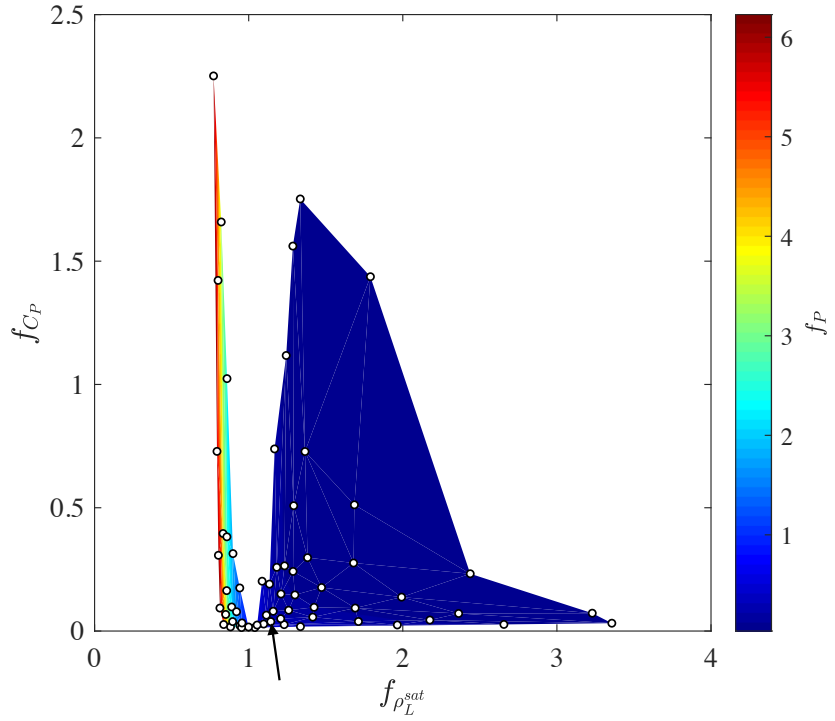

(a)

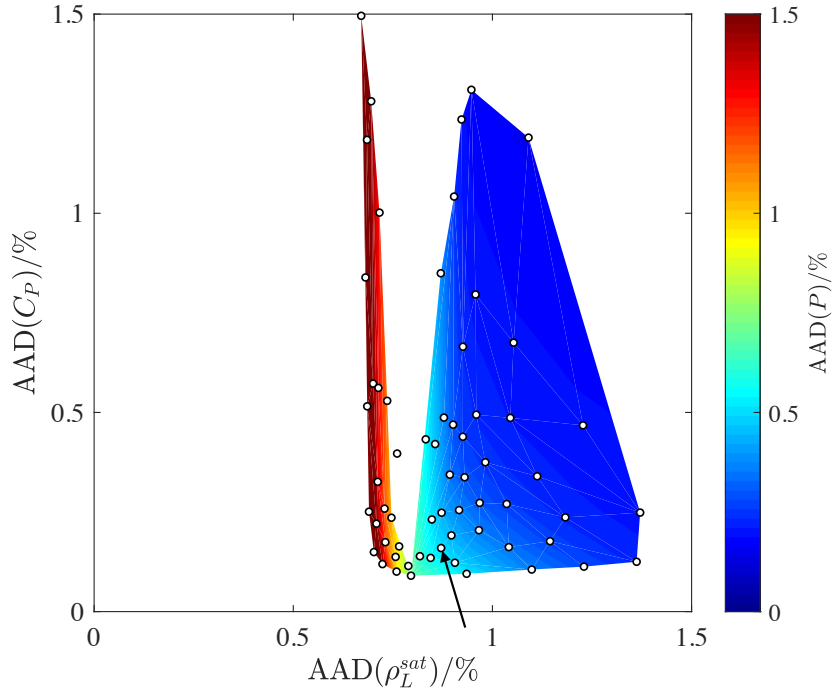

(b)

Figure 47: Pareto front for three objectives $f_{P^{vap}}$, $f_{\rho_L^{sat}}$ and f_{C_P} for non-spherical models of water. The open circles are the individual Pareto points calculated by the sandwich algorithm. The black line corresponds to the Pareto curve when only f_P and $f_{\rho_L^{sat}}$ are considered, i.e., the blue curve in Figure 39a. The Pareto front is indicated by the coloured region. The white areas indicate either that there are no models with such combinations of objective function values or that such models are dominated. The black arrows indicates model 5NS as detailed in section 4.4.3.1. Note that this figure differs from Figure 46 in that we have swapped the C_P and P^{sat}.

4.4.3.1 *Choice of Pareto point*

There is no rigorous way of defining the process in which a Pareto point should be chosen. This is partly due to each Pareto point being equally optimal to the MOP from a mathematical perspective. However, in practical scenarios the decision maker tends to choose points "in the middle and near the bulge" of the Pareto front Das (1999). Among other methods, a simple yet effective way of characterising a point on this "bulge" is to find the Pareto point that minimizes the Euclidean distance between the utopia point (a vector with the minimum value of each objective in the set of non-dominated solutions) (Cheikh et al., 2010) and the Pareto point. We therefore assign a distance measure, d_k, to each Pareto point P_k according to:

$$d_k = \sqrt{\sum_{j=1}^{N_P} (P_{kj} - u_j)^2}. \tag{100}$$

where u_j is the minimum value of objective j in the non-dominated set and P_{kj} represents the jth index of Pareto point P_k. d_k represents the distance between each Pareto point P_k and the Utopia point $\boldsymbol{u}$. Using this metric we can rank the Pareto points. However, since some Pareto points present unphysical thermodynamic behaviour, the models that we recommend in this work, P_{ref} are determined by finding P_k that corresponds to the result of the optimization:

$$\begin{aligned} &\underset{k}{\text{minimize}} && d_k \\ &\text{subject to} && \text{model is physical} \end{aligned}$$

The specification that the model should produce physical results refers to the anomolalies seen in the saturated density envelope which is discussed further in the appendix to this chapter (Section 4.6.2). We will now select some interesting models for further analysis. Information on these points can be found in Table 15.

1. Model 1L: The existing SAFT-VR Mie model for water in the literature (Dufal et al., 2015b).

2. Model 2S: The model that corresponds to the minimum d_k for the three-dimensional Pareto front for spherical water models.

3. Model 3S: The model that is obtained with an equal weight vector for the three-dimensional Pareto front for spherical water models. This point is chosen since this weight vector may typically be chosen *a priori*.

4. Model 4S: A model chosen from three-dimensional Pareto front for spherical water models that does not show anomalous vapour density behaviour near the critical point. Model 4S corresponds to P_{ref}, and is obtained by ranking the Pareto points according to Equation 100 and finding the lowest ranked model (rank 28) that does not exhibit a non-convex density phase envelope.

5. Model 5NS: The model that corresponds to P_{ref} for the three-dimensional Pareto front for non-spherical water models. This is the only non-spherical model shown because the model obtained with an equal weight vector is

essentially indistinguishable with Model 5NS when plotting the thermodynamic properties.

These models are indicated with arrows on the Pareto front in figures 45 and 47. By visual inspection, the reference points offer a good compromise between the three objectives.

Table 15: Models that are chosen for further analysis. The models are labelled with 'L' representing the literature model (Dufal et al., 2015b), 'S' representing spherical models picked from the three-dimensional Pareto front and 'NS' representing the non-spherical model picked from the three-dimensional Pareto front. The number in brackets indicates the model number as defined in Tables 16 and 17.

	w_i			f_i			AAD%(i)			Parameters, $\boldsymbol{x}$					
Model	ρ_L^{sat}	P^{vap}	C_P	ρ_L^{sat}	P^{vap}	C_P	ρ_L^{sat}	P^{vap}	C_P	m	(ϵ/k_B)/K	σ/Å	λ^r	$K^{HB}_{e,H}$/Å^3	$(\epsilon^{HB}_{e,H}/k_B)$/K
1L	-	-	-	2.62	2.40	120.52	1.06	1.28	10.52	1	266.68365	3.00627	17.02	101.685286	1985.44
2S (110)	0.42	0.33	0.25	7.61	4.29	3.35	2.26	1.63	1.66	1	415.14880	3.09142	30.41234	171.01197	1624.33576
3S (124)	0.33	0.33	0.33	10.11	2.75	1.82	2.62	1.30	1.06	1	419.76158	3.09607	27.89070	160.65411	1610.56455
4S (136)	0.23	0.70	0.08	12.73	0.78	3.07	2.93	0.76	1.71	1	406.56050	3.09117	23.09716	137.86527	1640.14137
5NS (29)	0.19	0.22	0.59	1.14	0.34	0.04	0.87	0.50	0.16	1.25656	351.23210	2.80242	25.12615	177.6236	1630.62645

We note that the parameters obtained in this study are somewhat different to those obtained by Dufal et al. (2015a), however, they are physically reasonable and are well within the range of values for other SAFT models for water found in the literature. In comparison with model 1L, the other models have a significantly higher value of ϵ (400 K for the spherical models) and 351 K for model 5NS, vs 267 K for model 1L. $\epsilon^{HB}_{e,H}$ is noticeably lower, with the models developed in this work all having values 1600 K compared with 1985 K in model 1L. This may indicate that the additional C_P data provides suitable information on how the dispersive and associative forces are distributed. λ^r is higher for the models obtained in this work compared to model 1L (values above 23 compared with 17 in the literature model). The values of σ are similar for the spherical models with m slightly above 3 Å, but the non-spherical model has a slightly lower value of 2.80 Å. The models obtained in this work all have a higher value of λ^r compared with the literature model (1L).

We proceed by analysing these water models by looking at the prediction of various thermodynamic properties, including the properties that are not considered in the parameter estimation. In Figure 48a, we show the level of agreement between the models and the experimental data for the saturated liquid density and saturated vapour densities. We see that models 2S, 3S and 4S all under-predict the saturated liquid density at temperatures between the triple point and 500 K, with a maximum relative deviation of 3% with respect to the experimental data at 350 K. Models 1L and 5NS are in better agreement with the experimental data in this temperature range, with a maximum relative deviation less than 0.5% for both models. We also note that all models have a similar curvature close to the experimental triple point, and none of these models are able to capture the experimentally observed maximum in the saturated liquid density at 273 K.

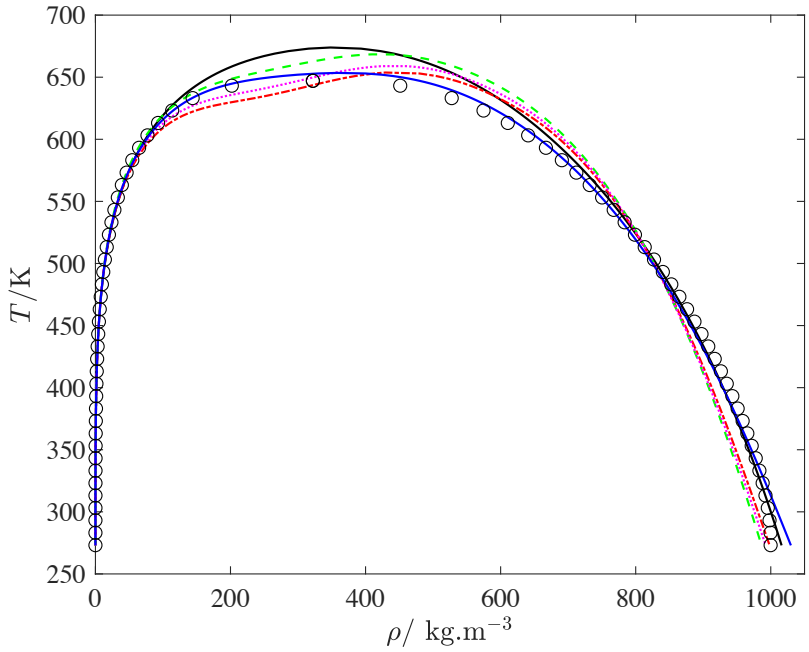

(a)

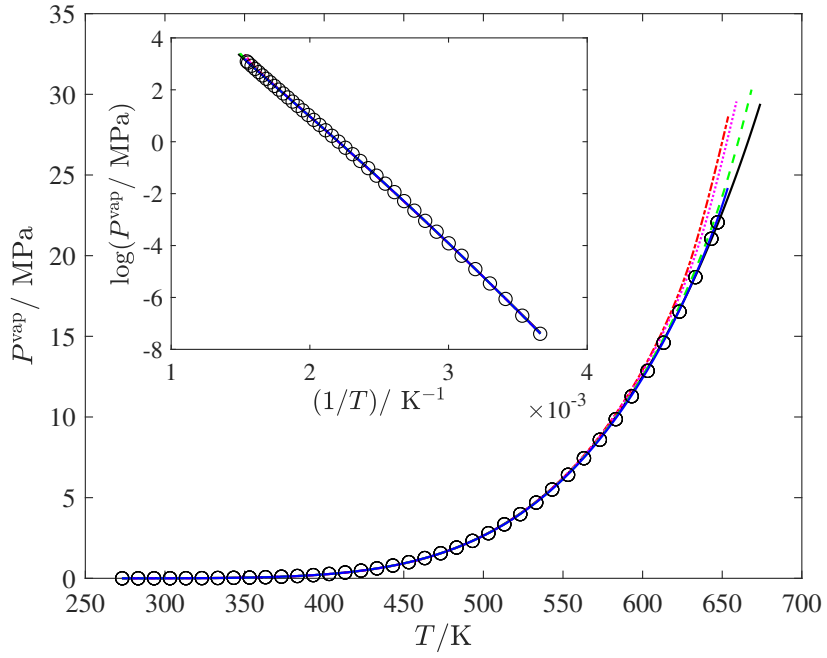

(b)

Figure 48: Model calculations vs experimental data for (a) Saturation densities of the vapour and liquid phase and (b) Vapour pressure (including the Clausius-Clapeyron representation) for models 1L, 2S, 3S, 4S and 5NS. Model 1L is the black solid curve, model 2S is the red dot-dashed curve, model 3S is the dotted magenta curve, model 4S is the dashed green curve and model 5NS is the solid blue curve. The open circles are the correlated experimental data from E.W. Lemmon and Friend (2018). These are the precise points used in the parameter estimation, apart from those above 95% of the critical temperature.

Models 2S and 3S show anomalous behaviour near the critical point. In section 4.6.2 we explain why this behaviour occurs and suggest some possible implementations to avoid generating such models. We characterise this 'anomalous' behaviour by saying that the phase envelope is non-convex. These models may not be desirable if one wishes to calculate thermodynamic properties close to the critical point, since the critical density is over-estimated and there is a large over-prediction of the vapour density in the near-critical region. Model 3S is obtained with an equal weight vector (typically chosen *a priori*). This analysis demonstrates that MOO provides a useful means of generating a set of numerous Pareto-optimal models from which models can be discriminated.

We propose model 4S as a suitable alternative to models 2S and 3S, as it ranks the best according to our definition of P_{ref}. In section 4.6.2 we discuss the reason behind this anomaly and suggest some possible implementations to avoid obtaining these models. Models 1L, 2S, 3S, 4S and 5NS predict the experimental critical temperature to 4.0%, 1.7%, 3.2%, 0.9% and 0.9% respectively. Model 5NS captures the near critical region much more accurately than the other models since it provides the correct curvature of both the saturated liquid and vapour densities and is quantitatively accurate between 500 K and 600 K with a maximum deviation of 0.17% at 600 K.

In Figure 48b we show the description of the vapour pressure. All models show a fairly good agreement with the experimental data and the models are indistinguishable from the experimental data in the Clausius Clapeyron representation. The only noticeable deviations are those given by models 2S and 4S in the near-critical region. These models over-predict the critical pressure by 17.5% and 24.7% respectively.

In Figure 49a we show the model description of the isobaric heat capacity along a single isobar (1 atm), and in Figure 49b we show the saturated liquid heat capacity between the experimental triple point and temperatures close to the experimental critical point. Model 1L under-predicts the heat capacity by an average of 10.5% across the isobar, with the highest deviation at 273 K (15 %). Models 2S, 3S, 4S and 5NS provide a very good agreement with the experimental heat capacity at 1 bar; model 5NS has the lowest average deviation of AAD (C_P) = 0.16%. Models 2S, 3S, 4S and 5NS are all able to predict a low temperature minimum in the saturated liquid heat capacity in contrast to model 1L. Model 5S is able to predict the temperature at which this minimum occurs with remarkable accuracy.

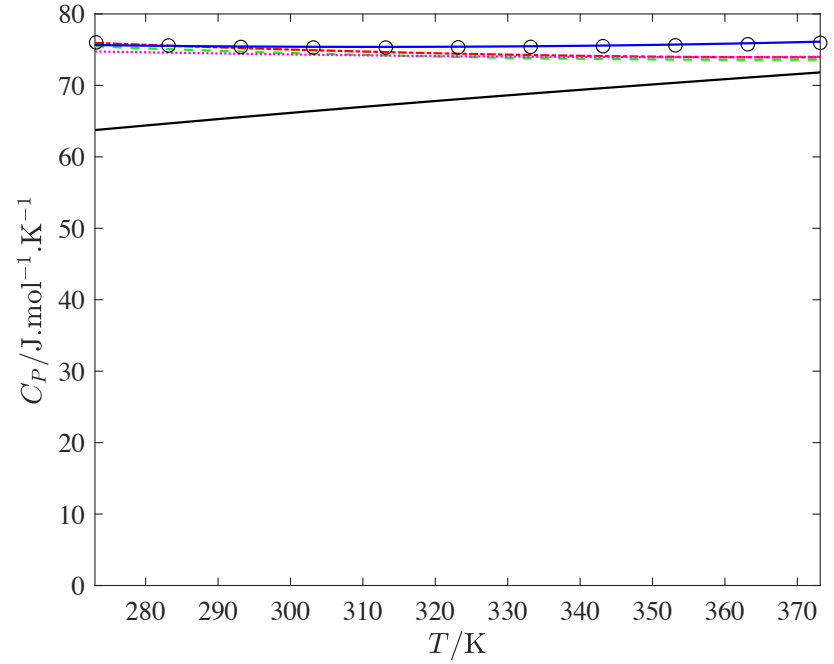

(a)

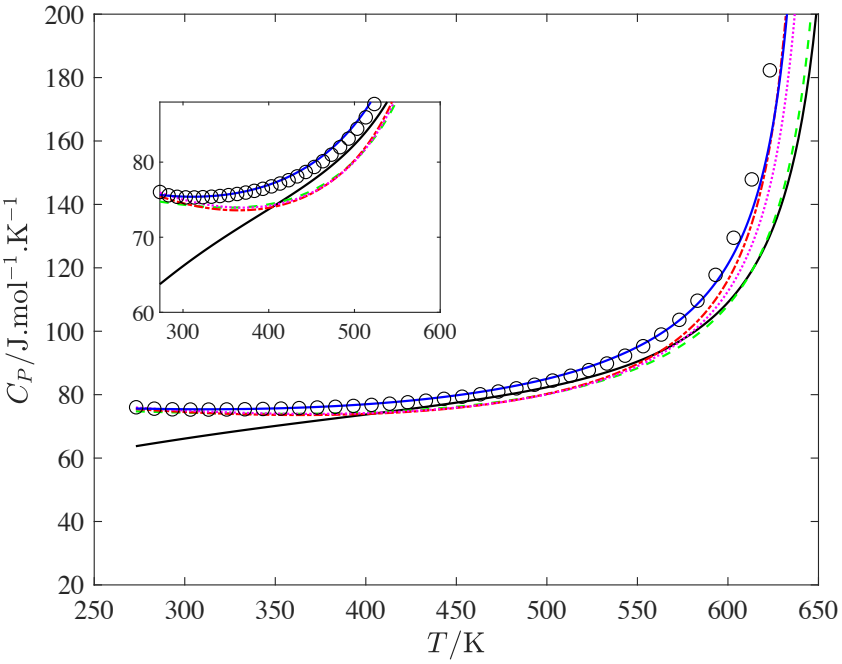

(b)

Figure 49: Model calculations and predictions vs experimental data for (a) liquid isobaric heat capacity at 1 atm and (b) saturated liquid heat capacity. Model 1L is the black solid curve, model 2S is the red dot-dashed curve, model 3S is the dotted magenta curve, model 4S is the dashed green curve and model 5NS is the solid blue curve. The open circles are the correlated experimental data from E.W. Lemmon and Friend (2018). The experimental data in (a) are the precise data points used in the parameter estimation.

In Figure 50, we show the predictions of the different models for the heat of vaporization; this property type was not included in the parameter regression. All models predict the property accurately away from the critical temperature. Models 2S and 3S show anomalous behaviour at near-critical temperatures.

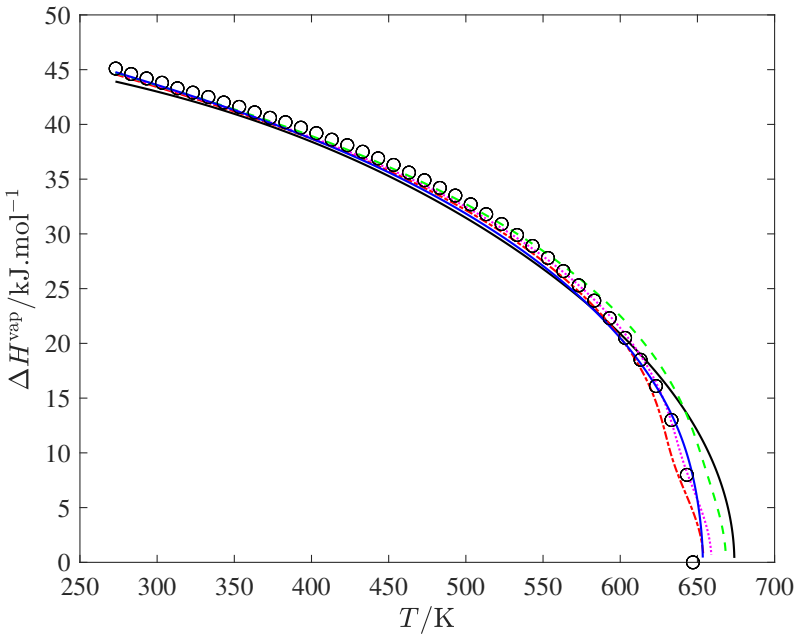

Figure 50: Model predictions vs experimental data for the heat of vapourization. Model 1L is the black solid curve, model 2S is the red dot-dashed curve, model 3S is the dotted magenta curve, model 4S is the dashed green curve and model 5NS is the solid blue curve. The open circles are the correlated experimental data from E.W. Lemmon and Friend (2018). The experimental data in (a) are the precise data points used in the parameter estimation.

In Figure 51, we show the predictions of the different models for the vapour-liquid interfacial tension, using the SAFT-VR Mie MF DFT derived in chapter 6, which requires no adjustable parameters. This property provides a stringent test of the models in terms of the way the dispersion (long-range) and association (short-range) forces are partitioned. Models 2S, 3S and 4S are able to predict the near-critical interfacial tensions well, but they over-predict the interfacial tension at lower temperatures. Model 1L performs worse in the near-critical region and performs the worst in describing the temperature dependence of the interfacial tension, with moderate (0.05 $\mathrm{N.m}^{-1}$) under-predictions at the lowest temperatures considered. Model 5NS is quantitatively accurate over the range of temperatures considered.

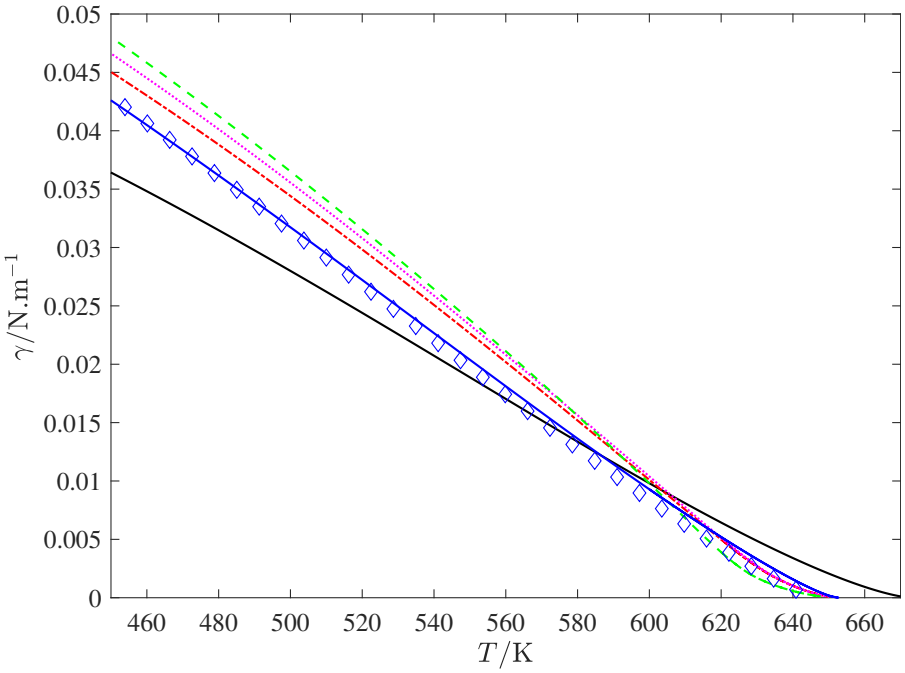

Figure 51: The vapour-liquid interfacial tension of water for the various water models, calculated using the SAFT-VR Mie DFT MF theory derived in chapter 6. The blue diamonds are the correlated experimental data from NIST (E.W. Lemmon and Friend, 2018). Model 1L is the continuous black line, model 2S is the red dot-dashed line, model 3S is the dotted magenta line, model 4S is the dashed green line and model 5NS is the continuous blue curve.

Due to the superior description of model 5S, we will assess it further by evaluating some other thermodynamic properties not considered in the parameter regression, to ensure that the parameters are physically sound. In figures 52 and 53, we show the property predictions of density, isobaric heat capacity, speed of sound and isochoric heat capacity over pressures varying by several orders of magnitude. The single phase densities are predicted accurately apart from the curvature in the low temperature region. The heat capacity in the liquid and vapour phase is predicted very well over the full pressure range (varying by several orders of magnitude), and the model is able to capture the C_P maximum, which is more pronounced at near-critical/ super-critical pressures. The speed of sound in the liquid phase is not predicted well (e.g., it over-predicts the speed of sound by approximately 85% at 273 K). This is due to the inability for any model to capture the correct curvature of the saturated liquid density at low temperatures. The isochoric heat capacity is predicted moderately well, with an average AAD of 17% across the full temperature range.

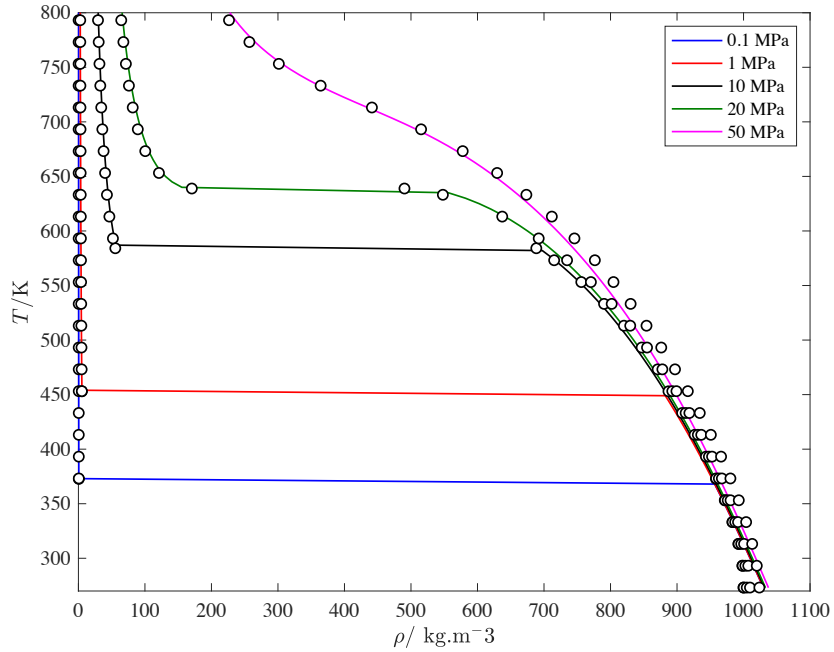

(a)

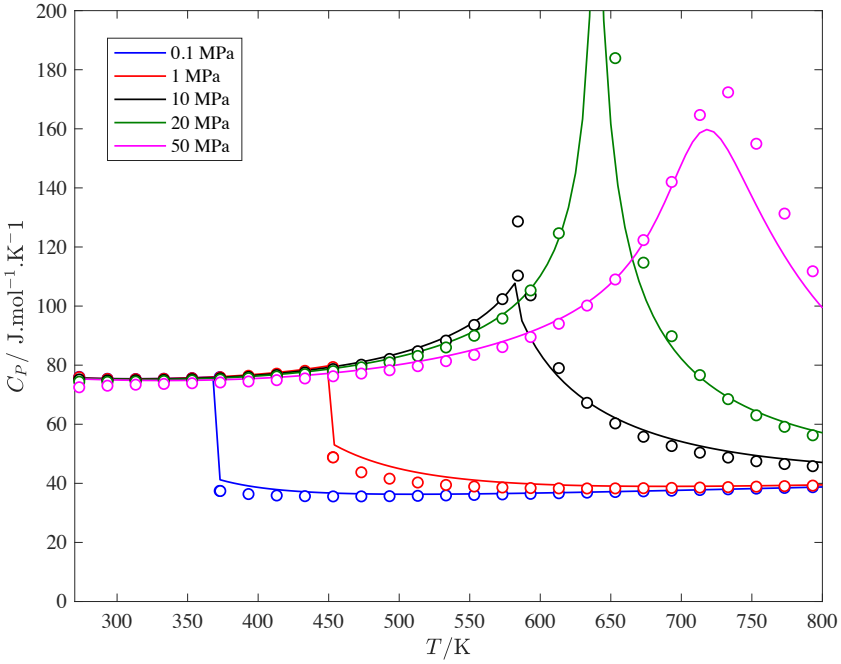

(b)

Figure 52: Isobaric properties for the newly developed water model (model 5NS). The coloured lines indicate the model predictions and the circles are the values taken from NIST (E.W. Lemmon and Friend, 2018). (a) Single phase density. (b) Isobaric heat capacity.

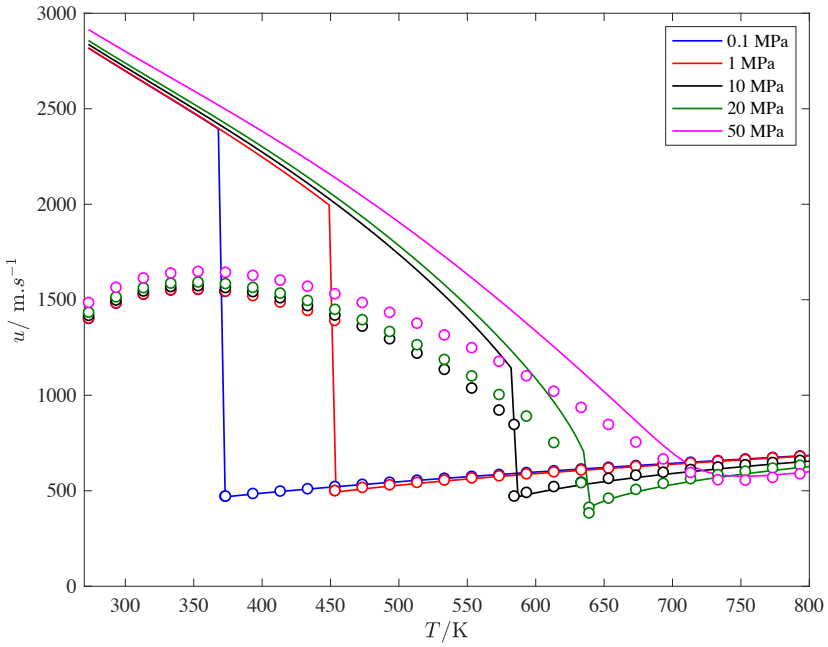

(a)

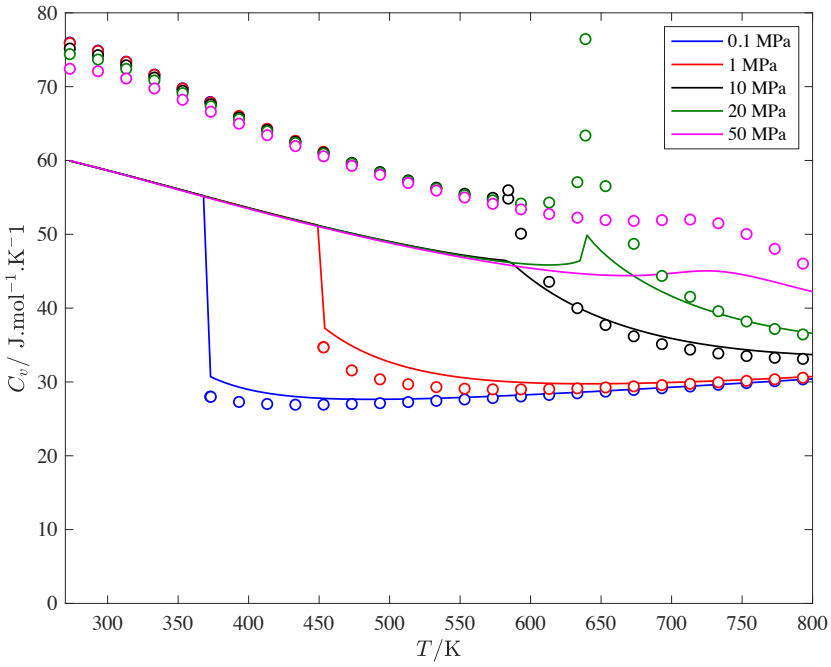

(b)

Figure 53: Isobaric properties for the newly developed water model (model 5NS). The coloured lines indicate the model predictions and the open circles are the values taken from NIST (E.W. Lemmon and Friend, 2018) (colours indicated in the legend). (a) Speed of sound, u. (b) Isochoric heat capacity, C_v.

As discussed in section 4.1, the degree of hydrogen bonding is frequently analysed against spectroscopic data when modelling SAFT models for water. The fraction of total possible O-H hydrogen bonds that are free, f_{free}^{OH} is given in Figure 54.

This is calculated from the fraction of association sites of type e and H not bonded, which is solved for implicitly in the SAFT EoS:

$$f_{free}^{OH} = X_H = X_e, \tag{101}$$

where X_H and X_e are the non-bonded fractions for H and e association types respectively. The reader is referred to the work of Clark et al. (2006) for a more detailed discussion on the derivation of Equation 101. It is gratifying to see that model 5NS is in remarkable agreement with the molecular simulations. This gives us some confidence that the balance between dispersive and association forces is physically sound, as the fraction of sites that are bonded is directly related to the hydrogen-bonding energy and volume.

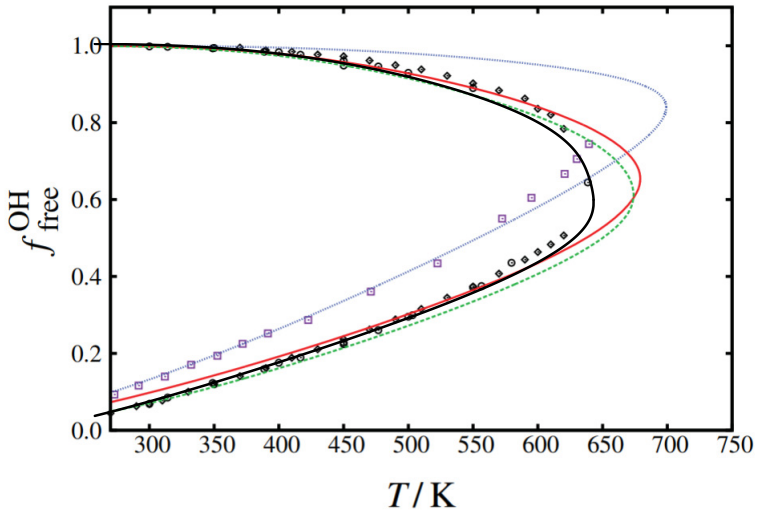

Figure 54: The fraction of free OH hydrogen bonds, f_{free}^{OH} for the vapour and liquid states of water. The black curve is the fraction of free hydrogen bonds predicted by the newly developed water model (Model 5NS). For comparison, we also plot the model of Dufal et al. (2015a) that uses the LJ kernel (Model 1L) (green dashed curve), the model of Dufal et al. (2015a) that uses the Mie kernel (red solid curve), the SAFT-VR SW model of Clark et al. (2006) (blue dotted curve). The purple squares are the spectroscopic data of Luck (1980). The black symbols are simulation results of Dufal et al. (2015a) using the SPC/E (circles) and TIP4P/2005 (diamonds) force fields. This figure is a modification of that of Dufal et al. (2015a).

4.5 CONCLUSION

In summary, we have extended on the novel work of Forte et al. (2018) by conducting multi-objective optimizations with more than one property type, and have shown how this approach is beneficial over the typical approaches used in the determination of equation of state parameters.

We have demonstrated how a multi-objective optimization approach can be used to parametrise equations of state. Careful attention was been paid towards the choice of an approach that best suits this cause, including minimizing the computational effort involved and providing a framework that can be retrofitted to

existing parameter estimation methods. We have applied the method for two and three dimensional problems, but the algorithm we propose is generally applicable to any number of dimensions. This allows for an efficient estimation of the Pareto front where numerous property types may be considered as competing objectives. We have demonstrated that this technique may be used as a platform for the rigorous comparison between different model types.

We applied the MOO technique to the development of water models for the SAFT-VR Mie EoS, and considered models where water is treated as a spherical model ($m=1$), or non-spherical by treating the number of segments, m, as an adjustable parameter. The technique provided numerous different Pareto-optimal models for water which may be used for further evaluation. By analysing the Pareto front and predictions of various thermodynamic properties, we identified that the most preferable non-dominated models were determined using a weight vector that would not typically be chosen *a priori* (e.g., not an equal weight vector). For the MOP we considered three property types as competing objectives: saturated liquid density (ρ_L^{sat}), vapour pressure (P^{vap}), and liquid isobaric heat capacity (C_P). It was shown that if only ρ_L^{sat} and P^{vap} are considered in the optimization problem (as is typically the case in regressing EoS parameters), a variety of non-dominated models are obtained and which predict C_P with varying degrees of accuracy (some accurate and some not). This exemplifies that producing a Pareto front using an MOO approach is a useful way of generating candidate models which can be tested against other properties not considered in the parameter regression.

We then considered the three-dimensional MOP which included the three properties ρ_L^{sat}, P^{vap} and C_P as objective functions. We showed that C_P is a particularly useful property for reducing the parameter degeneracy in this case, and that one is able to maintain a good description of C_P without compromising the quality of the prediction of ρ_L^{sat} and P^{vap}. The three-dimensional Pareto fronts were computed and preferable models were chosen through analysis of these fronts. We found that the non-spherical water model (5NS) outperforms the spherical models derived in this work (models 2S, 3S and 4NS) for all of the thermodynamic properties considered. The models developed when including C_P are able to capture the key thermodynamic properties better than the literature model (1L of Dufal et al. (2015b), which describes C_P relatively inaccurately), without compromising the description of ρ_L^{sat}, P^{vap}.

In further work, it would be useful to explore the effect of adding additional thermodynamic properties to the parameter estimation. It will be particularly useful to investigate the effect of including different second derivative properties, e.g., the speed of sound or isochoric liquid heat capacity in the MOO. Since the proposed MOO technique is applicable to dimensions higher than three, it will be useful to investigate the Pareto fronts obtained when a larger number of properties (or objective functions) are included. Furthermore, it will be useful to see the effect of including mixture properties at an earlier stage of the parameter development.

4.6 APPENDIX

4.6.1 *Tabulated Pareto points*

Table 16: Pareto-optimal models for spherical models of water ($m = 1$), when only $f_{\rho_L^{sat}}$ and $f_{P^{vap}}$ are treated as objectives. We also provide the deviations in C_P. The columns are sorted with $f_{\rho_L^{sat}}$ in increasing order.

	w_i			f_i			AAD%(i)			Parameters, x					
Pareto point	ρ_L^{sat}	P^{vap}	C_P	ρ_L^{sat}	P^{vap}	C_P	ρ_L^{sat}	P^{vap}	C_P	m	(ϵ/k_B)/K	σ/Å	λ^r	$K_{e,H}^{HB}$/Å^3	$(\epsilon_{e,H}^{HB}/k_B)$/K
1	0.9901	0.0099	0.0000	0.6194	6.9906	52.4530	0.5905	2.1887	7.0610	1	337.80287	3.03114	28.25278	147.08527	1840.58221
2	0.9616	0.0384	0.0000	0.6550	5.0907	64.7120	0.6204	1.9510	7.8490	1	328.31646	3.02607	26.88362	143.95944	1857.10720
3	0.9267	0.0733	0.0000	0.6876	4.5189	74.9030	0.6480	1.8467	8.4340	1	318.42870	3.02106	25.29042	137.44404	1880.16773
4	0.8741	0.1259	0.0000	0.7364	4.0619	87.3960	0.6840	1.7517	9.0220	1	306.88405	3.01552	23.56082	129.91951	1907.25622
5	0.8004	0.1996	0.0000	0.8033	3.7071	100.3040	0.7237	1.6721	9.6610	1	294.44697	3.00995	21.87371	122.29255	1935.95367
6	0.6971	0.3029	0.0000	0.8927	3.4351	111.0290	0.7665	1.6054	10.1700	1	283.92050	3.00609	20.49043	116.05522	1959.13400
7	0.5852	0.4148	0.0000	1.0140	3.2155	119.1040	0.8127	1.5488	10.5090	1	275.18560	3.00363	19.36393	110.97833	1977.48461
8	0.5000	0.5000	0.0000	1.1923	3.0124	114.2610	0.8802	1.4975	10.2860	1	278.38985	3.00784	19.23058	111.01864	1968.60269
9	0.4471	0.5529	0.0000	1.3328	2.8831	121.1450	0.9191	1.4604	10.5620	1	271.38001	3.00598	18.43544	107.29818	1983.02618
10	0.4002	0.5998	0.0000	1.5199	2.7475	118.8330	0.9725	1.4233	10.4400	1	272.52796	3.00816	18.26557	106.86603	1979.14882
11	0.3282	0.6718	0.0000	1.9784	2.4878	115.2320	1.0941	1.3520	10.3090	1	272.82700	3.01162	17.79038	105.19051	1975.79311
12	0.2774	0.7226	0.0000	2.5976	2.2211	109.5830	1.2423	1.2752	10.0370	1	275.05570	3.01619	17.43385	104.10442	1967.92583
13	0.2389	0.7611	0.0000	3.3213	1.9723	102.0180	1.4091	1.2000	9.7090	1	279.87340	3.02155	17.28108	103.97918	1954.51768
14	0.2067	0.7933	0.0000	4.1621	1.7331	94.8840	1.5841	1.1223	9.3810	1	283.68725	3.02633	17.05033	103.35989	1943.15761
15	0.1817	0.8183	0.0000	5.1357	1.4994	85.7140	1.7757	1.0413	8.8730	1	289.93519	3.03195	16.97441	103.48767	1926.46549
16	0.1602	0.8398	0.0000	6.2878	1.2653	72.6770	1.9977	0.9579	8.1860	1	300.83182	3.03935	17.17551	104.99422	1899.64923
17	0.1407	0.8593	0.0000	7.3675	1.0736	66.5060	2.1755	0.8776	7.8200	1	304.85362	3.04354	16.96611	104.23066	1887.73446
18	0.1246	0.8754	0.0000	8.7460	0.8624	54.7030	2.3886	0.7844	7.0530	1	315.19019	3.05012	17.08512	105.13793	1861.65890
19	0.1088	0.8912	0.0000	10.1938	0.6715	42.8890	2.5931	0.6901	6.3230	1	326.33165	3.05670	17.24536	106.13407	1833.72872
20	0.0945	0.9055	0.0000	11.5457	0.5170	32.8000	2.7710	0.6034	5.5560	1	337.28783	3.06262	17.43693	107.16714	1806.39249
21	0.0807	0.9193	0.0000	13.3992	0.3371	19.2640	2.9982	0.4872	4.2440	1	356.71533	3.07200	17.99663	109.97873	1758.92134
22	0.0667	0.9333	0.0000	15.0471	0.2059	9.5340	3.1857	0.3820	3.0430	1	374.43513	3.07992	18.50414	112.34087	1714.95475
23	0.0514	0.9486	0.0000	16.6635	0.1038	3.5050	3.3585	0.2737	1.7210	1	394.07641	3.08829	19.12669	115.12702	1665.66220
24	0.0335	0.9665	0.0000	18.1875	0.0352	1.1050	3.5123	0.1618	0.4500	1	415.04273	3.09678	19.84072	118.21748	1612.01748
25	0.0099	0.9901	0.0000	19.5617	0.0035	2.9880	3.6441	0.0523	1.3710	1	437.19481	3.10538	20.66490	121.75049	1553.92136

Table 17: Pareto-optimal models for non-spherical models of water ($m \geqslant 1$), when only $f_{\rho_L^{sat}}$ and f_P are treated as objectives. We also provide the deviations in C_P. The columns are sorted with $f_{\rho_L^{sat}}$ in increasing order.

	w_i			f_i			AAD%(i)			Parameters, x					
Pareto point	ρ_L^{sat}	P^{vap}	C_P	ρ_L^{sat}	P^{vap}	C_P	ρ_L^{sat}	P^{vap}	C_P	m	(ϵ/k_B)/K	σ/Å	λ^r	$K_{e,H}^{HB}$/Å^3	$(\epsilon_{e,H}^{HB}/k_B)$/K
1	0.9901	0.0099	0.0000	0.6194	6.9883	52.0250	0.5904	2.1886	7.0730	1.00000	337.75987	3.03112	28.24623	147.05562	1840.69549
2	0.9798	0.0202	0.0000	0.6373	5.7063	57.4990	0.6041	2.0442	7.4160	1.00000	334.47266	3.02930	27.87635	147.35113	1844.03705
3	0.9690	0.0310	0.0000	0.6481	5.2840	61.5330	0.6136	1.9820	7.6770	1.00000	330.86469	3.02739	27.30268	145.51528	1851.44217
4	0.9560	0.0440	0.0000	0.6615	4.9475	63.6970	0.6258	1.9250	7.7770	1.00237	328.04744	3.02341	26.77826	143.97359	1856.12122
5	0.9468	0.0532	0.0000	0.7030	4.1577	51.1990	0.6494	1.7661	6.9870	1.02857	330.13712	2.99679	26.51523	146.76066	1835.48255
6	0.9392	0.0608	0.0000	0.7456	3.4518	36.4470	0.6712	1.6094	5.9060	1.05883	335.18845	2.96860	26.66534	152.06939	1804.62657
7	0.9304	0.0696	0.0000	0.7920	2.7810	24.0180	0.6946	1.4439	4.8070	1.09064	339.65932	2.93978	26.72327	157.38033	1773.53096
8	0.9189	0.0811	0.0000	0.8409	2.1768	13.4560	0.7180	1.2768	3.5790	1.12425	345.24842	2.91109	26.95946	164.17938	1737.41107
9	0.9066	0.0934	0.0000	0.8850	1.7131	6.8800	0.7385	1.1335	2.5710	1.15290	349.28501	2.88723	27.06414	169.71561	1707.85087
10	0.8914	0.1086	0.0000	0.9313	1.2993	2.6340	0.7597	0.9883	1.5860	1.18193	353.02710	2.86375	27.13743	175.37069	1678.21288
11	0.8709	0.1291	0.0000	0.9766	0.9625	0.4850	0.7794	0.8514	0.5910	1.21049	357.16610	2.84169	27.30995	181.81064	1647.03618
12	0.8450	0.1550	0.0000	1.0241	0.6731	0.2610	0.7996	0.7131	0.4050	1.23866	360.34800	2.82020	27.34463	187.57936	1618.31453
13	0.8075	0.1925	0.0000	1.0738	0.4349	2.0290	0.8213	0.5737	1.3660	1.26817	363.97545	2.79858	27.45117	194.37886	1586.67667
14	0.7523	0.2477	0.0000	1.1241	0.2535	5.1900	0.8432	0.4387	2.2370	1.29678	366.91760	2.77802	27.47369	200.71517	1557.14185
15	0.6638	0.3362	0.0000	1.1774	0.1205	9.7150	0.8664	0.3045	3.0290	1.32500	368.82805	2.75787	27.34959	206.10767	1530.64678
16	0.5960	0.4040	0.0000	1.2049	0.0732	12.3330	0.8784	0.2386	3.3660	1.33907	369.60073	2.74796	27.25961	208.64714	1517.84524
17	0.5000	0.5000	0.0000	1.2332	0.0382	14.5810	0.8907	0.1739	3.6830	1.35249	369.67963	2.73832	27.07443	210.27491	1507.73458
18	0.3192	0.6808	0.0000	1.2682	0.0126	16.5710	0.9060	0.1022	3.9700	1.36756	368.91007	2.72724	26.73373	210.97036	1499.17827
19	0.0099	0.9901	0.0000	1.3051	0.0044	16.9690	0.9292	0.0575	4.0240	1.37826	367.22287	2.71932	26.17634	209.07780	1496.33243

Table 18: Pareto points and parameters for water models where with $m = 1$. The columns are sorted with $f_{\rho_L^{sat}}$ in increasing order.

	w_i			f_i			AAD%(i)			Parameters, $\boldsymbol{x}$					
P_K	ρ_L^{sat}	P^{vap}	C_P	ρ_L^{sat}	P_{sat}	C_P	ρ_L^{sat}	P^{vap}	C_P	m	(ϵ/k_B)/K	σ/Å	λ^r	$K_{e,H}^{HB}$/Å^3	$(\epsilon_{e,H}^{HB}/k_B)$/K
1	0.9804	0.0098	0.0098	0.6517	14.1300	25.2830	0.6499	2.8436	4.9834	1	367.53841	3.04818	33.56824	164.62466	1774.31730
2	0.9494	0.0399	0.0108	0.6628	7.9364	34.8796	0.6459	2.3360	5.8595	1	361.58200	3.04495	32.92614	168.30664	1775.11750
3	0.8800	0.1102	0.0098	0.6664	5.8178	48.5804	0.6631	2.0639	6.8659	1	345.59187	3.03663	29.48471	156.03468	1812.52240
4	0.7777	0.2125	0.0098	0.7337	4.7058	60.4582	0.7105	1.8761	7.6107	1	332.18496	3.03049	26.69834	144.87712	1844.95346
5	0.8154	0.1611	0.0235	0.7607	6.5204	37.6405	0.7489	2.1637	6.0801	1	358.50354	3.04517	31.35607	164.56748	1779.18382
6	0.9113	0.0591	0.0296	0.7632	10.2025	23.7610	0.7352	2.5588	4.8673	1	377.46647	3.05490	36.14391	180.85571	1734.37307
7	0.9552	0.0098	0.0350	0.7733	33.0080	9.2640	0.7525	4.2015	3.0415	1	390.45510	3.06182	38.21938	175.05650	1729.54724
8	0.8430	0.1240	0.0330	0.7983	8.0673	28.6943	0.7748	2.3537	5.3372	1	370.68664	3.05199	34.01176	174.70272	1748.80367
9	0.9291	0.0287	0.0422	0.8151	16.7503	15.0339	0.7757	2.9879	3.8759	1	388.10231	3.06104	38.41947	184.60724	1716.34650
10	0.8881	0.0098	0.1021	0.8388	65.8909	2.6647	0.7984	6.0660	1.6236	1	400.83947	3.06840	39.53367	171.16408	1722.28340
11	0.7189	0.2583	0.0228	0.8780	5.2975	44.6224	0.8106	1.9739	6.5885	1	349.24593	3.04145	28.88369	155.31290	1801.47944
12	0.8818	0.0616	0.0566	0.8949	12.9829	16.7848	0.8244	2.7504	4.0952	1	387.90028	3.06186	38.07096	187.14218	1709.88976
13	0.9003	0.0278	0.0719	0.8965	23.8938	10.0560	0.8215	3.4318	3.1648	1	394.73430	3.06555	39.34556	184.85993	1706.21829
14	0.7091	0.0098	0.2811	0.9354	92.3154	0.5325	0.8511	7.3942	0.7062	1	405.25596	3.07184	38.92119	163.73707	1725.71258
15	0.8739	0.0212	0.1048	0.9401	37.8256	5.7241	0.8506	4.4073	2.3778	1	399.82207	3.06875	39.82501	181.13267	1705.04996
16	0.8223	0.1169	0.0608	0.9875	10.1984	19.4775	0.8810	2.5505	4.4119	1	384.49597	3.06090	36.63574	184.66905	1714.14202
17	0.6215	0.3641	0.0144	0.9933	4.0708	60.9243	0.8415	1.7493	7.6289	1	330.54564	3.03250	25.38992	140.40301	1847.45812
18	0.7341	0.2238	0.0421	1.0280	6.7488	29.9651	0.8933	2.1822	5.4468	1	368.01105	3.05256	32.17302	169.24478	1753.88890
19	0.8528	0.0602	0.0870	1.0424	15.7297	12.6042	0.9046	2.9003	3.5426	1	393.75167	3.06618	38.70085	188.24054	1698.22077
20	0.8378	0.0346	0.1276	1.0990	28.6982	6.6959	0.9354	3.7725	2.5662	1	400.52266	3.07024	39.58270	184.63964	1695.03693
21	0.7976	0.0232	0.1792	1.1092	47.0912	3.1832	0.9428	5.0175	1.7517	1	404.27868	3.07239	39.63630	178.04883	1700.43663

Table 18 Continued

	w_i			f_i			AAD%(i)			Parameters, x					
P_k	ρ_L^{sat}	P^{vap}	C_P	ρ_L^{sat}	P_{sat}	C_P	ρ_L^{sat}	P^{vap}	C_P	m	$(\epsilon/k_B)/K$	$\sigma/Å$	λ^r	$K_{e,H}^{HB}/Å^3$	$(\epsilon_{e,H}^{HB}/k_B)/K$
22	0.7540	0.1879	0.0581	1.1156	8.1056	23.0267	0.9387	2.3396	4.7925	1	378.45360	3.05861	34.38438	177.83569	1727.53435
23	0.5518	0.4384	0.0098	1.1259	3.4693	74.8018	0.8759	1.6181	8.4021	1	316.10525	3.02599	23.12063	130.18223	1881.91932
24	0.7269	0.0179	0.2551	1.1299	64.5210	1.4154	0.9537	6.0471	1.1498	1	406.18339	3.07359	39.17057	171.43850	1707.73228
25	0.8242	0.0510	0.1248	1.1992	20.9022	8.6144	0.9792	3.2097	2.9148	1	399.21583	3.07009	39.17561	187.38935	1690.26536
26	0.7988	0.1096	0.0915	1.2086	11.8553	14.5645	0.9815	2.6522	3.8100	1	392.18082	3.06636	37.72349	188.41622	1695.91795
27	0.6162	0.0160	0.3678	1.2268	74.0940	0.6601	0.9954	6.6117	0.7605	1	407.42564	3.07481	38.47438	166.75764	1711.31176
28	0.5994	0.3756	0.0249	1.2321	4.4280	46.4877	0.9480	1.8118	6.7082	1	345.76636	3.04213	27.11424	148.99007	1808.91810
29	0.4028	0.0098	0.5874	1.2371	91.4259	0.1420	0.9991	7.5397	0.3229	1	407.10232	3.07478	37.36208	158.93433	1723.54118
30	0.6375	0.3206	0.0419	1.3599	5.4924	32.6586	1.0110	1.9918	5.6709	1	363.11144	3.05187	30.00203	161.72254	1765.08853
31	0.7358	0.1775	0.0867	1.4126	9.2841	16.8757	1.0543	2.4421	4.1057	1	388.35290	3.06536	35.91562	184.10770	1702.29862
32	0.7828	0.0867	0.1306	1.4386	14.8970	10.2017	1.0681	2.8197	3.1722	1	398.71468	3.07095	38.46849	189.40948	1683.48647
33	0.7751	0.0498	0.1750	1.4462	24.9968	5.8813	1.0729	3.5083	2.3852	1	403.70739	3.07370	39.16294	185.88775	1683.01538
34	0.5121	0.4700	0.0178	1.4666	3.6023	56.7316	1.0072	1.6471	7.3644	1	333.58441	3.03717	24.69590	138.56834	1838.38428
35	0.6117	0.0226	0.3657	1.4840	58.9976	1.0146	1.0876	5.8359	0.9340	1	408.70348	3.07663	38.37843	170.71434	1698.95451
36	0.7422	0.0400	0.2178	1.5059	32.8709	3.8486	1.0937	4.1194	1.9066	1	406.25100	3.07534	39.15667	182.44843	1684.14493
37	0.6557	0.2860	0.0583	1.5144	6.3977	25.0884	1.0719	2.1169	4.9940	1	374.03576	3.05832	31.94133	169.98481	1737.14733
38	0.4736	0.0195	0.5070	1.6899	64.4619	0.4800	1.1565	6.2428	0.5993	1	409.47510	3.07787	37.31564	165.54182	1702.30452
39	0.6313	0.0306	0.3381	1.7039	46.1878	1.5847	1.1591	5.0811	1.1725	1	409.46196	3.07784	38.44533	175.18116	1687.87326
40	0.7492	0.0761	0.1748	1.7112	17.9210	7.1957	1.1551	2.9960	2.6394	1	403.49265	3.07460	38.62423	188.51207	1675.25631
41	0.4284	0.5618	0.0098	1.7205	2.9346	73.4015	1.0582	1.4876	8.3131	1	315.61931	3.02955	21.98910	126.07180	1880.77022
42	0.6763	0.0384	0.2852	1.7479	36.8614	2.5259	1.1713	4.4467	1.5098	1	408.89055	3.07766	38.72825	179.63578	1681.43071
43	0.6610	0.2602	0.0788	1.7573	7.2545	19.2839	1.1531	2.2137	4.3889	1	383.34324	3.06414	33.51921	176.66211	1713.16647

Table 18 Continued

	w_i			f_i			AAD%(i)			Parameters, x					
P_k	ρ_L^{sat}	P^{vap}	C_P	ρ_L^{sat}	P_{sat}	C_P	ρ_L^{sat}	P^{vap}	C_P	m	(ϵ/k_B)/K	σ/Å	λ^r	$K_{e,H}^{HB}$/Å^3	$(\epsilon_{e,H}^{HB}/k_B)$/K
44	0.7245	0.1454	0.1301	1.7662	11.2734	11.4185	1.1685	2.5738	3.3582	1	397.92591	3.07184	37.37644	189.15692	1679.45883
45	0.3090	0.0137	0.6773	1.8330	71.4861	0.1798	1.1996	6.7251	0.3397	1	408.83142	3.07813	36.04581	159.17708	1710.47521
46	0.7003	0.0543	0.2454	1.8969	26.2407	3.9673	1.2132	3.6491	1.9161	1	408.13504	3.07774	38.72168	184.51861	1673.11548
47	0.5152	0.4529	0.0319	1.9018	4.0065	39.7148	1.1526	1.7222	6.2140	1	352.34639	3.04867	26.76551	148.99702	1790.88175
48	0.6534	0.2359	0.1108	2.1778	8.1864	13.8505	1.2747	2.2979	3.7143	1	392.82544	3.07051	34.84933	182.36931	1688.78659
49	0.6964	0.1275	0.1761	2.1832	12.7704	8.1133	1.2863	2.6419	2.7979	1	404.06364	3.07644	37.78233	190.21733	1665.72376
50	0.6857	0.0737	0.2406	2.1879	20.0945	4.7282	1.2904	3.1494	2.0911	1	408.55347	3.07884	38.40002	187.15315	1664.99720
51	0.4793	0.0292	0.4915	2.1938	47.5620	0.8083	1.2959	5.2981	0.7639	1	411.57671	3.08058	37.08806	170.15071	1685.59555
52	0.5860	0.3453	0.0687	2.2169	5.7054	21.7131	1.2665	1.9999	4.6503	1	377.96409	3.06288	31.12577	168.32929	1725.62337
53	0.6317	0.0519	0.3164	2.2424	28.7606	2.6559	1.3060	3.8936	1.5167	1	411.04173	3.08034	38.23327	181.93216	1668.77334
54	0.4059	0.5780	0.0161	2.2734	2.9139	56.4887	1.2195	1.4837	7.3336	1	331.93560	3.03995	23.17861	132.78927	1840.27056
55	0.5228	0.4316	0.0455	2.2767	4.3890	30.1785	1.2628	1.7890	5.4488	1	364.40408	3.05617	28.19810	156.08461	1759.81283
56	0.6525	0.1928	0.1547	2.5311	9.6975	9.6120	1.3660	2.4143	3.0643	1	401.46561	3.07605	36.28701	187.60016	1667.70478
57	0.1426	0.0098	0.8476	2.5383	65.0754	0.0806	1.3853	6.5642	0.2362	1	408.39688	3.08018	33.82458	152.97294	1710.94382
58	0.6636	0.1061	0.2304	2.5465	14.9914	5.6002	1.3758	2.7646	2.2774	1	408.83489	3.07996	37.94123	189.48842	1657.03087
59	0.5960	0.3055	0.0985	2.6433	6.5617	15.2557	1.3760	2.0985	3.9031	1	389.05973	3.06986	32.78701	175.66967	1696.89830
60	0.5032	0.0433	0.4535	2.6757	33.9959	1.3284	1.4107	4.3810	0.9795	1	413.62013	3.08291	37.17836	175.97739	1668.70481
61	0.5273	0.4123	0.0604	2.6961	4.7051	23.4377	1.3703	1.8354	4.8225	1	374.14479	3.06231	29.36757	161.83788	1734.43563
62	0.4395	0.5279	0.0327	2.7852	3.3731	36.3826	1.3667	1.5838	5.9483	1	354.88070	3.05288	25.73817	145.74172	1782.79099
63	0.3004	0.0243	0.6753	2.7954	47.8816	0.3868	1.4442	5.4718	0.4838	1	412.13258	3.08263	35.21583	163.38949	1687.12696
64	0.3980	0.0358	0.5662	2.9203	38.0467	0.7911	1.4705	4.7531	0.6995	1	413.92632	3.08375	36.15728	170.55471	1673.10753
65	0.6051	0.0850	0.3099	2.9313	18.3792	3.4707	1.4650	3.0241	1.7178	1	413.03259	3.08314	37.76290	186.76992	1651.49463

Table 18 Continued

	w_i			f_i			AAD%(i)			Parameters, x					
P_k	ρ_L^{sat}	P^{vap}	C_P	ρ_L^{sat}	P_{sat}	C_P	ρ_L^{sat}	P^{vap}	C_P	m	$(\epsilon/k_B)/K$	$\sigma/Å$	λ^r	$K_{e,H}^{HB}/Å^3$	$(\epsilon_{e,H}^{HB}/k_B)/K$
66	0.6210	0.1649	0.2141	3.1180	10.8929	6.3751	1.5007	2.4645	2.4356	1	408.69023	3.08127	36.81349	189.41695	1650.60082
67	0.5329	0.0699	0.3972	3.2267	21.8412	2.2206	1.5325	3.3821	1.2898	1	415.41625	3.08509	37.29487	182.99613	1650.57203
68	0.5842	0.2765	0.1393	3.3259	7.1861	10.2429	1.5336	2.1460	3.1769	1	399.02243	3.07666	33.84917	180.69125	1670.91174
69	0.5148	0.4066	0.0786	3.4142	4.7917	17.4969	1.5331	1.8337	4.1784	1	382.98105	3.06860	29.93445	165.31156	1710.88355
70	0.4341	0.0546	0.5113	3.4888	26.3679	1.3101	1.5903	3.8480	0.9057	1	416.25988	3.08619	36.31751	176.76322	1655.19039
71	0.5848	0.1329	0.2823	3.5143	12.6873	4.3176	1.5867	2.5674	1.9250	1	413.55061	3.08467	37.07605	189.19244	1641.22981
72	0.2901	0.7001	0.0098	3.6259	2.0944	61.1259	1.5065	1.2584	7.5883	1	323.58414	3.04067	20.77653	122.26775	1856.82544
73	0.4630	0.4788	0.0582	3.6502	3.8511	21.9174	1.5686	1.6685	4.6615	1	374.73374	3.06499	27.89445	156.73278	1731.45219
74	0.5342	0.3561	0.1097	3.7787	5.5230	12.4230	1.6143	1.9295	3.5181	1	393.06105	3.07453	31.52018	172.38175	1684.77867
75	0.5755	0.2303	0.1941	3.8190	8.2438	6.8554	1.6376	2.2257	2.5434	1	407.29658	3.08197	34.98792	185.13888	1650.34092
76	0.3250	0.0424	0.6326	3.8228	30.1471	0.7658	1.6589	4.2495	0.6902	1	415.72941	3.08672	34.87544	169.36151	1662.56659
77	0.5240	0.1021	0.3739	3.8569	15.3673	2.7653	1.6572	2.7784	1.4379	1	416.85139	3.08712	36.85030	186.18742	1637.88463
78	0.3932	0.5687	0.0381	4.0356	2.9334	28.5506	1.6293	1.4751	5.2861	1	363.56833	3.06037	25.44993	145.83762	1759.12927
79	0.3263	0.6534	0.0203	4.0917	2.3038	41.4280	1.6237	1.3197	6.3054	1	345.95004	3.05212	22.89436	133.37934	1802.65450
80	0.5235	0.1324	0.3441	4.2403	12.2262	3.2201	1.7256	2.5061	1.5744	1	416.89497	3.08782	36.34828	187.14235	1632.60446
81	0.1163	0.0142	0.8695	4.2881	43.9780	0.1134	1.7572	5.4484	0.2740	1	409.66125	3.08467	31.12231	149.29987	1695.08949
82	0.4528	0.0916	0.4557	4.3542	16.0887	2.0049	1.7505	2.8904	1.1290	1	418.63662	3.08902	36.01962	182.46593	1635.63635
83	0.3964	0.0718	0.5318	4.3922	19.3217	1.4390	1.7624	3.2629	0.9507	1	418.40946	3.08905	35.40724	177.63445	1641.98856
84	0.1977	0.0280	0.7743	4.5192	33.7775	0.3275	1.7984	4.6738	0.4468	1	413.05510	3.08675	32.17799	157.24511	1676.18812
85	0.5351	0.1923	0.2725	4.5414	9.0513	4.3447	1.7729	2.2498	1.9221	1	414.24622	3.08691	35.30756	186.22877	1633.75992
86	0.3169	0.0557	0.6274	4.6704	22.3658	0.9336	1.8198	3.6262	0.7693	1	417.41979	3.08912	34.06994	170.36699	1650.33334
87	0.5197	0.3276	0.1527	4.6919	5.7647	8.0364	1.7884	1.9327	2.7960	1	402.72591	3.08116	32.20298	176.15816	1659.13130

Table 18 Continued

	w_i			f_i			AAD%(i)			Parameters, x					
P_k	ρ_L^{sat}	P^{vap}	C_P	ρ_L^{sat}	P_{sat}	C_P	ρ_L^{sat}	P^{vap}	C_P	m	$(\epsilon/k_B)/K$	$\sigma/Å$	λ^r	$K_{e,H}^{HB}/Å^3$	$(\epsilon_{e,H}^{HB}/k_B)/K$
88	0.4442	0.4810	0.0748	4.7806	3.6666	15.4910	1.7876	1.6152	3.9308	1	384.66083	3.07218	28.15369	159.16011	1704.65130
89	0.3937	0.5536	0.0527	5.0337	2.9222	19.9209	1.8239	1.4607	4.4410	1	375.71969	3.06825	26.21479	150.41691	1727.12604
90	0.4767	0.1593	0.3640	5.1893	9.7667	2.8932	1.8945	2.2730	1.4431	1	418.48273	3.09020	34.98466	184.30014	1625.10892
91	0.4211	0.1145	0.4643	5.2319	12.3148	2.0125	1.9088	2.5167	1.1305	1	419.92773	3.09113	34.86609	181.12136	1627.20873
92	0.3629	0.0884	0.5487	5.3646	14.6127	1.4520	1.9369	2.8244	0.9547	1	419.68797	3.09130	34.11544	175.90624	1633.16638
93	0.4581	0.4377	0.1042	5.3665	4.0181	10.6537	1.8973	1.6646	3.2563	1	394.53862	3.07809	29.30187	164.84241	1678.68728
94	0.2306	0.0434	0.7260	5.4251	23.4757	0.5486	1.9563	3.8362	0.5860	1	415.60155	3.08947	31.82485	160.61768	1658.96538
95	0.5023	0.2833	0.2144	5.4312	6.2118	5.1687	1.9232	1.9535	2.1654	1	410.77144	3.08645	32.86660	179.22706	1638.47093
96	0.3369	0.6270	0.0361	5.4955	2.3030	24.3928	1.8952	1.3115	4.8884	1	367.53146	3.06516	24.40619	142.00772	1747.23448
97	0.2781	0.0677	0.6542	6.0339	16.0922	0.9044	2.0519	3.0890	0.7613	1	418.29670	3.09165	32.09899	166.22003	1641.75722
98	0.2826	0.6941	0.0233	6.0776	1.8164	29.0682	1.9870	1.1716	5.3057	1	359.28778	3.06237	22.73142	133.95104	1766.86533
99	0.2217	0.7685	0.0098	6.1798	1.4410	44.6497	1.9936	1.0444	6.4995	1	337.20676	3.05292	20.21743	120.92786	1819.45372
100	0.4599	0.3796	0.1605	6.2922	4.3814	6.1658	2.0542	1.6955	2.4268	1	405.95453	3.08515	30.37620	170.22729	1648.60204
101	0.4537	0.2249	0.3214	6.2963	6.7194	3.0671	2.0699	1.9548	1.5176	1	417.79950	3.09132	33.00602	179.52341	1621.71492
102	0.3972	0.1499	0.4529	6.3485	8.7529	2.0318	2.0876	2.1438	1.1333	1	420.62464	3.09300	33.25622	177.95029	1619.96347
103	0.3894	0.5357	0.0749	6.3618	2.8325	12.3667	2.0493	1.4240	3.5125	1	388.80932	3.07673	26.88627	154.68731	1692.14959
104	0.3190	0.1021	0.5789	6.6430	10.9500	1.2989	2.1414	2.4628	0.9109	1	420.24395	3.09334	32.13402	170.51363	1627.68677
105	0.1057	0.0210	0.8732	6.7768	26.4505	0.1454	2.1886	4.2634	0.3044	1	410.96104	3.08901	28.15059	143.57129	1677.88097
106	0.3354	0.6142	0.0504	6.7989	2.1876	15.7803	2.1167	1.2686	3.9562	1	380.77418	3.07350	25.04272	146.05747	1712.17569
107	0.4023	0.1948	0.4029	7.0037	6.6773	2.2457	2.1823	1.9140	1.1873	1	420.26317	3.09353	32.27886	176.19869	1616.65611
108	0.4088	0.4690	0.1223	7.2438	3.1557	6.9075	2.1977	1.4702	2.6006	1	401.87891	3.08429	28.20532	161.46067	1657.64701
109	0.2877	0.6778	0.0346	7.3033	1.7180	19.2302	2.1945	1.1354	4.3457	1	373.29513	3.07072	23.46589	138.34927	1730.53036

Table 18 Continued

	w_i			f_i			AAD%(i)			Parameters, x					
P_k	ρ_L^{sat}	P^{vap}	C_P	ρ_L^{sat}	P_{sat}	C_P	ρ_L^{sat}	P^{vap}	C_P	m	(ϵ/k_B)/K	σ/Å	λ^r	$K_{e,H}^{HB}$/Å^3	$(\epsilon_{e,H}^{HB}/k_B)$/K
110	0.4231	0.3285	0.2484	7.6145	4.2859	3.3481	2.2645	1.6335	1.6603	1	415.14880	3.09142	30.41234	171.01197	1624.33576
111	0.1704	0.0453	0.7844	7.6336	16.3857	0.3872	2.3162	3.2798	0.4913	1	414.94972	3.09197	28.46866	149.94940	1654.75947
112	0.2431	0.0807	0.6762	7.6943	11.0445	0.8160	2.3160	2.5798	0.7203	1	418.65737	3.09385	29.79935	159.75708	1635.00003
113	0.3284	0.1572	0.5144	7.9621	6.5567	1.5235	2.3398	1.8730	0.9782	1	421.24822	3.09523	30.73827	168.87542	1616.56438
114	0.3767	0.2423	0.3810	8.1756	4.8164	2.1108	2.3588	1.6601	1.1468	1	420.24994	3.09474	30.55253	170.72278	1613.36277
115	0.2327	0.7460	0.0213	8.2195	1.2651	22.2627	2.3301	0.9800	4.6482	1	366.19228	3.06883	21.82404	130.16754	1746.86423
116	0.3377	0.5871	0.0751	8.2553	2.0647	8.9370	2.3455	1.2185	2.9835	1	394.15444	3.08167	25.62217	149.76887	1676.37167
117	0.3805	0.4269	0.1926	8.8987	2.8610	3.4204	2.4471	1.3715	1.7286	1	412.68542	3.09138	28.16691	162.14349	1628.36055
118	0.2840	0.6662	0.0498	8.9739	1.5104	10.9567	2.4464	1.0572	3.3005	1	387.69785	3.07946	23.92676	141.47286	1692.20108
119	0.1742	0.8160	0.0098	9.1606	0.9119	27.7951	2.4605	0.8315	5.1490	1	354.49801	3.06528	19.98670	120.60527	1773.25014
120	0.3463	0.5347	0.1189	9.2860	2.1099	4.8696	2.4953	1.2105	2.1642	1	405.54359	3.08818	26.41597	154.15871	1646.01850
121	0.2531	0.1275	0.6194	9.3029	5.9892	0.9806	2.5413	1.8572	0.7888	1	420.33208	3.09617	28.39240	157.83966	1621.01754
122	0.3129	0.2288	0.4583	9.6211	3.7930	1.4954	2.5687	1.4632	0.9585	1	421.36256	3.09670	28.65216	162.51983	1610.23038
123	0.1948	0.0849	0.7203	9.7176	7.5810	0.5953	2.6071	2.1889	0.6124	1	417.96782	3.09544	27.03840	149.29199	1632.89044
124	0.0337	0.0098	0.9565	9.8384	18.4750	0.0578	2.6457	3.6694	0.2093	1	408.64571	3.09119	24.30685	128.89563	1677.43894
125	0.3333	0.3333	0.3333	10.1088	2.7515	1.8215	2.6222	1.3004	1.0667	1	419.76158	3.09607	27.89070	160.65411	1610.56455
126	0.2867	0.6360	0.0773	10.3863	1.3927	5.5845	2.6406	1.0039	2.3467	1	400.79016	3.08686	24.48329	144.83885	1657.21115
127	0.3272	0.5007	0.1721	10.5181	1.8788	2.7669	2.6638	1.1285	1.5436	1	413.13974	3.09291	26.29528	153.95257	1625.37918
128	0.2444	0.1828	0.5728	10.9319	3.3171	0.9772	2.7507	1.3683	0.7813	1	420.97197	3.09766	26.73006	152.71020	1612.98799
129	0.0919	0.0351	0.8729	10.9952	10.3433	0.1621	2.7845	2.7135	0.3244	1	412.59384	3.09383	24.25039	132.76548	1654.98893
130	0.2030	0.7688	0.0281	11.0751	0.8241	10.4258	2.7248	0.7910	3.2072	1	384.89974	3.08029	21.82214	130.80256	1696.84541
131	0.2827	0.6012	0.1162	11.4371	1.2828	3.0916	2.7775	0.9529	1.6915	1	409.43161	3.09173	24.72057	146.31240	1633.93705

Table 18 Continued

	w_i			f_i			AAD%(i)			Parameters, x					
P_k	ρ_L^{sat}	P^{vap}	C_P	ρ_L^{sat}	P_{sat}	C_P	ρ_L^{sat}	P^{vap}	C_P	m	$(\epsilon/k_B)/K$	$\sigma/Å$	λ^r	$K_{e,H}^{HB}/Å^3$	$(\epsilon_{e,H}^{HB}/k_B)/K$
132	0.1759	0.1274	0.6967	12.2828	3.2558	0.5477	2.9280	1.4396	0.5853	1	418.74971	3.09757	24.63408	140.93526	1621.68645
133	0.1344	0.8558	0.0098	12.3123	0.4930	13.8278	2.8749	0.6133	3.6545	1	373.28226	3.07676	19.85287	120.09880	1723.20404
134	0.2735	0.5039	0.2225	12.3354	1.2533	1.5628	2.8938	0.9211	1.0401	1	417.67711	3.09630	25.00930	147.71856	1612.29768
135	0.2444	0.2965	0.4591	12.3497	1.6935	1.0210	2.9137	1.0091	0.7872	1	421.21464	3.09842	25.39218	148.29559	1606.47089
136	0.2263	0.6986	0.0751	12.7278	0.7768	3.0739	2.9313	0.7557	1.7140	1	406.56050	3.09117	23.09716	137.86527	1640.14137
137	0.1173	0.0728	0.8099	13.0295	4.3111	0.2660	3.0243	1.7414	0.3983	1	415.31995	3.09643	23.16076	131.30275	1635.36247
138	0.1600	0.8093	0.0308	13.6999	0.4408	4.4079	3.0402	0.5811	2.0869	1	397.91599	3.08792	21.32724	128.10920	1661.04567
139	0.2209	0.4267	0.3525	13.7289	0.8864	0.9280	3.0664	0.7642	0.7318	1	420.43040	3.09851	23.94856	141.74233	1605.12276
140	0.2192	0.6455	0.1352	13.7294	0.6753	1.4720	3.0508	0.6966	1.0737	1	414.87535	3.09552	23.26273	138.69506	1617.90032
141	0.1584	0.1965	0.6451	14.3337	1.2598	0.4947	3.1584	0.8965	0.5507	1	418.99854	3.09865	22.93060	133.97819	1614.09426
142	0.1654	0.6162	0.2184	15.4225	0.3561	0.7142	3.2455	0.5095	0.6334	1	418.69554	3.09807	22.23318	132.60271	1606.94409
143	0.0876	0.0985	0.8139	15.8594	1.4618	0.1985	3.3361	1.0493	0.3595	1	414.12353	3.09738	20.99247	121.57431	1628.94425
144	0.1355	0.3002	0.5643	15.8827	0.4561	0.4306	3.3206	0.5473	0.5060	1	418.52538	3.09894	21.70424	128.21162	1610.43494
145	0.0868	0.9020	0.0112	15.9004	0.1628	2.7274	3.2804	0.3544	1.6324	1	399.08175	3.08974	19.97264	120.07966	1654.98762
146	0.0098	0.0098	0.9804	16.2254	3.5659	0.0716	3.4262	1.6809	0.2276	1	407.27064	3.09634	19.92167	112.86677	1653.84095
147	0.0779	0.5524	0.3698	17.7383	0.0734	0.3085	3.5067	0.2443	0.4323	1	416.34854	3.09855	20.23600	120.25753	1610.89222
148	0.0373	0.1234	0.8393	18.9514	0.2569	0.1190	3.6633	0.4608	0.2962	1	408.78085	3.09743	18.82192	110.33025	1631.46323
149	0.0098	0.9804	0.0098	19.0067	0.0140	0.4702	3.6008	0.1051	0.6125	1	421.77481	3.09985	19.83148	117.56479	1594.06433
150	0.0098	0.4712	0.5189	20.2645	0.0408	0.1285	3.8982	0.1703	0.3089	1	408.65723	3.10253	18.56456	109.98060	1626.91189

Table 19: Pareto points and parameters for water models where with $m \geqslant 1$. The columns are sorted with $f_{\rho_L^{sat}}$ in increasing order.

	w_i			f_i			AAD%(i)			Parameters, $\boldsymbol{x}$					
P_k	ρ_L^{sat}	P^{vap}	C_P	ρ_L^{sat}	P_{sat}	C_P	ρ_L^{sat}	P^{vap}	C_P	m	$(\epsilon/k_B)/K$	$\sigma/Å$	λ^r	$K_{e,H}^{HB}/Å^3$	$(\epsilon_{e,H}^{HB}/k_B)/K$
1	0.9804	0.0098	0.0098	0.7719	6.2275	2.2512	0.6706	1.8767	1.4957	1.11773	371.50797	2.93110	31.39086	180.15540	1680.81699
2	0.9716	0.0100	0.0184	0.7942	6.0024	0.7286	0.6813	1.8259	0.8388	1.13396	374.29928	2.91758	31.53519	184.00066	1662.19418
3	0.9738	0.0140	0.0122	0.8012	4.5335	1.4220	0.6852	1.6365	1.1844	1.13182	372.68108	2.91864	31.49293	185.44185	1663.85288
4	0.9586	0.0098	0.0316	0.8034	6.0970	0.3072	0.6856	1.8424	0.5154	1.14215	375.24596	2.91063	31.48800	185.07336	1654.66835
5	0.9061	0.0098	0.0841	0.8132	6.1915	0.0932	0.6901	1.8877	0.2508	1.15264	374.71137	2.90089	31.07680	184.53258	1650.27798
6	0.9665	0.0237	0.0098	0.8219	3.2685	1.6589	0.6956	1.4586	1.2811	1.13972	370.49508	2.91021	31.07029	186.93011	1660.53970
7	0.9555	0.0178	0.0267	0.8338	3.6252	0.3955	0.7004	1.4727	0.5724	1.15216	374.38711	2.90107	31.43029	190.19240	1643.37314
8	0.6677	0.0098	0.3225	0.8376	5.2910	0.0265	0.7023	1.7994	0.1495	1.17033	370.33900	2.88287	29.87199	181.76605	1650.75594
9	0.8271	0.0156	0.1574	0.8510	3.7632	0.0673	0.7088	1.4755	0.2207	1.17053	371.89983	2.88348	30.38047	186.85978	1641.21627
10	0.9180	0.0223	0.0597	0.8572	2.9603	0.1639	0.7120	1.3439	0.3259	1.16687	373.43135	2.88748	30.94974	191.25963	1635.00362
11	0.9468	0.0299	0.0234	0.8583	2.6154	0.3821	0.7137	1.3084	0.5616	1.16296	372.32603	2.89034	30.93058	191.54188	1638.44977
12	0.9485	0.0416	0.0098	0.8592	2.3294	1.0237	0.7165	1.2694	1.0017	1.15960	368.18918	2.89112	30.26195	187.95819	1651.19855
13	0.4141	0.0098	0.5761	0.8820	3.3107	0.0169	0.7239	1.4225	0.1193	1.18904	366.09880	2.86437	28.91049	181.88390	1646.51051
14	0.8674	0.0341	0.0986	0.8895	2.0923	0.0976	0.7291	1.1723	0.2585	1.18306	370.23201	2.87165	30.07703	190.93115	1630.99619
15	0.6954	0.0230	0.2816	0.8958	2.2775	0.0383	0.7311	1.1876	0.1743	1.19017	367.46658	2.86409	29.30879	186.55900	1637.18188
16	0.9259	0.0589	0.0152	0.8980	1.7620	0.3140	0.7358	1.1172	0.5291	1.18131	367.25982	2.87162	29.64280	189.41987	1638.23797
17	0.8747	0.0602	0.0651	0.9210	1.5172	0.0782	0.7465	1.0348	0.2357	1.19494	367.29650	2.85995	29.36376	190.49775	1629.04797
18	0.8972	0.0930	0.0098	0.9421	1.2451	0.1747	0.7607	0.9561	0.3968	1.20015	362.74795	2.85320	28.45624	186.66266	1637.88933
19	0.5412	0.0317	0.4272	0.9435	1.3911	0.0217	0.7569	0.9705	0.1373	1.20797	363.25104	2.84681	28.33412	185.77280	1634.52741
20	0.1783	0.0098	0.8119	0.9537	1.4074	0.0142	0.7593	0.9685	0.1005	1.21334	361.16260	2.84118	27.87938	183.40497	1638.35826
21	0.7810	0.0743	0.1447	0.9563	1.1438	0.0327	0.7657	0.9108	0.1637	1.21004	363.54923	2.84528	28.40757	188.02054	1629.43721

Table 19 Continued

	w_i			f_i			AAD%(i)			Parameters, x					
P_k	ρ_L^{sat}	P^{vap}	C_P	ρ_L^{sat}	P_{sat}	C_P	ρ_L^{sat}	P^{vap}	C_P	m	$(\epsilon/k_B)/K$	$\sigma/Å$	λ^r	$K_{e,H}^{HB}/Å^3$	$(\epsilon_{e,H}^{HB}/k_B)/K$
22	0.8528	0.1374	0.0098	0.9989	0.8186	0.0164	0.7888	0.7849	0.1146	1.22488	359.53340	2.83100	27.44930	185.49637	1630.24497
23	0.0098	0.0098	0.9804	1.0399	0.6499	0.0141	0.7956	0.6968	0.0902	1.23882	356.32783	2.81742	26.92255	185.37793	1628.94752
24	0.7522	0.1887	0.0591	1.0546	0.5356	0.0243	0.8179	0.6421	0.1391	1.24449	354.64271	2.81267	26.31932	182.01214	1631.30549
25	0.7606	0.2296	0.0098	1.0871	0.4029	0.2020	0.8325	0.5591	0.4325	1.25995	354.52660	2.80032	26.06227	183.18016	1621.17614
26	0.2473	0.1709	0.5818	1.0972	0.4172	0.0285	0.8448	0.5610	0.1348	1.25175	352.54771	2.80630	25.66531	179.91774	1630.85291
27	0.6383	0.2689	0.0928	1.1145	0.3352	0.0644	0.8479	0.5108	0.2313	1.26341	349.64239	2.79527	25.24397	178.31599	1633.23677
28	0.6737	0.3039	0.0224	1.1349	0.2717	0.1904	0.8562	0.4620	0.4206	1.27398	349.76269	2.78703	25.13530	179.35368	1625.95602
29	0.1940	0.2199	0.5861	1.1434	0.3379	0.0382	0.8712	0.5037	0.1596	1.25656	351.23210	2.80242	25.12615	177.6236	1630.62645
30	0.3333	0.3333	0.3333	1.1590	0.2525	0.0802	0.8724	0.4359	0.2482	1.27100	347.26919	2.78867	24.58727	175.71894	1633.94231
31	0.6273	0.3629	0.0098	1.1678	0.1845	0.7386	0.8703	0.3822	0.8494	1.29083	350.70344	2.77456	25.03419	181.71037	1611.65480
32	0.5834	0.3896	0.0270	1.1820	0.1793	0.2584	0.8782	0.3738	0.4870	1.28850	346.01617	2.77410	24.38553	176.59154	1627.40023
33	0.1408	0.2689	0.5903	1.2078	0.2671	0.0501	0.8970	0.4431	0.1913	1.26180	350.09497	2.79832	24.59792	175.39033	1629.39518
34	0.3189	0.4707	0.2104	1.2095	0.1628	0.1503	0.8930	0.3450	0.3438	1.28750	343.03392	2.77389	23.80463	172.75207	1635.85910
35	0.0663	0.1502	0.7835	1.2301	0.3345	0.0259	0.9058	0.4952	0.1227	1.24979	353.63873	2.81008	25.00890	176.81948	1625.75383
36	0.4343	0.5158	0.0499	1.2326	0.1203	0.2645	0.9012	0.2969	0.4693	1.30134	341.29706	2.76227	23.53922	172.66032	1632.77546
37	0.4401	0.5501	0.0098	1.2434	0.0812	1.1175	0.9038	0.2465	1.0419	1.31622	345.84190	2.75321	24.00988	178.64380	1609.24096
38	0.1449	0.4028	0.4523	1.2594	0.1906	0.0845	0.9162	0.3702	0.2548	1.27272	347.18776	2.78863	23.96077	172.76385	1630.55164
39	0.2569	0.7333	0.0098	1.2865	0.0495	1.5611	0.9224	0.1950	1.2355	1.33137	344.13926	2.74139	23.56392	177.92134	1604.01163
40	0.1890	0.6630	0.1480	1.2879	0.0960	0.2418	0.9257	0.2625	0.4390	1.30408	339.17107	2.76008	22.90371	169.10635	1635.57306
41	0.2379	0.7315	0.0306	1.2920	0.0702	0.5083	0.9259	0.2302	0.6650	1.32142	338.52033	2.74616	22.91348	171.28099	1627.59867
42	0.1469	0.5461	0.3070	1.2999	0.1275	0.1464	0.9301	0.2972	0.3372	1.28741	343.27997	2.77543	23.28348	170.05583	1632.65640
43	0.0510	0.9392	0.0098	1.3347	0.0386	1.7523	0.9472	0.1725	1.3100	1.33780	343.61283	2.73734	23.11968	176.17845	1599.75877

Table 19 Continued

	w_i			f_i			AAD%(i)			Parameters, x					
P_k	ρ_L^{sat}	P^{vap}	C_P	ρ_L^{sat}	P_{sat}	C_P	ρ_L^{sat}	P^{vap}	C_P	m	(ϵ/k_B)/K	σ/Å	λ^r	$K_{e,H}^{HB}$/Å^3	$(\epsilon_{e,H}^{HB}/k_B)$/K
44	0.0098	0.0412	0.9490	1.3358	0.3683	0.0179	0.9352	0.5186	0.0949	1.24010	356.69676	2.81991	25.13331	176.91324	1621.50113
45	0.0503	0.9279	0.0218	1.3654	0.0521	0.7279	0.9576	0.1996	0.7961	1.32823	339.36753	2.74286	22.50439	170.11667	1618.20145
46	0.0804	0.8240	0.0956	1.3818	0.0704	0.2976	0.9595	0.2301	0.4943	1.31173	338.08926	2.75489	22.32681	166.58421	1631.96313
47	0.0778	0.3268	0.5953	1.4157	0.1869	0.0564	0.9661	0.3620	0.2043	1.26343	350.03607	2.79864	23.80916	171.41937	1625.60122
48	0.0897	0.4801	0.4302	1.4243	0.1359	0.0962	0.9680	0.3048	0.2730	1.27539	346.75094	2.78763	23.30379	169.40713	1627.82656
49	0.0758	0.7006	0.2235	1.4728	0.0848	0.1765	0.9822	0.2459	0.3749	1.29299	342.27345	2.77211	22.54882	166.38978	1629.52166
50	0.0249	0.9178	0.0573	1.6804	0.0578	0.2760	1.0449	0.2094	0.4864	1.30275	342.09295	2.76614	21.95364	164.07908	1621.24596
51	0.0168	0.9582	0.0250	1.6859	0.0488	0.5119	1.0532	0.1926	0.6752	1.30796	344.38607	2.76350	22.14716	166.41554	1610.77227
52	0.0544	0.5448	0.4007	1.6910	0.1021	0.0932	1.0357	0.2641	0.2702	1.27346	347.58920	2.79104	22.76179	166.21902	1623.83739
53	0.0393	0.2812	0.6795	1.7121	0.1701	0.0387	1.0411	0.3459	0.1619	1.25378	353.03633	2.80925	23.54388	169.24769	1620.36697
54	0.0098	0.9804	0.0098	1.7899	0.0335	1.4370	1.0905	0.1599	1.1899	1.31059	351.06132	2.76552	22.63659	171.23157	1587.38629
55	0.0161	0.1409	0.8430	1.9643	0.1871	0.0246	1.0987	0.3634	0.1056	1.24216	356.50974	2.82109	23.61552	168.80043	1616.06082
56	0.0288	0.8031	0.1682	1.9921	0.0639	0.1376	1.1123	0.2185	0.3398	1.28230	345.88046	2.78494	21.93198	162.04784	1620.55440
57	0.0284	0.3835	0.5881	2.1755	0.1092	0.0446	1.1446	0.2724	0.1768	1.25372	353.30379	2.81116	22.74299	164.61070	1616.47529
58	0.0249	0.6222	0.3529	2.3623	0.0724	0.0713	1.1831	0.2271	0.2365	1.26301	350.82493	2.80339	22.08567	161.38225	1616.34056
59	0.0098	0.9501	0.0401	2.4376	0.0482	0.2323	1.2274	0.1915	0.4677	1.27927	350.10681	2.79158	21.72572	161.10134	1606.75502
60	0.0098	0.1709	0.8193	2.6561	0.1190	0.0268	1.2297	0.2827	0.1129	1.23831	357.82540	2.82658	22.76946	163.52130	1611.06279
61	0.0098	0.8565	0.1337	3.2295	0.0514	0.0724	1.3709	0.1974	0.2486	1.25473	353.81957	2.81451	21.39144	156.39127	1608.35986
62	0.0098	0.3253	0.6649	3.3565	0.0730	0.0318	1.3620	0.2259	0.1251	1.23661	358.25215	2.83008	21.96677	158.37690	1607.70377

4.6.2 *Anomalous density profiles*

Some of the Pareto-optimal spherical water models found during the optimization produced saturated density phase diagrams that appear unphysical at near-critical temperatures. This behaviour of the near-critical region contrasts with the well-known law of the rectilinear diameter, which states that the average of the densities ρ_L^{sat} and ρ_G^{sat} is a linear function of temperature (Zollweg and Mulholland, 1972) . After a detailed parametric investigation on the near-critical region of the ρ-T phase diagram, it was found that these shapes, which we may define as a non-convex vapour-liquid envelope, is caused by relatively high values of λ^r. The A_1 term in SAFT-VR Mie is parametrized for two Sutherland potentials with exponents ranging between $\lambda = 5$ and $\lambda = 100$ (where λ is the repulsive or attractive exponent), and the A_2 term is a function of $2\lambda^r$. Hence, the theory is strictly only applicable for values of $\lambda^r \leqslant 50$ as has been previously stated Lafitte et al. (2013b). However, when association is introduced, the critical temperature and the range of VLE coexistence increases, and the values of λ^r at which non-convex density profiles occurs is lower. We illustrate this point in Figure 55 by changing the value of λ^r while keeping other variables fixed to values that are similar to the values obtained for the water models developed in this work. Non-convex envelopes occur at values of λ^r above 30 for this particular set of parameters. We attribute this phenomenon to the increase in the number of density roots that appear in the near-critical region. Multiple density roots have been observed in the literature for SAFT-type equations of state (Alsaifi and Englezos, 2011; Privat et al., 2010; Alsaifi et al., 2017; Aslam and Sunol, 2006; Koak et al., 1999; Alsaifi et al., 2019). In the recent work of Alsaifi et al. (2019), the authors were able to show that as many as 10 density roots may occur in SAFT-VR Mie, via a sophisticated use of bifurcation diagrams that rigorously analyse the metastable region of the equation of state. In our testing, we found that 5 volume roots can appear at temperatures close to the critical point. The authors note that these non-physical predictions are inevitable in more sophisticated equations of state due to the empirical functional forms (for example, an empirical analytic expression for the pair distribution function at contact) required to approximate statistical mechanical theories with no exact solutions. It is possible to follow a rigorous method such as that proposed by Alsaifi et al. (2019) to identify models with non-physical regions, or simply inspecting the van der Waals loop on a pressure-volume diagram at various temperatures. It may be possible to include such checks as constraints within the MOP to avoid the generation of anomalous models, however such checks are not included in the current implementation as they would require significant computational effort. From an chemical engineering perspective, the spherical models of water that we have developed in this study are accurate for typical process operating conditions, but one must be careful when using these models to calculate properties at near-critical conditions.

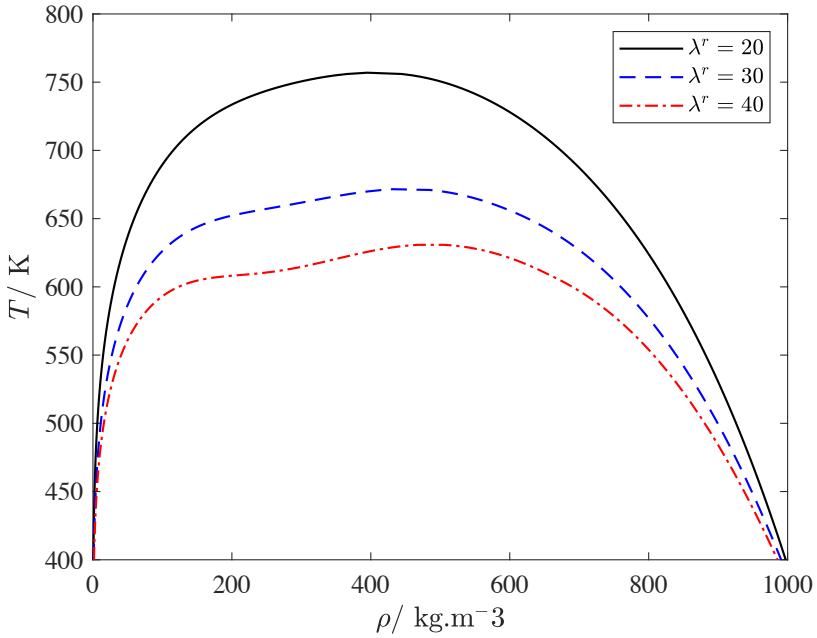

Figure 55: Effect of λ^r on the saturated liquid density and saturated vapour density. The values of the other parameters are fixed to the typical values for water $m = 1$, $\lambda^a = 6$, $K^{HB}_{e,H} = 180\text{Å}^3$, $\sigma = 3\text{Å}$, $\epsilon/k_B = 390$ K and $\epsilon^{HB}_{e,H} = 1700$ K.

5 DEVELOPING SAFT-γ MIE MODELS FOR CO_2-MEA-H_2O-N_2

5.1 INTRODUCTION

The main motivation of this chapter is to develop models for the CO_2-MEA-H_2O-N_2 system that accurately describe the phase equilibria and the caloric properties of the mixtures. This is to provide improved thermodynamic models that may be used in a process modelling context, for example modelling the absorption process as discussed in chapter 3. Currently, there are no SAFT-γ Mie (or SAFT-VR Mie) models in the literature that are able to describe the CO_2-MEA-H_2O-N_2 system, but there exist models for the SAFT-VR SW EoS ((Mac Dowell et al., 2009) and (Rodríguez et al., 2012)), and SAFT-γ SW EoS (Chremos et al., 2016).

The thermodynamic modelling of carbon dioxide with aqueous amine systems has been discussed in some detail in the section 2.3 of the introductory chapter. In this chapter, we develop homonuclear models for the SAFT-γ Mie (equivalently, SAFT-VR Mie) equation of state, following an approach similar to Mac Dowell et al. (2011), Rodríguez et al. (2012) and Chremos et al. (2016). A key concept used in these approaches is that the inherent chemical reactions in CO_2-aqueous alkanolamine mixtures can be modelled via a physical association scheme and ionic products are not considered explicitly. This treatment was first proposed by Button and Gubbins (1999) for CO_2 reacting with aqueous MEA. Such an approach leads to simplified thermodynamic models and simplified process model equations, as seen in chapter 3. This simplification sacrifices some degree of model accuracy compared to an explicit approach. The SAFT methodology is not limited to using a physical association scheme to model the reactions because electrolyte extensions to SAFT are available (Galindo et al., 1999; Liu et al., 1999; Gil-Villegas et al., 2001; Patel et al., 2003a; Behzadi et al., 2005; Cameretti et al., 2005; Held et al., 2008; Held and Sadowski, 2009; Schreckenberg et al., 2014; Eriksen et al., 2016), where the equation proposed by Eriksen et al. (2016) is an extension to SAFT-VR Mie.

In this work we will focus on the development of models that provide an accurate description of both the VLE and caloric properties of the pure compounds and their mixtures. This will be achieved by including isobaric heat capacity in the model regression in addition to VLE data. It was shown in chapter 4 that this property is particularly useful for systems with a high degree of hydrogen bonding, i.e., the systems studied here, because it reduces the parameter degeneracy in the model regression, and we discussed why an accurate description of this property is particularly important in the context of process modelling. We use the MOO methodology for the development of the key parameters that mediate the chemical reactions present in the ternary mixture of CO_2-MEA-H_2O when estimating to partial pressure data.

We also focus on accurately describing of the heat of absorption and take a careful look at the experimental methodologies used to measure this property. The heat of absorption is strongly correlated to the operating cost of amine absorption processes (Gupta et al., 2013), so it is therefore vital that the thermodynamic

model is able to accurately predict this property. Furthermore, it provides specific information on the enthalpies of the inherent reactions (Gupta et al., 2013). With the newly-developed model for water (model 5NS in chapter 4)), which provides an excellent description of the isobaric heat capacity for a wide range of temperatures, we expect an improvement in the mixture heat capacity and the heat of absorption compared to the literature SAFT-VR Mie model (model 1L in chapter 4).

5.2 METHODOLOGY

To develop the SAFT-γ Mie parameters required to describe the thermodynamic mixtures consisting of CO_2, MEA, H_2O and N_2 we will regress some of the SAFT parameters to available experimental data. The parameters to be determined describe the like- and unlike interactions between pairs of molecules and their association schemes. To avoid having too many parameters in the regressions (which may lead to unphysical parameters and models), we will fix some parameters *a-priori* by appealing to physical concepts. We also make sure that the SAFT parameters lie within bounds that are physically realistic and within the range that SAFT-γ Mie is valid.

5.3 DEFINITION OF PARAMETERS

The definitions of the all of the parameters used this chapter are summarized in Table 20. The reader is referred to Papaioannou et al. (2014) for information on the SAFT-γ Mie EoS for more details on the equation and the combining rules (CR) that are used to fix some of the unlike parameters.

Table 20: Definition of the SAFT-γ Mie parameters

Parameter	Definition
v_k^*	Number of segments in group k
S_k	Shape factor for group k
σ_{kl}	Segment diameter between groups k and l
λ_{kl}^r	Repulsive exponent between groups k and l
λ_{kl}^a	Attractive exponent between groups k and l
ϵ_{kl}	Depth of potential well between groups k and l
λ_{kl}^r	Repulsive exponent of the Mie potential between groups k and l
$N_{ST,k}$	Number of site types on group k
$n_{k,a}$	Number of sites of type a on group k
$\epsilon_{kl,ab}^{HB}$	Association energy between sites of types a and b on groups k and l
$K_{kl,ab}^{HB}$	Association energy between sites of types a and b on groups k and l

5.4 DEFINITION OF THE MODELS AND THEIR ASSOCIATION SCHEMES

We will first define the association schemes used to model CO_2, MEA, H_2O and their mixtures. This determines the number of site types on group k ($N_{ST,k}$), $k = \{CO_2, MEA, H_2O\}$, and the number of sites of type a on group k ($n_{k,a}$).

As discussed in section 2.3 of this thesis, the main reactions that occur when CO_2 absorbs into aqueous MEA are reactions r_1-r_3:

$$\underset{}{CO_2} + \underset{\text{MEA}}{2\,HO(CH_2)_2NH_2} \rightleftharpoons \underset{\text{Carbamate pair}}{[HO(CH_2)_2NHCOO^- + HO(CH_2)_2NH_3^+]} \quad (r_1)$$

$$HO(CH_2)_2NHCOO^- + H_3O^+ \rightleftharpoons \underset{\text{Bicarbonate pair}}{[HO(CH_2)_2NH_3^+ + HCO_3^-]} \quad (r_2)$$

$$CO_2 + H_2O \rightleftharpoons \underset{\text{Carbonic acid}}{[HCO_3^- + H^+]}. \quad (r_3)$$

The reaction products involving ion pairs are represented by square brackets and these are assumed to be tightly-bound species with no net charge. This assumption is somewhat justified by the relatively low dielectric constant of aqueous alkanolamine solutions (2-5 times lower than that of water Rodríguez et al. (2012)).

In Figure 56, we show schematics for the molecular models that are to be developed. These are illustrations of the potential functions that define the molecular interactions.

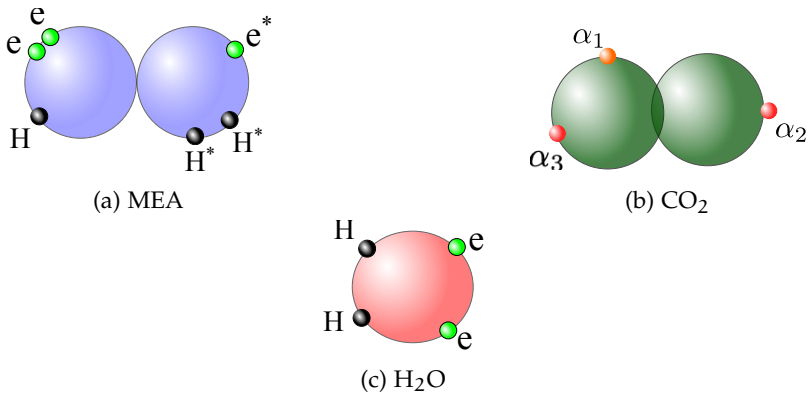

(a) MEA (b) CO_2

(c) H_2O

Figure 56: Schematic showing the association sites for the models developed in this research. The large spheres represent the monomeric segments which interact via a Mie potential. The small spheres represent the association sites, which may interact via other sites (representing chemical association). a) MEA (HOCH2CH2NH2) is modelled with two tangentially bonded monomeric segments ($\nu^*_{MEA} = 2, S_{MEA} = 1$). Two e sites represent the lone pair of electrons on the oxygen atom; the H site represents the hydrogen atom attached to the oxygen atom. The e^* site represents the lone pair of electrons on the nitrogen atom and and two H^* sites represent the hydrogen atoms attached to the nitrogen atom. b) CO_2 is modelled by two fused segments ($\nu^*_{CO_2} = 2, S_{CO_2} = 0.847$). The three sites α_1, α_2 and α_3 do not self-associate but represent the ability for CO_2 to chemically associate with MEA and H_2O as discussed in the text. c): H_2O is modelled as a slightly non-spherical molecule ($\nu^*_{CO_2} = 1, S_{CO_2} = 1.2566$) with four association sites, two e sites and two H sites, representing the lone pairs of electrons and the hydrogen atoms respectively.

In Figure 57, we illustrate the physical association scheme used to treat reactions r_1, r_2 and r_3. Note that the thermodynamic model only treats each group k, k = {CO_2, MEA, H_2O}, explicitly, while the reaction products are accounted for implicitly via the association interactions depicted in the figure.

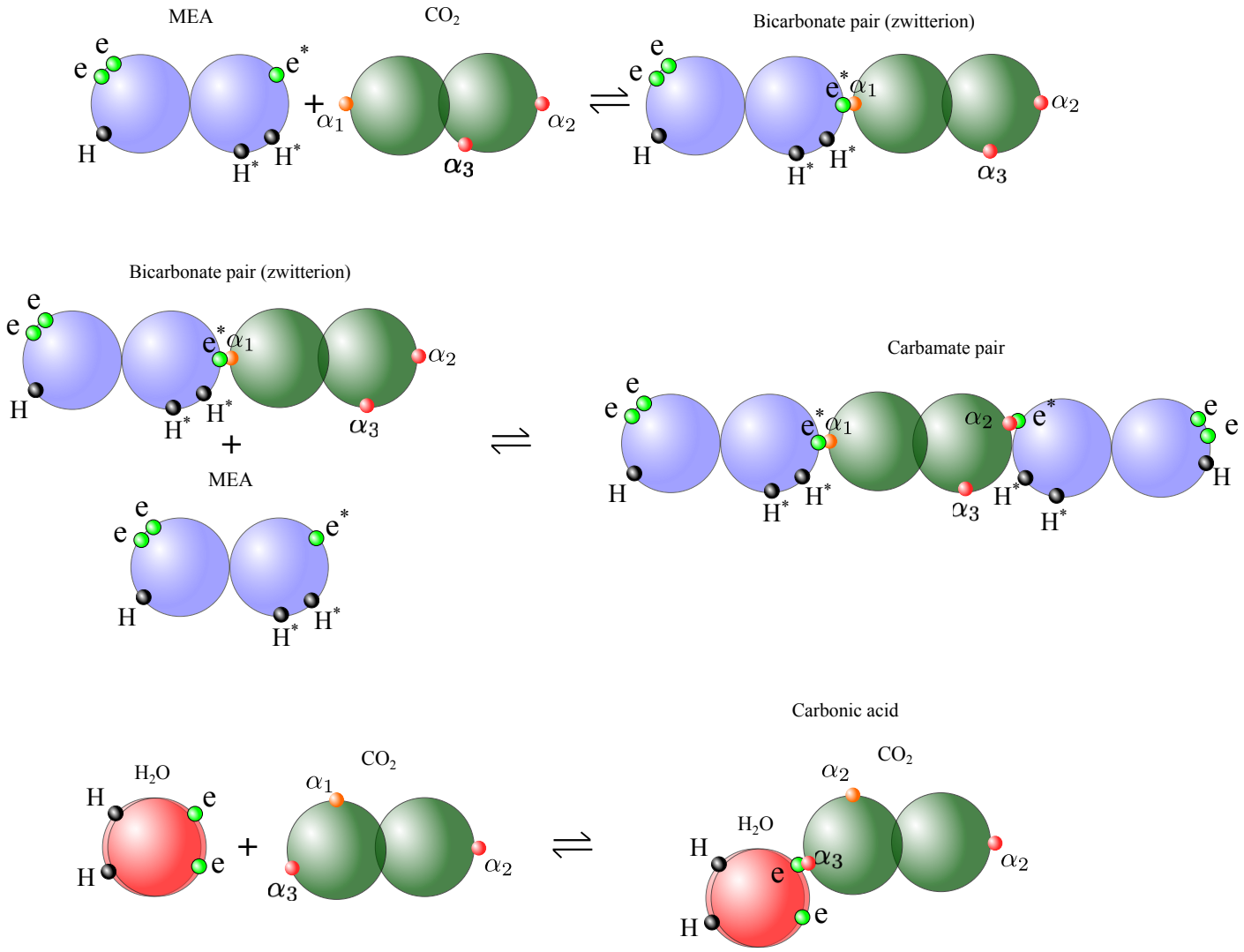

Figure 57: Schematic to show the physical association schemes used to mediate reactions r_1, r_2 and r_3 (top to bottom in the diagram respectively). The large spheres represent the monomeric segments which interact via a Mie potential. We use fused spheres to represent a non-integer number of spherical of segments and tangential spheres to represent an integer number of spherical segments. The smaller spheres are association sites. *e* represents a lone pair of electrons, H represents a hydrogen atom and the superscript '*' is used to distinguish between the different association site types assigned to MEA. *e*-H bonding represents a hydrogen bonding interaction and α-*e* bonding represents a different type of chemical interaction (explained in the text).

In the following text we justify the particular type of model and the association schemes used in this work.

In Figure 56a) we show the association scheme used to model MEA. Due to its molecular weight, and the extensive investigations on the number of segments conducted by Mac Dowell et al. (2009), MEA (HOCH2CH2NH2) is modelled with two tangentially bonded monomeric segments ($\nu^*_{MEA} = 2, S_{MEA} = 1$). Two *e* sites and one H site represent the the lone pair of electrons and the hydrogen atom on the oxygen atom. Similarly, the e^* and two H^* sites on the nitrogen atom can hydrogen bond with other association sites. This corresponds to the asymmetric

association scheme of Mac Dowell et al. (2009) and Rodríguez et al. (2012), which was found to provide a better description of the phase behaviour of mixtures compared to treating the association behaviour of the sites on the different functional groups identically. The e^* site can also associate with the α_1 and α_2 sites on CO_2, which allows for reactions r_1 and r_2. We let e^* associate with both α_1 and α_2 to preserve the stoichiometry of reactions r_1 and r_2. The α_1-e^* and α_2-e^* characterises three types of chemical association in an effective manner. In reaction r_1), a CO_2 molecule is bonded to two molecules of MEA. Therefore, if both α_1-e^* α_2-e^* are bonded, we can approximate one bond that captures the physics of the covalent C-N bond in the carbamate, and the other bond that captures the physics of the chemical association attributed to the tightly-bound ion pair. On the other hand, if only one (α_1 or α_2) site is bonded then this captures the physics attributed to the chemical association of the tightly-bound bicarbonate ion pair (where a CO_2 is bonded to a molecule of MEA).

In Figure 56b) we show the association scheme used to model CO_2. CO_2 is modelled with a non-integer number of segments indicating 2 fused spheres ($v^*_{CO_2} = 2, S_{CO_2} = 0.847$), and is modelled with three sites, α_1, α_2 and α_3, which do not self-associate. The α_1 and α_2 interactions were detailed in the previous paragraph. The pure component parameters for CO_2 are not developed in this work and are taken from the literature model (Papaioannou et al., 2016). In contrast to the previous approach of Mac Dowell et al. (2009) and Rodríguez et al. (2012), we include an association site, α_3 that associates with the electronegative e site on water. This accounts for the various solvation forces that occur in the CO_2-H_2O binary system, including contributions to the free energy that occur in the formation of bicarbonate (reaction r_3). Solvation is expected to be physically present and by adding an association site, one is able to improve the agreement CO_2-water mixture data, including the minimum solubility of water at low temperatures (Kontogeorgis et al., 2006; Papaioannou et al., 2016; Sun and Dubessy, 2010; Diamantonis and Economou, 2012), indicating a more physical model compared to models that do not consider an explicit association interaction. This same approach has been used in a recent paper by Wang et al. (2018a) using the PR-CPA equation of state, where three sites are used on CO_2 to model the MEA-CO_2-H_2O system via a physical approach to the reactions.

In Figure 56c) we show the association scheme used to model H_2O. H_2O is modelled as a slightly non-spherical molecule ($v^*_{CO_2} = 1, S_{CO_2} = 1.2566$) with four association sites, two e sites and two H sites representing the lone pairs of electrons and the hydrogen atoms respectively. This model was developed in chapter 4.

5.5 PARAMETER ESTIMATION

Now that we have assigned the association schemes needed to model the molecules developed in this work, there are numerous like- and un-like parameters that need to be regressed to experimental data. We will first describe the methodology that is used to regress these parameters in section 5.5.1. We then proceed with the typical approach for estimating equation of state parameters by first estimating the pure component parameters (section 5.5.2.1) and then transfer-

ring these to the binary mixtures (section 5.5.2.2) and the ternary mixture (section 5.5.3).

5.5.1 *Methodology*

In order to determine the SAFT parameters we minimize an objective function (WSP($\boldsymbol{w}$) in Chapter 4 which we repeat here) to be minimized :

$$\begin{aligned} \underset{\boldsymbol{x}}{\text{minimize}} \quad & \boldsymbol{w}^{\mathsf{T}} \boldsymbol{f}(\boldsymbol{x}) = \sum_{i=1}^{N_{\text{dim}}} w_i f_i(\boldsymbol{x}) \\ \text{subject to} \quad & \boldsymbol{x} \in X, \end{aligned} \tag{WSP($\boldsymbol{w}$))}$$

where f_i is the error function for property type i, N_{dim} is the number of property types, w_i is the weighting given to property type i, and $\boldsymbol{x}$ is a vector of model parameters to be estimated. X refers to the feasible set of parameters, which implicitly includes any inequality constraints, such as lower and upper bounds on the EoS variables, or equality constraints, in this case when we set certain parameters to be equal.

The individual objective functions representing the deviation between the model and the experiment are defined as follows:

$$f_i(\boldsymbol{x}) = \frac{10^4}{N_i} \sum_{j=1}^{N_i} \left[\frac{Z_{i,j}^{\text{exp.}} - Z_{i,j}^{\text{model.}}(\boldsymbol{x})}{Z_{i,j}^{\text{exp.}}} \right]^2, \tag{102}$$

where $Z_{i,j}^{\text{exp.}}$ is the experimental result for property type i and data point j, $Z_{i,j}^{\text{model.}}$ is the result predicted by the EoS for property type i and data point j, and N_i is the number of data points for each property type i. We report the absolute average deviation ($AAD_i\%$) for property type i to provide a quantitative measure of the accuracy of the fit to experimental data:

$$AAD_i\%(\boldsymbol{x}) = \frac{100}{N_i} \sum_{j=1}^{N_i} \left| \frac{Z_{i,j}^{\text{exp.}} - Z_{i,j}^{\text{model.}}(\boldsymbol{x})}{Z_{i,j}^{\text{exp.}}} \right|. \tag{103}$$

In all cases, the value of the repulsive exponent for the parameters that were regressed was set to 6, following the arguments of Ramrattan et al. (2015), in that an approximate conformal description for any $\lambda^r - \lambda^a$ Mie potential can be obtained with a λ^r-6 potential.

The optimizations are solved using the python implementation of gSAFT (Lafitte et al., 2017), where the Python lmfit package (Newville et al., 2016) is used for the optimization routine which uses a Levenberg-Marquadt algorithm. We use a multi-start algorithm were the initial parameter guesses to the optimization are sampled with a Sobol' sequence (Sobol', 1967). 2048 Sobol points used in every weighted-sum optimization.

5.5.2 *Results*

All of the models resulting from the parameter estimation are clearly exposed in a number of tables. The pure component like-interaction parameters and their asso-

ciation schemes are shown in Table 22; the cross-dispersion interactions are shown in Table 25; and the cross- association interaction parameters are shown in Table 23. Note that the parameter labelled with "*" may be substituted for any of the other set of parameters in tables 29 and 30 in the appendix, as multi-objective optimization was conducted when determining the parameters from ternary partial pressure data, which led to several optimal solutions.

5.5.2.1 *Pure components*

We will first estimate the pure component parameters using pure component experimental data. In order to reduce the parameter degeneracy for the like MEA interactions, the $e^* - H^*$ and $e - H$ association interactions are taken from the self-interactions for ethylamine and ethanol respectively following Mac Dowell et al. (2009). It is assumed that $\epsilon^{HB}_{MEA,MEA,H^*,e} = \epsilon^{HB}_{MEA,MEA,e^*,H}$ and $K^{HB}_{MEA,MEA,H^*,e} = K^{HB}_{MEA,MEA,e^*,H}$ following their work. The pure component parameters that need to be developed are those for ethanol (EtOH), ethylamine ($EtNH_2$), monoethanolamine (MEA) and nitrogen (N_2). The model for CO_2 is taken from the literature ((Papaioannou et al., 2016)) and the model for water used here (model 5NS) is taken from the previous chapter.

For all pure components, we estimate their parameters using saturated liquid density (ρ_L^{sat}), vapour pressure (P^{vap}) and isobaric liquid heat capacity (C_P) (apart from N_2 because it is an inert gas) data along an isotherm. Since we are estimating to heat capacity data, we require an accurate model for the ideal gas heat capacity. All of the parameters used in the ideal gas heat capacity correlations are shown in Table 21, which were taken from Reid et al. (1977). The saturated properties are taken from between the experimental triple point and 95 % of the experimental critical point. C_P data is taken between the experimental triple point and 5 K below the saturation temperature.

As the model is able to predict the experimental data to within the accuracy of the experimental measurements in all cases, we decide not to formulate the parameter estimation of the pure components as a multi-objective problem. For each pure component, we include isobaric heat capacity data at 1 bar in the liquid phase, in addition to saturated liquid density and vapour pressure data, in order to predict this property better and reduce the parameter degeneracy.

Table 21: Ideal gas heat capacity coefficients, according to the polynomial $C_{P,0} = a + bT + cT^2 + dT^3$. The parameters are obtained from (Reid et al., 1977).

Compound	a	b	c	d
H_2O	3.22400E+01	1.92400E-03	1.05500E-05	-3.59600E-09
MEA	9.31100E+00	3.00900E-01	-1.81800E-04	4.65600E-08
CO_2	1.98000E+01	7.34400E-02	-5.60200E-05	1.71500E-08
N_2	3.11498E+01	-1.35700E-02	2.68000E-05	-1.20000E-08
EtOH	9.00800E+00	2.13900E-01	-8.38500E-05	1.37200E-09
$EtNH_2$	3.69029E+00	2.74972E-01	-1.58197E-04	3.80577E-08

In Tables 22 and 23 we define all of the component association sites and show the parameters obtained from the optimization. Note that Table 23 also contains

the unlike cross-association parameters which we will refer back to when these parameters are developed.

Table 22: The like-group parameters for use within the SAFT-γ Mie approach, describing the models for ethanol, ethylamine, carbon dioxide, water and nitrogen. Each chemical functional group in this study represents a single compound. v_k^*, S_k and σ_{kk} are the number of segments in group k, the shape factor, and the segment diameter of group k respectively. λ_{kk}^r and $\lambda_k k^a$ are the repulsive and attractive exponents, and ϵ_{kk} is the dispersion energy between two k groups. $N_{ST,k}$ is the number of association site types on group k, with $n_{k,H}$ and $n_{k,e}$ denoting the number of association sites of type H and e respectively. The CO_2 model is from the literature (Papaioannou et al., 2016), and this table has been adapted from the same reference.

k	Group k	v_k^*	S_k	λ_{kk}^r	λ_{kk}^a	σ_{kk}/Å	(ϵ_{kk}/k_B)/K	$N_{ST,k}$	$n_{k,H}$	$n_{k,e}$	n_{k,H^*}	n_{k,e^*}	n_{k,α_1}	n_{k,α_2}	n_{k,α_3}
1	H2O	1	1.2566	25.1262	6.0000	2.8024	351.2321	2	2	2	0	0	0	0	0
2	MEA	2	1.0000	46.7485	6.0000	3.6701	454.3745	4	1	2	2	1	0	0	0
3	CO_2	2	0.8470	26.4080	5.0550	3.0500	207.8910	3	0	0	0	0	1	1	1
4	N2	2	0.6996	10.0804	6.0000	3.1941	74.1572	0	0	0	0	0	0	0	0
5	EtOH	3	0.7522	12.2824	6.0000	3.2903	238.9664	2	1	2	0	0	0	0	0
6	$EtNH_2$	3	0.7525	11.1842	6.0000	3.3740	226.2855	2	2	1	0	0	0	0	0

Table 23: Group association energies ϵ_{kl}/k_B, bonding volumes $K_{kl,ab}/Å^3$. Then interactions are symmetrical for self association, for example $\epsilon_{kl}/k_B = \epsilon_{lk}/k_B$. The CO_2 self association interactions are set to zero. The parameters labelled with a '*' are determined by multi-objective optimization, and may be substituted by one of the other Pareto-optimal models in Tables 29 and 30.

k	l	Group k	Group l	Site a of group k	Site b of group l	$(\epsilon_{kl}/k_B)/K$	$K_{kl,ab}/Å^3$
1	1	H2O	H2O	H	e	1630.6265	177.6264
1	2	H2O	MEA	e	H	1874.4372	86.6348
1	2	H2O	MEA	H	e	1874.4372	86.6348
1	2	H2O	MEA	e	H*	1108.8370	490.2502
1	2	H2O	MEA	H	e*	1108.8370	490.2502
1	3	H2O	CO_2	e	α_3	1846.4441	15.9580
1	5	H2O	EtOH	e	H	1874.4732	86.6348
1	5	H2O	EtOH	H	e	1874.4732	86.6348
1	6	H2O	$EtNH_2$	e	H	1108.8370	490.2502
1	6	H2O	$EtNH_2$	H	e	1108.8370	490.2502
2	2	MEA	MEA	e*	H*	851.8558	112.0841
2	2	MEA	MEA	e	H	2247.2930	42.7936
2	2	MEA	MEA	e	H*	863.5966	1098.4637
2	2	MEA	MEA	e*	H	863.5966	1098.4637
3	2	CO_2	MEA	α_1	e*	2556.9986*	2830.8090*
3	2	CO_2	MEA	α_2	e*	7734.4758*	0.01706985*
5	5	EtOH	EtOH	H	e	2247.2930	42.7936
6	6	$EtNH_2$	$EtNH_2$	H	e	851.8558	112.0841

In Table 24 we show the level of agreement of pure component models with respect to the experimental data. Here we also detail the specific temperature ranges used in the estimation, the number of points used, and the specific reference where this data was obtained from. The models are all in good agreement with respect to the experimental data for the three properties considered. The only appreciable deviations (AAD > 1%) are for the MEA model, with AAD(ρ_L^{sat}), AAD(P^{vap}) and isobaric heat capacity AAD(C_P) being 1.25%, 1.81% and 2.05% respectively.

Table 24: Percentage average absolute deviations (%AAD) for the vapour pressure ($P^{vap}(T)$) and the saturated liquid densities $\rho_L^{sat}(T)$ obtained in this study for the pure components. For compactness, we label the references accordingly: [1] (Thomson, 1996); [2] (E.W. Lemmon and Friend, 2018);[3] (Liessmann et al., 1995); [4-6] (Rubini et al., 2007; Peleteiro et al., 2005; Anouti et al., 2010; Peleteiro et al., 2004)

Compound	T range	n	%AAD	Ref.	T range	n	%AAD	Ref.	T range	n	%AAD	Ref.
	K		$P^{vap}(T)$		K		$\rho_L^{sat}(T)$		K		C_P	
EtOH	159.1 - 488.3	34	0.267	[1]	159.1 - 488.3	34	0.127	[1]	293.15 - 303.15	29	0.757	[4]-[6]
$EtNH_2$	193 - 410	22	0.81	[1]	243.15 - 403.15	8	0.184	[3]	223.15 - 423.15	10	0.503	[2]
MEA	283.6 - 633.6	376	1.25	[3]	283.6 - 633.6	35	1.81	[3]	300 - 440	3	2.049	[1]
N_2	63.15 - 118.15	11	0.276	[3]	63.15 - 118.15	11	0.54	[2]	-	-	-	-

5.5.2.2 *Binary mixtures*

Having obtained the pure component parameters, we will now estimate the unlike interaction parameters from binary mixtures. The cross interaction parameters containing the α_1 and α_2 sites are not estimated in this section because the reactions they represent do not occur in the binary mixtures.

The unlike association parameters obtained in this section are displayed in Table 23 and the unlike dispersion parameters are displayed in Table 25.

Table 25: Group dispersion interaction energies. λ^a_{kl}, λ^r_{kl} and σ_{kl} are determined from combining rules. $\epsilon_{kl} = \epsilon_{lk}$. CR are the combining rules as defined in reference (Papaioannou et al., 2014). The parameters labelled with a * are determined by multi-objective optimization, and may be substituted by one of the other Pareto-optimal models in Tables 29 and 30.

k	l	Group k	Group l	(ϵ_{kl}/k_B)/K	T range/ K
1	3	H_2O	MEA	427.7310	362-443
1	2	H_2O	CO_2	269.8034	323-353
1	4	H_2O	N_2	CR	-
1	5	H_2O	EtOH	295.2827	351-373
1	6	H_2O	$EtNH_2$	296.0555	285-375
2	3	MEA	CO_2	261.1739*	313-393
2	4	MEA	N_2	CR	-
2	5	MEA	EtOH	CR	-
2	6	MEA	$EtNH_2$	CR	-
3	4	CO_2	N_2	CR	-

ETOH + H_2O To reduce parameter degeneracy in the development of the models for MEA-H_2O, the cross-association parameters are transferred from the binary EtOH-H_2O mixture. We assume that the $e-H$ type hydrogen bonds have the same energy and bonding volume as the $H-e$ type bonds, i.e., $\epsilon^{HB}_{MEA,H_2O,e,H} = \epsilon^{HB}_{MEA,H_2O,H,e} = \epsilon^{HB}_{EtOH,H_2O,H,e} = \epsilon^{HB}_{EtOH,H_2O,e,H}$ and $K^{HB}_{MEA,H_2O,e,H} = K^{HB}_{MEA,H_2O,H,e} = K^{HB}_{EtOH,H_2O,H,e} = K^{HB}_{EtOH,H_2O,e,H}$. We estimate the cross interaction parameters $K^{HB}_{MEA,H_2O,e,H}$ and $\epsilon^{HB}_{EtOH,H_2O,e,H}$ from binary T-x data with pressures ranging from 6666 Pa to 2 MPa and 3000 data points. In Figure 58 we show the description of the model at 1 atm. We obtain a good description of the phase behaviour, including the temperature and composition of the azeotrope, with an average %AAD of 0.1 in the bubble temperature across all pressures.

ETNH$_2$ + H_2O To obtain the MEA-H_2O cross association parameters attributed to the amine functional group, we assume that the association is similar to that between ethylamine and water, and that the $e-H$ type hydrogen bonds have the same energy and bonding volume as the $H-e$ type bonds, i.e., $\epsilon^{HB}_{MEA,H_2O,e^*,H} = \epsilon^{HB}_{MEA,H_2O,H^*,e} = \epsilon^{HB}_{EtNH_2,H_2O,H,e} = \epsilon^{HB}_{EtNH_2,H_2O,e,H}$, and $K_{MEA,H_2O,e^*,H} = K_{MEA,H_2O,H^*,e} = K_{EtNH_2,H_2O,H^*,e} = K_{EtNH_2,H_2O,e^*,H}$. T-x data were used in the

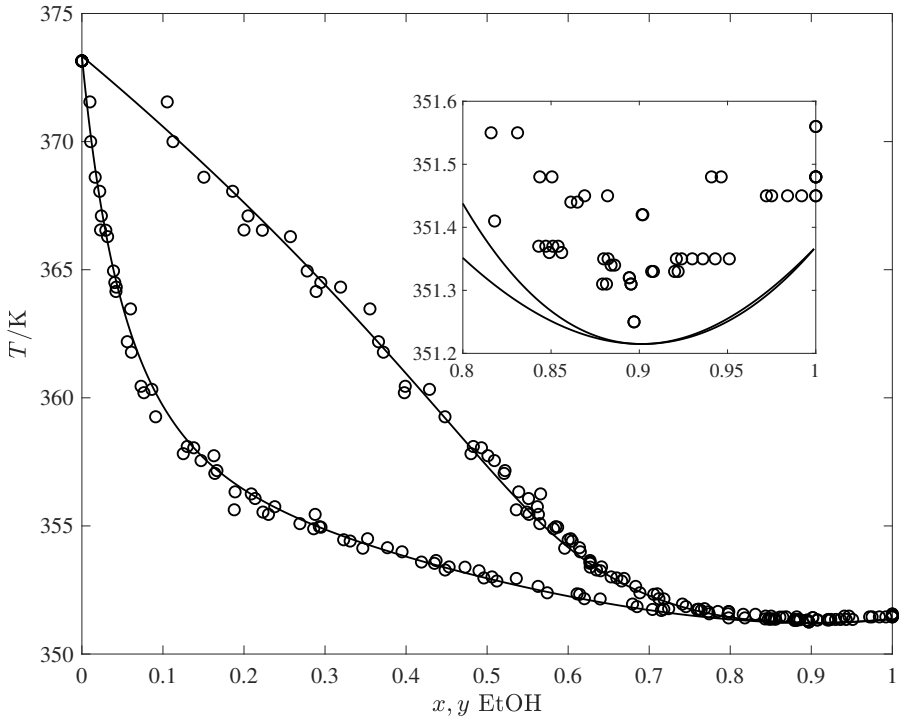

Figure 58: Ethanol-water binary T-x data at 1 atm. The data sets used in the estimation are at several isobars ranging between 6666 Pa and 2 MPa with 3000 different data points Liessmann et al. (1995).

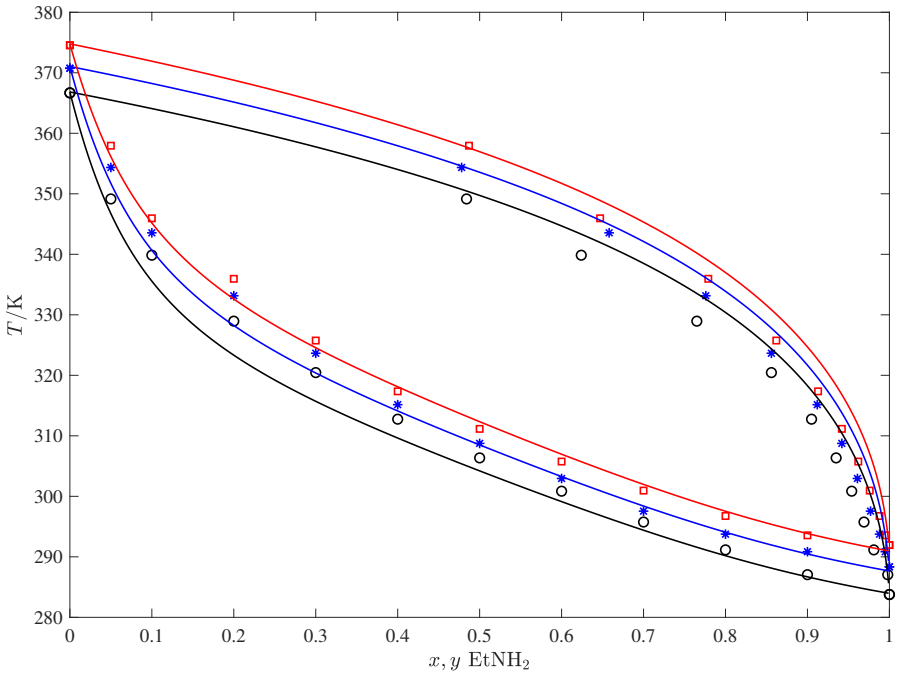

Figure 59: Comparison between the model and the experiments for the binary mixture of $EtNH_2$ and H_2O: binary phase diagrams at three different isobars. The isobars are distinguished by their colours: 79993 Pa (black), 93326 Pa (blue), 106660 Pa (red). The experimental data is from Bittrich (1963).

parameter regression. In Figure 59 we show that a good description of the binary VLE is obtained.

MEA + H_2O After transferring the parameters from the ethanol-water and ethylamine-water mixtures, only a single parameter needs to be estimated to obtain a good prediction of the MEA + H_2O mixture, ϵ_{MEA,H_2O}. This was determined by regression to two T-x isobars at 66.7 kPa and 101.3kPa, and a single P-x isotherm at 363.15 K. In Figures 60 and 61 we see that there is an excellent agreement with the experimental data.

CO_2 + H_2O For CO_2-H_2O there are three cross interaction parameters that need to be determined: ϵ_{CO_2,H_2O}, $\epsilon^{HB}_{CO_2,H_2O,\alpha_3,e}$ and $K_{CO_2,H_2O,\alpha_3,e}$. These are regressed to binary vapour liquid and liquid-liquid equilibria data presented in Figures 62a and 62b. The atypical curvature representing a minimum in solubility of water is captured with remarkable accuracy. Additionally, the water rich phase is captured to a high degree of accuracy. Although not shown here, we were not able to achieve the same curvature in the CO_2 rich phase without accounting for solvation. This model also provides a good prediction of the excess enthalpy of mixing, as shown in Figure 63. This is an important caloric property to accurately capture since it will have some contribution to the overall enthalpy change upon CO_2 absorption for the CO_2 + amine solvent mixture.

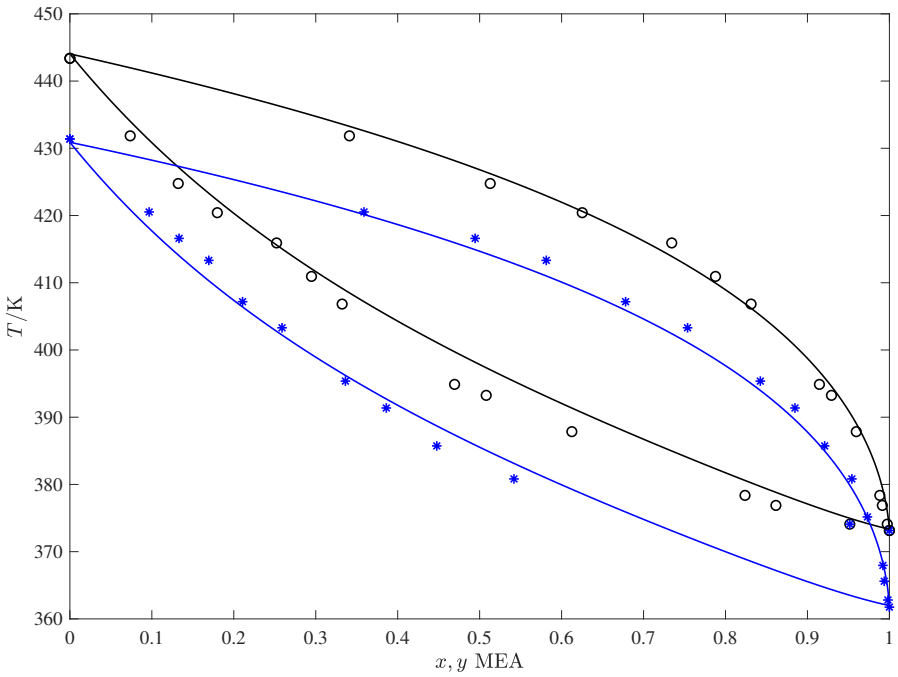

Figure 60: Comparison between the model and the experiments for the binary mixture of MEA and H_2O: binary phase diagrams at three different isobars. The isobars are distinguished by their colours: 66660 Pa (blue), 101330 Pa (black). The experimental data is from Cai et al. (1996).

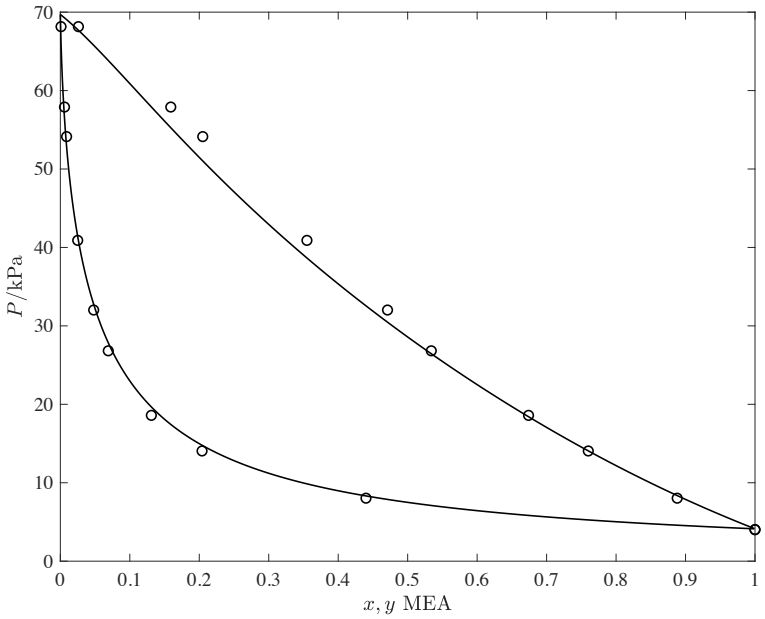

Figure 61:

Comparison between the model and the experiments for the binary mixture of MEA and H_2O: binary phase diagram for a single isotherm where T = 363.15 K. The experimental data is from Cai et al. (1996).

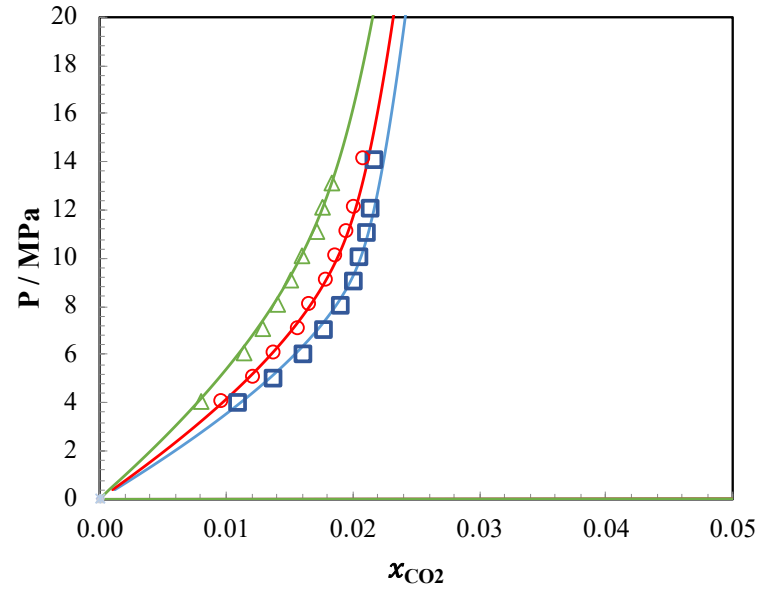

(a)

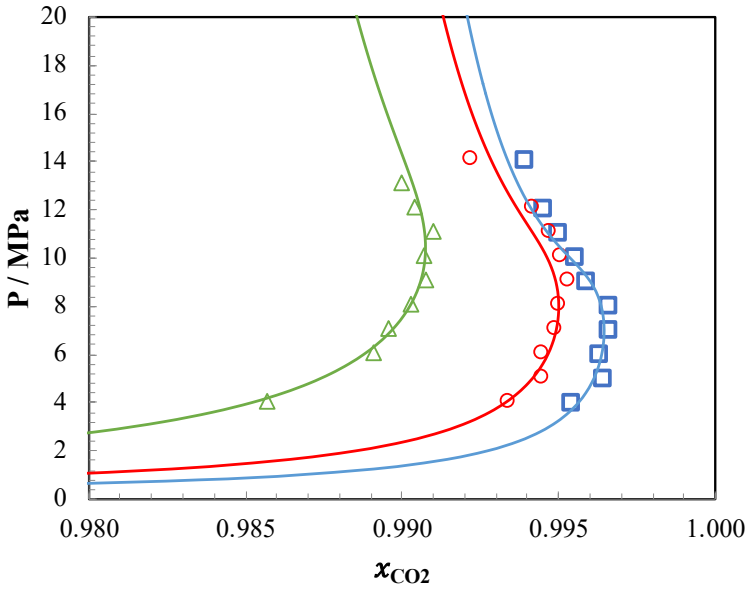

(b)

Figure 62: Isothermal pressure- mole fraction diagrams for the vapour-liquid and liquid-liquid equilibira of water and carbon dioxide. The symbols represent the experimental data of Bamberger et al. (2000), at T = 323.2 K (squares), T = 333.2 K (circles), and T = 353.1 K (triangles). The solid curve is the prediction of the SAFT-γ Mie equation of state. a) and b) represent the water rich and carbon dioxide rich phases respectively.

5.5.3 *Ternary mixture*

The unlike association parameters obtained in this section are displayed in Table 23 and the unlike dispersion parameters are displayed in Table 25. Ternary mixture data is required in order to determine the association parameters that mediate the

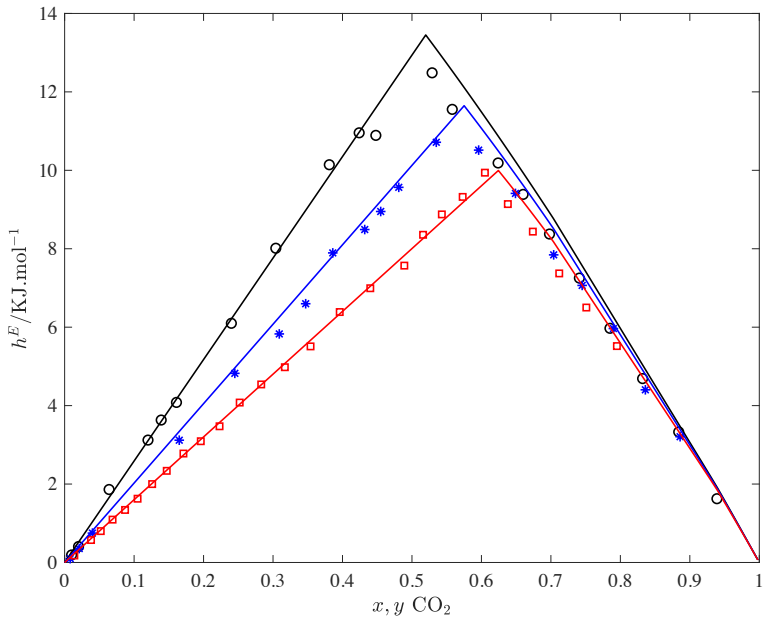

Figure 63: Isothermal-isobaric excess molar enthalpy of mixing for H_2O +CO_2. The symbols represent the experimental data at T = 523.15 K and pressures of P = 10.4 MPa (circles), P = 12.4 MPa (stars), and P = 15 MPa (squares). Some of the model and experimental values represent the two phase region. The experimental data is taken from Teng et al. (1997).

chemical reactions that occur in solution. Following the approaches of Mac Dowell et al. (2009) and Rodríguez et al. (2012), we use vapour pressure data to determine the parameters. Although heat capacity data is available, we do not include it in the fitting because it was found that the cross interaction parameters for CO_2-water have an insignificant effect on the mixture heat capacity. The parameters that need to be determined are: $\epsilon_{CO_2,MEA}$, $\epsilon^{HB}_{\alpha_1,e^*}$ and $K^{HB}_{\alpha_2,e^*}$,$K^{HB}_{\alpha_1,e^*}$ and $K^{HB}_{\alpha_2,e^*}$. In this case, we treat the estimation of these parameters as a multi-objective optimization, where we define the objectives to be:

$$f_i(\boldsymbol{x}) = \frac{1}{N_i}\sum_{j=1}^{N_i}\left[\log_{10}(P^{exp.}_{CO_2,i,j}) - \log_{10}(P^{model}_{CO_2,i,j})\right]^2, \tag{104}$$

where $P^{exp.}_{CO_2,i,j}$ is the jth data point for the experimental vapour pressure at the ith temperature and the $(P^{model}_{CO_2,i,j})$ refers to the model prediction. The logarithm of the partial pressure is chosen due to the experimental data spanning several orders of magnitude; using an objective function 102 would bias the goodness of fit to low partial pressures (e.g., Jou et al. (1995) report partial pressures as low as 1.5 Pa). We use the algorithm described in chapter 4 with $t = 0.0001$, and decide to stop the algorithm after the first 50 points are generated. The resulting Pareto surface from the multi-objective optimization problem is shown in Figure 64, while the %AAD representation of the surface is shown in Figure 65. All of the solutions are shown in Tables 29 and 30 in the appendix to this chapter. From the Pareto-optimal models found, it appears that the data is best represented by an α_2 site that bonds with a large bonding energy ($(\epsilon^{HB}_{\alpha_2,e^*}/k_B) \approx 8000$ K) and a relatively small bonding

volume ($K^{HB}_{\alpha_2,e^*}/Å^3 \approx 0.01$ Å^3), and an α_1 site that bonds with a lower bonding energy ($(\epsilon^{HB}_{\alpha_2,e^*}/k_B) \approx 2000$ K) and a relatively large bonding volume ($K^{HB}_{\alpha_2,e^*}/Å^3 \approx 10000$ Å^3). We expect that the $\alpha_2 - e^*$ bond is capturing the physics of the covalent C-N bond present in the carbamate (high energy, small volume), while the $\alpha_1 - e^*$ bond is capturing the physics of the chemical association due to ion pairing (lower energy and high volume). The latter bond type is present in both the carbamate and bicarbonate. Although the bonding volumes vary several orders of magnitude, the values are not unphysical, and they are effectively empirical parameters that incorporate site geometry as well as size. The association kernel in (Dufal et al., 2015b) is shown to vary exponentially with respect to the change in the radius of the association site.

Following the methodology used in the previous chapter we pick a Pareto point, P_{ref}, according to equation 100. We can see that this point, indicated in Figure 65 is close to the Pareto knee. The parameters and objectives for the chosen Pareto point are displayed in Tables 26 and 27 respectively. These represent the cross-interactions between CO_2 and MEA. In terms of the AADs, the deviations appear fairly large (e.g., approximately 10 % at 353 K). These large AAD values are mainly due to the large errors at very low partial pressures/ loadings. In Figure 66, we show the level of agreement of this model with respect to experimental partial pressure data. The model captures the highly nonlinear dependency of the partial pressure on the CO_2 loading well. This curvature is mainly due to the saturation of α_1 and α_2 sites, which can be seen by the inflexion points occurring at loadings close to 0.5 and 1. There is a significant deviation at low loading, where the partial pressures are very small. It is clear from the figure that the new SAFT-γ Mie models describe the experimental data more accurately than the SAFT-VR SW models of Rodríguez et al. (2012). In particular, the description of the SAFT-γ Mie models is better at higher temperatures, and we are able to predict the high temperature (433 K), which is not included in the parameter estimation, with excellent accuracy.

Table 26: Parameters for the chosen Pareto-optimal model for cross-interactions between CO_2 and MEA in aqueous solution.

Model	(ϵ/k_B)/K	$(\epsilon^{HB}_{\alpha_1,e^*}/k_B)$/K	$(\epsilon^{HB}_{\alpha_2,e^*}/k_B)$/K	$K^{HB}_{\alpha_1,e^*}/Å^3$	$K^{HB}_{\alpha_2,e^*}/Å^3$
13	261.1739	2556.999	7734.476	2.830809E+03	1.706985E-02

Table 27: Objective functions and %AADs for the chosen Pareto-optimal model for cross-interactions between CO_2 and MEA

Model	$f_{P_{CO_2}(T)}$			AAD %		
	T=313 K	T = 353 K	T=393 K	T=313 K	T = 353 K	T=393 K
13	0.0283	0.0252	0.0525	7.511	9.771	4.758

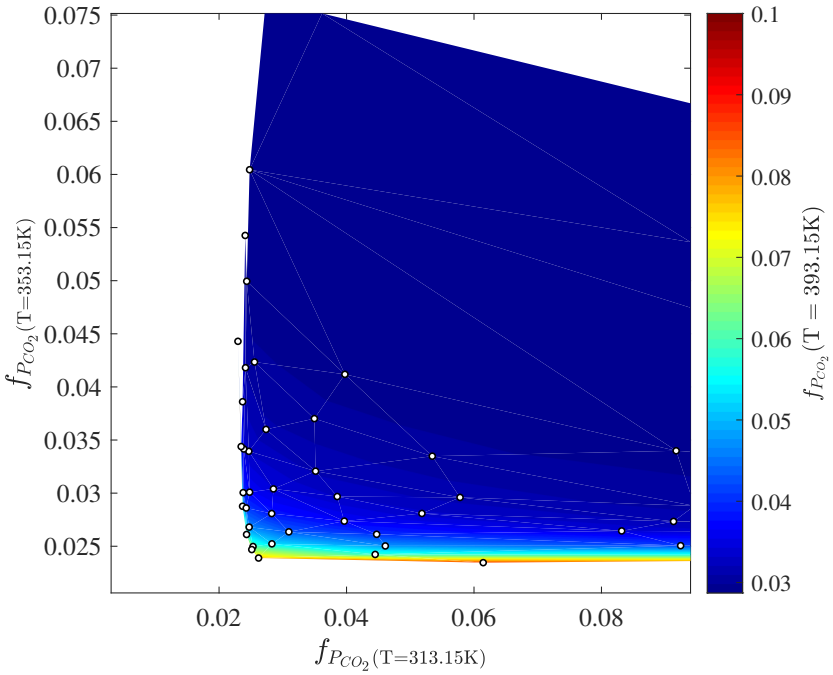

Figure 64: Pareto surface for the three dimensional multi-objective optimization problem considered in this chapter. The three objectives represent the deviation between the model and partial pressure data of Jou et al. (1995) at three different isotherms: 313.15 K, 353.15 K and 393.15 K. The open circles are the individual Pareto points.

5.6 ASSESSMENT OF THE MODELS

5.6.1 *Heat of absorption*

It is important to know the heat of absorption of CO_2 in aqueous amine solutions when designing acid gas removal plants. The temperature increase in the absorber, which occurs mainly due to the exothermic heat of reaction, affects the equilibrium amount of absorbed gas. The heat of desorption is directly related to the energy requirement of the re-boiler in the desorber unit. This heat, provided by hot steam passing through the re-boiler, is required in order to: heat the CO_2 solution to the boiling point, break the chemical bonds between CO_2 and the absorption solvent, and generate water vapour by both physical solubility and the chemical equilibrium for aqueous phase reactions occurring among CO_2, water, and amines. The overall enthalpy of reaction of gaseous CO_2 with aqueous alkanolamines is the sum of the individual enthalpies of reaction in the aqueous phase and the enthalpy of physical absorption of CO_2 from the gas phase to the aqueous phase (Gupta et al., 2013). Experimentally it is difficult to measure both these effects separately, the physical and chemical equilibrium are highly coupled, so these are usually combined and referred to by the overall "heat of absorption" (Svensson et al., 2013).

For chemical absorption systems, the Gibbs-Helmholtz equation relates the enthalpy of solution for a particular gas component, i, to the temperature derivative

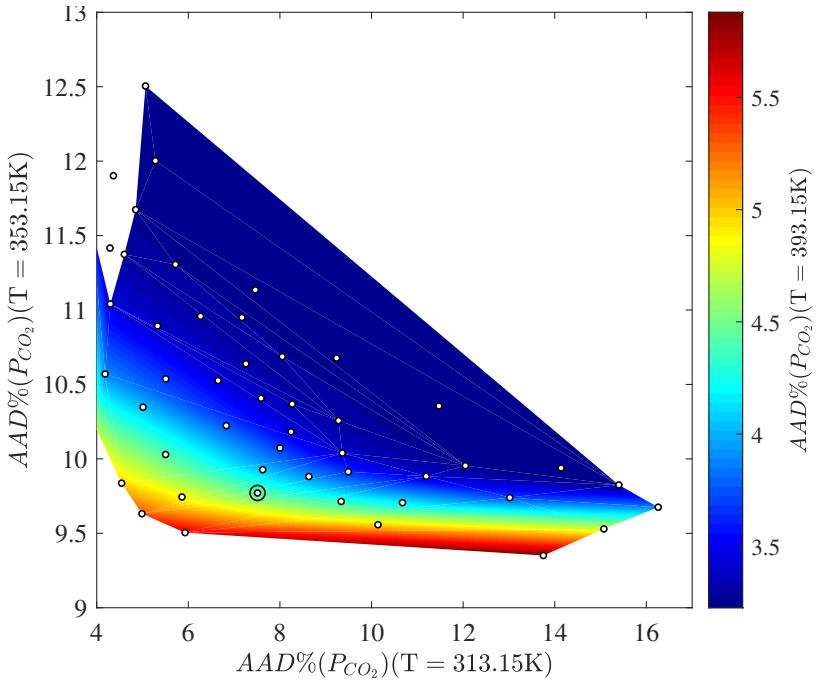

Figure 65: The %AAD representation of the Pareto optimal models for the three dimensional multi-objective optimization problem. The three objectives represent the deviation between the model and partial pressure data of Jou et al. (1995) at three different isotherms: 313.15 K, 353.15 K and 393.15 K. The open circles are the individual Pareto points. The Pareto point surrounded by another open black circle is model 13, which is the model we choose for further investigation.

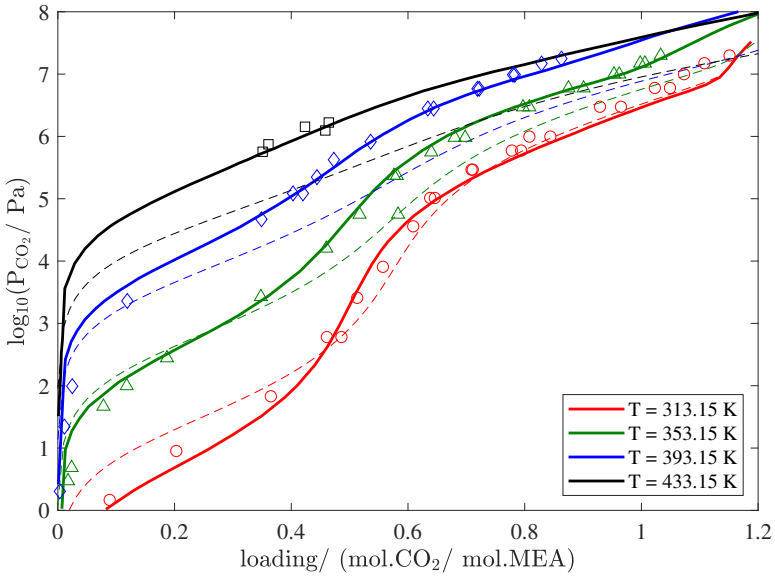

Figure 66: The partial pressure of CO_2 for a 30 wt% (mass) solution of MEA and water. Note that this mass percentage corresponds to the composition of the solution in the liquid phase with no CO_2. The experimental data is from Jou et al. (1995) (313.15 K, 353.15 K and 393.15 K), and Xu and Rochelle (2011) (433.15 K). The temperature at 433.15 K is not included in the parameter estimation. The dotted lines are the predictions of the SAFT-VR SW models of Rodríguez et al. (2012).

of its fugacity in the liquid phase at the bubble pressure and fixed apparent composition. We take its formal definition from Mathias and O'Connell (2012):

$$\Delta\tilde{H}_{0i} = \left(\frac{\partial H}{\partial n_{0i}}\right)_{T,P,n_{0j\neq i}} - h_i^* = R\left(\frac{\partial \ln f_i}{\partial(1/T)}\right)_{\{P,x_0\}}. \tag{105}$$

In this notation, the subscript "o" refers to apparent chemical species Where $\Delta\tilde{H}_{0i}$ is the differential enthalpy of solution of component i, ∂n_{0i} indicates an infinitesimal amount of gas absorbing in to the liquid phase at constant T, P, and n_{0j} is the apparent composition of the liquid phase, i.e., the composition assuming that there are no reactions occurring in the liquid. h_i^* is the ideal gas enthalpy of the absorbing gas (i) at the reference pressure. Although this is a precise thermodynamic definition, it is difficult to measure the partial derivates experimentally and is therefore subject to numerous approximations. For example, the fugacity is substituted for partial pressure, or the partial derivative is carried out along the saturation curve (Kim and Svendsen, 2007). Mathias and O'Connell (2012) determined that under suitable approximations, which are valid for absorption of CO_2 into MEA, the differential heat of absorption can be written in terms of experimental partial pressure measurements:

$$(P_{CO_2})_{\sigma,\theta,T_1} = (P_{CO_2})_{\sigma,\theta,T_0} * \exp\left[\int_{1/T_0}^{1/T_1} \frac{\Delta\tilde{H}_{0CO_2}}{R} d(1/T)\right], \tag{106}$$

where θ is the loading, and T_0 is a base temperature for which the partial pressure at T_0 is known. The authors show that according to the partial pressure data of Jou et al. (1995), used in our estimations, a constant heat of absorption of approximately -85 kJ.mol^{-1} CO_2 provides a good fit to the partial pressure data between the full range of temperatures (298.15 and 423.15 K). The heats of absorption quoted by Arcis et al. (2011) and Carson et al. (2000) are in close accordance with this observation, with average values of -88 kJ.mol^{-1} and -82 kJ.mol^{-1} over the full temperature range respectively. The authors found inconsistencies between the partial pressure and heat of absorption data for the quoted values by Mathonat et al. (1998) and Kim and Svendsen (2007), because applying the Gibbs-Helmholtz equation to this data provides poor predictions, particularly at high temperatures. Kim et al. (2014) improve on their measurement technique in their later work, reporting not such a large temperature dependency on the heat of absorption, however, the results are still not in accordance with the partial pressure data. Due to these arguments, we choose to model the experiment of Arcis et al. (2011) as a reliable measurement of the heat of absorption. Rather than applying the Gibbs-Helmholtz equation to the SAFT-γ Mie equation of state, we decide to simulate the experiment that was conducted, to avoid any misinterpretation of the definition of the quoted heat of absorption given by the authors.

5.6.1.1 *Simulation of a flow calorimetry experiment*

Arcis et al. (2011) measure the heat of absorption (or heat of solution) of CO_2 in MEA solution in a constant volume flow device. Each experiment is run at a constant temperature (322.5 and 372.9) K and constant pressure between 0.5 MPa and 5 MPa. Two streams enter the calorimeter, one is pure CO_2 and the other is

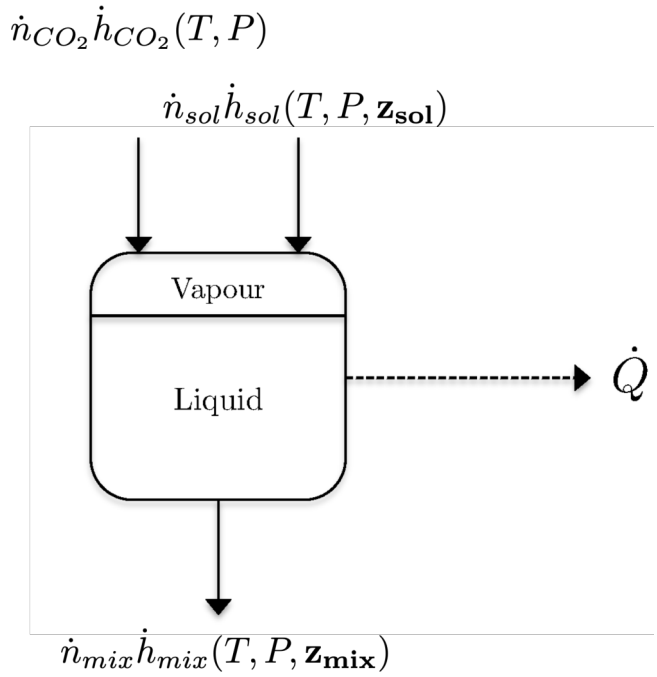

Figure 67: Schematic of the model for the experiment by Arcis et al. (2012).

an unloaded solution of aqueous MEA at a specified mass composition. Streams enter the calorimeter at the same temperature and pressure as the mixing device, and exit the device as a mixture of either one phase or two phases, depending on the ratio of the flowrates of CO_2 and the solvent. At pressures above 3 MPa, the authors note that there were some issues with mixing inside the calorimeter, so these pressures were not considered. The change in enthalpy was obtained from the thermophile signal (μV). A baseline signal was measured whilst only the aqueous MEA solution was flowing through the calorimeter, this is the baseline signal where no enthalpy change is present. The heat of absorption was calculated from the measured quantities in Equation 107:

$$\Delta H_{abs}(kJ/mol - CO_2) = \frac{\Delta_{signal}}{E \times \dot{n}} \tag{107}$$

where Δ_{signal} is the difference between the thermophile signal (the electronic signal from the thermometer) during mixing and the baseline signal. E is the conversion from the thermophile signal to heat power, determined from calibration with the same experiment with water+ethanol with a well-known enthalpy of mixing. $\dot{n}$ is the total molar flow rate of CO_2 or MEA entering the calorimeter. The enthalpy change measured is therefore the integral heat of absorption at a given CO_2 loading, θ. An energy balance around the reactor vessel gives:

$$\dot{Q} = \dot{n}_{mix}h_{mix}(T,P,z_{mix}) - \dot{n}_{sol}h_{sol}(T,P,z_{sol}) - \dot{n}_{CO_2}h_{CO_2}(T,P), \tag{108}$$

where $\dot{Q}$ is the heat output from the reactor measured by the thermophile; $\dot{n}$ are the molar flowrates, h is the molar enthalpy ($kJ.mol^{-1}$); z are the mole fractions; subscript "mix" refers to the total mole fraction of the entire mixture inside the

calorimeter (MEA + CO_2 + H_2O); "sol" refers to the total mole fraction of the solvent (MEA + H_2O); and "CO_2" is the pure gaseous stream of CO_2 that enters the calorimeter. The SAFT EoS may be used to determine the enthalpy terms on the right hand side of equation 108, while the other terms are independent variables. When calculating the enthalpies with T,P,z as inputs, a TP-flash is used to determine the enthalpy. When the stable solution is two phases, the enthalpy is the sum of the total enthalpies of the two phases.

The heat power is divided by the molar flow rate of the CO_2 stream:

$$\Delta H_{abs}(kJ/mol - CO_2) = \frac{\dot{n}_{mix}h_{mix}(T,P,z_{mix}) - \dot{n}_{sol}h_{sol}(T,P,z_{sol}) - \dot{n}_{CO_2}h_{CO_2}(T,P)}{\dot{n}_{CO_2}} \tag{109}$$

The total number of moles does not change during each measurement assuming steady state is reached. Dividing through by $\dot{n}_{tot}$ gives

$$\Delta H_{abs,CO_2} = \frac{h_{mix}(T,P,z_{mix}) - (1-z_{CO_2})h_{sol}(T,P,z_{sol}) - z_{CO_2}h_{CO_2}(T,P)}{z_{CO_2}} \tag{110}$$

The loading, θ, is defined by the inlet flow rates to the mixing vessel:

$$\theta = \frac{\dot{n}_{tot,CO_2}}{\dot{n}_{tot,MEA}} = \frac{z_{CO_2}}{z_{MEA}}. \tag{111}$$

The amounts of MEA and H_2O are related via the mass fraction of the solvent solution:

$$\gamma = \frac{z_{MEA}}{z_{H_2O} + z_{MEA}} \frac{MW_{MEA}}{MW_{H_2O}}. \tag{112}$$

Where γ is the mass fraction of the solvent and MW_i are the molecular weights for component i.

5.6.1.2 *Results*

In Figure 68 we show the model predictions for the simulated experiment. The curvature can be described as follows. At a loading of 0.5, there is a drop in the heat of absorption due to the α_1 and α_2 sites on CO_2 becoming saturated, i.e., it is not possible to form any more carbamate due to the reaction stoichiometry. The change in curvature close to loadings of 1.2 represent the formation of a vapour phase. The values of the heat of absorption at low loadings are in accordance with the experiment of Arcis et al. (2011), with the model predicting values of approximately -90 kJ.mol^{-1}. We find that this value is insensitive to the pressure and solvent concentration at low loadings, in accordance with the experiment. The SAFT-VR SW models of Rodríguez et al. (2012) predict a heat of absorption at low loadings of approximately -70 kJ.mol^{-1}. The quality of the prediction is particularly good at T=372.9 K and 30 wt% solvent, where the heat of absorption is predicted with excellent accuracy over the entire range of CO_2 loadings.

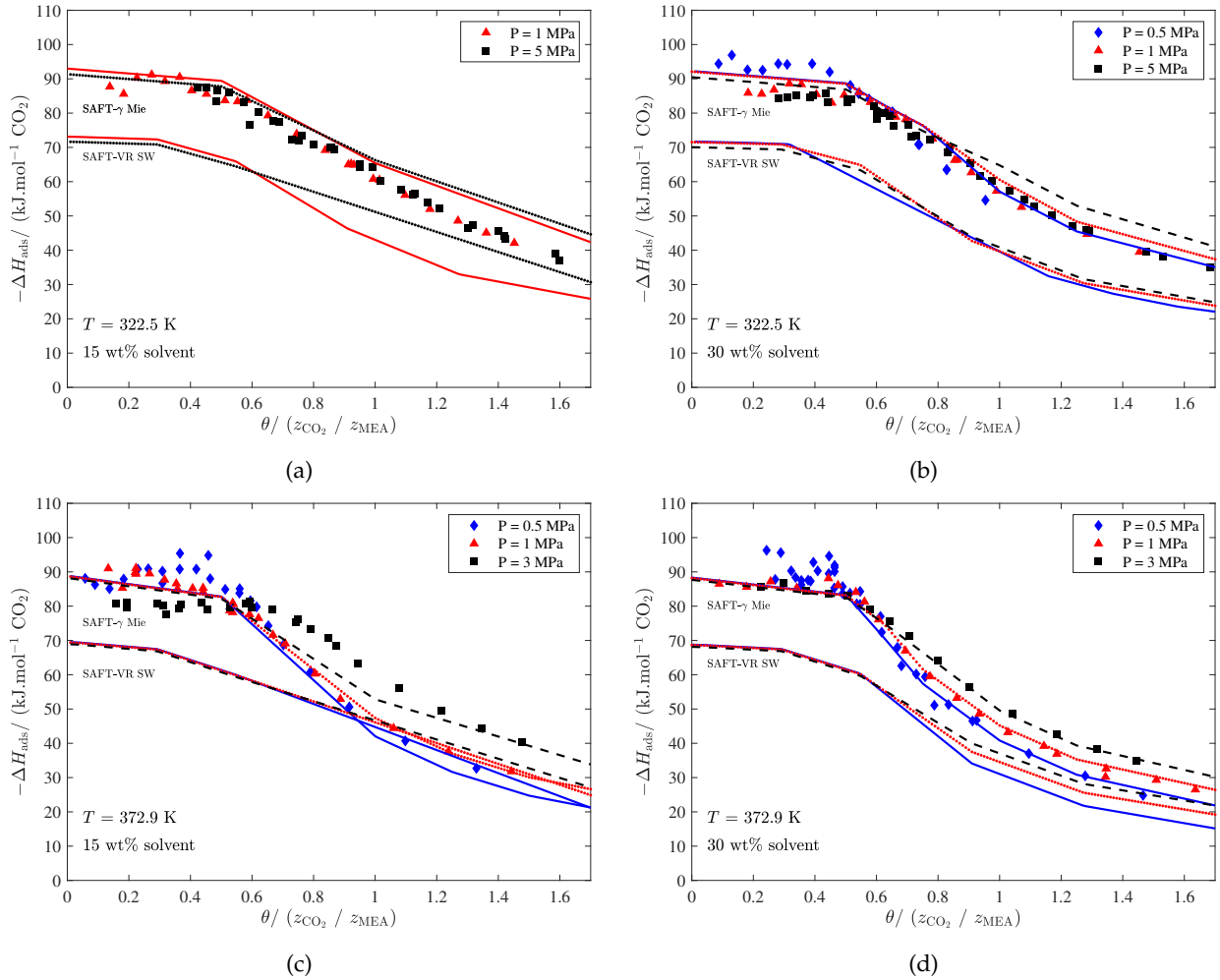

Figure 68: Comparison between the predictions of the SAFT-γ Mie models, the prediction of the SAFT-VR SW models of Rodríguez et al. (2012), and experimental data (Arcis et al., 2011) for the enthalpy of solution of CO_2 in aqueous MEA. a) T = 322.5 K, 15 wt% solvent. b) T = 322.5 K, 30 wt% solvent. c) T = 372.9 K, 15 wt% solvent. d) T = 372.9 K, 15 wt% solvent. The pressures are labelled in the figure legends according to the colour of the lines and scattered experimental data.

5.6.2 *Heat capacity*

The prediction of the heat capacity of the ternary mixture is shown in Figure 69. An excellent description of the heat capacity is obtained at low loadings, however we obtain the incorrect temperature dependence with respect to the CO_2 loading which leads to maximum deviations in the heat capacity of 7% at loadings of 0.5. This discrepancy is likely due to the simplified implicit approach used to model the reactions.

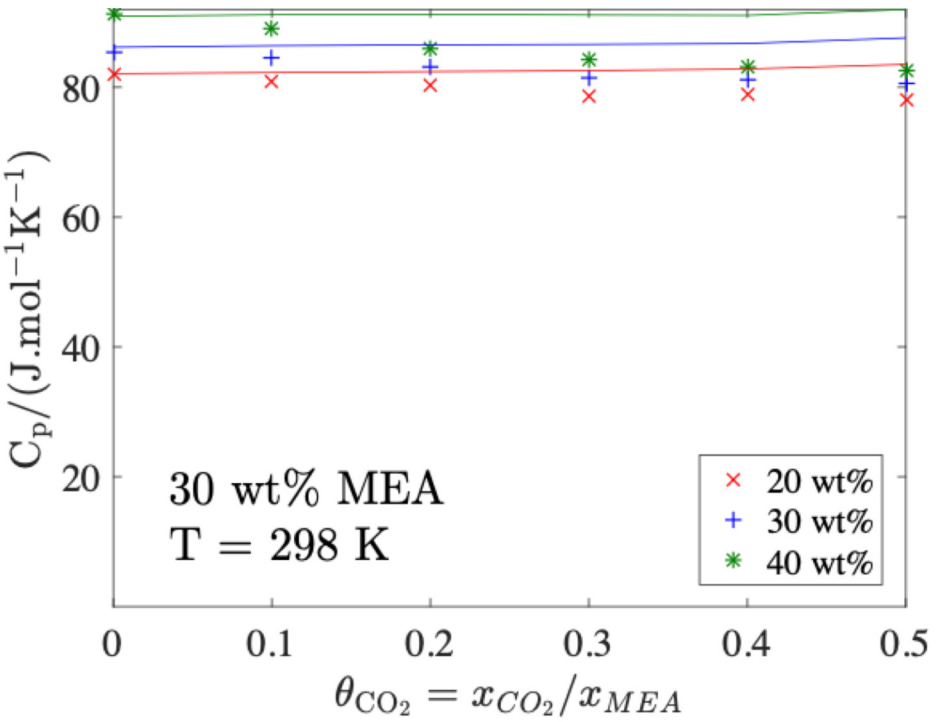

Figure 69: Isobaric heat capacity at 1 bar and three different temperatures using the newly developed SAFT-γ Mie models in this chapter. The symbols are experimental data points from Weiland et al. (1997).

5.6.3 *Chemical speciation*

In Figure 71 we show the predicted mole fractions of the key chemical species in solution, which were measured using NMR spectroscopy by Böttinger et al. (2008). The mole fractions are calculated according to a statistical analysis of the fractions of association sites not bonded, which is implicitly calculated in the SAFT equation of state within the association term. Note that this analysis on the fractions can be used to approximate the number density of any molecule that the association scheme permits, for example, a molecule with an "e" and "H" site that forms "e-H" bonds will form an infinite distribution of chain-like clusters (Jackson et al., 1988). The concentrations of the species are determined as follows:

Referring back to reaction (r_1) and Figure 57, a carbamate molecule is formed when both α_1 and α_2 are bonded. The bonded fractions can be treated as probabilities, so we multiply the probability that both sites are bonded:

$$x_{\text{carbamate}} = x_{CO_2}[(1 - X_{\alpha_{1,CO_2}})(1 - X_{\alpha_{2,CO_2}})]. \tag{113}$$

According to reaction (r_2), the concentration of bicarbonate can be calculated as the probability that α_1 is bonded and not α_2, plus the probability that α_2 is bonded and not α_1:

$$x_{\text{bicarbonate}} = x_{CO_2}[(1 - X_{\alpha_{1,CO_2}})X_{\alpha_{2,CO_2}} + (1 - X_{\alpha_{2,CO_2}})X_{\alpha_{1,CO_2}}]. \tag{114}$$

The amount of free CO_2 can be calculated by the probability that both sites are not bonded:

$$x_{CO_2,\text{monomer}} = x_{CO_2}X_{\alpha_{1,CO_2}}X_{\alpha_{2,CO_2}}. \tag{115}$$

Also measured by Böttinger et al. (2008) is the concentration of MEA and protonated MEA. This can be approximated by the total amount of MEA that does not exist in the form of a carbamate:

$$x_{MEA,MEAH+} = x_{MEA}[1 - x_{CO_2}(1 - X_{\alpha_{1,CO_2}})(1 - X_{\alpha_{2,CO_2}})]. \quad (116)$$

It is gratifying to see that all of the concentrations of the chemical species measured by Böttinger et al. (2008) are predicted well by the model. Note that this prediction is not purely due to the stoichiometry enforced by the association scheme and prediction of the experimental data requires that some of the α sites are not fully bonded or not bonded. In Figure 70 we show the fraction of site types that are bonded in the mixture. Up until loadings close to 0.5, the majority of the α_1 and α_2 sites are bonded, meaning that the most of the CO_2 is present in the carbamate at low loadings. This is also shown in Figure 71. The fraction of bonded α_1 sites begins to decrease prior to loadings of 0.5. Because both α_1 and α_2 are not maximally bonded (CO_2 can bond with 2 MEA molecules up until loadings of 0.5), the equilibrium positions of reactions (r_1) and (r_2) lie somewhere in the middle, indicating that there is some competition between entropic and enthalpic contributions to the free energy. It is clear that MEA has a preference to bond with the α_2 over the α_1 site from Figure 70, because the fraction of bonded α_1 sites is the first to decrease. The $\alpha_2 - e^*$ interaction should represent a covalent bond due to its high bonding energy and low bonding volume, but this bond should only be present in the carbamate. Hence, the bicarbonate may be characterised by an association energy that is unphysical. This issue could be resolved by accounting for bond cooperativity (Sear and Jackson, 1996c).

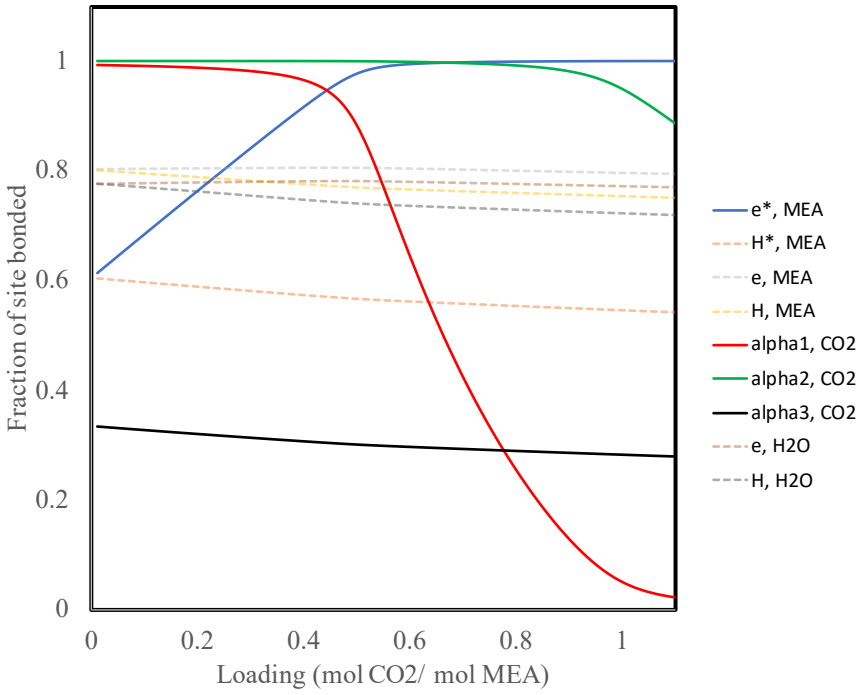

Figure 70: The fraction of sites bonded for each site type using the newly developed SAFT-γ Mie models used in this chapter.

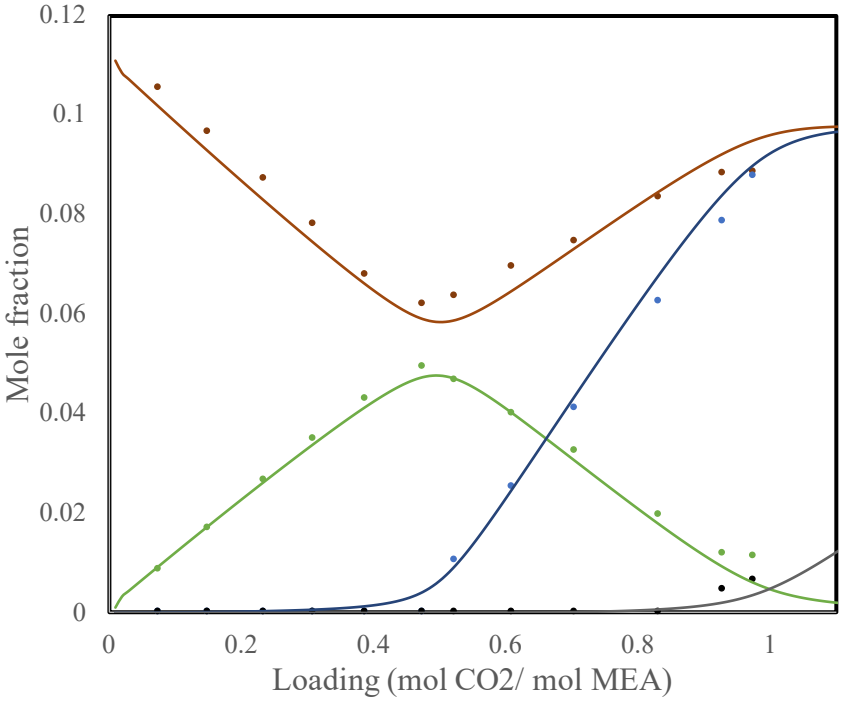

Figure 71: The prediction of the mole fraction of the reaction products newly developed SAFT-γ Mie models used in this chapter. The experimental data points are the symbols and the lines are the predictions of the model (Böttinger et al., 2008). Green is carbamate, blue is bicarbonate, brown is the combination of free MEA and protonated MEA, and black is free carbon dioxide.

5.7 RE-ASSESSMENT OF THE COLUMN PROFILES

Following the development of the new homonuclear SAFT-γ Mie models for the CO_2-MEA-H_2O-N_2 system, the thermodynamic models are input into the model for the absorber. We transfer the diffusivity scaling of the "apparent" mole fraction of CO_2 directly from the previous study ($\tau = 0.041$). In Table 28, we show the deviations in temperature, mole fraction and temperature between the two models. In figures 72-81 we show the comparison between the two thermodynamic models and with respect to the pilot plant data (Tontiwachwuthikul et al., 1992). By visual inspection of the column profiles, the two thermodynamic models perform very similar. In all cases but one (run T19), the new models do marginally better in terms of the temperature profile. The composition profiles are almost exactly the same. We reiterate that the previous SAFT-VR SW models may be predicting the temperature profile with a good degree of accuracy due to a cancellation of errors, i.e., the mixture heat capacity is under predicted by $\approx$ 15 %, and the heat of absorption is under predicted by $\approx$ 20 %.

5.8 CONCLUSION

In this chapter, new thermodynamic models were developed for the SAFT-γ Mie EoS. The parameters developed are independent of thermodynamic state. These models improve upon the previous SAFT-VR SW models of Rodríguez et al. (2012),

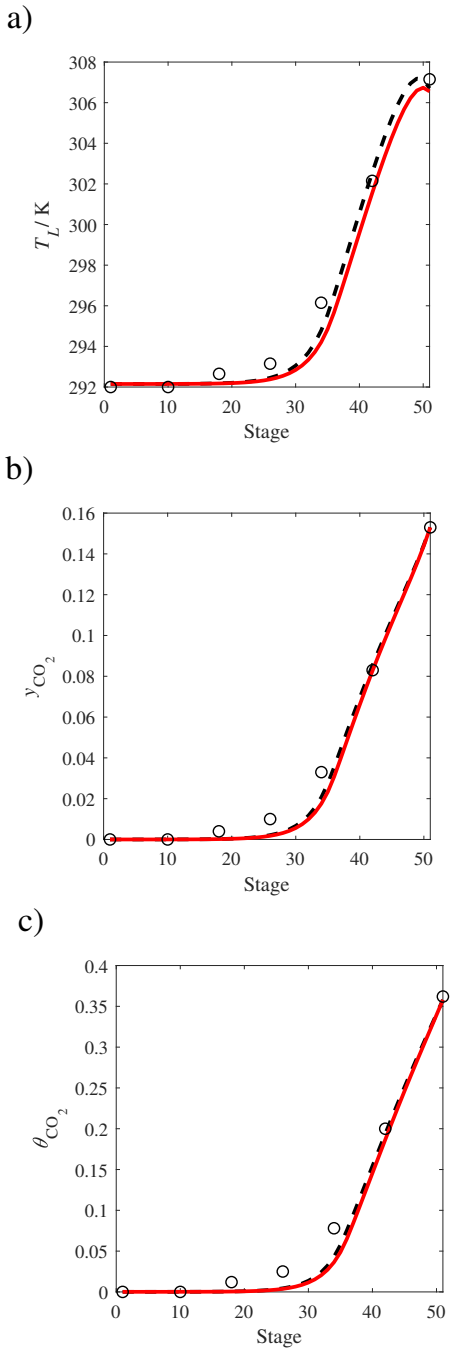

Figure 72: Comparison of the pilot-plant data (circles) (Tontiwachwuthikul et al., 1992) and the result of our model (curves) for Run T13. The dashed curves represent the previous result with the SAFT-VR SW models of Rodríguez et al. (2012) and the continuous curves the results for our new thermodynamic model using SAFT-γ Mie. Here we scale the CO_2 diffusivity in the liquid phase to 4.1% of its original value (τ = 0.041). a) Temperature profile for the liquid phase, b) gas-phase CO_2 concentration profile, and c) liquid-phase CO_2 loading. Stage 50 corresponds to the bottom of the column.

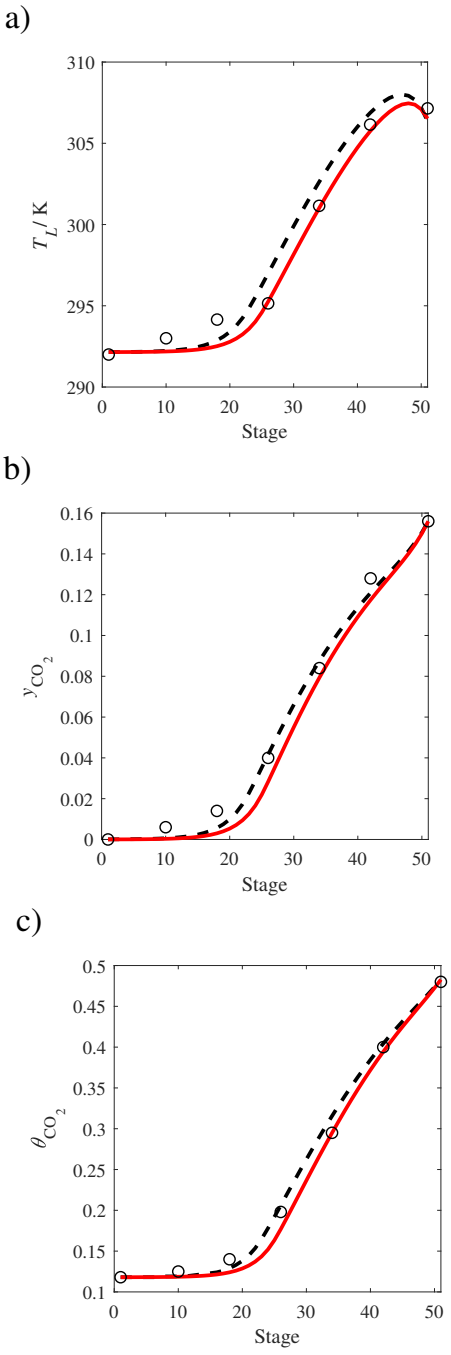

Figure 73: Comparison of the pilot-plant data (circles) (Tontiwachwuthikul et al., 1992) and the result of our model (curves) for Run T14. The dashed curves represent the previous result with the SAFT-VR SW models of Rodríguez et al. (2012) and the continuous curves the results for our new thermodynamic model using SAFT-γ Mie. Here we scale the CO_2 diffusivity in the liquid phase to 4.1% of its original value (τ = 0.041). a) Temperature profile for the liquid phase, b) gas-phase CO_2 concentration profile, and c) liquid-phase CO_2 loading. Stage 50 corresponds to the bottom of the column.

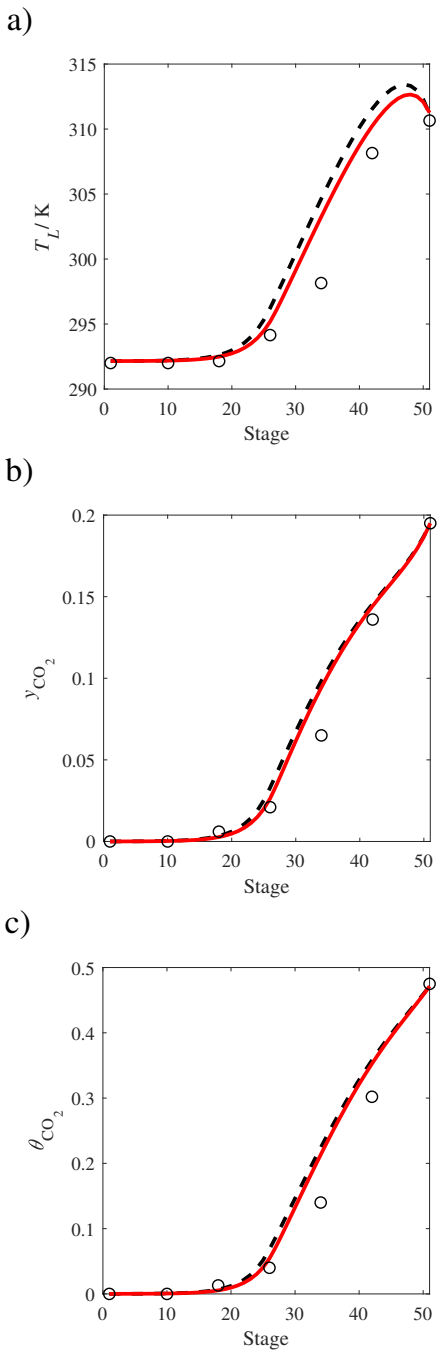

Figure 74: Comparison of the pilot-plant data (circles) (Tontiwachwuthikul et al., 1992) and the result of our model (curves) for Run T15. The dashed curves represent the previous result with the SAFT-VR SW models of Rodríguez et al. (2012) and the continuous curves the results for our new thermodynamic model using SAFT-γ Mie. Here we scale the CO_2 diffusivity in the liquid phase to 4.1% of its original value (τ = 0.041). a) Temperature profile for the liquid phase, b) gas-phase CO_2 concentration profile, and c) liquid-phase CO_2 loading. Stage 50 corresponds to the bottom of the column.

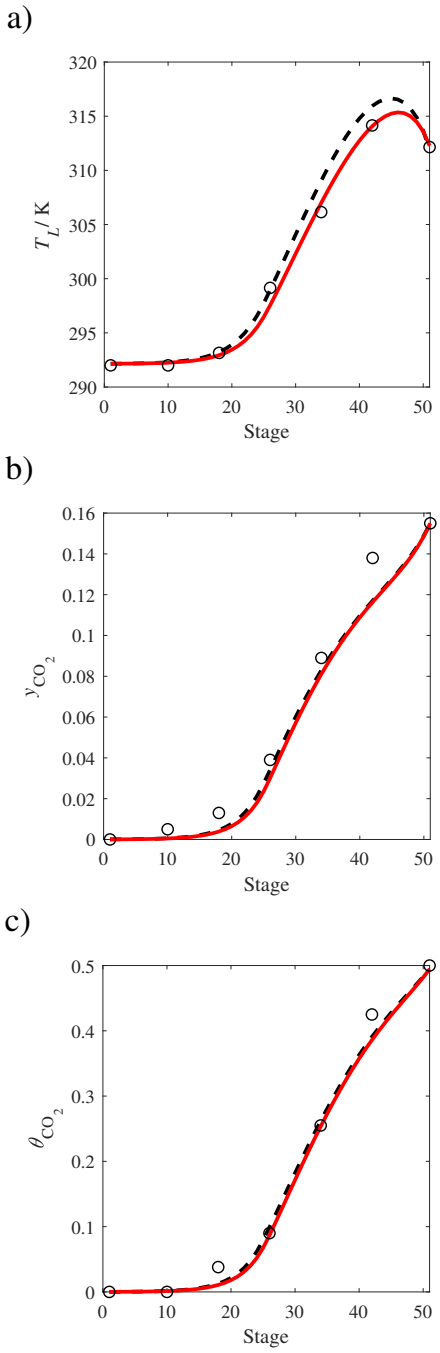

Figure 75: Comparison of the pilot-plant data (circles) (Tontiwachwuthikul et al., 1992) and the result of our model (curves) for Run T16. The dashed curves represent the previous result with the SAFT-VR SW models of Rodríguez et al. (2012) and the continuous curves the results for our new thermodynamic model using SAFT-γ Mie. Here we scale the CO_2 diffusivity in the liquid phase to 4.1% of its original value (τ = 0.041). a) Temperature profile for the liquid phase, b) gas-phase CO_2 concentration profile, and c) liquid-phase CO_2 loading. Stage 50 corresponds to the bottom of the column.

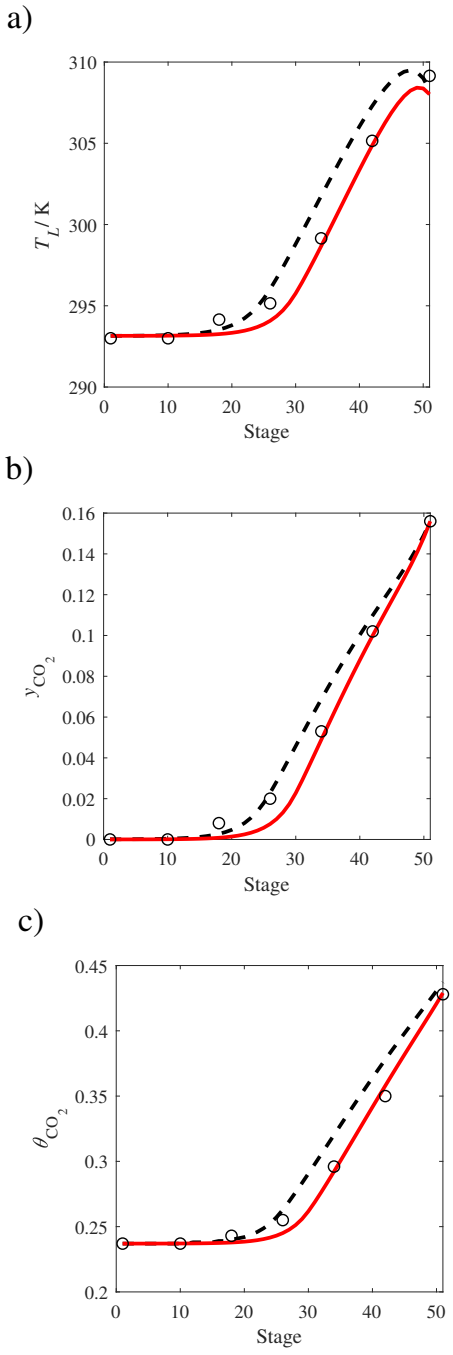

Figure 76: Comparison of the pilot-plant data (circles) (Tontiwachwuthikul et al., 1992) and the result of our model (curves) for Run T17. The dashed curves represent the previous result with the SAFT-VR SW models of Rodríguez et al. (2012) and the continuous curves the results for our new thermodynamic model using SAFT-γ Mie. Here we scale the CO_2 diffusivity in the liquid phase to 4.1% of its original value (τ = 0.041). a) Temperature profile for the liquid phase, b) gas-phase CO_2 concentration profile, and c) liquid-phase CO_2 loading. Stage 50 corresponds to the bottom of the column.

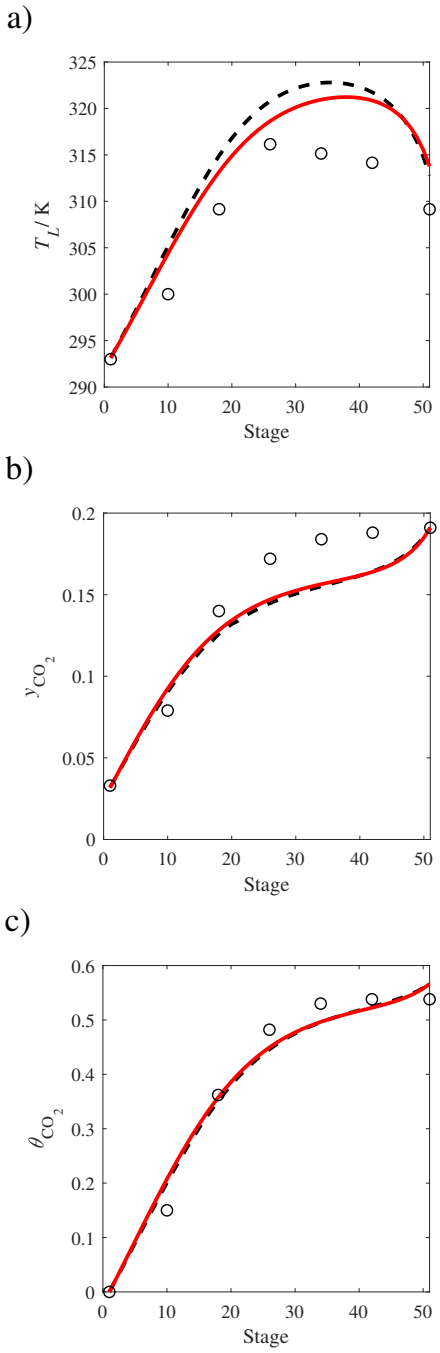

Figure 77: Comparison of the pilot-plant data (circles) (Tontiwachwuthikul et al., 1992) and the result of our model (curves) for Run T18. The dashed curves represent the previous result with the SAFT-VR SW models of Rodríguez et al. (2012) and the continuous curves the results for our new thermodynamic model using SAFT-γ Mie. Here we scale the CO_2 diffusivity in the liquid phase to 4.1% of its original value (τ = 0.041). a) Temperature profile for the liquid phase, b) gas-phase CO_2 concentration profile, and c) liquid-phase CO_2 loading. Stage 50 corresponds to the bottom of the column.

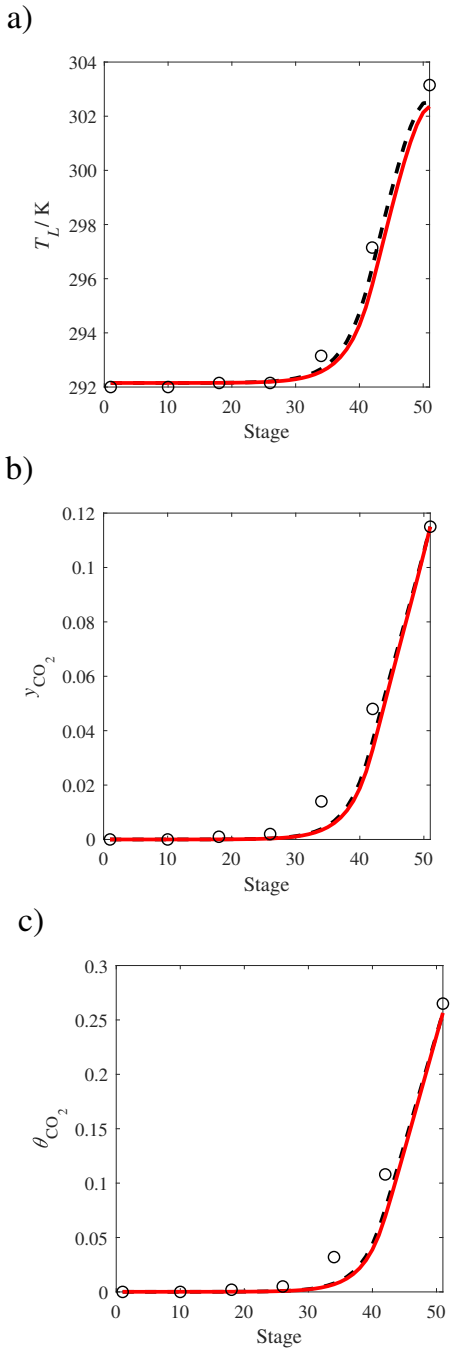

Figure 78: Comparison of the pilot-plant data (circles) (Tontiwachwuthikul et al., 1992) and the result of our model (curves) for Run T19. The dashed curves represent the previous result with the SAFT-VR SW models of Rodríguez et al. (2012) and the continuous curves the results for our new thermodynamic model using SAFT-γ Mie. Here we scale the CO_2 diffusivity in the liquid phase to 4.1% of its original value (τ = 0.041). a) Temperature profile for the liquid phase, b) gas-phase CO_2 concentration profile, and c) liquid-phase CO_2 loading. Stage 50 corresponds to the bottom of the column.

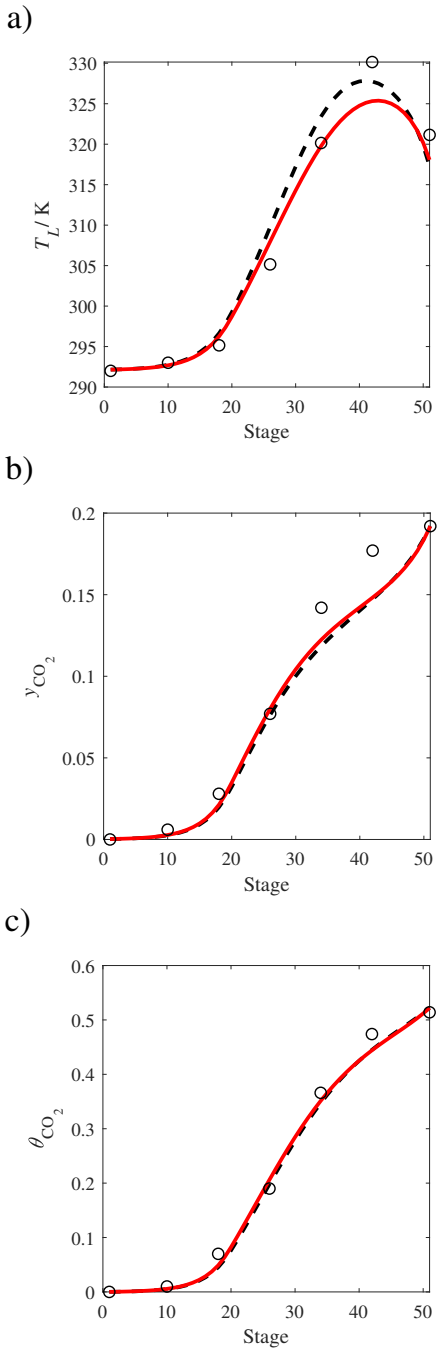

Figure 79: Comparison of the pilot-plant data (circles) (Tontiwachwuthikul et al., 1992) and the result of our model (curves) for Run T20. The dashed curves represent the previous result with the SAFT-VR SW models of Rodríguez et al. (2012) and the continuous curves the results for our new thermodynamic model using SAFT-γ Mie. Here we scale the CO_2 diffusivity in the liquid phase to 4.1% of its original value (τ = 0.041). a) Temperature profile for the liquid phase, b) gas-phase CO_2 concentration profile, and c) liquid-phase CO_2 loading. Stage 50 corresponds to the bottom of the column.

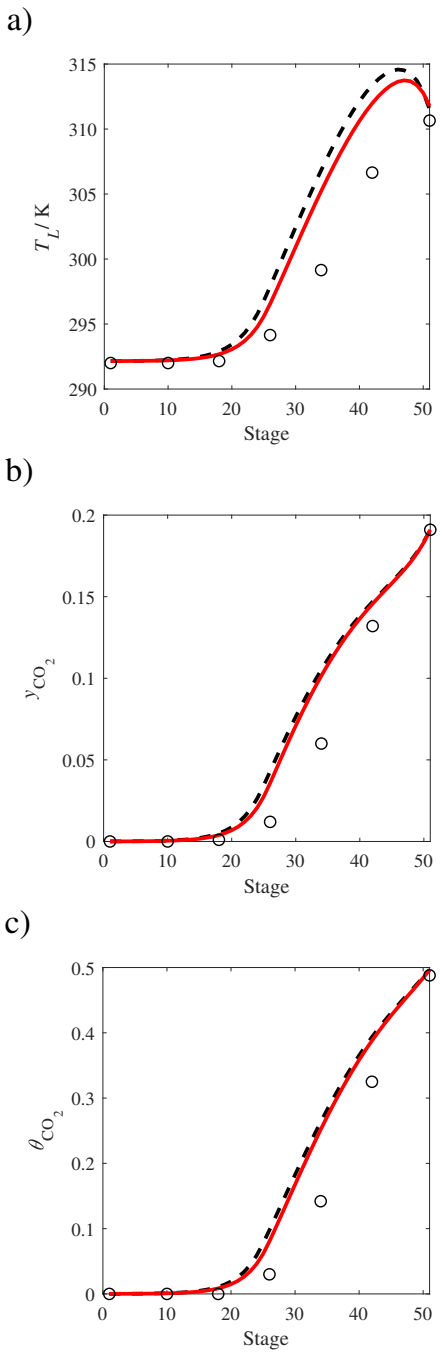

Figure 80: Comparison of the pilot-plant data (circles) (Tontiwachwuthikul et al., 1992) and the result of our model (curves) for Run T21. The dashed curves represent the previous result with the SAFT-VR SW models of Rodríguez et al. (2012) and the continuous curves the results for our new thermodynamic model using SAFT-γ Mie. Here we scale the CO_2 diffusivity in the liquid phase to 4.1% of its original value (τ = 0.041). a) Temperature profile for the liquid phase, b) gas-phase CO_2 concentration profile, and c) liquid-phase CO_2 loading. Stage 50 corresponds to the bottom of the column.

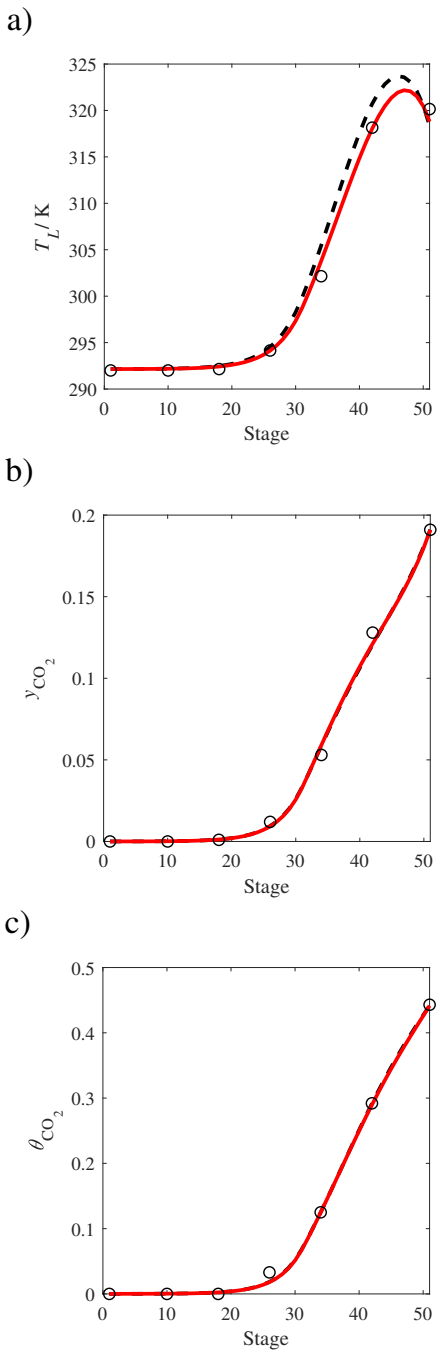

Figure 81: Comparison of the pilot-plant data (circles) (Tontiwachwuthikul et al., 1992) and the result of our model (curves) for Run T22. The dashed curves represent the previous result with the SAFT-VR SW models of Rodríguez et al. (2012) and the continuous curves the results for our new thermodynamic model using SAFT-γ Mie. Here we scale the CO_2 diffusivity in the liquid phase to 4.1% of its original value (τ = 0.041). a) Temperature profile for the liquid phase, b) gas-phase CO_2 concentration profile, and c) liquid-phase CO_2 loading. Stage 50 corresponds to the bottom of the column.

Table 28: Deviations in the composition and temperature profiles for the pilot plant runs of Tontiwachwuthikul et al. (1992). The %AAD in temperature is the average percentage relative deviation of the model with respect to the experimental value. The composition deviations are defined by the average absolute deviation between the experiment and model.

Run	% AAD (T_L)		Δy_{CO_2}		$\Delta\theta$	
	SW	Mie	SW	Mie	SW	Mie
13	0.270	0.226	0.0103	0.0132	0.0036	0.0132
14	0.548	0.186	0.0087	0.0075	0.0042	0.0075
15	0.971	0.451	0.0269	0.0214	0.0086	0.0214
16	0.615	0.155	0.0139	0.0112	0.0058	0.0112
17	0.367	0.199	0.0049	0.0040	0.0032	0.0040
18	2.088	1.298	0.0280	0.0246	0.0165	0.0246
19	0.095	0.150	0.0095	0.0112	0.0033	0.0112
20	0.826	0.571	0.0120	0.0135	0.0093	0.0135
21	1.338	0.749	0.0419	0.0344	0.0142	0.0344
22	0.615	0.172	0.0033	0.0031	0.0027	0.0031
Average	0.773	0.416	0.0159	0.0144	0.0071	0.0144

because they can simultaneously provide a good prediction of the vapour-liquid equilibria and the caloric properties of the mixture. This was achieved by including isobaric heat capacities at an early stage of the model development. The association scheme is different as we account for the solvation effect between CO_2 and H_2O with an association site. Ternary vapour pressure data was used to determine the association parameters that mediate the other reactions that occur within the ternary mixture. The parameter estimation was formulated as a multi-objective optimization problem, realising that the underlying assumptions in the physical approach may not capture the correct temperature dependence of the reaction equilibria, and that the experimental data can be subject to some uncertainty. Thus, a number of Pareto-optimal parameter sets, capturing the key parameters that determine the reaction equilibria, was obtained. A single model was chosen for further evaluation by choosing a point close to the Pareto knee. After a critical evaluation of the heat of absorption measurements, we determined that the model predictions are in good agreement with a particular set of experimental data, and they are in accordance with the heat of absorption calculated when applying the Gibbs-Helmholtz equation to vapour pressure data. This is significant in the context of process design of absorption columns, where the temperature profile determines mass transfer rates, and where the amount of heat required in the re-boiler constitutes a significant proportion of the total energy cost. A detailed assessment of the chemical association was conducted, by looking at the bonded fractions of all nine association sites present in solution. This provided some key statistical mechanical insights into the species distribution implicit in the SAFT

equation. The species distribution was shown to be in excellent agreement with the experimental data.

The new models were shown to provide a better overall description of pilot plant absorption column data compared to the previous models. This result also indicates that the diffusivity scaling parameter determined in Chapter 3 may be highly transferable to similar systems.

5.9 APPENDIX

Model	$f_{P_{CO_2}}$	$f_{P_{CO_2}}$	$f_{P_{CO_2}}$	AAD %	AAD %	AAD %	$(\epsilon_{CO_2,MEA}/k_B)$/K	$(\epsilon^{HB}_{\alpha_1,e^*}/k_B)$/K	$(\epsilon^{HB}_{\alpha_2,e^*}/k_B)$/K	$K^{HB}_{\alpha_1,e^*}$/Å^3	$K^{HB}_{\alpha_2,e^*}$/Å^3
	313.15 K	353.15 K	393.15 K	313.15 K	353.15 K	393.15 K					
1	0.0958	0.0233	0.2250	20.781	9.267	8.313	337.5819	100.6062	5310.3433	1.401140E+07	6.135786E+00
2	0.0262	0.0239	0.0781	5.929	9.505	5.612	296.8864	2424.0926	7310.1204	4.241227E+03	3.749112E-02
3	0.0283	0.0281	0.0384	6.829	10.223	3.944	225.6793	2502.0856	7934.9146	3.372420E+03	1.389771E-02
4	0.4003	0.0260	0.0293	15.400	9.825	3.226	237.2896	406.0204	9934.8057	1.752947E+06	4.609726E-05
5	0.0946	0.0288	0.0305	9.280	10.257	3.289	226.5126	1662.6388	8840.8008	3.793290E+04	1.049216E-03
6	0.0924	0.0251	0.0415	10.676	9.706	4.210	261.0456	1921.8867	8629.1303	1.694827E+04	1.389720E-03
7	0.0238	0.0300	0.0403	4.184	10.570	3.891	192.4267	2638.6270	7645.5613	2.238191E+03	4.516199E-02
8	0.0351	0.0321	0.0318	7.257	10.639	3.353	221.1463	2160.9887	8325.2081	9.558744E+03	4.522711E-03
9	0.0247	0.0339	0.0331	5.329	10.893	3.421	216.2662	2341.4264	7987.1357	5.692406E+03	1.202124E-02
10	0.0243	0.0261	0.0595	4.543	9.837	4.970	234.5493	2667.0986	7241.4007	1.973246E+03	9.799670E-02
11	0.0518	0.0281	0.0335	8.243	10.182	3.504	223.7072	2159.4538	8403.5570	8.982709E+03	3.804529E-03
12	0.3932	0.0250	0.0360	16.259	9.675	3.869	261.8135	382.7863	9931.9385	1.957824E+06	3.500313E-05
13	0.0283	0.0252	0.0525	7.511	9.771	4.758	261.1739	2556.9986	7734.4758	2.830809E+03	1.706985E-02
14	0.1598	0.0262	0.0314	11.194	9.883	3.408	235.5453	1448.5964	9038.3457	6.523150E+04	5.811370E-04
15	0.0397	0.0412	0.0294	7.464	11.135	3.251	230.5909	1702.9687	8697.7466	3.988003E+04	1.263362E-03
16	0.0241	0.0543	0.0298	4.364	11.902	3.410	220.1101	1824.4809	8342.7093	2.948326E+04	3.461843E-03
17	0.0256	0.0423	0.0300	5.719	11.306	3.267	227.1630	1988.7465	8299.5535	1.727929E+04	3.978589E-03
18	0.0447	0.0261	0.0402	8.631	9.882	4.114	243.0435	2339.6190	8193.2075	5.230414E+03	5.739869E-03
19	0.0247	0.0268	0.0468	5.504	10.030	4.460	237.4354	2574.1679	7571.9694	2.686298E+03	3.462569E-02
20	0.1868	0.0300	0.0290	11.472	10.355	3.246	231.8637	950.7713	9434.2879	3.143085E+05	1.788185E-04
21	0.0445	0.0242	0.0586	10.142	9.558	4.983	284.7315	2383.3059	8145.0927	4.693826E+03	4.107858E-03
22	0.0285	0.0304	0.0344	6.651	10.526	3.550	217.9407	2392.5816	8073.4063	4.767786E+03	9.822766E-03
23	0.0248	0.0301	0.0368	5.508	10.537	3.769	216.1696	2501.2064	7835.3757	3.433156E+03	1.970010E-02
24	0.0535	0.0335	0.0302	8.052	10.687	3.272	226.9524	1810.8749	8660.8471	2.682374E+04	1.604378E-03
25	0.0832	0.0264	0.0343	9.493	9.914	3.652	235.0847	1957.5048	8596.6699	1.540480E+04	2.016198E-03

Table 29: Pareto optimal models for the cross interaction parameters between CO_2 and MEA. We present the objective

Model	$f_{P_{CO_2}}$	$f_{P_{CO_2}}$	$f_{P_{CO_2}}$	AAD %	AAD %	AAD %	$(\epsilon_{CO_2,MEA}/k_B)/K$	$(\epsilon^{HB}_{\alpha_1,e^*}/k_B)/K$	$(\epsilon^{HB}_{\alpha_2,e^*}/k_B)/K$	$K^{HB}_{\alpha_1,e^*}/Å^3$	$K^{HB}_{\alpha_2,e^*}/Å^3$
	313.15 K	353.15 K	393.15 K	313.15 K	353.15 K	393.15 K					
25	0.0832	0.0264	0.0343	9.493	9.914	3.652	235.0847	1957.5048	8596.6699	1.540480E+04	2.016198E-03
26	0.0248	0.0604	0.0288	5.282	12.003	3.243	232.7813	1564.0027	8623.8076	6.731299E+04	1.275369E-03
27	0.0274	0.0764	0.0287	5.066	12.505	3.243	232.5981	1582.6195	8605.4997	7.062986E+04	1.216035E-03
28	0.2216	0.0269	0.0296	12.050	9.954	3.249	231.1405	1029.3323	9373.3203	2.274515E+05	2.316535E-04
29	0.2062	0.0241	0.0530	15.073	9.529	4.731	287.6100	1288.3116	9365.7461	1.060128E+05	1.267953E-04
30	0.0242	0.0418	0.0306	4.602	11.374	3.291	221.8659	2100.3620	8106.6463	1.219512E+04	7.300395E-03
31	0.0274	0.0360	0.0312	6.266	10.958	3.320	222.4887	2154.8132	8228.2584	1.012550E+04	5.525855E-03
32	0.0253	0.0250	0.0596	5.862	9.744	5.028	266.8528	2540.1005	7429.0509	2.960473E+03	3.799848E-02
33	0.0239	0.0342	0.0342	4.298	11.041	3.429	201.1972	2443.3059	7861.8387	4.143590E+03	2.038826E-02
34	0.0578	0.0296	0.0315	8.267	10.368	3.338	223.0794	1980.9787	8551.7434	1.544868E+04	2.436981E-03
35	0.0310	0.0264	0.0432	7.625	9.927	4.292	242.3556	2510.1783	7920.4006	3.240431E+03	1.236899E-02
36	0.0251	0.0247	0.0685	4.988	9.632	5.310	269.1221	2543.2305	7196.2540	2.878755E+03	7.420738E-02
37	0.0396	0.0274	0.0368	8.003	10.073	3.829	228.6902	2361.2666	8182.6838	4.991826E+03	6.804201E-03
38	0.0237	0.0288	0.0540	3.902	10.259	4.621	182.8121	2787.6515	7370.8052	1.399063E+03	1.208189E-01
39	0.0230	0.0443	0.0613	6.295	13.308	4.777	1.3229	3311.1506	8478.5943	3.724129E+02	3.354345E-02
40	0.0235	0.0344	0.0407	4.290	11.416	3.827	142.2953	2747.8465	7879.3600	1.660834E+03	3.871171E-02
41	0.2178	0.0253	0.0341	13.018	9.740	3.715	252.8191	1176.8311	9283.2706	1.421975E+05	2.421797E-04
42	0.0913	0.0273	0.0319	9.362	10.040	3.387	226.9034	1828.5609	8714.3531	2.267563E+04	1.553084E-03
43	0.0917	0.0340	0.0293	9.236	10.677	3.250	230.7947	1404.5632	9038.9044	8.747891E+04	5.230855E-04
44	0.0243	0.0499	0.0294	4.850	11.674	3.254	229.8766	1841.8820	8331.4721	2.772307E+04	3.264895E-03
45	0.3668	0.0268	0.0289	14.138	9.939	3.243	232.8280	278.1219	9898.2556	3.311829E+06	5.142820E-05
46	0.0237	0.0386	0.0347	3.887	11.564	3.652	182.0024	2426.7852	8001.0900	4.434186E+03	1.629323E-02
47	0.0385	0.0297	0.0331	7.589	10.408	3.454	220.1969	2242.9339	8290.8370	7.284071E+03	5.260378E-03
48	0.0350	0.0370	0.0302	7.171	10.950	3.274	226.8088	1936.5215	8484.0157	1.941106E+04	2.527749E-03
49	0.0461	0.0250	0.0475	9.339	9.714	4.528	263.5305	2346.1879	8169.3884	5.130736E+03	4.912321E-03
50	0.0614	0.0235	0.0868	13.752	9.351	5.879	320.0701	2329.5453	8594.3314	5.869760E+03	7.306289E-04
51	0.0243	0.0286	0.0411	5.011	10.347	4.088	219.0144	2568.5256	7652.9174	2.758188E+03	3.294576E-02

Table 30: Pareto optimal models for the cross interaction parameters between CO_2 and MEA. We present the objective

6

DEVELOPING A CLASSICAL DENSITY FUNCTIONAL THEORY FOR SAFT-VR MIE

6.1 INTRODUCTION

Interfacial phenomena play an important role in the design and modelling of chemical processes. In the context of this thesis, the ability to predict the interfacial tension between fluid phases is important because it affects mass transfer rates. In the modelling of the absorption column in chapter 3, the vapour-liquid interfacial tension appears in the mass transfer correlations as it directly affects the intefacial area density available for mass transfer. As noted by Gloor et al. (2007a), it is an important data type for decreasing the degeneracy of molecular parameters for associating substances.

In this chapter we derive a classical density functional theory (DFT) that is compatible with the SAFT-VR Mie equation of state, in order to be able to predict inhomogeneous properties of fluids, in particular the interfacial tension. At the pure component level, this approach is similar to that of Gloor et al. (2002); Gloor (2003); Gloor et al. (2007a), who developed a DFT for pure components utilizing the SAFT-VR SW equation of state, and is similar to the methodology used in the recently published work by Algaba et al. (2019), who developed a pure component DFT utilizing SAFT-VR Mie. The method described in this chapter expands on the work of Algaba et al. (2019) by considering associating species and the general case of mixtures, following a similar approach to Llovell et al. (2010). Due to the complex nature of the molecules inherent in carbon capture processes (consisting of hydrogen bonding and reactive systems), we focus on developing a theory that is numerically tractable, providing a method that is suitable for the rapid evaluation of thermodynamic models.

6.2 CLASSICAL DENSITY FUNCTIONAL THEORY

It is convenient to express an inhomogeneous mixture in terms of the chemical potential for each component, μ_i, the total system volume, V, and the temperature, T. In the absence of external fields, the grand potential functional, $\Omega[\{\tilde{\rho}_c(\boldsymbol{r})\}]$, of the system is given by (Evans, 1992):

$$\Omega[\{\tilde{\rho}_c(\boldsymbol{r})\}] = A[\{\tilde{\rho}_c(\boldsymbol{r})\}] - \sum_{i=1}^{n} \mu_i \int d\boldsymbol{r}\tilde{\rho}_i(\boldsymbol{r}), \tag{117}$$

where $A[\{\tilde{\rho}_c(\boldsymbol{r})\}]$ is the intrinsic Helmholtz free energy, μ_i is the chemical potential of component i, $\quad i = \{1, .., n\}$, and $\tilde{\rho}_i(\boldsymbol{r})$ is the average one-body density of component i at position vector $\boldsymbol{r}$. The square brackets indicate that Ω and A are functionals of $\{\tilde{\rho}(\boldsymbol{r})\}$, where the curly brackets indicate a set of density profiles for components c: $\{\tilde{\rho}_c(\boldsymbol{r})\} = [\rho_1(\boldsymbol{r}), \rho_2(\boldsymbol{r}), ..., \rho_n(\boldsymbol{r})]$. Since at thermodynamic equilibrium the grand potential must be a minimum, it can be shown (Evans, 1979) that

when $\tilde{\rho}_i(\boldsymbol{r}) = \rho_i(\boldsymbol{r})$, where $\rho_i(\boldsymbol{r})$ is the equilibrium density profile for component i, we obtain the following variation at thermodynamic equilibrium:

$$\left(\frac{\delta\Omega[\{\tilde{\rho}_c(\boldsymbol{r})\}]}{\delta\tilde{\rho}_i(\boldsymbol{r})}\right)_{T,V,\tilde{\rho}_{j\neq i}(\boldsymbol{r})} = 0, \quad \{\tilde{\rho}_c(\boldsymbol{r})\} = \{\rho_c(\boldsymbol{r})\}, \quad \Omega[\{\rho_c(\boldsymbol{r})\}] = \Omega. \tag{118}$$

Throughout this chapter, functional derivatives are taken at constant $T, V$and $\tilde{\rho}_{j\neq i}(\boldsymbol{r})$ unless specified otherwise. The minimization of the grand potential is equivalent to the minimization of the Helmholtz free energy functional, subject to the constraint that the total number of particles of each component in the system remains constant; the Lagrange multipliers for these constraints are the chemical potentials μ_i, i.e., the chemical potentials of the coexisting bulk phases. The equilibrium density profiles can then be obtained by applying functional derivatives to Equation 117, giving

$$\left(\frac{\delta A[\{\rho_c(\boldsymbol{r})\}]}{\delta\rho_i(\boldsymbol{r})}\right)_{T,V,\rho(\tilde{\boldsymbol{r}})_{j\neq i}} = \mu_i \qquad i = \{1, ..., n\}. \tag{119}$$

This specifies that the intrinsic chemical potential for each component is constant throughout the interface. Once the equilibrium density profile is obtained, the thermodynamic properties of the inhomogeneous system can be calculated. In this context, the interfacial tension, γ, can be determined by the thermodynamic relation:

$$\gamma = \frac{\Omega + PV}{\mathcal{A}}, \tag{120}$$

where $\mathcal{A}$ is the area of the interface and P is the pressure of the coexisting bulk phases.

6.3 DERIVATION OF THE SAFT-VR MIE DFT

We now seek to find a suitable approximation for the free energy functional, $A[\{\rho_c(\boldsymbol{r})\}]$, that is compatible with the SAFT-VR Mie equation of state (EoS) (Lafitte et al., 2013a; Dufal et al., 2015b). This EoS provides the free energy of a homogeneous fluid of associating chain molecules, where chains consist of a number (not necessarily an integer) of segments that interact via a Mie potential. The reader is referred to the original texts for details. Here, we outline some aspects of SAFT-VR Mie that are required for the DFT formulation.

The monomer contribution to the EoS considers the free energy due to spherical segments interacting via a Mie (generalised Lennard-Jones) potential. The Mie potential is defined as follows:

$$\phi_{ij}(r) = C_{ij}\varepsilon_{ij}\left[\left(\frac{\sigma_{ij}}{r}\right)^{\lambda^r_{ij}} - \left(\frac{\sigma_{ij}}{r}\right)^{\lambda^a_{ij}}\right], \tag{121}$$

where λ^a_{ij} is the attractive exponent, λ^r_{ij} is the repulsive exponent ($\lambda^r_{ij} > \lambda^a_{ij} > 3$), σ_{ij} is the diameter at which the Mie potential is repulsive, and ϵ_{ij} is the depth of the potential well. C is given by:

$$C_{ij} = \frac{\lambda^r_{ij}}{\lambda^r_{ij} - \lambda^a_{ij}}\left(\frac{\lambda^r_{ij}}{\lambda^a_{ij}}\right)^{\frac{\lambda^a_{ij}}{\lambda^r_{ij}-\lambda^a_{ij}}}. \tag{122}$$

The attractive part of the Mie potential (which we will consider to be the long range contribution in the DFT) is given by

$$\phi_{ij}^{att}(r) = \begin{cases} \phi_{ij}(r) & \text{if} \quad r \geqslant \sigma \\ 0 & \text{otherwise.} \end{cases} \tag{123}$$

Following Gloor et al. (2002); Gloor (2003); Gloor et al. (2007a), we split the free energy functional into terms that are local and non-local:

$$A[\{\rho_c(\boldsymbol{r})\}] = A^{ref}[\{\rho_c(\boldsymbol{r})\}] + A^{att}[\{\rho_c(\boldsymbol{r})\}]. \tag{124}$$

Here, A^{ref} is the reference free energy functional that incorporates all of the contributions to the free energy that are determined using the local density approximation (LDA), and A^{att} is the free energy functional that is determined by the long-range attractive contributions to the free energy which we treat non-locally. The LDA is a good approximation for fluid-fluid interfaces because the gradients in the density with respect to position are relatively small (e.g., compared to solid-fluid systems). The reference contribution is given by

$$A^{ref}[\{\rho_c(\boldsymbol{r})\}] = A^{SAFT}[\{\rho_c(\boldsymbol{r})\}] - A^{SAFT,lr}[\{\rho_c(\boldsymbol{r})\}]. \tag{125}$$

The first term is the free energy obtained when integrating the free energy density given by the SAFT equation over the system volume, while the second term excludes the long range attractive contributions to this free energy in the reference contribution (evaluated within the mean-field approximation). Therefore, A^{SAFT} is given by

$$A^{SAFT}[\{\rho_c(\boldsymbol{r})\}] = k_B T \int d\boldsymbol{r} \rho(\boldsymbol{r}) A^{SAFT}(\{\rho_c(\boldsymbol{r})\}), \tag{126}$$

Here, $A^{SAFT}(\{\rho_c(\boldsymbol{r})\})$ is the dimensionless free energy (normalized by $1/(Nk_BT)$) obtained directly from SAFT-VR Mie, which includes the ideal, hard-sphere, the perturbative contributions due to attractive interactions, chain contributions, and association contributions, while k_B is the Boltzmann constant and $\rho(\boldsymbol{r}) = \sum_i^n \rho_i(\boldsymbol{r})$, the total number density of chain molecules at position vector $\boldsymbol{r}$. From Equation 126 it is clear that a local density approximation (LDA) has been used because variables inside the integrals are only functions of the local position coordinate ($\boldsymbol{r}$). The long-range mean-field contribution to A^{SAFT} which we subtract is given by

$$\begin{aligned} A^{SAFT,lr}[\{\rho_c(\boldsymbol{r})\}] &= \frac{1}{2}\sum_{i=1}^{n}\sum_{j=1}^{n}\int d\boldsymbol{r} m_i m_j \rho_i(\boldsymbol{r})\rho_j(\boldsymbol{r}) \int d\boldsymbol{r}' \phi_{ij}^{att}(|\boldsymbol{r}-\boldsymbol{r}'|) \\ &= \frac{1}{2}\sum_{i=1}^{n}\sum_{j=1}^{n}\int d\boldsymbol{r} m_i m_j \rho_i(\boldsymbol{r})\rho_j(\boldsymbol{r}) \alpha_{ij}^{vdW}. \end{aligned} \tag{127}$$

Here, α_{ij}^{vdW} is the van der Waals attractive constant for the interaction between spherical segments i and j, which can be obtained by integrating the attractive part of the Mie potential for the uniform fluid as follows:

$$\begin{aligned}\alpha_{ij}^{vdW} &= \int d\boldsymbol{r}' \phi_{ij}^{att}(|\boldsymbol{r}-\boldsymbol{r}'|) \\ &= \int_{\sigma}^{\infty} dr(4\pi r^2)\phi_{ij}^{att}(r) \\ &= -4\pi C_{ij}\varepsilon\sigma_{ij}^3\left(\frac{1}{3-\lambda_{ij}^r}-\frac{1}{3-\lambda_{ij}^a}\right).\end{aligned} \tag{128}$$

The non-local attractive contribution is given by:

$$A^{att}[\{\rho_c(\boldsymbol{r})\}] = \frac{1}{2}\sum_{i=1}^{n}\sum_{j=1}^{n}\int d\boldsymbol{r} m_i\rho_i(\boldsymbol{r})\int d\boldsymbol{r}' m_j\rho_j(\boldsymbol{r}')\phi_{ij}^{att}(|\boldsymbol{r}-\boldsymbol{r}'|). \tag{129}$$

In order for the DFT theory to be consistent with the bulk SAFT-VR Mie EoS, we require that if the densities are constant throughout the fluid, the free energy functional $A[\{\rho_c(\boldsymbol{r})\}]$ is the same as the free energy computed via the EoS $A^{SAFT}[\{\rho_c(\boldsymbol{r})\}]$. From equations 124 and 125 it is clear that this requires that $A^{SAFT,lr} = A^{att}$, which is the case because the number densities $\rho_i(\boldsymbol{r})$ can be taken outside of the integrals in equations 127 and 129 and the two contributions become identical.

The next step is to determine the explicit forms of the functional derivatives used in Equation 119. The free energy functional is given by:

$$\begin{aligned}A[\{\rho_c(\boldsymbol{r})\}] &= A^{ref}[\{\rho_c(\boldsymbol{r})\}] + A^{att}[\{\rho_c(\boldsymbol{r})\}] \\ &= \underbrace{A^{SAFT}[\{\rho_c(\boldsymbol{r})\}] - A^{SAFT,lr}[\{\rho_c(\boldsymbol{r})\}]}_{\text{short range contribution}} + A^{att}[\{\rho_c(\boldsymbol{r})\}].\end{aligned} \tag{130}$$

Taking the functional derivative with respect to $\rho_i(\boldsymbol{r})$ gives:

$$\begin{aligned}\frac{\delta A[\{\rho_c(\boldsymbol{r})\}]}{\delta\rho_i(\boldsymbol{r})} &= \frac{\delta A^{SAFT}[\{\rho_c(\boldsymbol{r})\}]}{\delta\rho_i(\boldsymbol{r})} - \frac{\delta A^{SAFT,lr}[\{\rho_c(\boldsymbol{r})\}]}{\delta\rho_i(\boldsymbol{r})} + \frac{\delta A^{att}[\{\rho_c(\boldsymbol{r})\}]}{\delta\rho_i(\boldsymbol{r})} \\ &= \mu_i^{SAFT}(\{\rho_c(\boldsymbol{r})\}) - \mu_i^{SAFT,lr}(\{\rho_c(\boldsymbol{r})\}) + \mu_i^{att}[\{\rho_c(\boldsymbol{r})\}].\end{aligned} \tag{131}$$

In the appendix to this chapter (section 6.10.2) we show the methodology for computing these functional derivatives. $\mu^{SAFT}[\{\rho_c(\boldsymbol{r})\}]$ is simply the chemical potential directly obtained from the SAFT-VR Mie equation of state for the uniform fluid. The long-range contribution to this chemical potential (which we subtract), is given by

$$\mu_i^{SAFT,lr}(\{\rho_c(\boldsymbol{r})\}) = \sum_{j=1}^{n} m_i m_j \rho_j(\boldsymbol{r})\alpha_{ij}^{vdW}. \tag{132}$$

The contribution due to long range attractive forces is given by:

$$\mu_i^{att}[\{\rho_c(\boldsymbol{r})\}] = \sum_{j=1}^{n} m_i m_j \int d\boldsymbol{r}'\rho_j(\boldsymbol{r}')\phi_{ij}^{att}(|\boldsymbol{r}-\boldsymbol{r}'|). \tag{133}$$

Finally, we obtain the Euler-Lagrange equation which can be used to solve for the density profile:

$$\mu_i = \mu_i^{SAFT}(\{\rho_c(\boldsymbol{r})\}) - \sum_{j=1}^{n} m_i m_j \rho_j(\boldsymbol{r}) \alpha_{ij}^{vdW} + \sum_{j=1}^{n} m_i m_j \int d\boldsymbol{r'} \rho_j(\boldsymbol{r'}) \phi_{ij}^{att}(|\boldsymbol{r} - \boldsymbol{r'}|). \tag{134}$$

6.4 TRANSFORMING TO THE PLANAR INTERFACE

In this chapter we will consider only planar interfaces, meaning that the density profile varies in only one Cartesian coordinate perpendicular to the surface normal. Here we define a new potential function, $\phi_{ij}^{att^*}(|z - z'|)$, that defines the total potential between two *planes* of particles at positions z and z':

$$\phi_{ij}^{att^*}(|z - z'|) = \begin{cases} \int_0^{2\pi} d\theta \int_{\sqrt{\sigma_{ij}^2 - |z-z'|^2}}^{\infty} d\zeta \phi_{ij}\left(\sqrt{\zeta^2 + |z - z'|^2}\right) \zeta, & \text{if } |z - z'| \leqslant \sigma_{ij}, \\ \int_0^{2\pi} d\theta \int_0^{\infty} d\zeta \phi_{ij}\left(\sqrt{\zeta^2 + |z - z'|^2}\right) \zeta, & \text{if } |z - z'| > \sigma_{ij}. \end{cases} \tag{135}$$

To determine Equation 135 we have converted to cylindrical coordinates (θ, ζ, r) to simplify the mathematics, and have made the substitution that:

$$r = \sqrt{\zeta^2 + |z - z'|^2}, \tag{136}$$

where ζ is the radial distance and $|z - z'|$ denotes the distance between two planes at positions z and z', and θ is the angle in radians for the cylindrical coordinate system, as depicted in Figure 82.

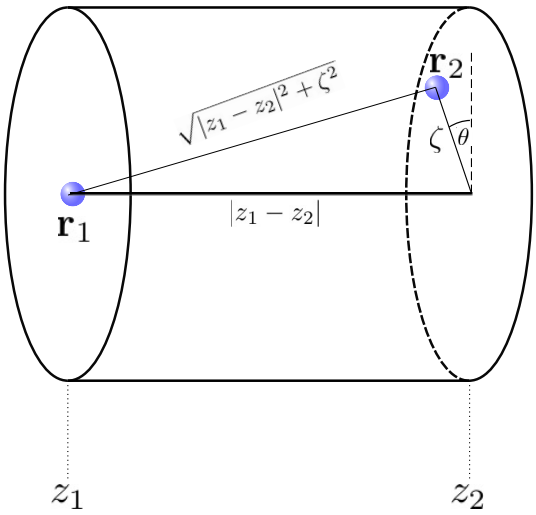

Figure 82: Schematic describing the conversion to cylindrical coordinates between two particles at positions r_1 and r_2. In this figure, r_1 and r_2 are equivalent to r and r', and z_1 and z_2 are equivalent to z and z', to be consistent with the notation used in this chapter.

The lower limits of integration over the radial coordinate (ζ) are included explicitly to avoid integration over particle separations where $\phi_{ij}^{att} > 0$. If $|z-z'| \leqslant \sigma_{ij}$ then the integration over the radial distance will have a lower bound greater than zero due to the lower limit on the range of the attractive part of the Mie potential due to the overlaps between the repulsive cores. For separation distances above σ_{ij}, the integration over ζ is between 0 and ∞. The inner integrals in Equation 135 can be solved analytically for the Mie interaction to give

$$\int d\zeta \phi_{ij}^{att}\left(\sqrt{\zeta^2+(z-z')^2}\right)\zeta = C_{ij}\epsilon_{ij}(|z-z'|^2+\zeta^2)\left[\frac{1}{2-\lambda_{ij}^r}\left(\frac{\sigma_{ij}}{\sqrt{|z-z'|^2+\zeta^2}}\right)^{\lambda_{ij}^r} - \frac{1}{2-\lambda_{ij}^a}\left(\frac{\sigma_{ij}}{\sqrt{|z-z'|^2+\zeta^2}}\right)^{\lambda_{ij}^a}\right] + \text{constant.} \tag{137}$$

Applying the limits of integration given in Equation 135, the potential function is

$$\phi_{ij}^{att^*}(|z-z'|) = \begin{cases} -2\pi C_{ij}\epsilon_{ij}\sigma_{ij}^2\left[\frac{1}{2-\lambda_{ij}^r}-\frac{1}{2-\lambda_{ij}^a}\right], & \text{if } |z-z'| \leqslant \sigma_{ij}, \\ -2\pi C_{ij}\epsilon_{ij}|z-z'|^2\left[\frac{1}{2-\lambda_{ij}^r}\left(\frac{\sigma_{ij}}{|z-z'|}\right)^{\lambda_{ij}^r}-\frac{1}{2-\lambda_{ij}^a}\left(\frac{\sigma_{ij}}{|z-z'|}\right)^{\lambda_{ij}^a}\right] & \text{if } |z-z'| > \sigma_{ij}. \end{cases} \tag{138}$$

The Euler-Lagrange equation is then given by

$$\mu_i = \mu_i^{SAFT}(\{\rho_c(z)\}) - \sum_{j=1}^{n} m_i m_j \rho_j(z) \alpha_{ij}^{vdW} + \sum_{j=1}^{n} m_i m_j \int dz \rho_j(z') \phi_{ij}^{att^*}(|z-z'|) \tag{139}$$

The individual contributions to the free energy functional are given by:

$$A^{SAFT}[\{\rho_c(z)\}] = k_B T \mathcal{A} \int dz \rho(z) A^{SAFT}(\{\rho_c(z)\}), \tag{140}$$

$$A^{SAFT,lr}[\{\rho_c(\boldsymbol{r})\}] = \frac{1}{2}\mathcal{A} \sum_{i=1}^{n}\sum_{j=1}^{n} \int dz m_i m_j \rho_i(z)\rho_j(z) \alpha_{ij}^{vdW}, \tag{141}$$

and

$$A^{att}[\{\rho_c(z)\}] = \frac{1}{2}\mathcal{A} \sum_{i=1}^{n}\sum_{j=1}^{n} \int dz m_i \rho_i(z) \int dz' m_j \rho_j(z') \phi_{ij}^{att^*}(|z-z'|). \tag{142}$$

6.5 NUMERICAL IMPLEMENTATION

The numerical method we use in this work to solve the DFT equations is fairly unique compared to the other methods used to solve similar problems in the literature. Typically, a damped direct substitution algorithm (Picard iteration) is used (see e.g., Gloor (2003)). In this work, we use an equation-oriented programming language, gPROMS (Process Systems Enterprise, 2016), to solve the system of equations. This is a powerful tool for solving these types of problem because, after specifying the parameters, variables and equations of the problem, the powerful internal solvers of gPROMS are used for numerical solution. This requires little user input as to the procedural way of solving the DFT equation.

In this section we describe the precise way in which the equations are solved using the gPROMS (equation-oriented) software package, and detail the modifications to the DFT equations that are used to facilitate their numerical solution.

6.5.1 *Modification of the DFT equations*

For integrations over the auxiliary z' coordinate, we determine suitable bounds to the width of the interface by specifying a lower and upper bound on z: z_{LB} and z_{UB} respectively, outside of which the component number densities are approxi-

mately equal to their bulk densities, such that we can take these densities outside of the integral. We modify the Euler-Lagrange equation (Equation 139) as follows:

$$\mu_i = \mu_i^{SAFT}(\{\rho_c(z)\}) - \sum_{j=1}^{n} m_i m_j \rho_j(z) \alpha_{ij}^{vdW} + \sum_{j=1}^{n} m_i m_j \left[\rho_j^{B,I} \int_{-\infty}^{z_{LB}} dz \phi_{ij}^{att^*}(|z-z'|) + \int_{z_{LB}}^{z_{UB}} dz \rho_j(z') \phi_{ij}^{att^*}(|z-z'|) + \rho_j^{B,II} \int_{z_{UB}}^{\infty} dz \phi_{ij}^{att^*}(|z-z'|) \right], \tag{143}$$

where $\rho_j^{B,I}$ and $\rho_j^{B,II}$ are the number densities of component j in bulk phases I and II respectively. These bulk densities are found by solving for phase equilibria with the homogeneous EoS. Similarly, the attractive free energy functional is modified by splitting the integral in Equation 142:

$$A^{att}[\{\rho_c(z)\}] = \frac{1}{2} \sum_{i=1}^{n} \sum_{j=1}^{n} \int dz m_i m_j \rho_i(z) \left[\rho_j^{B,I} \int_{-\infty}^{z_{LB}} dz' \phi_{ij}^{att^*}(|z-z'|) + \int_{z_{LB}}^{z_{UB}} dz' \rho_j(z') \phi_{ij}^{att^*}(|z-z'|) + \rho_j^{B,II} \int_{z_{UB}}^{\infty} dz' \phi_{ij}^{att^*}(|z-z'|) \right] \tag{144}$$

The analytic expressions for the integration of the attractive potential are given by

$$\int_{-\infty}^{z_{LB}} dz' \phi_{ij}^{att^*}(|z-z'|) = \begin{cases} -2\pi C_{ij} \epsilon_{ij} \sigma_{ij}^2 \left[\frac{\sigma_{ij}}{3-\lambda_{ij}^r} - \frac{\sigma_{ij}}{3-\lambda_{ij}^a} - \frac{|z_{LB}-z|}{2-\lambda_{ij}^r} + \frac{|z_{LB}-z|}{2-\lambda_{ij}^a} \right] & \text{if } |z_{LB}-z| < \sigma_{ij}, \\ -2\pi C_{ij} \epsilon_{ij} \left[\frac{|z_{LB}-z|^{3-\lambda_{ij}^a} \sigma_{ij}^{\lambda_i^a j}}{(2-\lambda_{ij}^a)(3-\lambda_{ij}^a)} - \frac{|z_{LB}-z|^{3-\lambda_{ij}^r} \sigma^{\lambda_{ij}^r}}{(2-\lambda_{ij}^r)(3-\lambda_{ij}^r)} \right] & \text{if } |z_{LB}-z| \geqslant \sigma_{ij} \end{cases} \tag{145}$$

and similarly,

$$\int_{z_{UB}}^{\infty} dz' \phi_{ij}^{att^*}(|z-z'|) = \begin{cases} -2\pi C_{ij} \epsilon_{ij} \sigma_{ij}^2 \left[\frac{\sigma_{ij}}{3-\lambda_{ij}^r} - \frac{\sigma_{ij}}{3-\lambda_{ij}^a} - \frac{|z_{UB}-z|}{2-\lambda_{ij}^r} + \frac{|z_{UB}-z|}{2-\lambda_{ij}^a} \right] & \text{if } |z_{UB}-z| < \sigma_{ij}, \\ -2\pi C_{ij} \epsilon_{ij} \left[\frac{|z_{UB}-z|^{3-\lambda_{ij}^a} \sigma_{ij}^{\lambda_i^a j}}{(2-\lambda_{ij}^a)(3-\lambda_{ij}^a)} - \frac{|z_{UB}-z|^{3-\lambda_{ij}^r} \sigma^{\lambda_{ij}^r}}{(2-\lambda_{ij}^r)(3-\lambda_{ij}^r)} \right] & \text{if } |z_{UB}-z| \geqslant \sigma_{ij}. \end{cases} \tag{146}$$

The equation for the interfacial tension is given by

$$\gamma = \frac{\Omega + PV}{\mathcal{A}} = \frac{\Omega}{\mathcal{A}} + P|z_{UB} - z_{LB}|. \tag{147}$$

6.5.2 *Solution to the density profile*

The key numerical challenge is to find the set of density profiles, $\{\rho_c(z)\}$, that satisfy Equations 143, 145 and 146. Within the gPROMS formalism, z is declared as a distribution domain with lower and upper bounds of z_{LB} and z_{UB} respectively with N_{dist} discretized points. $|z-z'|$ is declared as a distribution domain with lower and upper bounds of 0 and $|z_{UB}-z_{LB}|$ respectively with $2N_{dist}$ discretized points. The method used to solve numerical integrations over these distribution domains is set to a sixth order centred finite difference method. Numerical integrations are performed by splitting the integral into a number of sub-integrals. For example,

$$\int_a^b f dx = \int_{x_i}^{x_{i+1}} f dx + \int_{x_{i+1}}^{x_{i+2}} f dx + ... + \int_{x_{i+m-1}}^{x_{i+m}} f dx + \int_{x_{i+m}}^{b} f dx \tag{148}$$

Each sub-integral in Equation 148 is integrated using a polynomial approximation consistent with the numerical method (used to approximate partial derivatives) specified for the distribution domain.

The solution to Equations 143, 145 and 146 requires a robust initialization procedure because the system of equations is unlikely to converge unless a good initial guess is given for $\{\rho_c(z)\}$. To aid convergence, we start with a system of equations that is easily solvable by gPROMS and then gradually move to the final system of equations using the in-built initialization procedure. We first start by rearranging Equation 143 and defining the residual term r_i as a free variable

$$\begin{aligned} r_i(z) = -\mu_i + \mu_i^{SAFT}(\{\rho_c(z)\}) - \sum_{j=1}^{n} m_i m_j \rho_j(z) \alpha_{ij}^{vdW} \\ + \sum_{j=1}^{n} m_i m_j \left[\rho_j^{B,I} \int_{-\infty}^{z_{LB}} dz \phi_{ij}^{att^*}(|z-z'|) \right. \\ + \int_{z_{LB}}^{z_{UB}} dz \rho_j(z') \phi_{ij}^{att^*}(|z-z'|) \\ \left. + \rho_j^{B,II} \int_{z_{UB}}^{\infty} dz \phi_{ij}^{att^*}(|z-z'|) \right]. \end{aligned} \tag{149}$$

Note that by setting $r_i(z) = 0$ at all z we obtain the Euler-Lagrange equation. By relaxing the constraint on $r_i(z)$ we can specify $\{\rho_c(z)\}$ to initialize the problem. In this case, we converge from a step-change profile that changes between the two bulk densities at the midpoint of z_{LB} and z_{UB}. The initialization procedure is defined as follows. As a first step to the initialization procedure in gPROMS, Equation 150 is solved

$$\{\rho_c(z)\} = \text{step-change profile.} \tag{150}$$

Next, we gradually move to the new set of equations defined by

$$r_i(z) = 0 \quad \text{(Euler-Lagrange equation).} \tag{151}$$

We found that this solution procedure provides a robust method for convergence of the equations in all cases (even for three component mixtures). Once initialized,

one can move efficiently between different equilibrium density profiles by making gradual steps in the thermodynamic variables (e.g., temperature, pressure and mole fraction).

6.5.3 *Numerical options*

z_{LB} and z_{UB} are fixed to values suitably large such that they contain the interface where the density varies, typically $-30\sigma_{11}$ and $30\sigma_{11}$ respectively, however this inter-facial width is increased for near-critical calculations. The number of discretized points in the z domain, N_{dist}, is set to 500, and a sixth order centred finite difference method is used for the numerical integration. "DASOLV" is used as the numerical solver with default options, but with the absolute and relative tolerance options reduced to 10^{-10}.

6.6 RESULTS AND DISCUSSION

This section analyzes several aspects of the proposed DFT approach. To provide a stringent test of the theory, we will first test the validity of the proposed DFT approach by comparing the predictions of the theory with molecular simulations. To ensure a direct mapping between the potential function used in the SAFT theory and the simulations, the first section focuses on molecules that consist of Mie chains with an integer number of segments, without association interactions. We will then assess the predictive capacity of the DFT approach when applied to SAFT-VR Mie models parametrised for real molecules by comparing the predicted values in the interfacial tension with experimental data, including molecules that contain a non-integer number of segments and those that exhibit association interactions.

6.6.1 *Comparison with simulations*

In this section we will consider pure components and mixtures of Lennard-Jones chains consisting of 1,3 and 5 segments. We use the notation LJ_m to refer to a molecule consisting of m tangentially bonded Lennard-Jones segments ($\lambda_{ij}^r = 12$ and $\lambda_{ij}^a = 6$). We also consider the pure component 8-6 Mie fluid ($\lambda_{ij}^r = 8$ and $\lambda_{ij}^a = 6$). The variables in this section are reduced with respect to the pure component parameters of the first component, with σ_{11} and ϵ_{11} being the length and energy scaling units respectively. Therefore, the reduced variables are defined as follows: $T^* = Tk_B/\epsilon_{11}$, $P^* = P\sigma_{11}^3/\epsilon_{11}$,$\rho^* = \rho\sigma_{11}^3$, $\gamma^* = \gamma\sigma_{11}^2/\epsilon_{11}$ and $z^* = z/\sigma_{11}$.

6.6.1.1 *Pure components*

In Figure 83, we show the density profiles for the vapour-liquid interface for LJ_1 molecules ($m_{LJ_1} = 1$) at various temperatures compared to the molecular simulations of Duque et al. (2004). The results show excellent agreement with the molecular simulations, with densities following the typical hyperbolic tangent shape and the interfacial width captured accurately. In Figure 84 we show the level of agreement between the DFT and the interfacial tension obtained from molecular simulations in the literature. There is some disagreement in the literature values

due to the differences in the molecular simulation technique, but we see that the theory is quantitatively accurate in most cases.

In Figure 85, we show the density profiles for the vapour-liquid interface for an 8-6 Mie fluid at various temperatures compared to the molecular simulations of Lindeboom et al. (2019). This represents a longer-range attractive interaction compared with the Lennard-Jones fluids. Again, the DFT predicts the simulation result with remarkable accuracy. In Figure 86 we show that the DFT is in excellent agreement with the simulations.

In Figure 87 we include the prediction of the DFT when applied at low temperatures (green curve, $T^* = 0.4$), a temperature well-below the triple point ($T^* \approxeq 0.72$ (Ladd and Woodcock, 1977)). The theory predicts abnormal shapes in the density profiles at low temperatures (green curve); in fact the profile shown here exhibits two discontinuities. This is not an issue when applying the DFT to a simple LJ monomer because we are applying SAFT, a fluid theory, outside its range of applicability at temperatures where the simulation is expected to freeze. In section 6.7 we will see that this becomes an issue when applying the DFT to real molecules that contain a high degree of association, since the theory predicts discontinuous density profiles at temperatures far above the experimental triple point.

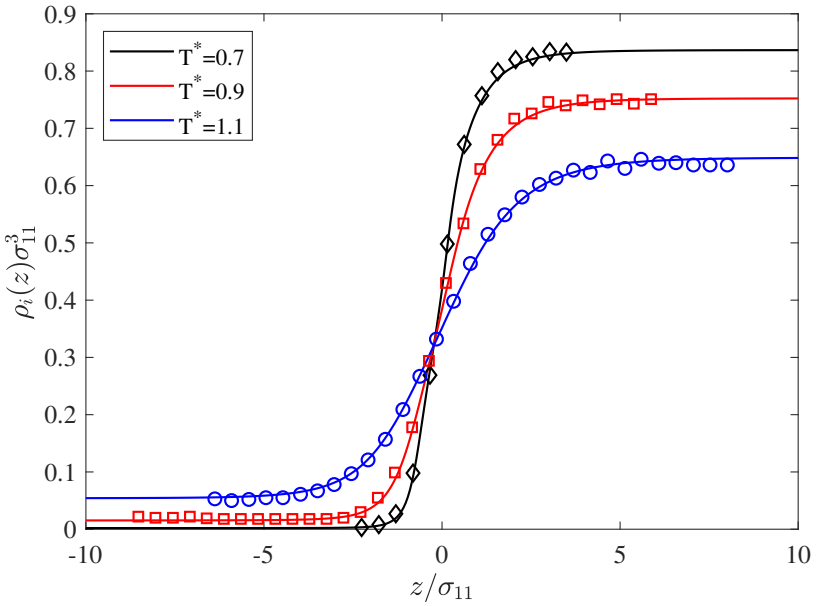

Figure 83: The density profile for a system of LJ_1 molecules at various temperatures compared to the molecular dynamic (NVT) simulations of Duque et al. (2004). The continuous lines are the SAFT-VR Mie MF DFT predictions and the scattered points are the molecular simulation results.

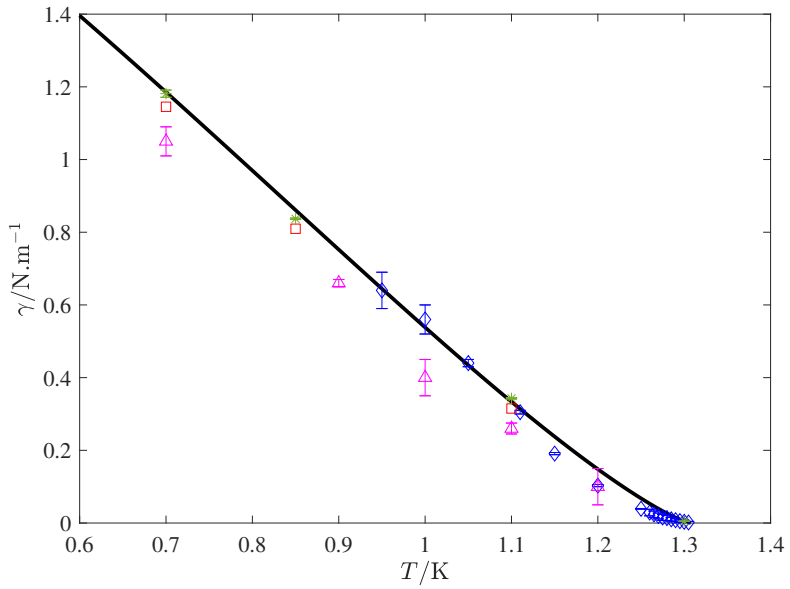

Figure 84: Comparison between the predicted interfacial tensions for the LJ_1 fluid and the result determined from molecular simulations at various temperatures. The solid black curve corresponds to the DFT calculation in this work. The simulation results are taken from various sources: blue diamonds (Potoff and Panagiotopoulos, 2000), green stars ((Errington, 2003)), magenta triangles Duque et al. (2004) and red squares (Mecke et al., 1997).

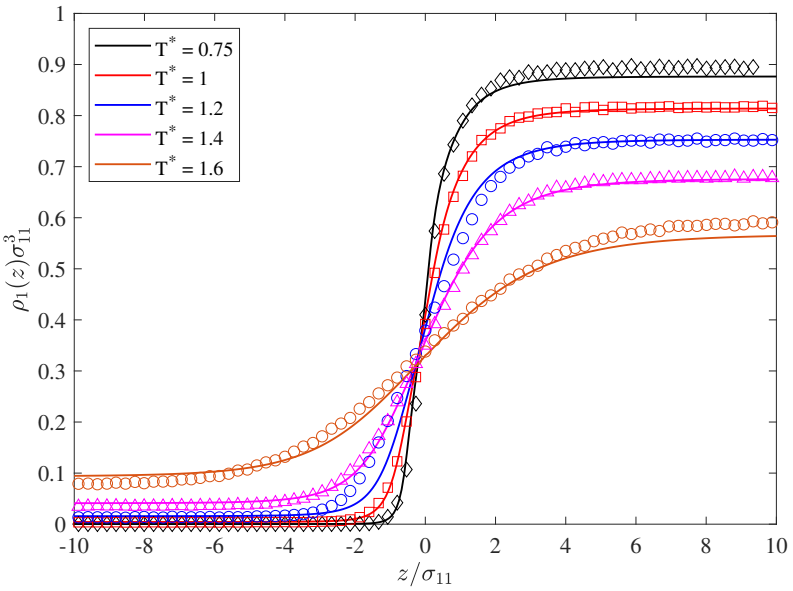

Figure 85: The vapour-liquid density profiles for an 8-6 Mie fluid at various temperatures compared to the molecular dynamic (NVT) simulations of (Lindeboom et al., 2019). The scattered points are the molecular simulation results, and the continuous lines are the predictions of our SAFT-VR Mie MF DFT

.

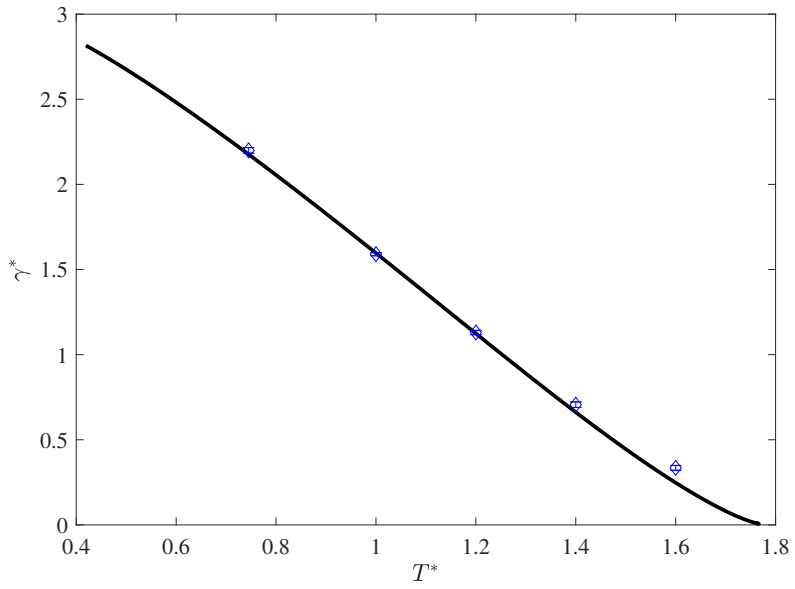

Figure 86: Comparison between the predicted interfacial tensions for the 8-6 Mie fluid and the result determined from molecular simulations at various temperatures. The solid black curve corresponds to the DFT calculation in this work. The blue diamonds are the simulation results (Lindeboom et al., 2019).

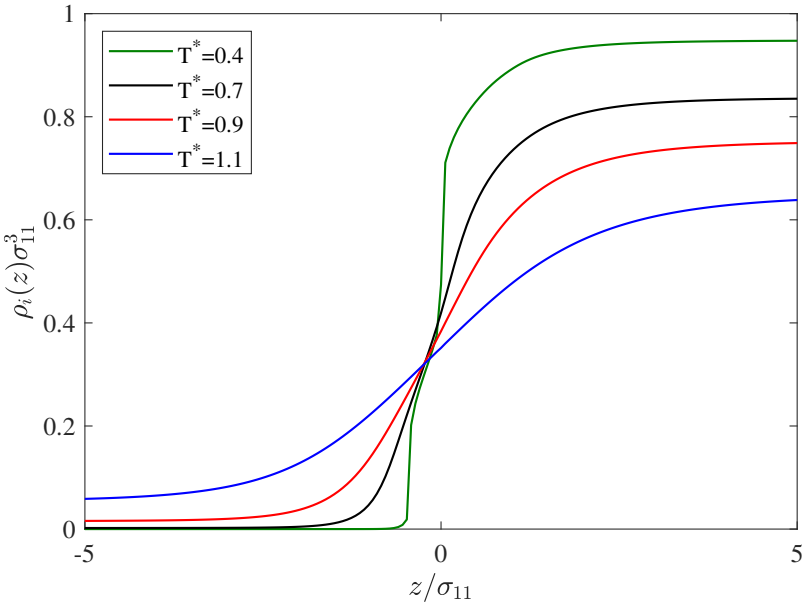

Figure 87: The density profile for a system of LJ_1 molecules at various temperatures.

6.6.1.2 *Mixtures*

The mixtures considered here are detailed in Table 31. For mixture 1 we consider a binary mixture of a monomer fluid (LJ_1) and a trimer, LJ_3 with three tangential Lennard Jones segments. For mixture 2 we consider a binary mixture of a monomer fluid (LJ_1) and a pentamer, LJ_5 with five tangential Lennard Jones seg-

ments. For mixture 3 we consider the mixture consisting of three components: LJ_1, LJ_2 and LJ_3. Details regarding the molecular simulations are covered in section 6.10.1.

Table 31: Thermodynamic properties for the three mixtures considered in this section that exhibit vapour-liquid equilibria. x refers to the liquid mole fraction. Subscripts 'sim' and 'DFT' refer to the simulation and DFT results respectively.

Mixture	T^*	x_{LJ_1}	x_{LJ_3}	x_{LJ_5}	$1000 \times P^*_{sim}$	$1000 \times P^*_{DFT}$	γ^*_{sim}	γ^*_{DFT}
1	1	0.722	0.278	-	6.9 ± 0.25	7.4	1.090 ± 0.013	1.130
2	1	0.450	-	0.550	16.4 ± 0.4	16.7	0.801 ± 0.026	0.804
3	0.833	0.564	0.309	0.127	3.0 ± 0.4	3.1	1.223 ± 0.0337	1.220

In Figure 88 we compare the density profile predicted by the DFT with the molecular simulation results for mixture 1, consisting of monomer LJ_1 and trimer LJ_3 Lennard-Jones molecules at fixed temperature ($T^* = 1$) and liquid phase composition (detailed in Table 31). The theory predicts the density profiles accurately and is able to correctly capture the inter-facial width. It is also able to capture the accumulation of the light component at the interface.

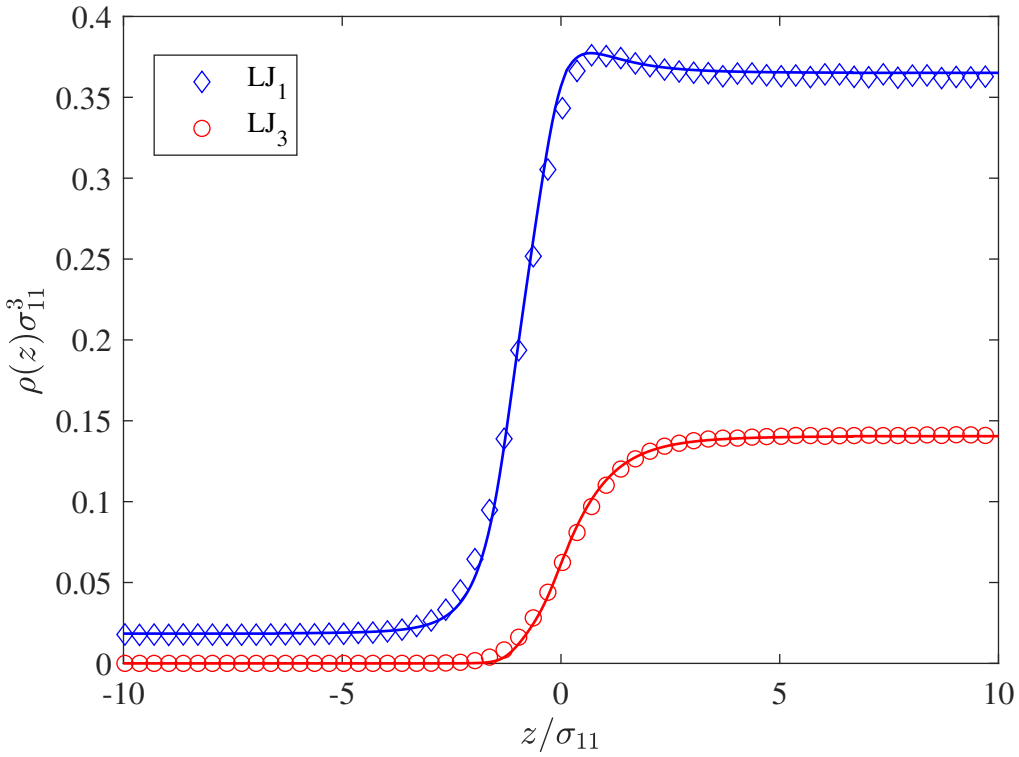

Figure 88: The vapour-liquid equilibrium density profile of the binary mixture of Lennard-Jones monomers LJ_1 ($m_{LJ_1} = 1$) and trimer LJ_3 ($m_{LJ_3} = 3$) molecules compared to molecular dynamic (NVT) simulations at a reduced temperature $T^* = 1$. The liquid phase composition in the simulations and the DFT theory is $x_{LJ_1} = 0.722$. The blue and red continuous curves correspond to the result of the SAFT-VR Mie MF DFT for LJ_1 and LJ_3 respectively. The blue diamonds (LJ_1) and red circles (LJ_3) correspond to the simulation results Lindeboom et al. (2019).

The second mixture we consider consists of monomer LJ_1 and pentamer chain LJ_5 molecules. The density profiles are compared with molecular simulations in Figure 89. In this case, the excess absorption of the light component at the interface is more pronounced, and the maximum in density of the light component is again predicted well by the SAFT-VR Mie MF DFT, although there is a small under-prediction. This deviation may be due to the use of the LDA in a region where there are large variations in density with respect to z. The theory slightly under-predicts the number density of the chains close to the bulk vapour phase.

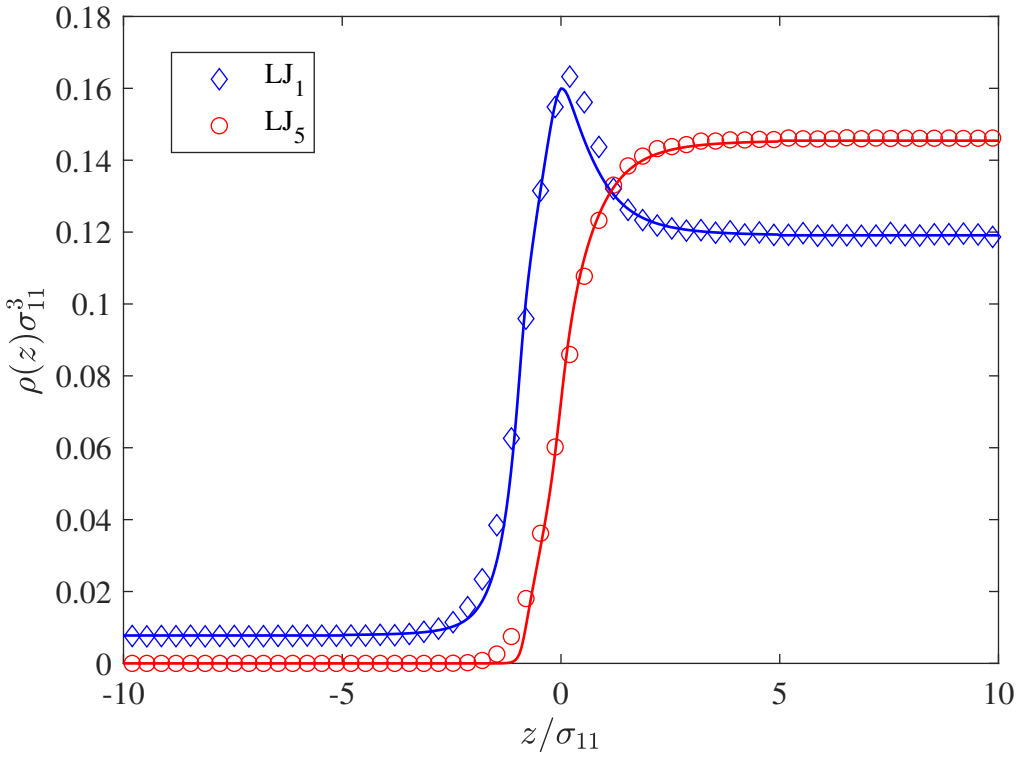

Figure 89: The vapour-liquid equilibrium density profile of the binary mixture of Lennard-Jones monomers LJ_1 ($m_{LJ_1} = 1$) and pentamer LJ_5 ($m_{LJ_5} = 5$) molecules compared to molecular dynamic (NVT) simulations at a reduced temperature $T^* = 1$. The liquid phase composition in the simulations and the DFT theory is $x_{LJ_1} = 0.450$. The blue and red continuous curves correspond to the result of the SAFT-VR Mie MF DFT for LJ_1 and LJ_5 respectively. The blue diamonds (LJ_1) and red circles (LJ_5) correspond to the simulation results Lindeboom et al. (2019).

The third mixture we consider is the ternary mixture consisting of monomer LJ_1, trimer LJ_3 and pentamer LJ_5 chain molecules. The vapour-liquid density profiles predicted by the DFT are compared with the molecular simulation results in Figure 90. Again, the theory is able to predict the density profiles both qualitatively and quantitatively, however the theory slightly under-predicts the densities near the bulk vapour phase. Furthermore, for all mixtures considered in this section we are able to predict the interfacial tension calculated from the simulation remarkably well (see Table 32).

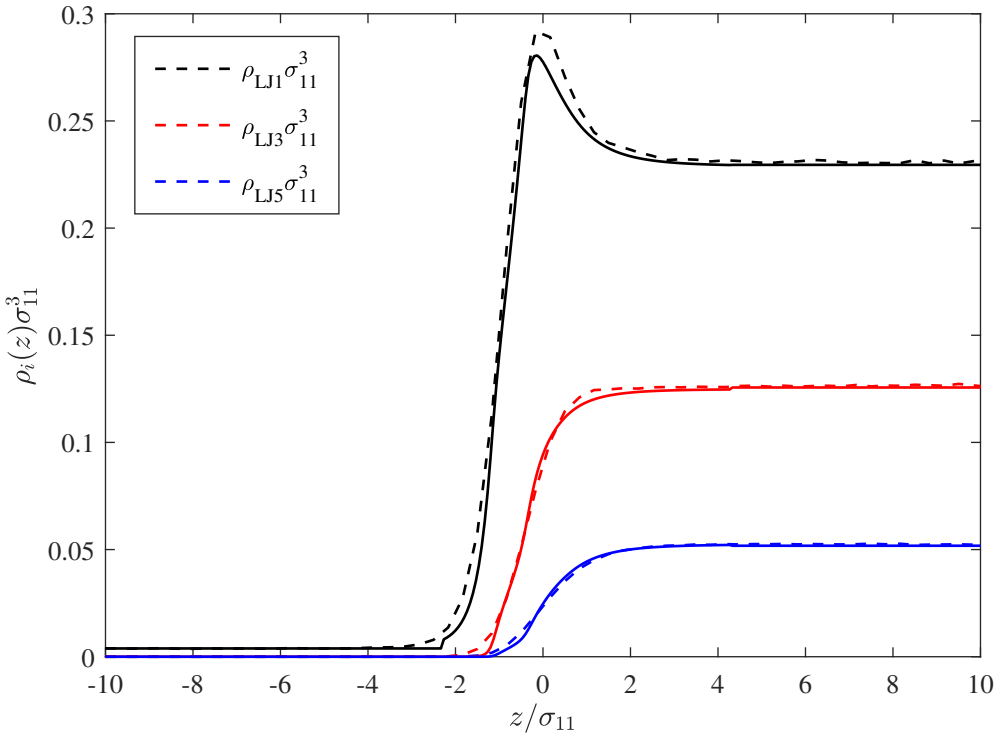

Figure 90: The vapour-liquid density profile of the ternary mixture of Lennard-Jones monomer LJ_1, trimer LJ_3 and pentamer LJ_5 chain molecules compared to molecular dynamic (NVT) simulations at reduced temperature $T^* = 0.833$. The liquid phase composition in the simulations and the DFT theory are $x_{LJ1} = 0.833$ and $x_{LJ3} = 0.550$. The black, red and blue continuous curves correspond to the result of the SAFT-VR Mie MF DFT for LJ_1, LJ_3 and LJ_5 respectively. The dashed curves correspond to the simulation results of Lindeboom et al. (2019).

Finally, we will consider a binary equimolar mixture of LJ_1 and LJ_1^* molecules, where we have used the superscript '*' to distinguish between the two identical molecules. The results are compared to the molecular simulations by Garrido et al. (2016). Liquid-liquid equilibria is achieved by setting an unfavourable unlike interaction between the two particles ($\varepsilon_{12} = \varepsilon_{21} = 0.5\varepsilon_{11}$). In Figure 91 we show the density profiles predicted by the theory and compare these with the molecular simulation results. The theory is able to predict the density profiles of the pure components, although the width of the interface is slightly over-predicted. The theory is also able to predict the minimum in the total number density of molecules at the middle of the interface. The prediction of the liquid-liquid interfacial tension for this system at various pressures is shown in Figure 92. One is able to predict the interfacial tension with quantitative accuracy, with only a small over-prediction.

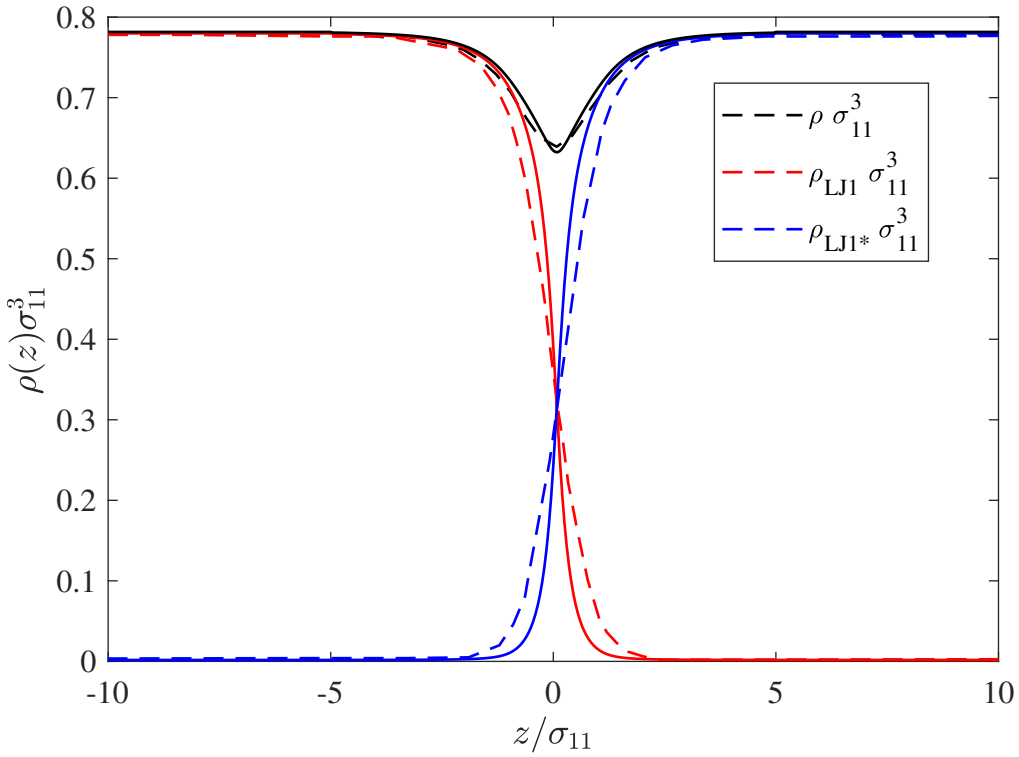

Figure 91: The liquid-liquid equilibrium density profile for the binary mixture of Lennard-Jones monomers LJ1 ($m_{LJ_1} = 1$) and LJ_1^* ($m_{LJ_1^*} = 1$) with an unlike interaction $\varepsilon_{12} = \varepsilon_{21} = 0.5\varepsilon_{11}$ compared to the molecular dynamic (NP_zAT) simulation results of Garrido et al. (2016) at a reduced temperature $T^* = 0.9$. The dashed curves are the simulation results and the continuous curves are the SAFT-VR Mie MF DFT predictions. The red and blue curves correspond to the number density of LJ_1 and LJ_1^* monomers respectively, and the black curves are the total number density of segments.

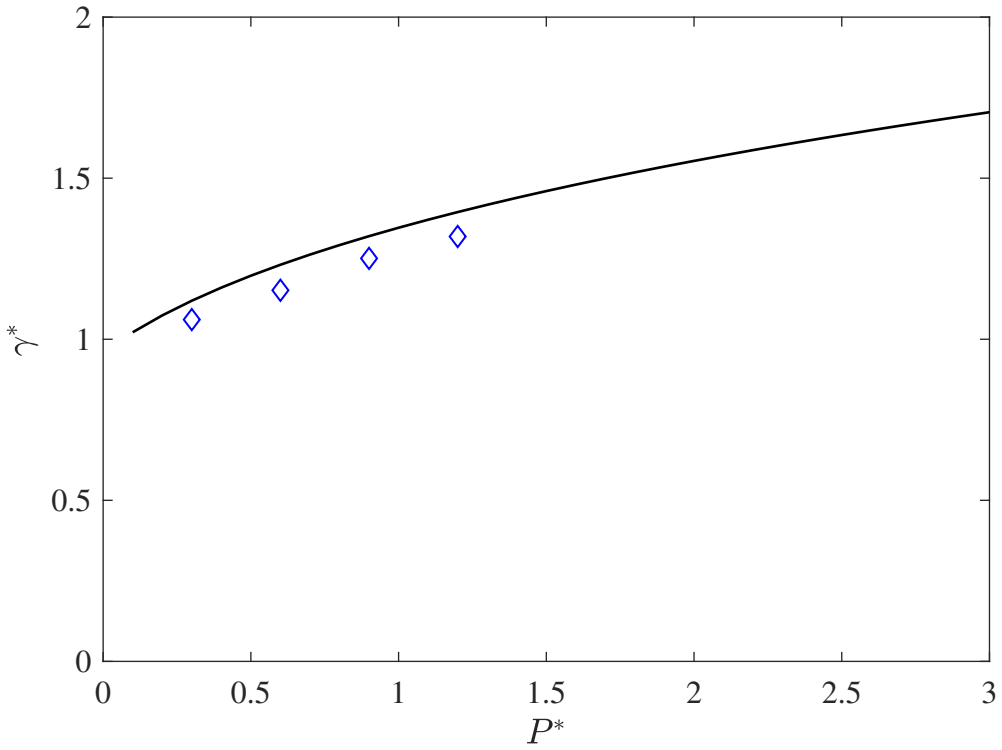

Figure 92: The interfacial tension for a mixture of LJ_1 and LJ_1^* monomers (continuous curve) with cross interaction $\varepsilon_{12}^* = \varepsilon_{21}^* = 0.5\varepsilon_{11}^*$ compared to the molecular dynamic (NP_zAT) simulation data (symbols) reported by Garrido et al. (2016) at a reduced temperature $T^* = 0.9$.

6.7 PREDICTION OF REAL FLUIDS

6.7.1 *Pure components*

The adequacy of the aforementioned DFT approach in predicting the interfacial tensions of real fluids is assessed in this subsection. We will first look at the series of n-alkanes and then assess the performance for molecules that contain association that are relevant to this thesis: water, ethylamine, ethanol and monoethanolamine, for which we have estimated the parameters in the previous chapter. We will also look at the prediction of the interfacial tension of carbon dioxide, a quadrupolar molecule, for two different SAFT-VR Mie models.

The models and their parameters are detailed in Table 32. In Table 33 we also show the AAD (%) for each of these models for saturated liquid density, vapour pressure and saturated liquid heat capacity.

Table 32: Interaction parameters used in this section

k	Group k	m_k	λ^r_{kk}	λ^a_{kk}	σ_{kk}/Å	(ϵ_{kk}/k_B)/K	$N_{ST,k}$	$n_{k,H}$	$n_{k,e}$	$\epsilon^{HB}_{e,H}/k_B$/K	$K^{HB}_{e,H}$/Å^3	Ref
1	ethanol	2.2563	12.2824	6	3.2903	238.966	2	1	2	2247.29	42.7936	current work
2	ethylamine	2.25735	11.18418	6	3.37402	226.285	2	2	1	851.856	112.08414	current work
3	carbon dioxide 1	1.694	26.408	5.055	3.05	207.891	-	-	-	-	-	Papaioannou et al. (2016)
4	carbon dioxide 2	1	23	6.66	3.741	353.55	-	-	-	-	-	Avendano et al. (2011)
5	water 1	1.2566	25.126	6	2.8024	351.23	2	2	2	1630.6	177.62	current work
6	water 2	1	17.02	6	3.0063	266.68	2	2	2	1985.4	101.69	Dufal et al. (2015a)
7	methane	1	12.319	6	3.7366	151.45	-	-	-	-	-	Dufal et al. (2015a)
8	hexane	2.2549	17.203	6	4.2968	321.81	-	-	-	-	-	Dufal et al. (2015a)
9	decane	3.0058	18.403	6	4.5727	396.17	-	-	-	-	-	Dufal et al. (2015a)

Table 33: Table of AAD (%) for the molecules considered in this section. The temperature range considered is between the experimental triple point up to 0.9*T_c.

k	Group k	AAD ρ_L^{sat} (%)	AAD P^{sat} (%)	AAD C_P (%)
1	ethanol	0.267	0.127	0.757
2	ethylamine	0.81	0.184	0.503
3	carbon dioxide 1	0.38	1.92	6.67
4	carbon dioxide 2	1.29	15.49	3.26
5	water 1	0.87	0.50	0.16
6	water 2	1.06	1.28	10.52
7	methane	0.75	0.4	1.23
8	hexane	0.29	0.16	0.87
9	decane	0.46	0.41	0.70

In Figure 93 we show the predictions of the interfacial tension for the n-alkane series: methane, propane, n-hexane and n-decane, the parameters for which were estimated by Dufal et al. (2015a) from vapour pressure and saturated liquid density data. The results show a good qualitative prediction of the experimental interfacial tension, however it is systematically over-predicted. This over-prediction appears worse than more sophisticated DFT of Gross (2009), which is based on the perturbed-chain statistical associating fluid theory (PC-SAFT) EoS, but we note that this difference in agreement may be due to the bulk EoS model rather than simplifications used in the DFT method because PC-SAFT uses a reference hard-chain free energy that is correlated to the series of n-alkanes (Gross and Sadowski, 2001) and is therefore likely to be more accurate for these molecules.

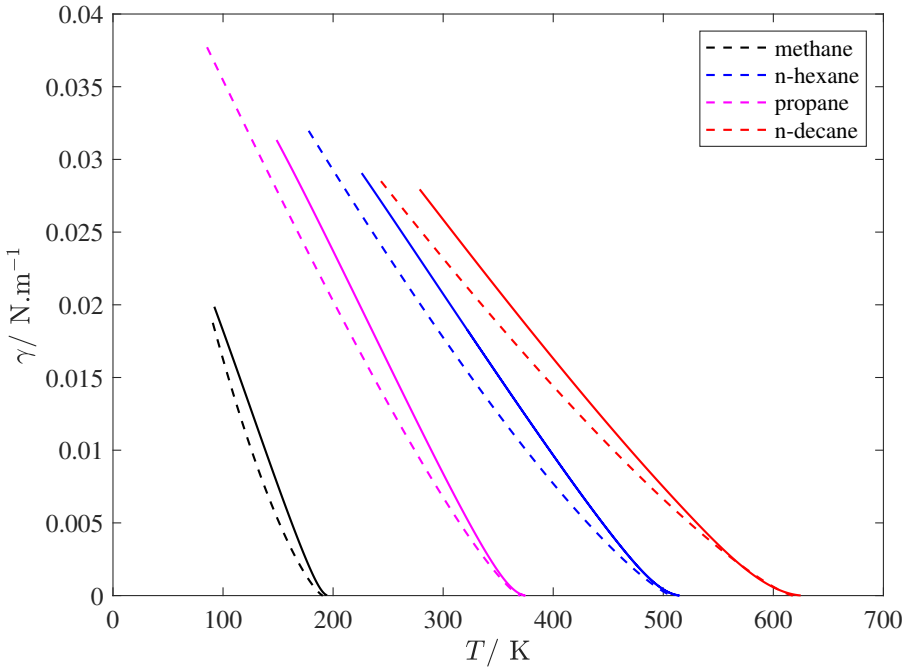

Figure 93: A comparison between the predicted interfacial tensions of the proposed DFT approach and experimental data for methane, n-propane, n-hexane and n-decane. The continuous curves are the predictions of the proposed SAFT-VR Mie MF DFT using the models given in reference (Dufal et al., 2015a). The dashed curves are the correlated data from NIST (E.W. Lemmon and Friend, 2018).

We now analyse two SAFT-VR Mie models for water. Group 5 in Table 32 is the water model (model 5NS) developed in chapter 4. The other model is group 6 in Table 32 which is taken from Dufal et al. (2015b) (labelled model 1L in chapter 4). Figure 94 we show the predictions of the SAFT-VR Mie MF DFT and compare these with experimental data. Model 5NS is quantitatively accurate over the range of temperatures where we do not experience a discontinuity in the equilibrium density profile, and is in better agreement with the experimental data than model 1L, which over-predicts the critical point and under-predicts the surface tension at lower temperatures.

We see from Figure 95 that the agreement is excellent for the model of monoethanolamine developed in this thesis. These results confirm the predictive capabilities of the DFT theory and the robustness of parameters developed for water and monoethanolamine. The interfacial tension is not calculated at low temperatures, due to the density profiles becoming discontinuous upon reducing the temperature, as depicted in Figure 96. Below these temperatures, gPROMS fails to find a solution to the Euler-Lagrange equation. As discussed in section 6.6.1, the theory predicts similar shaped profiles for a simple LJ_1 fluid at temperatures below the simulation triple point and therefore may indicate the presence of a solid phase. We suspect that this unphysical result at low temperatures for associating systems is due to the fact that we are evaluating properties at temperatures below the triple point of the *reference* Mie system.

The models for ethanol and ethylamine developed in this thesis both show an over-prediction of the interfacial tension, as depicted in Figures 97 and 98.

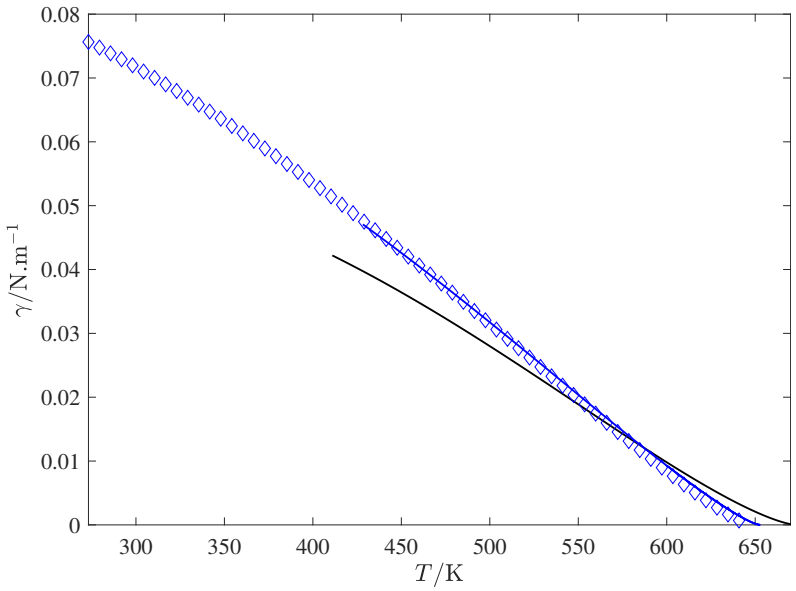

Figure 94: A comparison between the predicted interfacial tensions of the proposed SAFT-VR Mie MF DFT approach for water and experimental data. The black continuous curve is the prediction using the literature model of Dufal et al. (2015b) (group 6 in table 32). The blue continuous curve is the prediction using the non-shperical model of water developed in this thesis (group 5 in table 32). The blue diamonds are the correlated data from NIST (E.W. Lemmon and Friend, 2018).

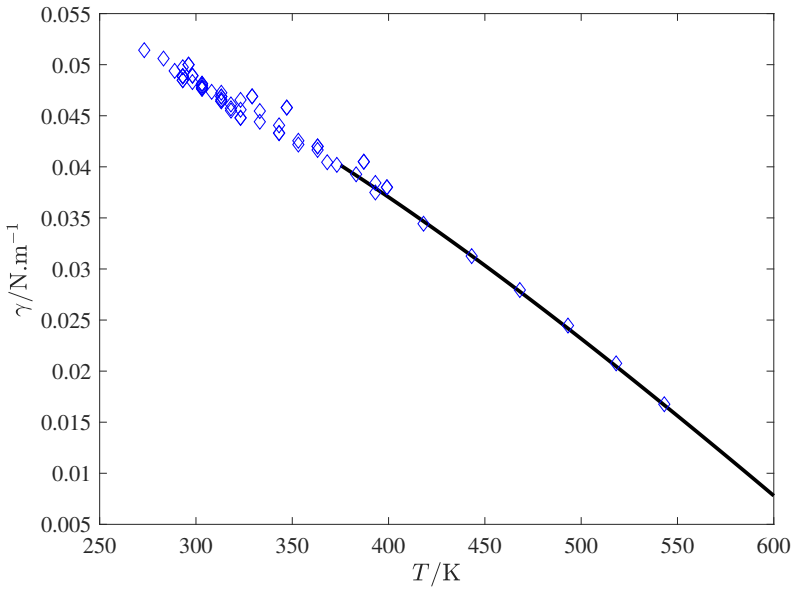

Figure 95: A comparison between the predicted interfacial tensions of the proposed DFT approach for monoethanolamine and experimental data. The continuous curve is the prediction of the SAFT-VR Mie MF DFT model for MEA derived in this thesis (cf. Table 32)). The blue diamonds are the experimental data from various sources (Liessmann et al., 1995).

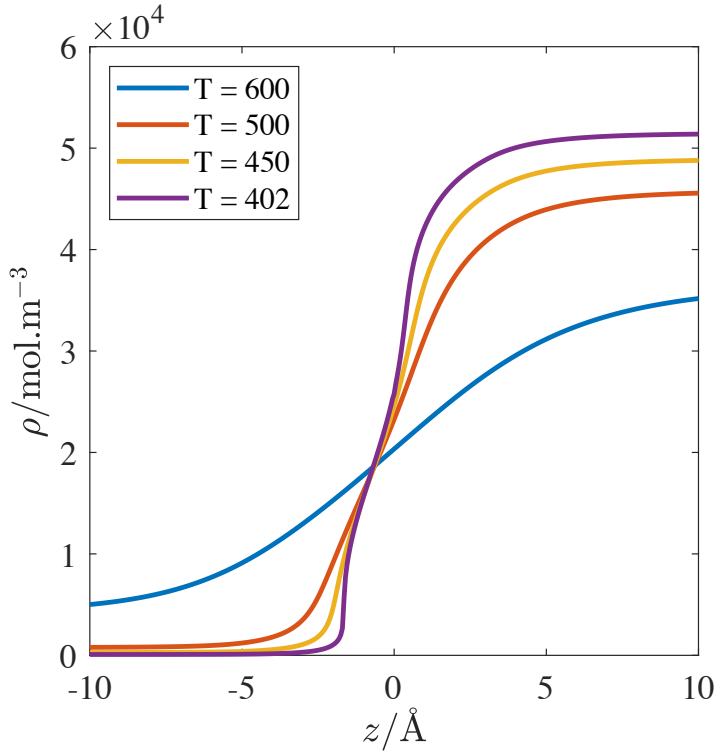

Figure 96: The density profile for the model of water at different temperatures (with the colours for each temperature indicated in the legend). Below 430 K, the equilibrium density profile becomes discontinuous.

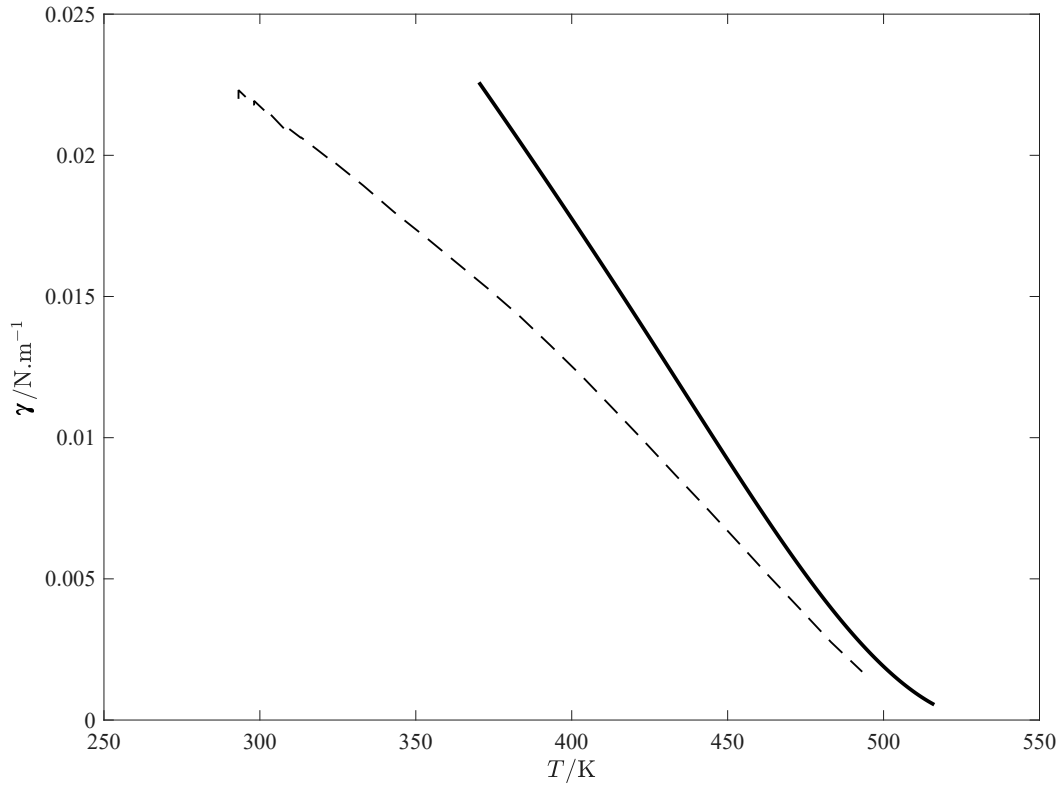

Figure 97: A comparison between the predicted interfacial tensions of the proposed SAFT-VR Mie MF DFT approach for ethanol and experimental data. The continuous black curve is the model developed in this thesis (cf. Table 32). The dashed curve is the correlated data from Fletcher et al. (1996)

.

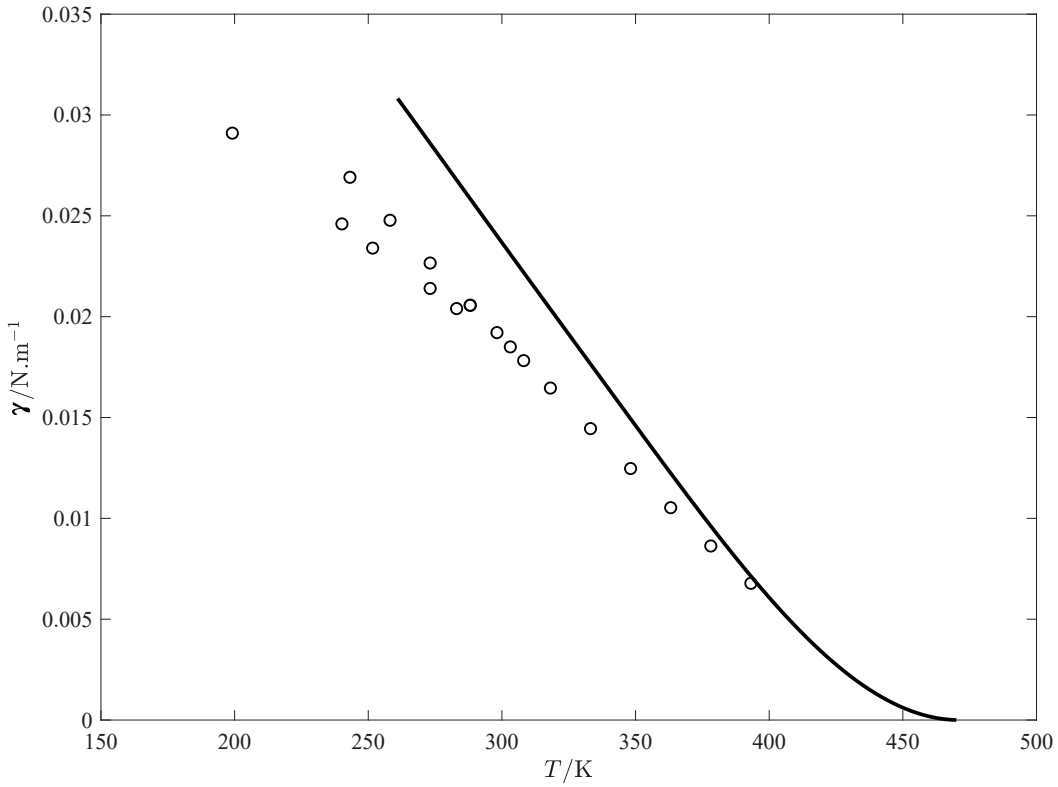

Figure 98: A comparison between the predicted interfacial tensions of the proposed SAFT-VR Mie MF DFT approach for ethylamine. The continuous black curve is the model developed in this work (cf. Table 32). The open circles are the experimental data (Fletcher et al., 1996).

In Figure 99, we show the predicted interfacial tension of carbon dioxide for two models: the SAFT-γ Mie model of Papaioannou et al. (2016), and the coarse-grained model of Avendano et al. (2011) with parameters scaled to match the experimental critical point. The former model over-predicts the interfacial tension, while the latter model is in excellent agreement with the experimental data. The discrepancy in prediction between the two models may be due to the way in which the models were parametrised. Both provide an excellent agreement with the experimental critical point, however the model of Avendano et al. (2011) was obtained by adjusting the parameters to saturated liquid density and vapour pressure data and then rescaling these parameters to match the critical point, thus the model offers large deviations with respect to the experimental liquid density and vapour-pressure. Nevertheless, it is gratifying to see that the DFT applied to the model of Avendano et al. (2011) provides a good prediction of the vapour-liquid interfacial tension, since the same model was confirmed to match the interfacial tension predicted by Monte-Carlo simulations. The large relative deviations of the model of Papaioannou et al. (2016) (AAD approximately 50 % for temperatures between the triple point and 0.9 T_c) indicates that there is potentially a better SAFT-VR Mie model for CO_2 for describing this property. Furthermore, we can see from Table 33 that the model of Avendano et al. (2011) more accurately describes C_P. This could indicate that parametrizing to C_P data is a useful route for thermodynamic model more accurately describing the interfacial tension.

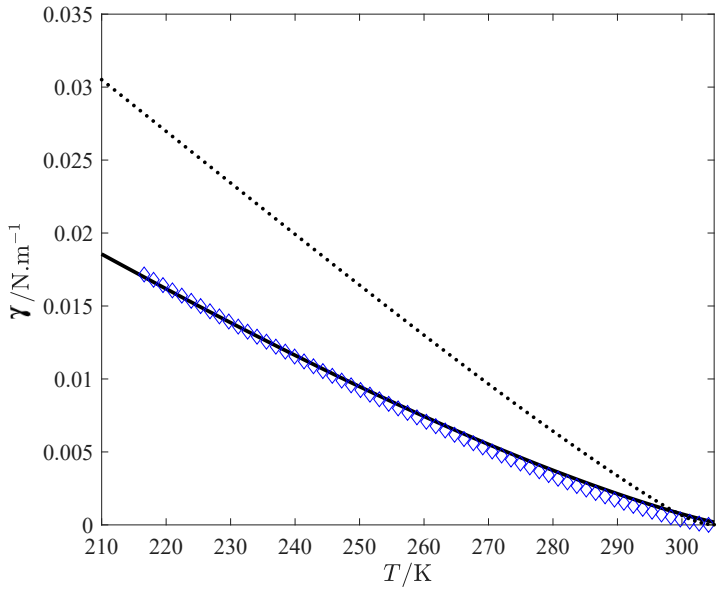

Figure 99: A comparison between the predicted interfacial tensions of the proposed SAFT-VR Mie MF DFT approach for carbon dioxide and experiments. The dotted black curve is obtained with the model of Papaioannou et al. (2016). The continuous black curve is obtained with the coarse-grained model of Avendano et al. (2011). The blue diamonds are the correlated data from NIST (E.W. Lemmon and Friend, 2018)

.

6.8 MIXTURES

In this section we will analyse the binary CO_2 - H_2O mixture, the parameters for which were developed in chapter 5, the binary mixture of MEA and H_2O, and the reactive ternary mixture of CO_2 - H_2O and MEA. All of the parameters for these systems can be found in chapter 5.

In Figure 100, we show the predicted interfacial tension for the binary mixture of CO_2 - H_2O when T = 469.15 K at several different pressures. A good qualitative and quantitative agreement is obtained over the pressure range considered. In Figure 101 we show the density profiles obtained at P =10.1 MPa and T = 469.15 K. We see that the theory predicts accumulation of CO_2 at the interface. Similar density profiles have been observed in the literature (see for example the results obtained by Lafitte et al. (2010) using density gradient theory).

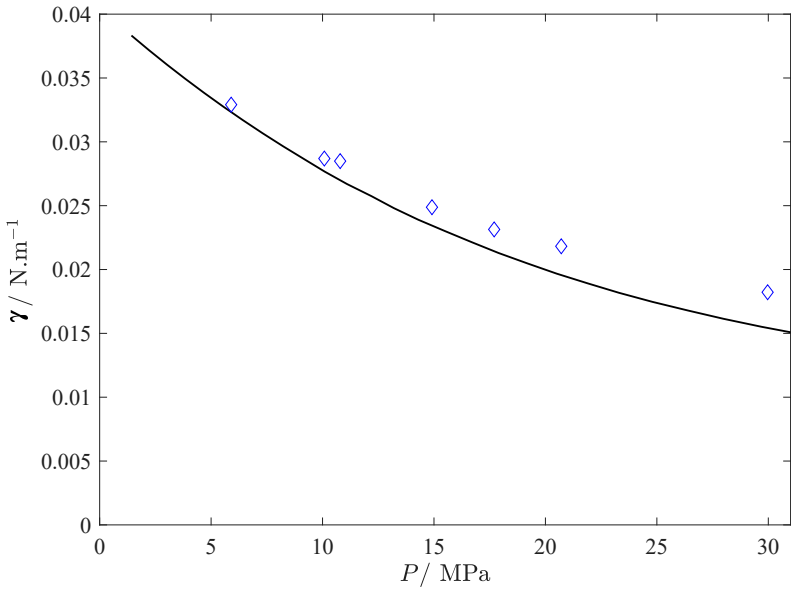

Figure 100: A comparison between the predicted interfacial tensions of the proposed DFT approach for the binary system of carbon dioxide and water at 469.15 K using the models developed in this thesis. The black line is the prediction of the proposed DFT approach. The blue diamonds are the experimental data from Pereira et al. (2016).

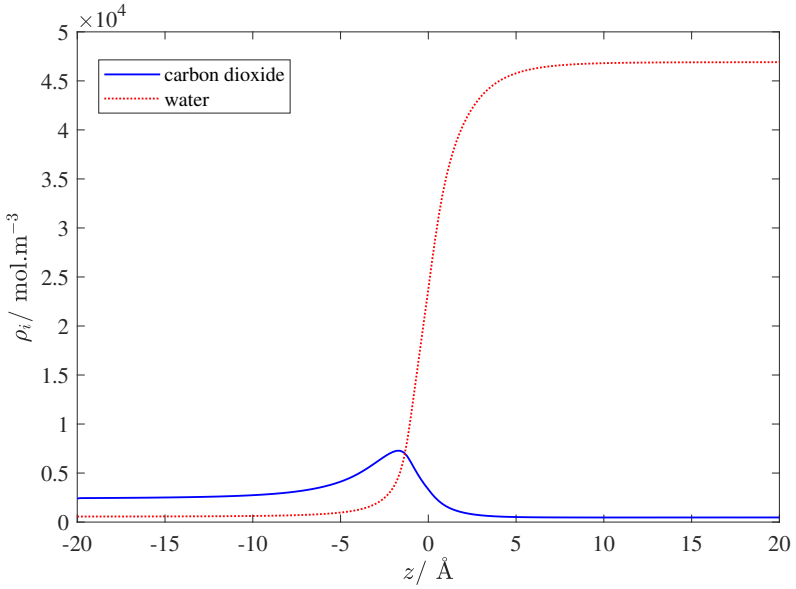

Figure 101: Figure to show the predicted density profiles between the vapour and liquid bulk phases for carbon dioxide and water at P = 10.1 MPa and T = 469.15 K.

In Figure 102, we show the predicted interfacial tension for the binary mixture of MEA - H_2O at various temperatures and compositions. We obtain a good qualitative prediction. In Figure 101 we show the density profiles obtained at P =10.1 MPa and T = 469.15 K.

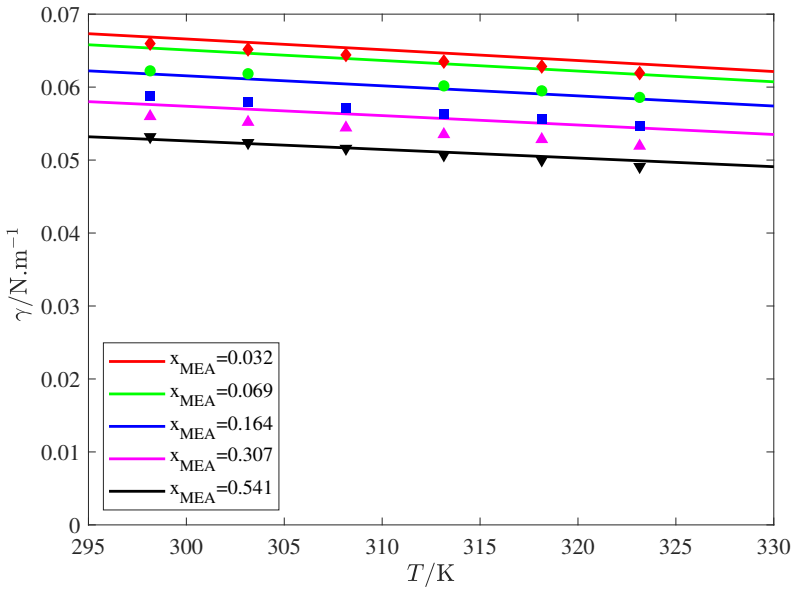

Figure 102: A comparison between the predicted interfacial tensions of the proposed SAFT-VR Mie MF DFT approach for the binary system of MEA and water at various temperatures and compositions. The continuous lines are the DFT predictions. The scattered data are the experimental data of Vázquez et al. (1997).

Finally, we will consider the ternary, *reactive* mixture of MEA, CO_2 and H_2O, where we treat the reactions implicity via a physical association scheme (cf. chapter 5). In Figure 103 we show the predicted intefacial tension for this mixture at a typical absorber temperature (T= 313.15 K). The theory predicts the interfacial tension of the binary mixture of MEA and H_2O accurately (at zero CO_2 loading), but it predicts that the interfacial tension decreases with CO_2 loading whereas the experimental evidence suggests that the interfacial tension increases. This discrepancy is likely due to our theory not explicitly treating the long-range electrostatic interactions present in the mixture. Matin et al. (2017) modelled the interfacial speciation of this mixture using the Pitzer equation to explicitly model the ionic species, and found that the increased ionic strength of the surface and bulk regions upon increasing CO_2 loading leads to an increase in the solution interfacial tension.

In chapter 3 we showed that using correlated interfacial tension data for the binary MEA + H_2O mixture of Vázquez et al. (1997) predicts column profiles fairly similar to the profiles obtained using the interfacial tensions of the ternary mixture of Jayarathna et al. (2013c) (Figure 27). Thus, explicit treatment of the electrostatic interactions may not be necessary for the good prediction of the chemisorption process.

Although our methodology does not predict the interfacial tension accurately for the reactive mixture at high CO_2 loadings, we can apply the SAFT-VR Mie MF DFT approach to gain physical insight into the distribution of species at the interface. In Figure 104 we show the density profile at T=450 K for the apparent densities of the three components (which includes both the reacted and un-reacted species). We see that all three components exhibit a maximum density at the interface. MEA and CO_2 accumulate at the interface.

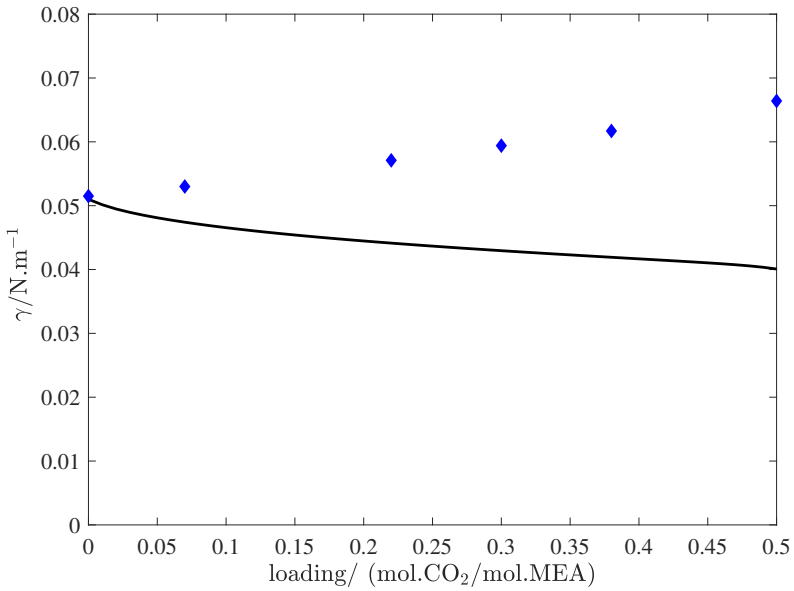

Figure 103: A comparison between the predicted interfacial tensions of the proposed SAFT-VR Mie MF DFT approach for the ternary system of CO_2, MEA and H_2O at 313.15 K and 80 wt% solvent in the liquid phase (mass of MEA/ (mass of MEA + mass of H_2O) using the models developed in this thesis. The black line is the prediction of the proposed DFT approach. The blue diamonds are the experimental data of Jayarathna et al. (2013a).

In Figure 105 we show the number density of the key reaction products: carbamate, bicarbonate and free (un-reacted) CO_2. These number densities are calculated by multiplying the mole fractions of each species (cf. Equations 113, 114 and 115 in chapter 5) by the total number density. We predict a large accumulation of carbamate and bicarbonate at the interface, while there is a small accumulation of free CO_2 close to the vapour side of the interface. In Figure 105 we also show the predicted mole fractions of these species. These density profiles give us an insight into what is happening at the vapour-liquid interface.

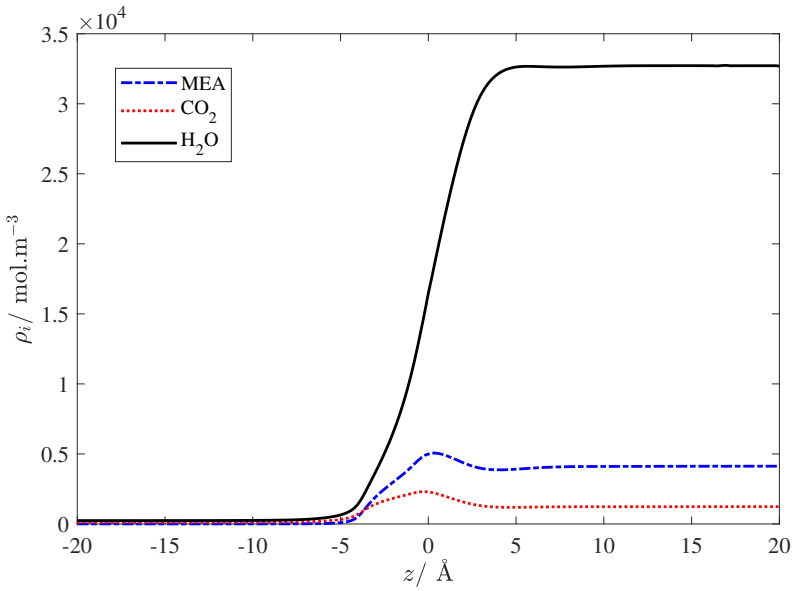

Figure 104: Figure to show the predicted density profiles for the reactive MEA, CO_2, H_2O system. The thermodynamic conditions are T = 450 K, 30 wt% solvent in the liquid phase (mass of MEA/ (mass of MEA + mass of H_2O)), and a CO_2 loading of 0.3 in the liquid phase (moles of CO_2/ moles of MEA). Here we plot the apparent densities for the three components.

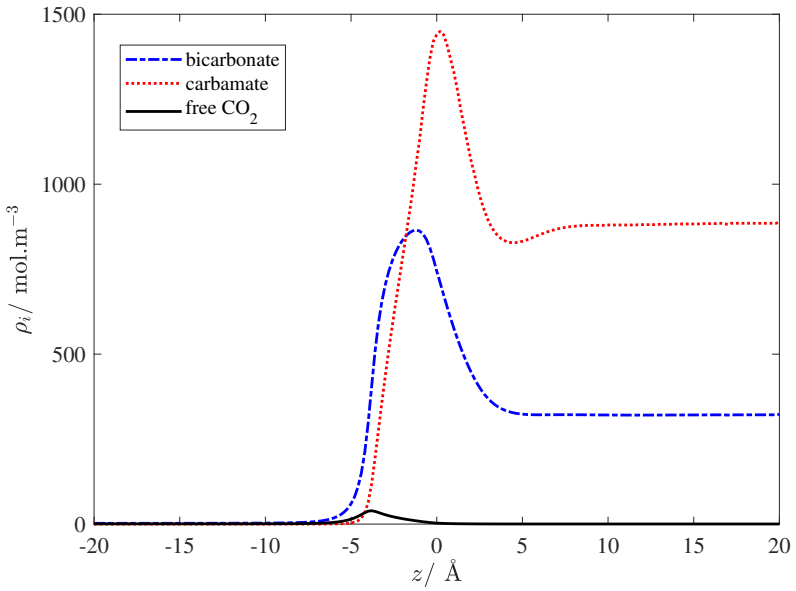

Figure 105: Figure to show the predicted density profiles for the reactive reactive MEA, CO_2, H_2O system. The thermodynamic conditions are T = 450 K, 30 wt% solvent in the liquid phase (mass of MEA/ (mass of MEA + mass of H_2O)), and a CO_2 loading of 0.3 in the liquid phase (moles of CO_2/ moles of MEA). Here we plot the density of the reacted species using the fractions of bonded association sites that mediate the reactions.

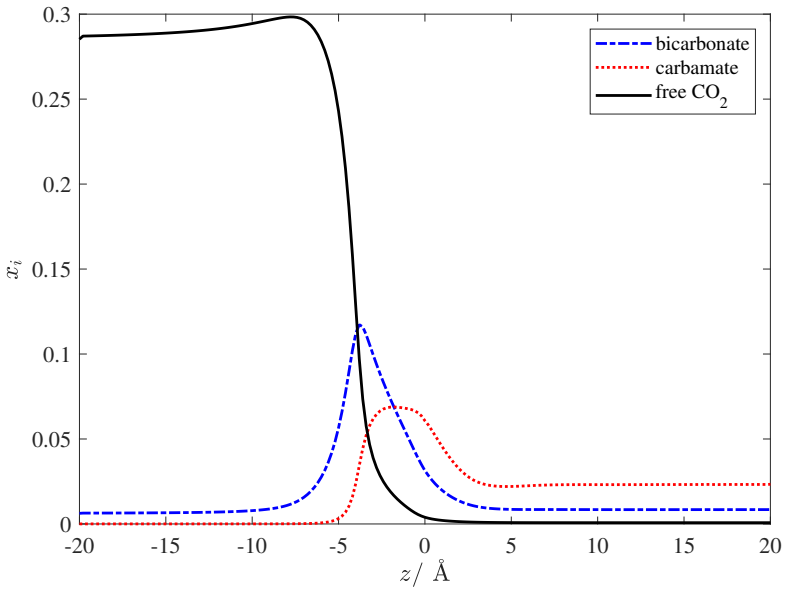

Figure 106: Figure to show the predicted concentration profiles for the reactive MEA, CO_2, H_2O system. x_i is the mole fraction of the species at each z coordinate. The thermodynamic conditions are T = 450 K, 30 wt% solvent in the liquid phase (mass of MEA/ (mass of MEA + mass of H_2O)), and a CO_2 loading of 0.3 in the liquid phase (moles of CO_2/ moles of MEA).

6.9 CONCLUSION

In this chapter, a new DFT was developed that is compatible with the SAFT-VR Mie EoS in order to predict the interfacial properties of fluids and fluid mixtures, which requires no additional parameters other than those used in the bulk EoS. The DFT was derived using suitable approximations so that the resulting system of equations are numerically tractable and therefore suitable for the rapid evaluation of SAFT-VR Mie models. An implementation was developed in gPROMS, providing an efficient solution method for systems containing any number of components, with minimal user input. A key approximation used in this work is that most of the contributions to the free energy functional can be treated at the mean-field level using a local density approximation, as suggested by Gloor et al. (2002). Another is that correlations are neglected when approximating the free energy functional due to segments interacting via a Mie potential. Although this may seem a crude approximation, we have demonstrated that the theory provides an excellent prediction of inhomogeneous properties. The resulting theory allows one to directly use the SAFT-VR Mie EoS without any modifications.

We first tested the theory by comparison with molecular simulation data for pure, two and three component Lennard-Jones molecules and the pure component 8-6 Mie fluid. The DFT predictions of the density profiles are in excellent agreement with the simulation results; for the systems analysed one can use the theory to accurately predict the interfacial width, excess absorption at the interface, and the interfacial tension. Next, the theory was tested against mixtures of single-segment Lennard-Jones fluids exhibiting liquid-liquid equilibria. The theory is in excellent agreement with molecular simulations in the literature, providing

an accurate prediction of the simulated density profiles (exhibiting phase density inversion) and interfacial tensions.

We then tested the theory against the experimental interfacial tension for real fluids that do no exhibit association, for SAFT-VR Mie models that were parametrised using bulk phase properties. Applying the DFT to the literature models for the series of n-alkanes, the results show a good qualitative and quantitative prediction of the interfacial tension, however we find that these are systematically over-predicted with the largest deviations at low temperatures. We also tested two different literature models for CO_2. The model of Papaioannou et al. (2016) systematically over-predicts the interfacial tension, whereas the model of Avendano et al. (2011) is in excellent agreement with the experimental data.

Next, we tested the performance of the DFT when applied to associating molecules. The molecules tested were: water, ethanol, ethylamine and monoethanolamine. In all cases there is a lower temperature limit (above the experimental triple point) where the DFT fails due to emerging discontinuities in the equilibrium density profile. Further work will need to be done to test if this issue is due to the inaccuracies in the DFT approach (e.g., including density correlations in the free energy functional), or if it is due to the application of the SAFT-VR Mie outside its range of validity. Applying the DFT to the water model developed in this thesis, the interfacial tension is predicted with remarkable accuracy. Similarly, the model for monoethanolamine is in excellent quantitative agreement with the theory. This may indicate that including C_P in the model parametrization is a useful route to obtaining the interfacial tension. Since the SAFT-VR Mie MF DFT approach can accurately predict the interfacial tension (with no adjustable parameters), the inclusion of interfacial tension in the model parameterization can be a useful way of obtaining more robust model parameters. The interfacial tensions of ethylamine and ethanol are predicted moderately well, however, they show the incorrect temperature dependence, indicating either issues with the underlying assumptions in the DFT theory, or the model parametrisation.

We then analysed the predictive capacity of the SAFT-VR Mie MF DFT approach when applied to associating mixtures. For the binary mixture of CO_2 and H_2O there is an excellent agreement with the experimental data at high temperatures (469.5 K) over a range of pressures (between 5 and 30 MPa). The theory predicts accumulation of CO_2 at the vapour-liquid interface. Next, we showed that one can obtain an accurate prediction of the interfacial tension of the MEA-H_2O mixture over a wide range of thermodynamic conditions. We then analysed the reactive ternary mixture consisting of CO_2, H_2O and MEA. The theory is accurate at low CO_2 loadings, but predicts the opposite trend in interfacial tension with respect to CO_2 loading due to not treating electostatic interactions explicity (we used a physical association scheme to treat the reactions). We then analysed the predictions of the SAFT-VR Mie MF DFT for the density and composition profiles for this reactive mixture. This gave a physical insight into the distribution of molecules at the vapour-liquid interface, and we showed that there is a large accumulation of the bicarbonate and carbamate species at the interface. This study showed that one can apply the proposed DFT approach (and numerical method for solving the equations) to evaluate interfacial properties of very complex mixtures.

The usefulness of the DFT methodology presented in this chapter is that, through the mean-field and local density approximations, the DFT equations are

simplified such that quick calculations may be made for the prediction of inhomogeneous properties. It is therefore possible to use this methodology for the rapid evaluation of different SAFT-VR Mie models, thus rendering the potential parameters more robust. Furthermore, it allows one to explore the density profiles within the interfacial region, providing physical insight into the way molecules behave at the interface.

6.10 APPENDIX

6.10.1 *Molecular dynamic simulation details*

The simulations in this chapter were undertaken in GROMACS (Berendsen et al., 1995) by Tom Lindeboom, Maziar Fayaz-Torshizi and Matthias Kiesel (Lindeboom et al., 2019) in the Molecular Sytems Engineering group at Imperial College, unless otherwise stated. The simulation options are detailed in Table 34 and the inputs specific to the mixtures studied are detailed in Table 35.

Table 34: Simulation details for the mixtures described in this section.

Potential cut off/ nm	2
Time step/ ps	0.005
Long range vdW corrections	PME
Thermostat	Nosé-Hoover
Thermostat time constant/ ps	2.5

Table 35: Specific simulation inputs for the mixtures studied in this work. # refers to the number of molecules of each type used in the simulation box.

Mixture	#LJ_1	#LJ_3	#LJ_5	Simulation time/ ns	Box dimensions (xyz)/ nm
1	4200	1400	-	500	3.8 x 3.8 x 30
2	4200	-	840	500	3.8 x 3.8 x 30
3	4200	1400	840	500	3.8 x 3.8 x 30

6.10.2 *Functional derivatives*

In this section we describe how to take the functional derivatives with respect to the various contributions to the Helmholtz free energy functional. Details regarding this method can be found in section 3.2 in (Hansen and McDonald, 1990). From 127 we have:

$$A^{\mathrm{SAFT,lr}}[\{\rho_c(\boldsymbol{r})\}] = \frac{1}{2}\sum_{j=1}^{n}\sum_{k=1}^{n} m_j m_k \alpha_{jk}^{vdW} \int d\boldsymbol{r'}\rho_j(\boldsymbol{r'})\rho_k(\boldsymbol{r'}), \tag{152}$$

The functional derivative with respect to $\rho_i(\boldsymbol{r})$ can be determined as follows:

$$\begin{aligned}
\frac{\delta A^{\mathrm{SAFT,lr}}[\{\rho_c(\boldsymbol{r})\}]}{\delta\rho_i(\boldsymbol{r})} &= \mu_i^{\mathrm{SAFT,lr}}[\{\rho_c(\boldsymbol{r})\}] \\
&= \frac{1}{2}\sum_{j=1}^{n}\sum_{k=1}^{n} m_j m_k \alpha_{jk}^{vdW} \int d\boldsymbol{r}' \left(\frac{\delta\rho_j(\boldsymbol{r}')}{\delta\rho_i(\boldsymbol{r})}\rho_k(\boldsymbol{r}') + \frac{\delta\rho_k(\boldsymbol{r}')}{\delta\rho_i(\boldsymbol{r})}\rho_j(\boldsymbol{r}')\right) \\
&= \frac{1}{2}\sum_{j=1}^{n}\sum_{k=1}^{n} m_j m_k \alpha_{jk}^{vdW} \int d\boldsymbol{r}'\delta(\boldsymbol{r}-\boldsymbol{r}')\left(\delta_{ij}\rho_k(\boldsymbol{r}') + \delta_{ik}\rho_j(\boldsymbol{r}')\right) \\
&= \frac{1}{2}\sum_{j=1}^{n}\sum_{k=1}^{n} m_j m_k \alpha_{jk}^{vdW} \left(\delta_{ij}\rho_j(\boldsymbol{r}) + \delta_{ik}\rho_j(\boldsymbol{r})\right) \\
&= \sum_{k=1}^{n} m_j m_k \rho_j(\boldsymbol{r}) \alpha_{jk}^{vdW}.
\end{aligned} \tag{153}$$

Here, we have used:

$$\frac{\delta\rho_i(\boldsymbol{r}')}{\delta\rho_i(\boldsymbol{r})} = \delta(\boldsymbol{r}-\boldsymbol{r}'), \tag{154}$$

and

$$\frac{\delta\rho_i(\boldsymbol{r}')}{\delta\rho_j(\boldsymbol{r})} = \delta_{ij}\delta(\boldsymbol{r}-\boldsymbol{r}'), \tag{155}$$

where δ_{ij} is the Kroneker delta function, which is defined by:

$$\delta_{ij} = \begin{cases} 1 & \text{if } i = j, \\ 0 & \text{if } i \neq j, \end{cases} \tag{156}$$

and δ is the Dirac delta distribution.

The functional derivative of the attractive free energy functional can be determined in a similar way. The functional is given by:

$$A^{\mathrm{att}}[\{\rho_c(\boldsymbol{r})\}] = \frac{1}{2}\sum_{j=1}^{n}\sum_{k=1}^{n} \int d\boldsymbol{r}' m_j \rho_j(\boldsymbol{r}') \int d\boldsymbol{r}'' m_k \rho_k(\boldsymbol{r}'') \phi_{jk}^{\mathrm{att}}(|\boldsymbol{r}'-\boldsymbol{r}''|). \tag{157}$$

The functional derivative with respect to $\rho_i(\boldsymbol{r})$ can be determined as follows:

$$\begin{aligned}
\frac{\delta A^{att}[\{\rho_c(\boldsymbol{r})\}]}{\delta\rho_i} &= \mu_i^{att}[\{\rho_c(\boldsymbol{r})\}] \\
&= \frac{1}{2}\sum_{j=1}^{n}\sum_{k=1}^{n} m_j m_k \int d\boldsymbol{r}' \frac{\delta\rho_j(\boldsymbol{r}')}{\delta\rho_i(\boldsymbol{r})} \int d\boldsymbol{r}'' \rho_k(\boldsymbol{r}'')\phi_{jk}^{att}(|\boldsymbol{r}'-\boldsymbol{r}''|) \\
&+ \frac{1}{2}\sum_{j=1}^{n}\sum_{k=1}^{n} m_j m_k \int d\boldsymbol{r}' \rho_j(\boldsymbol{r}') \int d\boldsymbol{r}'' \frac{\delta\rho_k(\boldsymbol{r}'')}{\delta\rho_i(\boldsymbol{r})}\phi_{jk}^{att}(|\boldsymbol{r}'-\boldsymbol{r}''|) \\
&= \frac{1}{2}\sum_{j=1}^{n}\sum_{k=1}^{n} m_j m_k \int d\boldsymbol{r}' \delta_{ji}\delta(\boldsymbol{r}-\boldsymbol{r}') \int d\boldsymbol{r}'' \rho_k(\boldsymbol{r}'')\phi_{jk}^{att}(|\boldsymbol{r}'-\boldsymbol{r}''|) \\
&+ \frac{1}{2}\sum_{j=1}^{n}\sum_{k=1}^{n} m_j m_k \int d\boldsymbol{r}' \rho_j(\boldsymbol{r}') \int d\boldsymbol{r}'' \delta_{ki}\delta(\boldsymbol{r}-\boldsymbol{r}'')\phi_{jk}^{att}(|\boldsymbol{r}'-\boldsymbol{r}''|) \\
&= \frac{1}{2}\sum_{j=1}^{n}\sum_{k=1}^{n} m_j m_k \delta_{ji} \int d\boldsymbol{r}'' \rho_k(\boldsymbol{r}'')\phi_{jk}^{att}(|\boldsymbol{r}-\boldsymbol{r}''|) \\
&+ \frac{1}{2}\sum_{j=1}^{n}\sum_{k=1}^{n} m_j m_k \delta_{ki} \int d\boldsymbol{r}' \rho_j(\boldsymbol{r}')\phi_{jk}^{att}(|\boldsymbol{r}-\boldsymbol{r}''|) \\
&= \sum_{j=1}^{n} m_i m_j \int d\boldsymbol{r}' \rho_j(\boldsymbol{r}')\phi_{ij}^{att}(|\boldsymbol{r}-\boldsymbol{r}'|).
\end{aligned} \tag{158}$$

The free energy functional obtained by the SAFT EoS is given by:

$$A^{SAFT}[\{\rho_c(\boldsymbol{r})\}] = k_B T \int d\boldsymbol{r}' \sum_{j=1}^{n} \rho_j(\boldsymbol{r}') A^{SAFT}(\{\rho_c(\boldsymbol{r}')\}). \tag{159}$$

Taking the functional derivative with respect to $\rho_i(\boldsymbol{r})$ gives:

$$\begin{aligned}
\frac{\delta A^{SAFT}[\{\rho_c(\boldsymbol{r})\}]}{\delta\rho_i(\boldsymbol{r})} &= k_B T \int d\boldsymbol{r}' \sum_{j=1}^{n} \delta_{ij}\delta(\boldsymbol{r}-\boldsymbol{r}') A^{SAFT}(\{\rho_c(\boldsymbol{r}')\}) + \sum_{j=1}^{n} \rho_j(\boldsymbol{r}') \frac{\delta A^{SAFT}(\{\rho_c(\boldsymbol{r}')\})}{\delta\rho_i(\boldsymbol{r})} \\
&= k_B T \int d\boldsymbol{r}' \delta(\boldsymbol{r}-\boldsymbol{r}') A^{SAFT}(\{\rho_c(\boldsymbol{r}')\}) + \sum_{j=1}^{n} \rho_j(\boldsymbol{r}') \frac{\partial A^{SAFT}(\{\rho_c(\boldsymbol{r}')\})}{\partial\rho_i(\boldsymbol{r}')} \frac{\delta\rho_i(\boldsymbol{r}')}{\delta\rho_i(\boldsymbol{r})} \\
&= k_B T \int d\boldsymbol{r}' \delta(\boldsymbol{r}-\boldsymbol{r}') A^{SAFT}(\{\rho_c(\boldsymbol{r}')\}) + \sum_{j=1}^{n} \rho_j(\boldsymbol{r}') \frac{\partial A^{SAFT}(\{\rho_c(\boldsymbol{r}')\})}{\partial\rho_i(\boldsymbol{r}')} \delta(\boldsymbol{r}-\boldsymbol{r}') \\
&= k_B T \left[A^{SAFT}(\{\rho_c(\boldsymbol{r})\}) + \sum_{j=1}^{n} \rho_j(\boldsymbol{r}) \frac{\partial A^{SAFT}(\{\rho_c(\boldsymbol{r})\})}{\partial\rho_i(\boldsymbol{r})} \right] \\
&= k_B T \left[A^{SAFT}(\{\rho_c(\boldsymbol{r})\}) + \rho(\boldsymbol{r}) \frac{\partial A^{SAFT}(\{\rho_c(\boldsymbol{r})\})}{\partial\rho_i(\boldsymbol{r})} \right] \\
&= \mu^{SAFT}(\{\rho_c(\boldsymbol{r})\})
\end{aligned} \tag{160}$$

The last step in the derivation above uses a known thermodynamic identity.

7

CONCLUSIONS AND FUTURE WORK

7.1 CONCLUSIONS

Carbon capture, utilisation and storage (CCUS) is widely considered to be a comprehensive strategy to reduce the impact of the carbon dioxide (CO_2) that is produced through the use of fossil fuels across a range of human activities. Carbon-capture is an important first step in the implementation of such an approach. Despite the significant effort devoted to the development of carbon capture techniques, their implementation remains challenging due to the high energetic costs, large environmental impacts, and rapid degradation of capture materials associated with some of the current processes. Modelling studies can be used as a tool in addressing these costs, however, there are a significant number of variables to consider in the search for a process that is feasible and economical: the process configuration, operating conditions, and numerous decisions that need to be made on a molecular level: for example reaction kinetics, toxicity of the solvent, and the thermodynamics of the solvent. In this thesis, we have focused on only one part of the task: developing thermodynamic models that are predictive outside of the range of experimental data. Unfortunately, the modelling of CO_2-Amine-H_2O is made particularly complex due to the different types of intermolecular interactions in present in solution. The species form hydrogen bonds and chemical reactions lead to the formation of covalent bonds and ionic species. The more commonly adopted cubic equations of state do not lend themselves to the treatment of these reaction types, and therefore more sophisticated thermodynamic models are required.

The association theory developed by Wertheim (1984a,b, 1986a,b) and its incorporation into a sophisticated equation of state, SAFT, allows us to model the thermodynamics of these systems predictively. SAFT equation of state have a firm grounding in statistical mechanics, and the Hamiltonian is well-defined by a single set of state-independent parameters. Chemical association is mediated using "sticky spot" models, where molecules can interact via an attractive potential placed on the outside of a repulsive core. This directional interaction essentially captures a quantum mechanical effect, corresponding to the change in internal electronic configurations, rotational degrees of freedom, etc. upon association. By defining the thermodynamic system in terms of its monomer densities and state-independent association potentials, one can greatly reduce the reliance on experimental data compared to explicit treatments; the reaction products are outputs from the theory rather than inputs.

Button and Gubbins (1999) were the first to apply this physical approach to treat the MEA-CO_2-H_2O systems, and Mac Dowell et al. (2009); Rodríguez et al. (2012) realised that the underlying assumptions may be valid due to the strong ion pairing between ionic species and the low dielectric medium of the mixture, meaning that effectively the reaction products can be treated as neutral species. Due to the fast kinetics of the bicarbonate and carbamate formation reactions, it is also a fair assumption to assume thermodynamic equilibrium and that the process

modelling of a typical absorption-desorption process may be assumed to be mass-transfer limited. This lead to the work of Brand (2013), who developed a process model based on the SAFT-VR equation of state. In this thesis the first step was to revisit this work in chapter 2, due to complications in the energy balance, resulting in a different process model.

In this chapter, we showed an absorber model for CO_2 capture, developed with the aim of being as predictive as possible, in order to support solvent design activities prior to extensive experimental investigations. The thermodynamics were provided by the SAFT-VR SW model of Rodríguez et al. (2012), incorporating the chemical reactions implicitly, thus it assumed that reaction kinetics are not rate-determining. The absorber equations therefore considered apparent concentrations of the molecular species rather than the true concentrations, allowing for a vastly simplified exposition. However, this meant that mass transfer rates had to be scaled accordingly to the aggregated species. Without making use of pilot-plant data in model development, we found that the proposed model can generally be used to obtain a best-case performance of the solvent in question. This modelling approach is valuable for narrowing the solvent search space as solvents may be quickly rejected by comparing their performance in such a test. With very limited pilot-plant data we found that by adjusting a single parameter that corrects for the diffusivity of CO_2 in the liquid phase, the model can be used to predict with quantitative accuracy a variety of different operating conditions. Excellent predictions were obtained for the liquid-phase temperature profiles and the liquid- and gas-phase compositions along the column in most cases, with moderate deviations in a few cases. The comparison of the absorption performance of different solvents via this method may further aid in the narrowing of the solvent search space, and then a more quantitative comparison could be carried out. Following accurate predictions of the column profiles, a careful sensitivity analysis was conducted. We found that the liquid viscosity and diffusivity, and to a lesser extent the vapour-liquid surface tension, are key properties for the prediction of the composition profiles. The column profiles are also shown to be sensitive to the thermodynamic properties that are major sources of heat generation or dissipation. The main benefit of the proposed modelling framework in this chapter, is the ability to assess new solvents for which there may be limited data available.

Upon assessment of the SAFT-VR thermodynamic model of Rodríguez et al. (2012), it was found that the heat capacity of the mixture was under-predicted by approximately 15%, and the heat of absorption was similarly under-predicted by approximately 15% at the absorber conditions. Therefore, the good predictive capacity may be due to a fortunate cancellation of errors and the models may not be correctly capturing the physics of the thermodynamic system. Among the many variations of the original SAFT, many of which treat the dispersion interactions between monomeric segments with a square well potential, Lafitte et al. (2006b, 2013b) showed that by incorporating a variable range Mie potential, one can fine tune to properties that are sensitive to slopes of the molecular potential, particularly the slope of the repulsive exponent. The increased level of accuracy of this equation of state meant that one can obtain a simultaneous description of the vapour-liquid equilibria and properties that are second derivatives of the Helmholtz free energy. This improvement essentially set the president for the work in this thesis, recognising that the important caloric properties that determine the

temperatures in the absorption column: the heat of absorption and the heat capacity, are second derivative properties that may be better characterised with the more recent equation of state. The following step was to develop new SAFT-VR Mie (or SAFT-γ Mie homonuclear) models, for the MEA-CO_2-H_2O system.

The new theory and increased number of data types led to two issues that needed to be addressed. Firstly, we realized that upon changes in the theory, an extensive amount of research time needs to be spent on determining new parameters. This may inhibit more extensions to the theory, and the time spent on parametrisation needed to be addressed. Secondly, by arbitrarily lumping together several properties into an objective function, one has little control over the distributions of the deviations across the data types. Frequently a single thermodynamic model is developed using single set of weightings for experimental properties. In chapter 3, we dealt specifically with these issues by formulating the parameter estimation technique as a multi-objective optimization, where the deviation for each property type is treated as an individual optimization, and the output of the optimization is a set of different models that are "Pareto optimal" with respect to the numerous property types. We argue that this approach has several advantages over the single weighted sum optimization: it provides a rigorous comparison between different model types, models may be chosen more effectively by visualisation of the Pareto surface, and there are numerous Pareto optimal models that may be brought forwards for further investigation. With a set of Pareto optimal models, one can simply pick a model from the Pareto front in future investigations, rather than having to set up a new parameter estimation problem. This can significantly reduce the time spent on model development. Another important point we note is that via the multi-objective approach, one can be slightly more relaxed about the uncertainty in the experimental data. In-keeping with our goal to reduce the time spent to parameter estimation, we tailored a multi-objective algorithm for the regression of equation of state parameters that was as efficient as possible. A thorough review of the sandwiching algorithms was required because many of the algorithms in the literature we not suited for a general dimensional multi-objective optimization. The resulting algorithm is fully automated, requires little user input, and is able to very efficiently sample the Pareto surface. Upon realising that the only available SAFT-VR Mie model for water under-predicts the heat capacity by approximately 15% in the liquid phase at the absorber conditions, and that the majority of the solvent is liquid, we demonstrated the multi-objective optimization approach by developing new water models where saturated liquid density vapour pressure and heat capacity were used in the objective functions. The study showed that heat capacity was an excellent property for reducing the degeneracy between the dispersion and hydrogen bonding forces. By comparison of the Pareto surfaces, it was found that by accounting for the slight non-sphericity of water, one is able to obtain a significant improvement in the description of all three properties. A suitable water model that showed good trade-offs between the three properties was brought forward, and the parameters proven to be robust by assessing the prediction of properties not considered in the parameter estimation including the fractions of bonded association sites and surface tension.

Subsequently, we developed parameters for the ternary MEA+CO_2+H_2O system. The approach followed closely that of Mac Dowell et al. (2009); Rodríguez et al. (2012), with a few important exceptions. Caloric properties, (heat capacities,

heats of mixing, heats of absorption) were included in the parameter estimation or used for validation at all stages. In addition to the bicarbonate and carbamate formation reactions, we also accounted for the solvation of CO_2 in water. The key parameters in this study were those that mediate the reactions. These were determined from vapour pressure data, and the parameter estimation was formulated using the multi-objective optimization technique used previously. The different objectives represented the deviations from the partial pressure data of Jou et al. (1982). This led to a variety of Pareto-optimal models. After an in-depth analysis of the heat of absorption data, some data was rejected due to it being fundamentally inconsistent with the partial pressure data via the Gibbs-Helmholtz equation. By modelling the experiment in detail, the new Mie models were shown to provide excellent description of the heat of absorption (within the range of experimental error), in addition to the heat capacity. A detailed assessment of the association fractions showed that the speciation data was also in good accordance. We identified that the inclusion of cooperative bonding into the theory may improve the physical description. The thermodynamic model led to an improved description of the absorption column pilot plant data, transferring the same diffusivity parameter

In the final chapter, a new DFT model was developed using the SAFT-γ Mie EoS in order to predict the interfacial surface tension of fluid phases without any adjustable parameters (SAFT-VR Mie MF DFT). A robust algorithm was applied to satisfy the system of Euler-Lagrange equations, in order to obtain the one dimensional density profiles across the interface of two-phase systems. The methodology follows from the work of Gloor et al. (2002); Gloor (2003); Gloor et al. (2007a), who realised that one can treat some of the additive free energy contributions of SAFT as "local contributions", and some long range, allowing for a significant reduction in the complexity of the free energy functional. The methodology was extended to incorporate soft core Mie potential, and by applying even the simplest form of the theory (i.e., the mean field approximation to the radial distribution function), one is able to obtain extremely accurate predictions for the interfacial tension for a variety of fluids and fluid mixtures. Additionally, the interfacial density profiles of the theory agree with molecular simulations. This was used as further evidence for the robustness of the thermodynamic models developed in the previous sections. The theory showed slight over-predictions for other molecules, the alkane series, ethanol and ethylamine. Further investigations would need to be carried out to identify if this is due to the DFT theory of the molecular models used.

It is hoped that the tools developed in this thesis and its specific outcomes will benefit the scientific community. The multi-objective optimization methodology may be useful in any scenario where multiple conflicting objectives occur; the density functional theory may be used as a predictive tool for inhomogeneous properties; and the novel approaches to parameter estimation the process modelling have provided predictive models which may be used in the context of reducing anthropogenic carbon emissions.

7.2 FUTURE WORK

This section summarises some possible avenues for future research following the key findings presented in this thesis.

Though the physical approach has been shown to be predictive in principle (both in this thesis and in previous work), it is important to also understand its underlying assumptions and potential short-comings. To name a few: it does not allow one to include reaction kinetics in the description; it assumes that the intermolecular interactions of the bonded species are the same as non-bonded and charge effects are not accounted for. An equation of state that combines the predictive capabilities of Wertheim's theory and the level of detail captured in chemical approaches is certainly an interesting avenue for future research.

In Chapter 3 we analysed a particular set of pilot plant data by Tontiwachwuthikul et al. (1989) that used aqueous MEA as the solvent. There are in fact numerous pilot plant data for absorption via aqueous alkanolamines (to name just a few, (Knudsen et al., 2007; Dugas et al., 2009; Notz et al., 2012; Mangalapally et al., 2012). In future work it would useful to analyse wether the same modelling technique can be applied to other pilot plant runs. In particular, it would be useful to see if the scaling parameter (τ), applied to reduce the diffusion coefficient of CO_2, is transferable to different pilot plant runs or even different solvent molecules. Furthermore, it would be useful if one can correctly model the rate of mass transfer without having to regress parameters to the pilot plant data. A potential idea for the future development of the implicit approach is that one can make use of the fractions of association sites bonded by incorporating true species concentrations into the mass transfer equations, for example, CO_2 will diffuse more slowly if it is in its associated form. This treatment may allow for more predictive diffusion models such as the Stokes-Einstein equation.

In Chapter 4 we developed a multi-objective optimization technique suitable for regressiong equation-of-state parameters. In future work it would be interesting to perform the same analysis with different properties (e.g., replacing C_P with a different second-derivative property) to see the effect on the models obtained. This type of analysis may help guide experimental investigations. Furthermore, it will be useful to apply the technique to higher dimensional problems and include more property types in the regression.

In Chapter 6 we showed that a relatively simple density functional provides accurate predictions of the interfacial tensions and density profiles for pure components and mixtures when using the SAFT-VR Mie parameters. However, we saw that there are issues for associating systems at low temperatures where the density profile becomes discontinuous. Future work will need to rectify this issue. A possible solution may be to formulate of a more sophisticated non-local DFT. Another would be to assess whether the radial distribution function of the SAFT reference fluid is in fact suitable for highly associating systems.

BIBLIOGRAPHY

Aasen, A., Hammer, M., Ervik, Å., Müller, E. A., and Wilhelmsen, Ø. (2019). Equation of state and force fields for Feynman–Hibbs-corrected Mie fluids. I. Application to pure helium, neon, hydrogen, and deuterium. *The Journal of Chemical Physics*, 151(6):064508.

Abildskov, J., Constantinou, L., and Gani, R. (1996). Towards the development of a second-order approximation in activity coefficient models based on group contributions. *Fluid Phase Equilibria*, 118(1):1–12.

Aboudheir, A., Tontiwachwuthikul, P., and Idem, R. (2006). Rigorous Model for Predicting the Behavior of CO_2 Absorption into AMP in Packed-Bed Absorption Columns. *Industrial & Engineering Chemistry Research*, 45(8):2553–2557.

Adjiman, C. S. and Galindo, A., editors (2011). *Molecular Systems Engineering*, volume 6 of *Process Systems Engineering*. Wiley-VCH, Weinheim, Germany.

Adjiman, C. S., Galindo, A., and Jackson, G. (2014). Molecules matter: The expanding envelope of process design. In Mario R. Eden, J. D. S. and Towler, G. P., editors, *Proceedings of the 8th International Conference on Foundations of Computer-Aided Process Design*, volume 34 of *Computer Aided Chemical Engineering*, pages 55–64. Elsevier.

Afkhamipour, M. and Mofarahi, M. (2013). Comparison of rate-based and equilibrium-stage models of a packed column for post-combustion CO_2 capture using 2-amino-2-methyl-1-propanol (AMP) solution. *International Journal of Greenhouse Gas Control*, 15:186–199.

Afkhamipour, M. and Mofarahi, M. (2014). Sensitivity analysis of the rate-based CO_2 absorber model using amine solutions (MEA, MDEA and AMP) in packed columns. *International Journal of Greenhouse Gas Control*, 25:9–22.

Akram, M., Ali, U., Best, T., Blakey, S., Finney, K., and Pourkashanian, M. (2016). Performance evaluation of PACT Pilot-plant for CO_2 capture from gas turbines with Exhaust Gas Recycle. *International Journal of Greenhouse Gas Control*, 47:137–150.

Al-Baghli, N. A., Pruess, S. A., Yesavage, V. F., and Selim, M. S. (2001). A rate-based model for the design of gas absorbers for the removal of CO_2 and H_2S using aqueous solutions of MEA and DEA. *Fluid Phase Equilibria*, 185(1-2):31–43.

Al-Rashed, O. A. and Ali, S. H. (2012). Modeling the solubility of CO_2 and H_2S in DEA–MDEA alkanolamine solutions using the electrolyte–UNIQUAC model. *Separation and Purification Technology*, 94:71–83.

Algaba, J., Míguez, J. M., Mendiboure, B., and Blas, F. J. (2019). An accurate density functional theory for the vapor-liquid interface of chain molecules based on

the statistical associating fluid theory for potentials of variable range for Mie chainlike fluids. *Physical Chemistry Chemical Physics*.

Alhajaj, A., Mac Dowell, N., and Shah, N. (2016). A techno-economic analysis of post-combustion CO_2 capture and compression applied to a combined cycle gas turbine: Part I. A parametric study of the key technical performance indicators. *International Journal of Greenhouse Gas Control*, 44:26–41.

Alsaifi, N. M., Al Aslani, I., Binous, H., and Wang, Z.-G. (2017). A priori determination of the region of the three physical volume root loci in the perturbed-chain saft eos. *Fluid Phase Equilibria*, 434:152–166.

Alsaifi, N. M., Alkhater, M., Binous, H., Al Aslani, I., Alsunni, Y., and Wang, Z.-G. (2019). Nonphysical behavior in several statistical mechanically based equations of state. *Industrial & Engineering Chemistry Research*.

Alsaifi, N. M. and Englezos, P. (2011). Prediction of multiphase equilibrium using the PC-SAFT equation of state and simultaneous testing of phase stability. *Fluid Phase Equilibria*, 302(1-2):169–178.

Anouti, M., Jacquemin, J., and Lemordant, D. (2010). Volumetric properties, viscosities, and isobaric heat capacities of imidazolium octanoate protic ionic liquid in molecular solvents. *Journal of Chemical & Engineering Data*, 55(12):5719–5728.

Apostolakou, A. and Adjiman, C. S. (2002). Optimization methods in CAMD-II. In Achenie, L. E., Gani, R., and Venkatasubramanian, V., editors, *Computer Aided Molecular Design: Theory and Practice*, volume 12 of *Computer Aided Chemical Engineering*, chapter 4, pages 63–93. Elsevier.

Arce, A., Mac Dowell, N., Shah, N., and Vega, L. F. (2012). Flexible operation of solvent regeneration systems for CO_2 capture processes using advanced control techniques: Towards operational cost minimisation. *International Journal of Greenhouse Gas Control*, 11:236–250.

Arcis, H., Ballerat-Busserolles, K., Rodier, L., and Coxam, J.-Y. (2011). Enthalpy of Solution of Carbon Dioxide in Aqueous Solutions of Monoethanolamine at Temperatures of 322.5 K and 372.9 K and Pressures up to 5 MPa. *Journal of Chemical & Engineering Data*, 56(8):3351–3362.

Arcis, H., Ballerat-Busserolles, K., Rodier, L., and Coxam, J.-Y. (2012). Measurement and Modeling of Enthalpy of Solution of Carbon Dioxide in Aqueous Solutions of Diethanolamine at Temperatures of (322.5 and 372.9) K and Pressures up to 3 MPa. *Journal of Chemical & Engineering Data*, 57(3):840–855.

Arstad, B., Blom, R., and Swang, O. (2007). CO_2 absorption in aqueous solutions of alkanolamines: mechanistic insight from quantum chemical calculations. *The Journal of Physical Chemistry A*, 111(7):1222–1228.

Aschenbrenner, O. and Styring, P. (2010). Comparative study of solvent properties for carbon dioxide absorption. *Energy & Environmental Science*, 3:1106–1113.

ASHRAE (2011). *2011 ASHRAE Handbook*. ASHRAE, Atlanta, GA 30329.

Aslam, N. and Sunol, A. K. (2006). Reliable computation of all the density roots of the statistical associating fluid theory equation of state through global fixed-point homotopy. *Industrial & Engineering Chemistry Research*, 45(9):3303–3310.

Astarita, G. (1967). *Mass Transfer with Chemical Reaction*. Elsevier.

Astarita, G. and Savage, D. W. (1980). Gas absorption and desorption with reversible instantaneous chemical reaction. *Chemical Engineering Science*, 35(8):1755–1764.

Astarita, G., Savage, D. W., and Brito, A. (1983). *Gas Treating with Chemical Solvents*. John Wiley & Sons.

Austgen, D. M., Rochelle, G. T., and Chen, C. C. (1991). Model of Vapor-Liquid Equilibria for Aqueous Acid Gas-Alkanolamine Systems. 2. Representation of H_2S and CO_2 Solubility in Aqueous MDEA and CO_2 Solubility in Aqueous Mixtures of MDEA with MEA or DEA. *Industrial & Engineering Chemistry Research*, 30:543–555.

Austgen, D. M., Rochelle, G. T., Peng, X., and Chen, C. C. (1989). Model of vapor liquid equilibria for aqueous acid gas alkanolamine systems using the electrolyte NRTL equation. *Industrial & Engineering Chemistry Research*, 28:1060–1073.

Avendano, C., Lafitte, T., Galindo, A., Adjiman, C. S., Jackson, G., and Müller, E. A. (2011). SAFT-γ force field for the simulation of molecular fluids. 1. A single-site coarse grained model of carbon dioxide. *The Journal of Physical Chemistry B*, 115(38):11154–11169.

Bala, A. M. and Lira, C. T. (2016). Relation of wertheim association constants to concentration-based equilibrium constants for mixtures with chain-forming components. *Fluid Phase Equilibria*, 430:47–56.

Bamberger, A., Sieder, G., and Maurer, G. (2000). High-pressure (vapor+ liquid) equilibrium in binary mixtures of (carbon dioxide+ water or acetic acid) at temperatures from 313 to 353 k. *The Journal of Supercritical Fluids*, 17(2):97–110.

Barber, C. B., Dobkin, D. P., and Huhdanpaa, H. (1996). The quickhull algorithm for convex hulls. *ACM Transactions on Mathematical Software (TOMS)*, 22(4):469–483.

Bard, Y. (1974). Nonlinear parameter estimation.

Bardow, A., Steur, K., and Gross, J. (2009). A continuous targeting approach for integrated solvent and process design based on molecular thermodynamic models. In Alves, R., N. C. and Biscaia, E.C., E., editors, *10th International Symposium on Process Systems Engineering: Part A*, volume 27 of *Computer Aided Chemical Engineering*, pages 813–818.

Bardow, A., Steur, K., and Gross, J. (2010). Continuous-molecular targeting for integrated solvent and process design. *Industrial & Engineering Chemistry Research*, 49(6):2834–2840.

Barker, J. A. and Henderson, D. (1976). What is “liquid"? Understanding the states of matter. *Reviews of Modern Physics*, 48:587–671.

Barzagli, F., Di Vaira, M., Mani, F., and Peruzzini, M. (2012). Improved solvent formulations for efficient CO_2 absorption and low-temperature desorption. *ChemSusChem*, 5(9):1724–1731.

Behzadi, B., Patel, B., Galindo, A., and Ghotbi, C. (2005). Modeling electrolyte solutions with the SAFT-VR equation using Yukawa potentials and the mean-spherical approximation. *Fluid Phase Equilibria*, 236(1-2):241–255.

Berendsen, H. J., van der Spoel, D., and van Drunen, R. (1995). GROMACS: a message-passing parallel molecular dynamics implementation. *Computer physics communications*, 91(1-3):43–56.

Biliyok, C., Lawal, A., Wang, M., and Seibert, F. (2012). Dynamic modelling, validation and analysis of post-combustion chemical absorption CO_2 capture plant. *International Journal of Greenhouse Gas Control*, 9:428 – 445.

Billet, R. and Schultes, M. (1999). Prediction of mass transfer columns with dumped and arranged packings - Updated summary of the calculation method of Billet and Schultes. *Chemical Engineering Research & Design*, 77(A6):498–504.

Bittrich, H. (1963). Isobaric vapour–liquid equilibrium measurements on the system monoethylamine–water, wiss. *Z. Tech. Hochsch. Chem. Leuna-Merseburg*, 5:21–24.

Blas, F. J. and Galindo, A. (2002). Study of the high pressure phase behaviour of CO_2 + n-alkane mixtures using the SAFT-VR approach with transferable parameters. *Fluid Phase Equilibria*, 194:501–509.

Blas, F. J. and Vega, L. F. (1997). Thermodynamic behaviour of homonuclear and heteronuclear Lennard-Jones chains with association sites from simulation and theory. *Molecular Physics*, 92(1):135–150.

Blas, F. J. and Vega, L. F. (1998). Prediction of binary and ternary diagrams using the statistical associating fluid theory (SAFT) equation of state. *Industrial & Engineering Chemistry Research*, 37:660–674.

Blauwhoff, P. M. M., Versteeg, G. F., and Van Swaaij, W. P. M. (1984). A study on the reaction between CO_2 and alkanolamine in aqueous solutions. *Chemical Engineering Science*, 39:207–225.

Blekherman, G., Parrilo, P. A., and Thomas, R. R. (2012). *Semidefinite optimization and convex algebraic geometry*. SIAM.

Bokrantz, R. and Forsgren, A. (2011). A dual algorithm for approximating pareto sets in convex multi-criteria optimization. *Optimization Online*.

Bollas, G. M., Chen, C. C., and Barton, P. I. (2008). Refined electrolyte-NRTL model: Activity coefficient expressions for application to multi-electrolyte systems. *AIChE Journal*, 54(6):1608–1624.

Bommareddy, S., Chemmangattuvalappil, N. G., Solvason, C. C., and Eden, M. R. (2010). An algebraic approach for simultaneous solution of process and molecular design problems. *Brazilian Journal of Chemical Engineering*, 27:441–450.

Bortz, M., Burger, J., Asprion, N., Blagov, S., Böttcher, R., Nowak, U., Scheithauer, A., Welke, R., Küfer, K.-H., and Hasse, H. (2014). Multi-criteria optimization in chemical process design and decision support by navigation on pareto sets. *Computers & Chemical Engineering*, 60:354–363.

Böttinger, W., Maiwald, M., and Hasse, H. (2008). Online NMR spectroscopic study of species distribution in MEA-H_2O-CO_2 and DEA-H_2O-CO_2. *Fluid Phase Equilibria*, 263:131–143.

Boulougouris, G. C., Voutsas, E. C., Economou, I. G., Theodorou, D. N., and Tassios, D. P. (2001). Henry's constant analysis for water and nonpolar solvents from experimental data, macroscopic models, and molecular simulation. *The Journal of Physical Chemistry B*, 105(32):7792–7798.

Boyd, S. and Vandenberghe, L. (2004). *Convex optimization*. Cambridge university press.

Brand, C. (2013). *CO_2 capture using monoethanolamine solutions: Development and validation of a process model based on the SAFT-VR equation of state*. PhD thesis, Imperial College London.

Brand, C. V., Graham, E., Rodríguez, J., Galindo, A., Jackson, G., and Adjiman, C. S. (2016). On the use of molecular-based thermodynamic models to assess the performance of solvents for co2 capture processes: monoethanolamine solutions. *Faraday discussions*, 192:337–390.

Brand, C. V., Rodríguez, J., Galindo, A., Jackson, G., and Adjiman, C. S. (2012). Validation of an absorber model of carbon dioxide capture in an aqueous amine solvent developed based on the SAFT-VR framework. *Computer-Aided Chemical Engineering*, 31:930–934.

Brand, C. V., Rodriguez, J., Galindo, A., Jackson, G., and Adjiman, C. S. (2013). Validation of a process model of CO_2 capture in an aqueous solvent , using an implicit molecular based treatment of the reactions. *Energy Procedia*.

Bravo, J. L. and Fair, J. R. (1982). Generalized correlation for mass-transfer in packed distillation-columns. *Industrial & Engineering Chemistry Process Design And Development*, 21(1):162–170.

Burger, J., Papaioannou, V., Gopinath, S., Jackson, G., Galindo, A., and Adjiman, C. S. (2015). A hierarchical method to integrated solvent and process design of physical co 2 absorption using the saft-γ m ie approach. *AIChE Journal*, 61(10):3249–3269.

Button, J. and Gubbins, K. (1999). SAFT prediction of vapour-liquid equilibria of mixtures containing carbon dioxide and aqueous monoethanolamine or diethanolamine. *Fluid Phase Equilibria*, 158:175–181.

Buxton, A., Livingston, A. G., and Pistikopoulos, E. N. (1999). Optimal design of solvent blends for environmental impact minimization. *AIChE Journal*, 45(4):817–843.

Cai, Z., Xie, R., and Wu, Z. (1996). Binary isobaric vapor- liquid equilibria of ethanolamines+ water. *Journal of Chemical & Engineering Data*, 41(5):1101–1103.

Cameretti, L. F., Sadowski, G., and Mollerup, J. M. (2005). Modeling of aqueous electrolyte solutions with perturbed-chain statistical associated fluid theory. *Industrial & Engineering Chemistry Research*, 44:3355–3362.

Caplow, M. (1968). Kinetics of carbamate formation and breakdown. *Journal of the American Chemical Society*, 90(24):6795–6803.

Carson, J. K., Marsh, K. N., and Mather, A. E. (2000). Enthalpy of solution of carbon dioxide in (water+ monoethanolamine, or diethanolamine, orn-methyldiethanolamine) and (water+ monoethanolamine+ n-methyldiethanolamine) att= 298.15 k. *The Journal of Chemical Thermodynamics*, 32(9):1285–1296.

Cerdeiriña, C. A., González-Salgado, D., Romani, L., Del Carmen Delgado, M., Torres, L. A., and Costas, M. (2004). Towards an understanding of the heat capacity of liquids. A simple two-state model for molecular association. *Journal of Chemical Physics*, 120(14):6648–6659.

Cerdeirina, C. A., Troncoso, J., Gonzalez-Salgado, D., García-Miaja, G., Hernandez-Segura, G. O., Bessières, D., Medeiros, M., Romaní, L., and Costas, M. (2007). Heat capacity of associated systems. experimental data and application of a two-state model to pure liquids and mixtures. *The Journal of Physical Chemistry B*, 111(5):1119–1128.

Chakma, A. (1997). CO_2 capture processes - Opportunities for improved energy efficiencies. *Energy Conversion and Management*, 38.

Chapman, W. G., Gubbins, K. E., Jackson, G., and Radosz, M. (1989). SAFT - equation-of-state solution model for associating fluids. *Fluid Phase Equilibria*, 52:31–38.

Chapman, W. G., Gubbins, K. E., Jackson, G., and Radosz, M. (1990). New reference equation of state for associating liquids. *Industrial & Engineering Chemistry Research*, 29:1709–1721.

Chapman, W. G., Jackson, G., and Gubbins, K. E. (1988). Phase equilibria of associating fluids: Chain molecules with multiple bonding sites. *Molecular Physics*, 65(5):1057–1079.

Cheikh, M., Jarboui, B., Loukil, T., and Siarry, P. (2010). A method for selecting pareto optimal solutions in multiobjective optimization. *Journal of Informatics and Mathematical Sciences*, 2(1):51–62.

Chemmangattuvalappil, N. G. and Eden, M. R. (2013). A novel methodology for property-based molecular design using multiple topological indices. *Industrial & Engineering Chemistry Research*, 52:7090–7103.

Chen, C.-C. and Evans, L. B. (1986a). A local composition model for excess Gibbs energy of aqueous electrolyte systems. *Institute of Chemical Engineering Journal*, 32(3):444–454.

Chen, C.-C. and Evans, L. B. (1986b). A local composition model for the excess Gibbs energy of aqueous electrolyte systems. *AIChE Journal*, 32(3):444–454.

Chen, S., Chen, S., Fei, X., Zhang, Y., and Qin, L. (2015). Solubility and characterization of CO_2 in 40 mass% N-Ethylmonoethanolamine Solutions: Explorations for an Efficient Nonaqueous Solution. *Industrial & Engineering Chemistry Research*, 54(29):7212–7218.

Choi, S., Drese, J. H., and Jones, C. W. (2009a). Adsorbent materials for carbon dioxide capture from large anthropogenic point sources. *ChemSusChem*, 2(9):796–854.

Choi, W.-J., Seo, J.-B., Cho, S.-W., Park, S.-W., and Oh, K.-J. (2009b). Simultaneous absorption of CO_2 and SO_2 into aqueous AMP/NH_3 solutions in binary composite absorption system. *Korean Journal of Chemical Engineering*, 26(3):705–710.

Chong, F. K., Foo, D. C. Y., Eljack, F. T., Atilhan, M., and Chemmangattuvalappil, N. G. (2015). Ionic liquid design for enhanced carbon dioxide capture by computer-aided molecular design approach. *Clean Technologies and Environmental Policy*, 17:1301–1312.

Chremos, A., Forte, E., Papaioannou, V., Galindo, A., Jackson, G., and Adjiman, C. S. (2013). Modelling the fluid phase behaviour of multifunctional alkanolamines and carbon dioxide using the SAFT-γ approach. *Chemical Engineering Transactions*, 35:427–432.

Chremos, A., Forte, E., Papaioannou, V., Galindo, A., Jackson, G., and Adjiman, C. S. (2016). Modelling the phase and chemical equilibria of aqueous solutions of alkanolamines and carbon dioxide using the SAFT-γ SW group contribution approach. *Fluid Phase Equilibria*, 407:280–297. Aqueous Solutions.

Churi, N. and Achenie, L. E. K. (1997). On the use of a mixed integer nonlinear programming model for refrigerant design. *International Transactions of Operational Research*, 4:45–54.

Clark, G. N., Haslam, A. J., Galindo, A., and Jackson, G. (2006). Developing optimal Wertheim-like models of water for use in Statistical Associating Fluid Theory (SAFT) and related approaches. *Molecular Physics*, 104(22-24):3561–3581.

Constantinou, L. and Gani, R. (1994). New group contribution method for estimating properties of pure compounds. *AIChE Journal*, 40(10):1697–1710.

Costa, A., da Silva, F., and Pessoa, F. (2000). Parameter estimation of thermodynamic models for high-pressure systems employing a stochastic method of global optimization. *Brazilian Journal of Chemical Engineering*, 17(3):349–354.

Cottrell, A. J., McGregor, J. M., Jansen, J., Artanto, Y., Dave, N., Morgan, S., Pearson, P., Attalla, M. I., Wardhaugh, L., Yu, H., Allport, A., and Feron, P. H. M. (2009).

Post-combustion capture R&D and pilot plant operation in Australia. *Energy Procedia*, 1(1):1003–1010.

Craft, D. L., Halabi, T. F., Shih, H. A., and Bortfeld, T. R. (2006). Approximating convex Pareto surfaces in multiobjective radiotherapy planning. *Medical physics*, 33:3399–3407.

Cripwell, J. T., Smith, S. A., Schwarz, C. E., and Burger, A. J. (2018). Saft-vr mie: Application to phase equilibria of alcohols in mixtures with n-alkanes and water. *Industrial & Engineering Chemistry Research*, 57(29):9693–9706.

Danckwerts, P. (1979a). The reaction of co 2 with ethanolamines. *Chemical Engineering Science*, 34(4):443–446.

Danckwerts, P. V. (1970). *Gas-Liquid Reactions*. McGraw-Hill.

Danckwerts, P. V. (1979b). The reaction of CO_2 with ethanolamines. *Chemical Engineering Science*, 34:443–446.

Das, I. (1999). On characterizing the "knee" of the pareto curve based on normal-boundary intersection. *Structural optimization*, 18(2-3):107–115.

Das, I. and Dennis, J. E. (1997). A closer look at drawbacks of minimizing weighted sums of objectives for Pareto set generation in multicriteria optimization problems. *Structural optimization*, 14(1):63–69.

DeCoursey, W. J. (1982). Enhancement factors for gas absorption with reversible reaction. *Chemical Engineering Science*, 37(10):1483–1489.

Diamantonis, N. I. and Economou, I. G. (2012). Modeling the phase equilibria of a h2o–co2 mixture with pc-saft and tpc-psaft equations of state. *Molecular Physics*, 110(11-12):1205–1212.

Dolezalek, F. (1908). Theory of binary mixtures and concentrated solutions. *Zeitschrift für Physikalische Chemie*, 64:727–747.

Dufal, S., Lafitte, T., Galindo, A., Jackson, G., and Haslam, A. J. (2015a). Developing intermolecular-potential models for use with the SAFT-VR Mie Equation of State. *AIChE Journal*, 61:2891–2912.

Dufal, S., Lafitte, T., Haslam, A. J., Galindo, A., Clark, G. N., Vega, C., and Jackson, G. (2015b). The A in SAFT: developing the contribution of association to the Helmholtz free energy within a Wertheim TPT1 treatment of generic Mie fluids. *Molecular Physics*, 113(9-10):948–984.

Dufal, S., Papaioannou, V., Sadeqzadeh, M., Pogiatzis, T., Chremos, A., Adjiman, C. S., Jackson, G., and Galindo, A. (2014). Prediction of thermodynamic properties and phase behavior of fluids and mixtures with the SAFT-γ Mie group-contribution equation of state. *Journal of Chemical & Engineering Data*, 59(10):3272–3288.

Dugas, R., Alix, P., Lemaire, E., Broutin, P., and Rochelle, G. (2009). Absorber model for co2 capture by monoethanolamine—application to castor pilot results. *Energy Procedia*, 1(1):103–107.

Dugas, R. E. (2006). *Pilot Plant Study of Carbon Dioxide Capture by Aqueous Monoethanolamine by Ross E . Dugas Revision of M . S . E . Thesis The University of Texas at Austin May 2006*. PhD thesis, University of Texas at Austin.

Duque, D., Pàmies, J. C., and Vega, L. F. (2004). Interfacial properties of lennard-jones chains by direct simulation and density gradient theory. *The Journal of chemical physics*, 121(22):11395–11401.

Duvedi, A. P. and Achenie, L. E. K. (1996). Designing environmentally safe refrigerants using mathematical programming. *Chemical Engineering Science*, 51:3727–3739.

Economou, I. G. and Donohue, M. D. (1991). Chemical, quasi-chemical and perturbation theories for associating fluids. *AIChE Journal*, 37(12):1875–1894.

Economou, I. G. and Donohue, M. D. (1992). Equation of state with multiple associating sites for water and water-hydrocarbon mixtures. *Industrial & engineering chemistry research*, 31(10):2388–2394.

Economou, I. G. and Tsonopoulos, C. (1997). Associating models and mixing rules in equations of state for water/hydrocarbon mixtures. *Chemical Engineering Science*, 52(4):511–525.

Eden, M. R., Jørgensen, S. B., Gani, R., and El-Halwagi, M. M. (2004). A novel framework for simultaneous separation process and product design. *Chemical Engineering and Processing: Process Intensification*, 43:595–608.

Eichfelder, G. (2008). *Adaptive scalarization methods in multiobjective optimization*, volume 436. Springer.

Eljack, F. T., Solvason, C. C., Chemmangattuvalappil, N., and Eden, M. R. (2008). A property based approach for simultaneous process and molecular design. *Chinese Journal of Chemical Engineering*, 16:424–434.

Elliott Jr, J. R., Suresh, S. J., and Donohue, M. D. (1990). A simple equation of state for non-spherical and associating molecules. *Industrial & Engineering Chemistry Research*, 29:1476–1485.

Englezos, P. and Kalogerakis, N. (2000). *Applied parameter estimation for chemical engineers*. CRC Press.

Eriksen, D. K., Lazarou, G., Galindo, A., Jackson, G., Adjiman, C. S., and Haslam, A. J. (2016). Development of intermolecular potential models for electrolyte solutions using an electrolyte saft-vr mie equation of state. *Molecular Physics*, 114(18):2724–2749.

Errington, J. R. (2003). Evaluating surface tension using grand-canonical transition-matrix monte carlo simulation and finite-size scaling. *Physical Review E*, 67(1):012102.

Evans, R. (1979). The nature of the liquid-vapour interface and other topics in the statistical mechanics of non-uniform, classical fluids. *Advances in Physics*, 28(2):143–200.

Evans, R. (1992). Density functionals in the theory of nonuniform fluids. *Fundamentals of inhomogeneous fluids*, 1:85–176.

E.W. Lemmon, M. M. and Friend, D. (2018). Thermophysical properties of fluid systems. In Linstrom, P. and Mallard, W., editors, *NIST Chemistry WebBook, NIST Standard Reference Database Number 69*. National Institute of Standards and Technology, Gaithersburg MD, 20899.

Faramarzi, L., Kontogeorgis, G. M., Michelsen, M. L., Thomsen, K., and Stenby, E. H. (2010). Absorber model for CO_2 capture by monoethanolamine. *Industrial & Engineering Chemistry Research*, 49(8):3751–3759.

Faramarzi, L., Kontogeorgis, G. M., Thomsen, K., and Stenby, E. H. (2009). Extended UNIQUAC model for thermodynamic modeling of CO_2 absorption in aqueous alkanolamine solutions. *Fluid Phase Equilibria*, 282(2):121–132.

Fawzi, H. (2017). Topics in convex optimization.

Fletcher, D. A., McMeeking, R. F., and Parkin, D. (1996). The united kingdom chemical database service. *Journal of Chemical Information and Computer Sciences*, 36(4):746–749.

Forte, E., Burger, J., Langenbach, K., Hasse, H., and Bortz, M. (2018). Multi-Criteria Optimization for Parameterization of SAFT-Type Equations of State for Water. *AIChE Journal*, 64(1).

Fredenslund, A. (1977). *Vapor-liquid equilibria using UNIFAC: a group-contribution method*. Elsevier.

Fredenslund, A., Jones, R. L., and Prausnitz, J. M. (1975). Group-contribution estimation of activity coefficients in nonideal liquid mixtures. *AIChE Journal*, 21(6):1086–1099.

Friedlingstein, P., Andrew, R., Rogelj, J., Peters, G., Canadell, J., Knutti, R., Luderer, G., Raupach, M., Schaeffer, M., van Vuuren, D., et al. (2014). Persistent growth of co_2 emissions and implications for reaching climate targets. *Nature geoscience*, 7(10):709–715.

Fu, Y.-H. and Sandler, S. I. (1995). A simplified SAFT equation of state for associating compounds and mixtures. *Industrial & Engineering Chemistry Research*, 34:1897–1909.

Fuller, E. and Giddings, J. (1965). A comparison of methods for predicting gaseous diffusion coefficients. *Journal of Chromatographic Science*, 3(7):222–227.

Fuller, E. N., Ensley, K., and Giddings, J. C. (1969). Diffusion of halogenated hydrocarbons in helium. the effect of structure on collision cross sections. *The Journal of Physical Chemistry*, 73(11):3679–3685.

Fuller, E. N., Schettler, P. D., and Giddings, J. C. (1966). New method for prediction of binary gas-phase diffusion coefficients. *Industrial & Engineering Chemistry*, 58(5):18–27.

Gabrielsen, J., Michelsen, M. L., Stenby, E. H., and Kontogeorgis, G. M. (2005). A Model for estimating CO_2 solubility in aqueous alkanolamines. *Industrial & Engineering Chemistry Research*, 44(9):3348–3354.

Gabrielsen, J., Michelsen, M. L., Stenby, E. H., and Kontogeorgis, G. M. (2006). Modeling of CO_2 absorber using an AMP solution. *AIChE Journal*, 52(10):3443–3451.

Gabrielsen, J., Svendsen, H. F., Michelsen, M. L., Stenby, E. H., and Kontogeorgis, G. M. (2007). Experimental validation of a rate-based model for CO_2 capture using an AMP solution. *Chemical Engineering Science*, 62(9):2397–2413.

Galindo, A. and Blas, F. J. (2002). Theoretical examination of the global fluid phase behavior and critical phenomena in carbon dioxide + *n*-alkane binary mixtures. *The Journal of Physical Chemistry B*, 106(17):4503–4515.

Galindo, A., Burton, S. J., Jackson, G., Visco, D. P., and Kofke, D. A. (2002). Improved models for the phase behaviour of hydrogen fluoride: chain and ring aggregates in the SAFT approach and the AEOS model. *Molecular Physics*, 100(14):2241–2259.

Galindo, A., Davies, L. A., Gil-Villegas, A., and Jackson, G. (1998). The thermodynamics of mixtures and the corresponding mixing rules in the SAFT-VR approach for potentials of variable range. *Molecular Physics*, 93(2):241–252.

Galindo, A., Gil-Villegas, A., Jackson, G., and Burgess, A. N. (1999). SAFT-VRE : Phase Behavior of Electrolyte Solutions with the Statistical Associating Fluid Theory for Potentials of Variable Range. *Journal of Physical Chemistry B*, 103(46):10272–10281.

Gani, R. (2004). Chemical product design: challenges and opportunities. *Computers & Chemical Engineering*, 28(12):2441–2457.

Garrido, J. M., Piñeiro, M. M., Mejía, A., and Blas, F. J. (2016). Understanding the interfacial behavior in isopycnic lennard-jones mixtures by computer simulations. *Physical Chemistry Chemical Physics*, 18(2):1114–1124.

Ghonasgi, D., Perez, V., and Chapman, W. G. (1994). Intramolecular association in flexible hard chain molecules. *The Journal of Chemical Physics*, 101(8):6880–6887.

Gil-Villegas, A., Galindo, A., and Jackson, G. (2001). A statistical associating fluid theory for electrolyte solutions (SAFT-VRE). *Molecular Physics*, 99(6):531–546.

Gil-Villegas, A., Galindo, A., Whitehead, P. J., Mills, S. J., Jackson, G., and Burgess, A. N. (1997). Statistical associating fluid theory for chain molecules with attractive potentials of variable range. *The Journal of chemical physics*, 106(10):4168–4186.

Giovanoglou, A., Barlatier, J., Adjiman, C. S., Pistikopoulos, E. N., and Cordiner, J. L. (2003). Optimal solvent design for batch separation based on economic performance. *AIChE Journal*, 49(12):3095–3109.

Glass, M., Djelassi, H., and Mitsos, A. (2018). Parameter estimation for cubic equations of state models subject to sufficient criteria for thermodynamic stability. *Chemical Engineering Science*, 192:981–992.

Gloor, G. J. (2003). *Modelling the interfacial properties of complex fluids with density functional theory and computer simulation*. PhD thesis, Imperial College London (University of London).

Gloor, G. J., Blas, F. J., del R1'o, E. M., de Miguel, E., and Jackson, G. (2002). A SAFT–DFT approach for the vapour–liquid interface of associating fluids. *Fluid phase equilibria*, 194:521–530.

Gloor, G. J., Jackson, G., Blas, F., Del Rio, E. M., and De Miguel, E. (2007a). Prediction of the vapor- liquid interfacial tension of nonassociating and associating fluids with the saft-vr density functional theory. *The Journal of Physical Chemistry C*, 111(43):15513–15522.

Gloor, G. J., Jackson, G., Blas, F., Del Rio, E. M., and De Miguel, E. (2007b). Prediction of the vapor-liquid interfacial tension of nonassociating and associating fluids with the SAFT-VR density functional theory. *The Journal of Physical Chemistry C*, 111:15513–15522.

Gloor, G. J., Jackson, G., Blas, F. J., Del R10, E. M., and De Miguel, E. (2004a). An accurate density functional theory for the vapor-liquid interface of associating chain molecules based on the statistical associating fluid theory for potentials of variable range. *The Journal of Chemical Physics*, 121:12740–12759.

Gloor, G. J., Jackson, G., Blas, F. J., del R10, E. M., and de Miguel, E. (2004b). An accurate density functional theory for the vapor-liquid interface of associating chain molecules based on the statistical associating fluid theory for potentials of variable range. *The Journal of chemical physics*, 121(24):12740–12759.

Godini, H. R. and Mowla, D. (2008). Selectivity study of H_2S and CO_2 absorption from gaseous mixtures by MEA in packed beds. *Chemical Engineering Research and Design*, 86(4):401–409.

Gopinath, S., Jackson, G., Galindo, A., and Adjiman, C. S. (2016). Outer approximation algorithm with physical domain reduction for computer-aided molecular and separation process design. *AIChE Journal*, 62(9):3484–3504.

Graham, E., Gopinath, S., Forte, E., Jackson, G., Galindo, A., and Adjiman, C. S. (2017). The development of a molecular systems engineering approach to the design of carbon-capture solvents. In Papadopoulos, A. I. and Seferlis, P., editors, *Process Systems and Materials for CO_2 Capture: Modelling, Design, Control and Integration*, chapter 1. Wiley.

Gray, C. G., Gubbins, K. E., and Joslin, C. G. (2011). *Theory of Molecular Fluids 2: Applications. International Series of Monographs on Chemistry*. Oxford University Press.

Grenner, A., Kontogeorgis, G. M., Michelsen, M. L., and Folas, G. K. (2007). On the estimation of water pure compound parameters in association theories. *Molecular Physics*, 105(13-14):1797–1801.

Grenner, A., Schmelzer, J., von Solms, N., and Kontogeorgis, G. M. (2006). Comparison of two association models (elliott- suresh- donohue and simplified pc-saft) for complex phase equilibria of hydrocarbon- water and amine-containing mixtures. *Industrial & engineering chemistry research*, 45(24):8170–8179.

Gross, J., , and Sadowski, G. (2001). Perturbed-chain saft: An equation of state based on a perturbation theory for chain molecules. *Industrial and Engineering Chemistry Research*, 40(4):1244–1260.

Gross, J. (2005). An equation-of-state contribution for polar components: Quadrupolar molecules. *AIChE journal*, 51(9):2556–2568.

Gross, J. (2009). A density functional theory for vapor-liquid interfaces using the pcp-saft equation of state. *The Journal of chemical physics*, 131(20):204705.

Gross, J. and Sadowski, G. (2000). Application of perturbation theory to a hard-chain reference fluid: an equation of state for square-well chains. *Fluid Phase Equilibria*, 168(2):183–199.

Gross, J. and Sadowski, G. (2001). Perturbed-chain saft: An equation of state based on a perturbation theory for chain molecules. *Industrial & engineering chemistry research*, 40(4):1244–1260.

Gross, J. and Sadowski, G. (2002a). Application of the perturbed-chain SAFT equation of state to associating systems. *Industrial & Engineering Chemistry Research*, 41(22):5510–5515.

Gross, J. and Sadowski, G. (2002b). Application of the perturbed-chain saft equation of state to associating systems. *Industrial & engineering chemistry research*, 41(22):5510–5515.

Gross, J. and Vrabec, J. (2006). An equation-of-state contribution for polar components: Dipolar molecules. *AIChE journal*, 52(3):1194–1204.

Gubbins, K. E. (2016). Perturbation theories of the thermodynamics of polar and associating liquids: A historical perspective. *Fluid Phase Equilibria*, 416:3–17. Special Issue: {SAFT} 2015.

Gupta, M., da Silva, E. F., Hartono, A., and Svendsen, H. F. (2013). Theoretical study of differential enthalpy of absorption of co2 with mea and mdea as a function of temperature. *The Journal of Physical Chemistry B*, 117(32):9457–9468.

Habaki, H., Perera, J. M., Kentish, S. E., Stevens, G. W., and Fei, W. (2007). CO_2 Absorption Behavior with a Novel Random Packing: Super Mini Ring. *Separation Science and Technology*, 42(4):701–716.

Han, B., Sun, Y., Fan, M., and Cheng, H. (2013). On the CO_2 Capture in Water-Free Monoethanolamine Solution: An ab Initio Molecular Dynamics Study. *The Journal of Physical Chemistry. B*, 117(19):5971–5977.

Hansen, J.-P. and McDonald, I. R. (1990). *Theory of simple liquids*. Elsevier.

Haslam, A. J., Galindo, A., and Jackson, G. (2008). Prediction of binary intermolecular potential parameters for use in modelling fluid mixtures. *Fluid Phase Equilibria*, 266(1-2):105–128.

Haynes, W. N. (2011). *Handbook of Chemistry and Physics*. CRC Press.

Held, C., Cameretti, L. F., and Sadowski, G. (2008). Modeling aqueous electrolyte solutions: Part 1. fully dissociated electrolytes. *Fluid Phase Equilibria*, 270(1):87–96.

Held, C. and Sadowski, G. (2009). Modeling aqueous electrolyte solutions. Part 2. Weak electrolytes. *Fluid Phase Equilibria*, 279(2):141–148.

Hendriks, E., Kontogeorgis, G. M., Dohrn, R., de Hemptinne, J.-C., Economou, I. G., Žilnik, L. F., and Vesovic, V. (2010). Industrial requirements for thermodynamics and transport properties. *Industrial & engineering chemistry research*, 49(22):11131–11141.

Hernández, J. I. S. (2011). *Multi-objective optimization in mixed integer problems: With application to the beam selection optimization problem in IMRT*. PhD thesis, TU Kaiserslautern.

Hessen, E. T., Haug-Warberg, T., and Svendsen, H. F. (2010). The refined e-NRTL model applied to CO_2–H_2O–alkanolamine systems. *Chemical Engineering Science*, 65(11):3638–3648.

Hikita, H., Asai, S., Ishikawa, H., and Honda, M. (1977). The kinetics of reactions of carbon dioxide with monoethanolamine, diethanolamine and triethanolamine by a rapid mixing method. *The Chemical Engineering Journal*, 13:7–12.

Hoff, K. A. (2003). *Modeling and experimental study of carbon dioxide absorption in a membrane contactor*. PhD thesis, Norges Teknisk-Naturvitenskapelige Universitet.

Holtzman, J. M. and Halkin, H. (1966). Discretional convexity and the maximum principle for discrete systems. *SIAM Journal on Control*, 4(2):263–275.

Hostrup, M., Harper, P. M., and Gani, R. (1999). Design of environmentally benign processes: integration of solvent design and separation process synthesis. *Computers & Chemical Engineering*, 23:1395–1414.

Huang, S. H. and Radosz, M. (1990). Equation of state for small, large, polydisperse, and associating molecules. *Industrial & Engineering Chemistry Research*, 29(11):2284–2294.

Huang, S. H. and Radosz, M. (1991). Equation of state for small, large, polydisperse, and associating molecules: extension to fluid mixtures. *Industrial & Engineering Chemistry Research*, 30(8):1994–2005.

Hwang, G. S., Stowe, H. M., Paek, E., and Manogaran, D. (2015). Reaction mechanisms of aqueous monoethanolamine with carbon dioxide: a combined quantum chemical and molecular dynamics study. *Physical Chemistry Chemical Physics*, 17(2):831–839.

Jackson, G., Chapman, W. G., and Gubbins, K. E. (1988). Phase equilibria of associating fluids: Spherical molecules with multiple bonding sites. *Molecular Physics*, 65(1):1–31.

Jackson, P. and Attalla, M. (2011). Environmental impacts of post-combustion capture–new insights. *Energy Procedia*, 4:2277–2284.

Jayarathna, S. A., Jayarathna, C. K., Kottage, D. A., Dayarathna, S., Eimer, D. A., and Melaaen, M. C. (2013a). Density and surface tension measurements of partially carbonated aqueous monoethanolamine solutions. *Journal of Chemical & Engineering Data*, 58(2):343–348.

Jayarathna, S. A., Lie, B., and Melaaen, M. C. (2013b). Dynamic modelling of the absorber of a post-combustion co$_2$ capture plant: Modelling and simulations. *Computers & Chemical Engineering*, 53:178–189.

Jayarathna, S. A., Weerasooriya, A., Dayarathna, S., Eimer, D. A., and Melaaen, M. C. (2013c). Densities and surface tensions of CO_2 loaded aqueous monoethanolamine solutions with r = (0.2 to 0.7) at T = (303.15 to 333.15) K. *Journal of Chemical & Engineering Data*, Accepted(4):986–992.

Jog, P. K., Sauer, S. G., Blaesing, J., and Chapman, W. G. (2001). Application of dipolar chain theory to the phase behavior of polar fluids and mixtures. *Industrial & Engineering Chemistry Research*, 40:4641–4648.

Jou, F. Y., Mather, A. E., and Otto, F. D. (1982). Solubility of hydrogen sulfide and carbon dioxide in aqueous methyldiethanolamine solutions. *Industrial & Engineering Chemistry Process Design and Development*, 21(4):539–544.

Jou, F. Y., Mather, A. E., and Otto, F. D. (1995). The solubility of CO_2 in a 30 mass percent monoethanolamine solution. *The Canadian Journal of Chemical Engineering*, 73:140–147.

Kakalis, N. M., Kakhu, A. I., and Pantelides, C. C. (2004). Implementing SAFT-based thermodynamics in process modelling tools. In *Proc. 6th International Conf. on Foundations of Computer Aided Process Design, CACHE Publications*, pages 537–40. Citeseer.

Kale, C., Górak, A., and Schoenmakers, H. (2013). Modelling of the reactive absorption of CO_2 using mono-ethanolamine. *International Journal of Greenhouse Gas Control*, 17:294–308.

Kang, J. W., Abildskov, J., Gani, R., and Cobas, J. (2002). Estimation of mixture properties from first-and second-order group contributions with the UNIFAC model. *Industrial & Engineering Chemistry Research*, 41:3260–3273.

Karakatsani, E. K. and Economou, I. G. (2006). Perturbed chain-statistical associating fluid theory extended to dipolar and quadrupolar molecular fluids. *The Journal of Physical Chemistry B*, 110(18):9252–9261.

Karakatsani, E. K. and Economou, I. G. (2007). Phase equilibrium calculations for multi-component polar fluid mixtures with tPC-PSAFT. *Fluid Phase Equilibria*, 261(1):265–271.

Karakatsani, E. K., Kontogeorgis, G. M., and Economou, I. G. (2006). Evaluation of the truncated perturbed chain-polar statistical associating fluid theory for complex mixture fluid phase equilibria. *Industrial & Engineering Chemistry Research*, 45:6063–6074.

Karakatsani, E. K., Spyriouni, T., and Economou, I. G. (2005). Extended statistical associating fluid theory (SAFT) equations of state for dipolar fluids. *AIChE journal*, 51(8):2328–2342.

Kenarsari, S. D., Yang, D., Jiang, G., Zhang, S., Wang, J., Russell, A. G., Wei, Q., and Fan, M. (2013). Review of recent advances in carbon dioxide separation and capture. *RSC Advances*, 3:22739–22773.

Kenig, E. Y., Kucka, L., and Górak, A. (2003). Rigorous modeling of reactive absorption processes. *Chemical Engineering & Technology*, 26(6):631–646.

Kestin, J., Kobayashi, Y., and Wood, R. T. (1966). The viscosity of four binary, gaseous mixtures at 20 and 30 C. *Physica*, 32:1065–1089.

Khan, F., Krishnamoorthi, V., and Mahmud, T. (2011). Modelling reactive absorption of co_2 in packed columns for post-combustion carbon capture applications. *Chemical Engineering Research and Design*, 89(9):3679–3685. Special Issue on Carbon Capture &; Storage.

Khoury, F. M. (2005). *Multistage Separation Processes*. CRC Press.

Kim, I., Hoff, K. A., and Mejdell, T. (2014). Heat of absorption of co2 with aqueous solutions of mea: new experimental data. *Energy Procedia*, 63:1446–1455.

Kim, I. and Svendsen, H. F. (2007). Heat of absorption of carbon dioxide (CO_2) in monoethanolamine (MEA) and 2-(aminoethyl)ethanolamine (AEEA) solutions. *Industrial & Engineering Chemistry Research*, 46(17):5803–5809.

Kim, K.-J. and Diwekar, U. M. (2002). Integrated solvent selection and recycling for continuous processes. *Industrial & engineering chemistry research*, 41(18):4479–4488.

Klamroth, K., Tind, J., and Wiecek, M. M. (2003). Unbiased approximation in multicriteria optimization. *Mathematical Methods of Operations Research*, 56(3):413–437.

Kleiner, M. and Gross, J. (2006). An equation of state contribution for polar components: Polarizable dipoles. *AIChE Journal*, 52(5):1951–1961.

Kleiner, M. and Sadowski, G. (2007). Modeling of polar systems using PCP-SAFT: An approach to account for induced-association interactions. *The Journal of Physical Chemistry C*, 111(43):15544–15553.

Knudsen, J. N., Jensen, J. N., Vilhelmsen, P.-J., and Biede, O. (2007). First year operation experience with a 1 t/h co_2 absorption pilot plant at esbjerg coal-fired power plant. In *Proceedings of European Congress of Chemical Engineering (ECCE-6)*, volume 3, pages 57–61.

Koak, N., de Loos, T. W., and Heidemann, R. A. (1999). Effect of the power series dispersion term on the pressure- volume behavior of statistical associating fluid theory. *Industrial & Engineering Chemistry Research*, 38(4):1718–1722.

Kontogeorgis, G. M. and Folas, G. K. (2010). *Thermodynamic Models for Industrial Applications: From Classical and Advanced Mixing Rules to Association Theories*. John Wiley & Sons: New York.

Kontogeorgis, G. M., Michelsen, M. L., Folas, G. K., Derawi, S., von Solms, N., and Stenby, E. H. (2006). Ten years with the cpa (cubic-plus-association) equation of state. part 2. cross-associating and multicomponent systems. *Industrial & Engineering Chemistry Research*, 45(14):4869–4878.

Kontogeorgis, G. M., Yakoumis, I. V., Meijer, H., Hendriks, E., and Moorwood, T. (1999). Multicomponent phase equilibrium calculations for water–methanol–alkane mixtures. *Fluid Phase Equilibria*, 158:201–209.

Kortunov, P. V., Siskin, M., Baugh, L. S., and Calabro, D. C. (2015). In situ nuclear magnetic resonance mechanistic studies of carbon dioxide reactions with liquid amines in non-aqueous systems: evidence for the formation of carbamic acids and zwitterionic species. *Energy & Fuels*, 29(9):5940–5966.

Kraska, T. and Gubbins, K. E. (1996a). Phase equilibria calculations with a modified SAFT equation of state. 1. Pure alkanes, alkanols, and water. *Industrial & Engineering Chemistry Research*, 35:4727–4737.

Kraska, T. and Gubbins, K. E. (1996b). Phase equilibria calculations with a modified SAFT equation of state. 2. Binary mixtures of n-alkanes, 1-alkanols, and water. *Industrial & engineering chemistry research*, 35(12):4738–4746.

Krishnamurthy, R. and Taylor, R. (1985a). A nonequilibrium stage model of multicomponent separation processes. 1. model description and method of solution. *AIChE Journal*, 31(3):449–455.

Krishnamurthy, R. and Taylor, R. (1985b). A nonequilibrium stage model of multicomponent separation processes. 2. comparison with experiment. *AIChE Journal*, 31(3):456–465.

Kucka, L., Kenig, E. Y., and Górak, A. (2002). Kinetics of the gas-liquid reaction between carbon dioxide and hydroxide ions. *Industrial & Engineering Chemistry Research*, 41:5952–5957.

Kucka, L., Muller, I., Kenig, E. Y., and Górak, A. (2003a). On the modelling and simulation of sour gas absorption by aqueous amine solutions. *Chemical Engineering Science*, 58(16):3571–3578.

Kucka, L., Richter, J., Kenig, E. Y., and Górak, A. (2003b). Determination of gas-liquid reaction kinetics with a stirred cell reactor. *Separation and Purification Technology*, 31:163–175.

Kvamsdal, H. M., Hetland, J., Haugen, G., Svendsen, H. F., Major, F., Kårstad, V., and Tjellander, G. (2010). Maintaining a neutral water balance in a 450MWe

NGCC-CCS power system with post-combustion carbon dioxide capture aimed at offshore operation. *International Journal of Greenhouse Gas Control*, 4(4):613–622.

Kvamsdal, H. M. and Rochelle, G. T. (2008). Effects of the temperature bulge in CO_2 absorption from flue gas by aqueous monoethanolamine. *Industrial & Engineering Chemistry Research*, 47(3):867–875.

Ladd, A. and Woodcock, L. (1977). Triple-point coexistence properties of the lennard-jones system. *Chemical Physics Letters*, 51(1):155–159.

Laddha, S. S. and Danckwerts, P. V. (1981). Reaction of CO_2 with ethanolamines: kinetics from gas-absorption. *Chemical Engineering Science*, 36:479–482.

Lafitte, T., Apostolakou, A., Avendano, C., Galindo, A., Adjiman, C. S., Müller, E. A., and Jackson, G. (2013a). Accurate statistical associating fluid theory for chain molecules formed from mie segments. *The Journal of chemical physics*, 139(15):154504.

Lafitte, T., Apostolakou, A., Avendaño, C., Galindo, A., Adjiman, C. S., Müller, E. A., and Jackson, G. (2013b). Accurate statistical associating fluid theory for chain molecules formed from Mie segments. *The Journal of Chemical Physics*, 139(15):154504.

Lafitte, T., Bessières, D., Piñeiro, M. M., and Daridon, J.-L. (2006a). Simultaneous estimation of phase behavior and second-derivative properties using the statistical associating fluid theory with variable range approach. *The Journal of Chemical Physics*, 124(2):024509.

Lafitte, T., Bessieres, D., Piñeiro, M. M., and Daridon, J.-L. (2006b). Simultaneous estimation of phase behavior and second-derivative properties using the statistical associating fluid theory with variable range approach. *The Journal of Chemical Physics*, 124(2):024509.

Lafitte, T., Mendiboure, B., Pineiro, M. M., Bessieres, D., and Miqueu, C. (2010). Interfacial properties of water/co2: a comprehensive description through a gradient theory- saft-vr mie approach. *The Journal of Physical Chemistry B*, 114(34):11110–11116.

Lafitte, T., Papaioannou, V., Dufal, S., and Pantelides, C. C. (2017). gsaft: Advanced physical property prediction for process modelling. In *Computer Aided Chemical Engineering*, volume 40, pages 1003–1008. Elsevier.

Lafitte, T., Piñeiro, M. M., Daridon, J.-L., and Bessières, D. (2007). A comprehensive description of chemical association effects on second derivative properties of alcohols through a SAFT-VR approach. *Journal of Physical Chemistry B*, 111:3447–3461.

Lampe, M., Stavrou, M., Schilling, J., Sauer, E., Gross, J., and Bardow, A. (2015). Computer-aided molecular design in the continuous-molecular targeting framework using group-contribution PC-SAFT. *Computers & Chemical Engineering*, 81:278–287.

Lawal, A., Wang, M., Stephenson, P., Koumpouras, G., and Yeung, H. (2010). Dynamic modelling and analysis of post-combustion CO_2 chemical absorption process for coal-fired power plants. *Fuel*, 89(10):2791–2801.

Lawal, A., Wang, M., Stephenson, P., and Yeung, H. (2009). Dynamic modelling of CO_2 absorption for post combustion capture in coal-fired power plants. *Fuel*, 88(12):2455–2462.

Leibush, A. G. and Shorina, E. D. (1947). Physico-chemical properties of ethanolamines. *Zhurnal Prikladnoi Khimii*, 20:69–76.

Li, J., You, C., Chen, L., Ye, Y., Qi, Z., and Sundmacher, K. (2012). Dynamics of CO_2 absorption and desorption processes in alkanolamine with cosolvent polyethylene glycol. *Industrial & Engineering Chemistry Research*, 51:12081–12088.

Li, X.-S. and Englezos, P. (2003). Vapor- liquid equilibrium of systems containing alcohols using the statistical associating fluid theory equation of state. *Industrial & engineering chemistry research*, 42(20):4953–4961.

Li, X.-S. and Englezos, P. (2004). Vapor–liquid equilibrium of systems containing alcohols, water, carbon dioxide and hydrocarbons using saft. *Fluid phase equilibria*, 224(1):111–118.

Liessmann, G., Schmidt, W., and Reiffarth, S. (1995). Recommended thermophysical data. *Data compilation of the Saechsische Olefinwerke Boehlen Germany*, 1.

Lin, J. G. (1976). Three methods for determining pareto-optimal solutions of multiple-objective problems. In *Directions in large-scale systems*, pages 117–138. Springer.

Lindeboom, T., Fayaz-Torshizi, M., and Kiesel, M. (2019). Personal communication. unpublished.

Liu, W.-B., Li, Y.-G., and Lu, J.-F. (1999). A new equation of state for real aqueous ionic fluids based on electrolyte perturbation theory, mean spherical approximation and statistical associating fluid theory. *Fluid Phase Equilibria*, 158-160:595–606.

Llano-Restrepo, M. and Araujo-Lopez, E. (2015). Modeling and simulation of packed-bed absorbers for post-combustion capture of carbon dioxide by reactive absorption in aqueous monoethanolamine solutions. *International Journal of Greenhouse Gas Control*, 42:258–287.

Llovell, F., Galindo, A., Blas, F. J., and Jackson, G. (2010). Classical density functional theory for the prediction of the surface tension and interfacial properties of fluids mixtures of chain molecules based on the statistical associating fluid theory for potentials of variable range. *The Journal of Chemical Physics*, 133(2):024704.

Llovell, F. and Vega, L. F. (2006). Prediction of thermodynamic derivative properties of pure fluids through the soft-saft equation of state. *The Journal of Physical Chemistry B*, 110(23):11427–11437.

Luck, W. A. (1980). A model of hydrogen-bonded liquids. *Angewandte Chemie International Edition in English*, 19(1):28–41.

Lymperiadis, A., Adjiman, C. S., Galindo, A., and Jackson, G. (2007). A group contribution method for associating chain molecules based on the statistical associating fluid theory (SAFT-γ). *The Journal of Chemical Physics*, 127(23):234903.

Lymperiadis, A., Adjiman, C. S., Jackson, G., and Galindo, A. (2008a). A generalisation of the SAFT-γ group contribution method for groups comprising multiple spherical segments. *Fluid Phase Equilibria*, 274(1-2):85–104.

Lymperiadis, A., Adjiman, C. S., Jackson, G., and Galindo, A. (2008b). A generalisation of the saft-group contribution method for groups comprising multiple spherical segments. *Fluid Phase Equilibria*, 274(1):85–104.

Mac Dowell, N. (2010). *The integration of advanced molecular thermodynamics and process modelling for the design of amine-based CO_2 capture processes*. PhD thesis, Imperial College London.

Mac Dowell, N., Florin, N., Buchard, A., Hallett, J., Galindo, A., Jackson, G., Adjiman, C. S., Williams, C. K., Shah, N., and Fennell, P. (2010). An overview of co_2 capture technologies. *Energy & Environmental Science*, 3(11):1645–1669.

Mac Dowell, N., Galindo, A., Jackson, G., and Adjiman, C. S. (2010). Integrated solvent and process design for the reactive separation of CO_2 from flue gas. In Pierucci, S. and Ferraris, B. G., editors, *Computer Aided Process Engineering*, volume 28 of *Computer-Aided Chemical Engineering*, pages 1231–1236.

Mac Dowell, N., Llovell, F., Adjiman, C., Jackson, G., and Galindo, A. (2009). Modeling the fluid phase behavior of carbon dioxide in aqueous solutions of monoethanolamine using transferable parameters with the saft-vr approach. *Industrial & Engineering Chemistry Research*, 49(4):1883–1899.

Mac Dowell, N., Llovell, F., Adjiman, C. S., Jackson, G., and Galindo, A. (2010). Modeling the Fluid Phase Behavior of Carbon Dioxide in Aqueous Solutions of Monoethanolamine Using Transferable Parameters with the SAFT-VR Approach. *Industrial & Engineering Chemistry Research*, 49(4):1883–1899.

Mac Dowell, N., Pereira, F. E., Llovell, F., Blas, F. J., Adjiman, C. S., Jackson, G., and Galindo, A. (2011). Transferable SAFT-VR models for the calculation of the fluid phase equilibria in reactive mixtures of carbon dioxide, water, and n-alkylamines in the context of carbon capture. *The Journal of Physical Chemistry B*, 115(25):8155–8168. PMID: 21634388.

Mac Dowell, N., Samsatli, N. J., and Shah, N. (2013). Dynamic modelling and analysis of an amine-based post-combustion CO_2 capture absorption column. *International Journal of Greenhouse Gas Control*, 12:247–258.

Mac Dowell, N. and Shah, N. (2013). Identification of the cost-optimal degree of CO_2 capture: An optimisation study using dynamic process models. *International Journal of Greenhouse Gas Control*, 13:44–58.

Maham, Y., Liew, C. N., and Mather, A. E. (2002). Viscosities and excess properties of aqueous solutions of ethanolamines from 25 to 80C. *Journal of Solution Chemistry*, 31(9):743–756.

Mangalapally, H. P., Notz, R., Asprion, N., Sieder, G., Garcia, H., and Hasse, H. (2012). Pilot plant study of four new solvents for post combustion carbon dioxide capture by reactive absorption and comparison to MEA. *International Journal of Greenhouse Gas Control*, 8:205–216.

Mangalapally, H. P., Notz, R., Hoch, S., Asprion, N., Sieder, G., Garcia, H., and Hasse, H. (2009). Pilot plant experimental studies of post combustion CO_2 capture by reactive absorption with MEA and new solvents. In *Energy Procedia*, volume 1 of *Energy Procedia*, pages 963–970.

Marcoulaki, E., Kokossis, A., and Batzias, F. (2000). Novel chemicals for clean and efficient processes using stochastic optimization. *Computers & Chemical Engineering*, 24(2–7):705–710.

Marler, R. T. and Arora, J. S. (2004). Survey of multi-objective optimization methods for engineering. *Structural and multidisciplinary optimization*, 26(6):369–395.

Marler, R. T. and Arora, J. S. (2010). The weighted sum method for multi-objective optimization: new insights. *Structural and multidisciplinary optimization*, 41(6):853–862.

Mathias, P. M. and O'Connell, J. P. (2012). The gibbs–helmholtz equation and the thermodynamic consistency of chemical absorption data. *Industrial & Engineering Chemistry Research*, 51(13):5090–5097.

Mathonat, C., Majer, V., Mather, A. E., and Grolier, J.-P. E. (1998). Use of flow calorimetry for determining enthalpies of absorption and the solubility of co2 in aqueous monoethanolamine solutions. *Industrial & Engineering Chemistry Research*, 37(10):4136–4141.

Matin, N. S., Steckel, J. A., Thompson, J., Sarma, M., and Liu, K. (2017). Application of surface tension model for prediction of interfacial speciation of co2-loaded aqueous solutions of monoethanolamine. *Industrial & Engineering Chemistry Research*, 56(19):5747–5755.

Matthews, H. D., Solomon, S., and Pierrehumbert, R. (2012). Cumulative carbon as a policy framework for achieving climate stabilization. *Philosophical Transactions of the Royal Society of London A: Mathematical, Physical and Engineering Sciences*, 370(1974):4365–4379.

McCabe, C. and Galindo, A. (2010). SAFT associating fluids and fluid mixtures. In Goodwin, A. R. H., Sengers, J. V., and Peters, C. J., editors, *Applied Thermodynamics of Fluids*, pages 215–279. RSC Publishing.

McCabe, C. and Jackson, G. (1999). SAFT-VR modelling of the phase equilibrium of long-chain n-alkanes. *Phys. Chem. Chem. Phys.*, 1(9):2057–2064.

McCann, N., Phan, D., Wang, X., Conway, W., Burns, R., Attalla, M., Puxty, G., and Maeder, M. (2009). Kinetics and mechanism of carbamate formation from CO_2(aq), carbonate species, and monoethanolamine in aqueous solution. *The Journal of Physical Chemistry A*, 113(17):5022–5029.

Mecke, M., Winkelmann, J., and Fischer, J. (1997). Molecular dynamics simulation of the liquid–vapor interface: The lennard-jones fluid. *The Journal of chemical physics*, 107(21):9264–9270.

Morokoff, W. J. and Caflisch, R. E. (1994). Quasi-random sequences and their discrepancies. *SIAM Journal on Scientific Computing*, 15(6):1251–1279.

Neveux, T., Moullec, Y. L., Corriou, J.-P., and Favre, E. (2013). Modeling CO_2 capture in amine solvents: Prediction of performance and insights on limiting phenomena. *Industrial & Engineering Chemistry Research*, 52(11):4266–4279.

Newville, M., Stensitzki, T., Allen, D. B., Rawlik, M., Ingargiola, A., and Nelson, A. (2016). Lmfit: non-linear least-square minimization and curve-fitting for python. *Astrophysics Source Code Library*.

Ng, L. Y., Chong, F. K., and Chemmangattuvalappil, N. G. (2015). Challenges and opportunities in computer-aided molecular design. *Computers & Chemical Engineering*, 81:115–129.

Noeres, C., Kenig, E. Y., and Górak, A. (2003). Modelling of reactive separation processes: reactive absorption and reactive distillation. *Chemical Engineering and Processing*, 42:157–178.

Notz, R., Mangalapally, H. P., and Hasse, H. (2012). Post combustion CO_2 capture by reactive absorption: Pilot plant description and results of systematic studies with MEA. *International Journal of Greenhouse Gas Control*, 6:84–112.

Odele, O. and Macchietto, S. (1993). Computer aided molecular design: a novel method for optimal solvent selection. *Fluid Phase Equilibria*, 82(0):47–54.

Olajire, A. A. (2010). CO_2 capture and separation technologies for end-of-pipe applications — A review. *Energy*, 35:2610–2628.

Oliveira, M., Llovell, F., Coutinho, J., and Vega, L. (2016). New procedure for enhancing the transferability of statistical associating fluid theory (SAFT) molecular parameters: the role of derivative properties. *Industrial & Engineering Chemistry Research*, 55(37):10011–10024.

Onda, K., Sada, E., and Takeuchi, H. (1968a). Gas absorption with chemical reaction in packed columns. *Journal of Chemical Engineering of Japan*, 1:62–66.

Onda, K., Takeuchi, H., and Okumoto, Y. (1968b). Mass transfer coefficient between gas and liquid phases in packed columns. *Journal of Chemical Engineering of Japan*, 1:56–62.

Pacheco, M. A. and Rochelle, G. T. (1998). Rate-based modeling of reactive absorption of CO_2 and H_2S into aqueous methyldiethanolamine. *Industrial & Engineering Chemistry Research*, 37:4107–4117.

Pandya, J. D. (1983). Adiabatic gas-absorption and stripping with chemical-reaction in packed towers. *Chemical Engineering Communications*, 19(4-6):343–361.

Papadokonstantakis, S., Badr, S., Hungerbühler, K., Papadopoulos, A. I., Damartzis, T., Seferlis, P., Forte, E., Chremos, A., Galindo, A., Jackson, G., and Adjiman, C. S. (2015). Toward sustainable solvent-based postcombustion CO_2 capture: From molecules to conceptual flowsheet design. In You, F., editor, *Sustainability of Products, Processes and Supply ChainsTheory and Applications*, volume 36 of *Computer Aided Chemical Engineering*, chapter 11, pages 279–310. Elsevier.

Papadopoulos, A. I. and Linke, P. (2006). Efficient integration of optimal solvent and process design using molecular clustering. *Chemical Engineering Science*, 61:6316–6336.

Papaioannou, V. (2013). *A molecular-based group contribution equation of state for the description of fluid phase behaviour and thermodynamic derivative properties of mixtures*. PhD thesis, Imperial College London.

Papaioannou, V., Adjiman, C. S., Jackson, G., and Galindo, A. (2011a). Group contribution methodologies for the prediction of thermodynamic properties and phase behavior in mixtures. In Pistikopoulos, E. N., Georgiadia, M. C., and Dua, V., editors, *Process Systems Engineering: Molecular Systems Engineering*, volume 6, chapter 4, pages 135–172. Wiley-VCH, Weinheim, Germany.

Papaioannou, V., Adjiman, C. S., Jackson, G., and Galindo, A. (2011b). Simultaneous prediction of vapour–liquid and liquid–liquid equilibria (VLE and LLE) of aqueous mixtures with the SAFT-γ group contribution approach. *Fluid Phase Equilibria*, 306(1):82–96.

Papaioannou, V., Calado, F., Lafitte, T., Dufal, S., Sadeqzadeh, M., Jackson, G., Adjiman, C. S., and Galindo, A. (2016). Application of the SAFT-γ Mie group contribution equation of state to fluids of relevance to the oil and gas industry. *Fluid Phase Equilibria*, 416:104–119.

Papaioannou, V., Lafitte, T., Avendaño, C., Adjiman, C. S., Jackson, G., Müller, E. A., and Galindo, A. (2014). Group contribution methodology based on the statistical associating fluid theory for heteronuclear molecules formed from Mie segments. *The Journal of Chemical Physics*, 140(5):054107.

Paricaud, P., Galindo, A., and Jackson, G. (2004a). Modeling the cloud curves and the solubility of gases in amorphous and semicrystalline polyethylene with the SAFT-VR approach and Flory theory of crystallization. *Industrial & Engineering Chemistry Research*, 43:6871–6889.

Paricaud, P., Galindo, A., and Jackson, G. (2004b). Modeling the Cloud Curves and the Solubility of Gases in Amorphous and Semicrystalline Polyethylene with the SAFT-VR Approach and Flory Theory of Crystallization. *Industrial & Engineering Chemistry Research*, 43(21):6871–6889.

Paricaud, P., Tazi, L., and Borgard, J. (2010). Modeling the phase equilibria of the HIx mixture using the SAFT-VRE equation of state: Binary systems. *International Journal of Hydrogen Energy*, 35(3):978–991.

Park, Y., Lin, K.-Y. A., Park, A.-H. A., and Petit, C. (2015). Recent advances in anhydrous solvents for co_2 capture: ionic liquids, switchable solvents, and nanoparticle organic hybrid materials. *Frontiers in Energy Research*, 3:42.

Pascoletti, A. and Serafini, P. (1984). Scalarizing vector optimization problems. *Journal of Optimization Theory and Applications*, 42(4):499–524.

Patel, B. H., Paricaud, P., Galindo, A., and Maitland, G. C. (2003a). Prediction of the Salting-Out Effect of Strong Electrolytes on Water + Alkane Solutions. *Industrial & Engineering Chemistry Research*, 42(16):3809–3823.

Patel, B. H., Paricaud, P., Galindo, A., and Maitland, G. C. (2003b). Prediction of the salting-out effect of strong electrolytes on water+ alkane solutions. *Industrial & engineering chemistry research*, 42(16):3809–3823.

Paul, S., Ghoshal, A. K., and Mandal, B. (2008). Theoretical studies on separation of CO_2 by single and blended aqueous alkanolamine solvents in flat sheet membrane contactor (FSMC). *Chemical Engineering Journal*, 144(3):352–360.

Peleteiro, J., Troncoso, J., González-Salgado, D., Valencia, J., Cerdeirina, C., and Romani, L. (2004). Anomalous excess heat capacities of ethanol+ alkane mixtures. *International journal of thermophysics*, 25(3):787–803.

Peleteiro, J., Troncoso, J., González-Salgado, D., Valencia, J., Souto-Caride, M., and Romani, L. (2005). Excess isobaric molar heat capacities and excess molar volumes for ethanol+ n-decane and n-undecane systems. *The Journal of Chemical Thermodynamics*, 37(9):935–940.

Peng, Y., Goff, K. D., dos Ramos, M. C., and McCabe, C. (2009). Developing a predictive group-contribution-based SAFT-VR equation of state. *Fluid Phase Equilibria*, 277(2):131–144.

Penny, D. E. and Ritter, T. J. (1983). Kinetic study of the reaction between carbon dioxide and primary amines. *Journal of the Chemical Society, Faraday Transactions 1*, 79(9):2103–2109.

Pereira, F. E., Keskes, E., Galindo, A., Jackson, G., and Adjiman, C. S. (2008). *Integrated Design of CO_2 Capture Processes from Natural Gas*, volume 6 of *Process Systems Engineering*, pages 231–248. Wiley-VCH, Weinheim, Germany.

Pereira, F. E., Keskes, E., Galindo, A., Jackson, G., and Adjiman, C. S. (2011a). Integrated solvent and process design using a SAFT-VR thermodynamic description: High-pressure separation of carbon dioxide and methane. *Computers & Chemical Engineering*, 35:474–491.

Pereira, F. E., Keskes, E., Galindo, A., Jackson, G., and Adjiman, C. S. (2011b). Integrated solvent and process design using a SAFT-VR thermodynamic description: High-pressure separation of carbon dioxide and methane. *Computers & Chemical Engineering*, 35(3):474–491.

Pereira, L. M., Chapoy, A., Burgass, R., Oliveira, M. B., Coutinho, J. A., and Tohidi, B. (2016). Study of the impact of high temperatures and pressures on the equilibrium densities and interfacial tension of the carbon dioxide/water system. *The Journal of Chemical Thermodynamics*, 93:404–415.

Perkins, L. R. and Geankoplis, C. J. (1969). Molecular diffusion in a ternary liquid system with the diffusing component dilute. *Chemical Engineering Science*, 24(7):1035–1042.

Perry, R. H. and Green, D. W. (2008). *Perry's Chemical Engineers' Handbook*. McGraw Hill, 6th edition.

Pintola, T., Tontiwachwuthikul, P., and Meisen, A. (1993). Simulation of pilot plant and industrial CO_2-MEA absorbers. *Gas Separation and Purification*, 7(1):47–52.

Poling, B. E., Prausnitz, J. M., and O'Connell, J. P. (2001). *The properties of gases and liquids*, volume 5. McGraw-Hill Education: New York, 5th edition.

Potoff, J. J. and Panagiotopoulos, A. Z. (2000). Surface tension of the three-dimensional lennard-jones fluid from histogram-reweighting monte carlo simulations. *The Journal of Chemical Physics*, 112(14):6411–6415.

Prausnitz, J. M., Lichtenthaler, R. N., and de Azevedo, E. G. (1998). *Molecular thermodynamics of fluid-phase equilibria*. Pearson Education.

Privat, R., Gani, R., and Jaubert, J.-N. (2010). Are safe results obtained when the pc-saft equation of state is applied to ordinary pure chemicals? *Fluid Phase Equilibria*, 295(1):76–92.

Process Systems Enterprise (1997-2016). gPROMS ModelBuilder v4.2.0. http://www.psenterprise.com.

Ramrattan, N. S., Avendaño, C., Müller, E. A., and Galindo, A. (2015). A corresponding-states framework for the description of the Mie family of intermolecular potentials. *Molecular Physics*, 113:932–947.

Rangaiah, G. P. (2009). *Multi-objective optimization: techniques and applications in chemical engineering*, volume 1. World Scientific.

Raupach, M. R. (2013). The exponential eigenmodes of the carbon-climate system, and their implications for ratios of responses to forcings. *Earth System Dynamics*, 4(1):31–49.

Reid, R. C., Prausnitz, J. M., and Sherwood, T. K. (1977). The properties of gases and liquids. McGraw-Hill, 3rd edition.

Rennen, B. G., Dam, E. R. V., and Hertog, D. D. (2009). Enhancement of sandwich algorithms for approximating higher dimensional convex Pareto sets.

Rocha, J. A., Bravo, J. L., and Fair, J. R. (1993). Distillation Columns Containing Structured Packings:. *Industrial & Engineering Chemistry Research*, 32(4):641–651.

Rocha, J. A., Bravo, J. L., and Fair, J. R. (1996). Distillation columns containing structured packings: A comprehensive model for their performance. 2. Mass-transfer model. *Industrial & Engineering Chemistry Research*, 35(5):1660–1667.

Rodríguez, J., Mac Dowell, N., Llovell, F., Adjiman, C. S., Jackson, G., and Galindo, A. (2012). Modelling the fluid phase behaviour of aqueous mixtures of multifunctional alkanolamines and carbon dioxide using transferable parameters with the SAFT-VR approach. *Molecular Physics*, 110(11-12):1325–1348.

Rubini, K., Francesconi, R., Bigi, A., and Comelli, F. (2007). Excess molar enthalpies and heat capacities of dimethyl sulfoxide+ seven normal alkanols at 303.15 k and atmospheric pressure. *Thermochimica acta*, 452(2):124–127.

Sadegh, N., Stenby, E. H., and Thomsen, K. (2015). Thermodynamic modeling of CO_2 absorption in aqueous N-methyldiethanolamine using Extended UNIQUAC model. *Fuel*, 144:295–306.

Sadeqzadeh, M., Papaioannou, V., Dufal, S., Adjiman, C. S., Jackson, G., and Galindo, A. (2016). The development of unlike induced association-site models to study the phase behaviour of aqueous mixtures comprising acetone, alkanes and alkyl carboxylic acids with the SAFT-γ Mie group contribution methodology. *Fluid Phase Equilibria*, 407:39–57.

Saimpert, M., Puxty, G., Qureshi, S., Wardhaugh, L., and Cousins, A. (2013). A new rate based absorber and desorber modelling tool. *Chemical Engineering Science*, 96:10–25.

Salazar, J., Diwekar, U., Joback, K., Berger, A. H., and Bhown, A. S. (2013). Solvent selection for post-combustion co_2 capture. *Energy Procedia*, 37:257 – 264. GHGT-11.

Salkuyeh, Y. K. and Mofarahi, M. (2012). Reduction of CO_2 capture plant energy requirement by selecting a suitable solvent and analyzing the operating parameters. *International Journal of Energy Research*, 37(8):973–981.

Samudra, A. P. and Sahinidis, N. V. (2013). Optimization-based framework for computer-aided molecular design. *AIChE Journal*, 59:3686–3701.

Sartori, G. and Savage, D. W. (1983). Sterically hindered amines for carbon dioxide removal from gases. *Industrial & Engineering Chemistry Fundamentals*, 22:239–249.

Sauer, E., Stavrou, M., and Gross, J. (2014). Comparison between a homo- and a heterosegmented group contribution approach based on the perturbed-chain polar statistical associating fluid theory equation of state. *Industrial & Engineering Chemistry Research*, 53:14854–14864.

Sauer, S. G. and Chapman, W. G. (2003). A parametric study of dipolar chain theory with applications to ketone mixtures. *Industrial & Engineering Chemistry Research*, 42:5687–5696.

Schreckenberg, J. M., Dufal, S., Haslam, A. J., Adjiman, C. S., Jackson, G., and Galindo, A. (2014). Modelling of the thermodynamic and solvation properties of electrolyte solutions with the statistical associating fluid theory for potentials of variable range. *Molecular Physics*, 112(17):2339–2364.

Sear, R. P. and Jackson, G. (1994a). Thermodynamic perturbation theory for association into chains and rings. *Physical Review E*, 50(1):386–394.

Sear, R. P. and Jackson, G. (1994b). Thermodynamic perturbation theory for association into doubly bonded dimers. *Molecular Physics*, 82(5):1033–1048.

Sear, R. P. and Jackson, G. (1996a). The ring integral in a thermodynamic perturbation theory for association. *Molecular Physics*, 87(2):517–521.

Sear, R. P. and Jackson, G. (1996b). Thermodynamic perturbation theory for association with bond cooperativity. *The Journal of Chemical Physics*, 105(3):1113–1120.

Sear, R. P. and Jackson, G. (1996c). Thermodynamic perturbation theory for association with bond cooperativity. *The Journal of chemical physics*, 105(3):1113–1120.

Serna, J. I. (2009). Physics in Medicine & Biology Trade-off bounds for the Pareto surface approximation in multi-criteria IMRT planning Trade-off bounds for the Pareto surface approximation in multi-criteria IMRT planning.

Sheldon, T., Giner, B., Adjiman, C., Galindo, A., Jackson, G., Jacquemin, D., Wathelet, V., and Perpete, E. (2006). The derivation of size parameters for the SAFT–VR equation of state from quantum mechanical calculations. In *Computer Aided Chemical Engineering*, volume 22, pages 143–159. Elsevier.

Sivasubramanian, M. S., Sardar, H., and Weiland, R. H. (1985). Simulation mirrors commercial amine units. *Oil & Gas Journal*, 83(40):133–136.

Sobol', I. M. (1967). On the distribution of points in a cube and the approximate evaluation of integrals. *Zhurnal Vychislitel'noi Matematiki i Matematicheskoi Fiziki*, 7(4):784–802.

Solanki, R. S., Appino, P. A., and Cohon, J. L. (1993). Approximating the noninferior set in multiobjective linear programming problems. *European Journal of Operational Research*, 68(3):356–373.

Song, Y. and Chen, C.-C. (2009). Symmetric electrolyte nonrandom two-liquid activity coefficient model. *Industrial & Engineering Chemistry Research*, 48:7788–7797.

Songolzadeh, M., Soleimani, M., Ravanchi, M. T., and Songolzadeh, R. (2014). Carbon dioxide separation from flue gases: A technological review emphasizing reduction in greenhouse gas emissions. *The Scientific World Journal*, 2014.

Sreenivasulu, B., Gayatri, D., Sreedhar, I., and Raghavan, K. (2015). A journey into the process and engineering aspects of carbon capture technologies. *Renewable and Sustainable Energy Reviews*, 41:1324–1350.

Sun, R. and Dubessy, J. (2010). Prediction of vapor–liquid equilibrium and pvtx properties of geological fluid system with saft-lj eos including multi-polar contribution. part i: Application to h2o–co2 system. *Geochimica et Cosmochimica Acta*, 74(7):1982–1998.

Svendsen, H. F., Hessen, E. T., and Mejdell, T. (2011). Carbon dioxide capture by absorption, challenges and possibilities. *Chemical Engineering Journal*, 171(3):718–724.

Svensson, H., Hulteberg, C., and Karlsson, H. T. (2013). Heat of absorption of co 2 in aqueous solutions of n-methyldiethanolamine and piperazine. *International Journal of Greenhouse Gas Control*, 17:89–98.

Takahashi, M., Kobayashi, Y., and Takeuchi, H. (1982). Diffusion Coefficients and Solubilities of Carbon Dioxide in Binary Mixed Solvents. *Journal of Chemical & Engineering Data*, 27(3):328–331.

Tamouza, S., Passarello, J.-P., Tobaly, P., and de Hemptinne, J.-C. (2004). Group contribution method with SAFT EOS applied to vapor liquid equilibria of various hydrocarbon series. *Fluid Phase Equilibria*, 222:67–76.

Taylor, R. and Krishna, R. (1993). *Multicomponent Mass Transfer*. John Wiley & Sons.

Teng, H., Yamasaki, A., Chun, M.-K., and Lee, H. (1997). Solubility of liquid co2in water at temperatures from 278 k to 293 k and pressures from 6.44 mpa to 29.49 mpa and densities of the corresponding aqueous solutions. *The Journal of Chemical Thermodynamics*, 29(11):1301–1310.

The European Commission (2011). A Roadmap for Moving to a Competitive Low Carbon Economy in 2050. http://eur-lex.europa.eu/legal-content/EN/TXT/PDF/?uri=CELEX:52011DC0112&from=EN.

Thi, T. X. N., Tamouza, S., Tobaly, P., Passarello, J.-P., and de Hemptinne, J.-C. (2005). Application of group contribution SAFT equation of state (GC-SAFT) to model phase behaviour of light and heavy esters. *Fluid Phase Equilibria*, 238(2):254–261.

Thomsen, K. and Rasmussen, P. (1999). Modeling of vapor–liquid–solid equilibrium in gas–aqueous electrolyte systems. *Chemical Engineering Science*, 54(12):1787–1802.

Thomson, G. (1996). The dippr® databases. *International journal of thermophysics*, 17(1):223–232.

Tihic, A., Kontogeorgis, G. M., von Solms, N., Michelsen, M. L., and Constantinou, L. (2007). A predictive group-contribution simplified PC-SAFT equation of state: Application to polymer systems. *Industrial & Engineering Chemistry Research*, 47:5092–5101.

Tobiesen, F. A. and Svendsen, H. F. (2006). Study of a Modified Amine-Based Regeneration Unit. *Industrial & Engineering Chemistry Research*, 45(8):2489–2496.

Tobiesen, F. A., Svendsen, H. F., and Juliussen, O. (2007). Experimental validation of a rigorous absorber model for CO_2 postcombustion capture. *AIChE Journal*, 53(4):846–865.

Tontiwachwuthikul, P., Meisen, A., and Lim, C. J. (1989). Novel pilot plant tchniques for sizing gas absorbers with chemical reactions. *The Canadian Journal of Chemical Engineering*, 67(4):602–607.

Tontiwachwuthikul, P., Meisen, A., and Lim, C. J. (1992). CO_2 absorption by NaOH, monoethanolamine and 2-amino-2-methyl-1-propanol solutions in a packed column. *Chemical Engineering Science*, 47(2):381–390.

Treybal, R. E. (1981). *Mass-Transfer Operations*. McGraw-Hill, 3rd edition.

Tumakaka, F., Gross, J., and Sadowski, G. (2005). Thermodynamic modeling of complex systems using PC-SAFT. *Fluid Phase Equilibria*, 228:89–98.

Tumakaka, F. and Sadowski, G. (2004). Application of the perturbed-chain SAFT equation of state to polar systems. *Fluid Phase Equilibria*, 217(2):233–239.

UNFCCC (2015). Adoption of the Paris Agreement. https://unfccc.int/resource/docs/2015/cop21/eng/l09r01.pdf.

van Swaaij, W. P. M. and Versteeg, G. F. (1992). Mass transfer accompanied with complex reversible chemical reactions in gas—liquid systems: an overview. *Chemical Engineering Science*, 47(13-14):3181–3195.

Vázquez, G., Alvarez, E., Navaza, J. M., Rendo, R., and Romero, E. (1997). Surface tension of binary mixtures of water+ monoethanolamine and water+ 2-amino-2-methyl-1-propanol and tertiary mixtures of these amines with water from 25 c to 50 c. *Journal of Chemical & Engineering Data*, 42(1):57–59.

Vazquez, G., Alvarez, E., Navaza, J. M., Rendo, R., and Romero, E. (1997). Surface tension of binary mixtures of water plus monoethanolamine and water plus 2-amino-2-methyl-1-propanol and tertiary mixtures of these amines with water from 25 degrees C to 50 degrees C. *Journal of Chemical & Engineering Data*, 42(1):57–59.

Vijande, J., Pineiro, M., Bessieres, D., Saint-Guirons, H., and Legido, J. (2004). Description of PVT behaviour of hydrofluoroethers using the PC-SAFT EOS. *Physical Chemistry Chemical Physics*, 6(4):766–770.

von Solms, N., Michelsen, M. L., and Kontogeorgis, G. M. (2003). Computational and physical performance of a modified PC-SAFT equation of state for highly asymmetric and associating mixtures. *Industrial & Engineering Chemistry Research*, 42:1098–1105.

Voutsas, E. C., Boulougouris, G. C., Economou, I. G., and Tassios, D. P. (2000). Water/hydrocarbon phase equilibria using the thermodynamic perturbation theory. *Industrial & engineering chemistry research*, 39(3):797–804.

Wang, T., El Ahmar, E., Coquelet, C., and Kontogeorgis, G. M. (2018a). Improvement of the pr-cpa equation of state for modelling of acid gases solubilities in aqueous alkanolamine solutions. *Fluid Phase Equilibria*, 471:74–87.

Wang, Y. and Achenie, L. E. (2002). Computer aided solvent design for extractive fermentation. *Fluid Phase Equilibria*, 201(1):1–18.

Wang, Y., Biegler, L. T., Patel, M., and Wassick, J. (2018b). Parameters estimation and model discrimination for solid-liquid reactions in batch processes. *Chemical Engineering Science*, 187:455–469.

Weiland, R. H., Dingman, J. C., and Cronin, D. B. (1997). Heat capacity of aqueous monoethanolamine, diethanolamine, n-methyldiethanolamine, and n-methyldiethanolamine-based blends with carbon dioxide. *Journal of Chemical & Engineering Data*, 42(5):1004–1006.

Weiland, R. H., Rawal, M., and Rice, R. G. (2004). Stripping of carbon dioxide from monoethanolamine solutions in a packed column. *AIChE Journal*, 28(6):963–973.

Wertheim, M. S. (1984a). Fluids with highly directional attractive forces. 1. Statistical thermodynamics. *Journal of Statistical Physics*, 35(1-2):19–34.

Wertheim, M. S. (1984b). Fluids with highly directional attractive forces. 2. Thermodynamic perturbation-theory and integral-equations. *Journal of Statistical Physics*, 35(1-2):35–47.

Wertheim, M. S. (1986a). Fluids with highly directional attractive forces. 3. Multiple attraction sites. *Journal of Statistical Physics*, 42(3-4):459–476.

Wertheim, M. S. (1986b). Fluids with highly directional attractive forces. 4. Equilibrium polymerization. *Journal of Statistical Physics*, 42(3-4):477–492.

Westmeier, S. (1977). Excess enthalpy, free excess enthalpy, excess volume and viscosity of selected binary-liquid mixtures. 4. Systems water-tertiary butanol and water- secondary butanol. *Chemische Technik*, 29(4):218–222.

Wilke, C. and Chang, P. (1955). Correlation of diffusion coefficients in dilute solutions. *AIChE Journal*, 1(2):264–270.

Wolbach, J. P. and Sandler, S. I. (1997). Using molecular orbital calculations to describe the phase behavior of hydrogen-bonding fluids. *Industrial & engineering chemistry research*, 36(10):4041–4051.

Wu, J. and Prausnitz, J. M. (1998). Phase equilibria for systems containing hydrocarbons, water, and salt: An extended peng- robinson equation of state. *Industrial & Engineering Chemistry Research*, 37(5):1634–1643.

Xu, Q. and Rochelle, G. (2011). Total pressure and co2 solubility at high temperature in aqueous amines. *Energy Procedia*, 4:117–124.

Ying, J. and Eimer, D. A. (2013). Determination and measurements of mass transfer kinetics of CO_2 in concentrated aqueous monoethanolamine solutions by a stirred cell. *Industrial & Engineering Chemistry Research*, 52(7):2548–2559.

Yu, C.-H., Huang, C.-H., and Tan, C.-S. (2012). A review of CO_2 capture by absorption and adsorption. *Aerosol and Air Quality Research*, 12:745–769.

YV, Y. H., Lasdon, L. S., and DA WISMER, D. (1971). On a bicriterion formation of the problems of integrated system identification and system optimization. *IEEE Transactions on Systems, Man and Cybernetics*, (3):296–297.

Zadeh, L. (1963). Optimality and non-scalar-valued performance criteria. *IEEE transactions on Automatic Control*, 8(1):59–60.

Zarogiannis, T., Papadopoulos, A. I., and Seferlis, P. (2016). Systematic selection of amine mixtures as post-combustion CO_2 capture solvent candidates. *Journal of Cleaner Production*, pages –.

Zhang, J., Agar, D. W., Zhang, X., and Geuzebroek, F. (2011a). CO_2 absorption in biphasic solvents with enhanced low temperature solvent regeneration. *Energy Procedia*, 4:67–74.

Zhang, J., Misch, R., Tan, Y., and Agar, D. W. (2011b). Novel thermomorphic biphasic amine solvents for CO_2 absorption and low-temperature extractive regeneration. *Chemical Engineering & Technology*, 34:1481–1489.

Zhang, J., Qiao, Y., and Agar, D. W. (2012a). Improvement of lipophilic-amine-based thermomorphic biphasic solvent for energy-efficient carbon capture. *Energy Procedia*, 23:92–101.

Zhang, J., Qiao, Y., and Agar, D. W. (2012b). Intensification of low temperature thermomorphic biphasic amine solvent regeneration for CO_2 capture. *Chemical Engineering Research and Design*, 90(6):743–749.

Zhang, Y., Que, H., and Chen, C.-C. (2011c). Thermodynamic modeling for CO_2 absorption in aqueous MEA solution with electrolyte NRTL model. *Fluid Phase Equilibria*, 311:67–75.

Zhao, H. and McCabe, C. (2006). Phase behavior of dipolar fluids from a modified statistical associating fluid theory for potentials of variable range. *The Journal of Chemical Physics*, 125(10):104504.

Zhou, T., McBride, K., Zhang, X., Qi, Z., and Sundmacher, K. (2015). Integrated solvent and process design exemplified for a diels–alder reaction. *AIChE Journal*, 61:147–158.

Zollweg, J. A. and Mulholland, G. W. (1972). On the law of the rectilinear diameter. *The Journal of Chemical Physics*, 57(3):1021–1025.

Zuiderweg, F. and Harmens, A. (1958). The influence of surface phenomena on the performance of distillation columns. *Chemical Engineering Science*, 9(2-3):89–103.